The Dissertation Committee for Holly Ann Balasubramanian certifies that this is the approved version of the following dissertation:

Heat-Mass-Momentum Transfer in Hollow Fiber Spinning

Committee:

Douglas R. Lloyd, Supervisor

G. Glenn Lipscomb

Roger T. Bonnecaze

Benny D. Freeman

Linda J. Hayes

Tess J. Moon

Heat-Mass-Momentum Transfer in Hollow Fiber Spinning

by

Holly Ann Balasubramanian, B.S., M.S.

Dissertation

Presented to the Faculty of the Graduate School of

The University of Texas at Austin

in Partial Fulfillment

of the Requirements

for the Degree of

Doctor of Philosophy

The University of Texas at Austin

December 2004

Dedication

To my family and true friends, who always support me without question and are always there to remind me of what is important.

Acknowledgments

First and foremost, I wish to thank my advisor, Douglas R. Lloyd, and my committee consisting of G. Glenn Lipscomb, Roger T. Bonnecaze, Benny D. Freeman, Tess J. Moon, and Linda J. Hayes. The encouragement, patience, and advice of these individuals made this research possible. I also appreciate the research collaborations that have greatly supplemented my academic experience, including a project exchange involving travel to Kyoto, Japan. I want to thank Hideto Matsuyama and his students; Akihiro Ariji; Takuya Hasegawa; and Takaaki Tanaka for helpful discussions and gracious hosting extended to me and my labmate, Jason Morehouse. Additionally, industrial collaboration with Baxter International Inc. proved very helpful in the completion of this research: many thanks to Tim Meluch, Mary Ann Murphy, Tom Sutliff, and S. Mookie Sternberg. John R. Howell, Mirko Gamba, Michael Schmerling, K. Irani, Gina Paroline, Professor Raul Quijada, and Wilfredo Yave very graciously assisted with system characterization and analysis of results during the course of this work. In addition, thanks are due to Melanie Batarseh, Paul Atkinson, Stefan Martula, Amy Nelson, Simon Sierra, James Stiehl, and M'Lissa Cortez for helping get this research off the ground. I also must thank Eddie Oliver, Mark Smith, Jim Smitherman, Kevin Haynes, Randy Rife, T. Stockman, Kay Swift, Eddie Ibarra, and Tammy McDade, UT employees who were always available to solve problems that no one else could. I am also very grateful to all the sources of financial support that contributed to this research, including the National Science Foundation, Department of Commerce Advanced Technology Program, and the UT College of Engineering through Mr. and Mrs. Lawrence and Helen Caldwell. Finally, thanks to my undergraduate professors at Tennessee Technological University, my family, and my friends for inspiration and encouragement.

Heat-Mass-Momentum Transfer in Hollow Fiber Spinning

Publication No._____________

Holly Ann Balasubramanian, Ph.D.
The University of Texas at Austin, 2004

Supervisor: Douglas R. Lloyd

The goal of this research is to develop the requisite fundamental knowledge necessary to tailor the production of hollow fiber membranes. Specifically, the focus of this work is a model describing the simultaneous heat, mass, and momentum transfer for hollow fiber membrane spinning. The model predicts radial concentration gradients and spinline dimensions as functions of axial position, as well as axial profiles of temperature, velocity, and core pressure that evolve during hollow fiber spinning. The modeling procedure requires little computational time and is applicable to hollow fiber membranes spun under various conditions.

Sensitivity of model-predicted spinline variables to surface tension effects was explored in the thin filament limit. While viscous effects dominate surface tension effects for typical pure-polymer melt spinning, membrane spinning results show that surface tension effects alter the evolution of spinline variables during the process, which can affect spinning stability.

Experimental diameter and axial velocity profiles obtained during spinning of hollow fiber membranes using a twin-screw extruder indicate that system viscosity can vary significantly due to diluent evaporation at the clad–air quench interface, which creates the concentration gradients modeled in this work. Experimental results show more rapid attenuation of the spinline than predicted by the model without accounting for the concentration dependence of viscosity. Incorporating the viscosity dependence on both concentration and temperature helps to resolve the discrepancy between model-predicted and measured spinline diameter and velocity profiles.

The sensitivity of hollow fiber membrane extent of anisotropy, the fraction of the fiber cross-section possessing a pore size gradient, to processing conditions and spinning system physical properties was examined. Results indicate that extent of anisotropy is sensitive to spinning temperature, core gas flow rate, air gap length, and diffusion coefficient, showing an increase in extent of anisotropy for an increase in these parameters. These results have important implications for membrane research, where development and optimization are largely trial-and-error approaches. This work is an important precursor to development of a complete model to predict membrane macrostructure (inner and outer diameters) and microstructure (pore size, pore size distribution, and anisotropy) as functions of spinning conditions and material properties.

Table of Contents

List of Tables

List of Figures

Chapter 1. Introduction

1.1 Research Objectives

The goal of this research was to develop the requisite fundamental knowledge necessary to tailor the production of hollow fiber membranes. Specifically, the focus of this work is a model describing the simultaneous heat, mass, and momentum transfer that occur during the spinning of hollow fiber membranes. The model predicts radial concentration gradients and spinline dimensions (inner and outer diameters) as functions of axial position, as well as the axial profiles of temperature, velocity, and core pressure that evolve during hollow fiber spinning. Henceforth in this document, “gradient” indicates variation in the radial direction, while “profile” indicates variation in the axial direction. Experimental results for the spinline outer diameter and axial velocity profiles are compared here to model predictions. Sensitivity of model-predicted spinline variables to surface tension effects is explored in the thin filament limit. In addition, the sensitivity of membrane extent of anisotropy, the fraction of the fiber cross-section possessing a pore size gradient, to processing conditions and spinning system physical properties is examined in detail with experimental comparison to model predictions.

1.2 Hollow Fiber Spinning

Hollow fiber membranes are of high commercial interest, with applications such as bioseparations (dialysis and virus removal from blood), water purification (reverse osmosis, ultrafiltration, microfiltration, and membrane bioreactors), liquid separations (pervaporation), gas separations (purification of natural gas), and membrane contactors (alternatives to gas absorbers and liquid/liquid extraction columns) at the forefront of research [1, 2]. Hollow fibers have a key advantage over other membrane configurations such as flat sheets: a high surface area to volume ratio provides the capability to achieve a given separation while occupying a much smaller space, and for this reason hollow fibers are more commonly used in industry than flat sheets [3, 4]. Use of hollow fiber membranes in typical processes involves packing them into shell-and-tube modules, an example of which appears in Figure 1.1. Such modules are typically packed to up to 60% of their volume with hollow fibers.

Figure 1.1 Hollow Fiber Membrane Module Used in the Hemodialysis Process

Numerous experimental studies characterizing the hollow fiber spinning process have been reported. These range from parametric studies that quantify the effects of various spinning parameters on specific macroscopic fiber properties, such as outer diameter and wall thickness, to experimental studies that relate process variables to hollow fiber microstructure, including surface porosity and membrane anisotropy [5-9]. Unfortunately, many of these experimental results are system-specific and thus not always applicable to a given hollow fiber spinning process. Similarly, generalized modeling work related to the hollow fiber spinning process is limited, resulting in a general lack of fundamental insight in terms of how the hollow fiber fabrication process relates to the structure and properties of the final product. To date, costly and time-consuming experimentation is often the main method for tailoring spinning process conditions to form a hollow fiber with desired properties, especially in terms of optimizing hollow fiber membrane structure for a particular application [10].

Development of a model to predict membrane macrostructure (inner and outer diameters, and thus fiber wall thickness) and microstructure (presence and characteristics of pores) as a function of processing conditions and material properties is the ideal solution to this problem. The research detailed here provides a valuable first step toward the generation of a widely applicable hollow fiber spinning model.

1.2.1 The Spinning Process for Hollow Fiber Production

In the spinning process, a polymeric sample is mixed and extruded through a spinneret, or annular die, to form a fiber. To form a hollow fiber, the extrudate (also called the clad or spinline) is usually co-extruded with a core fluid, which keeps the fiber open and hollow and potentially affects the fiber structure; alternatively, segmented arc spinnerets can be used, in which case entrained ambient air occupies and forms the fiber core [11]. The extruded filament is drawn and cooled until it solidifies and is taken up on a drum, collected much like a spool of sewing thread. Three general fiber spinning methods exist as follows [12, 13]:

1. Dry spinning: the fiber is extruded through an air gap before reaching the take-up drum
2. Wet spinning: the fiber is extruded directly into a liquid medium before take-up drum collection
3. Dry–wet or air gap spinning: the extruded fiber passes through an air gap and then into a liquid medium prior to take-up

The choice of spinning method depends on the desired scheme for fiber formation. The three processes have different implications for different spinning systems; for example, with spinning systems that contain a volatile solvent, evaporation may occur in the air gap, especially if spinning at high temperature. Similarly, the liquid medium may serve as a thermal quench and/or an exchange medium (coagulation bath) to induce phase separation or solidify the extruding fiber solution. For these situations, the solidification that follows phase separation is generally considered to occur instantaneously upon entering the liquid medium, thus restricting elongation to the air gap region. In short, depending on the physical properties of the system and the particular spinning process, prior to phase separation and/or solidification, hollow fiber spinning can involve solvent evaporation as well as cooling and elongation of the extruded filament. Evaporation, cooling, and elongation affect the dimensions (inner and outer diameters) as well as the concentration gradients and temperature profiles that develop in the fiber. These factors relate to both macrostructure (inner and outer diameters, and thus fiber wall thickness) and microstructure (presence and characteristics of pores) of the resulting hollow fibers as discussed in section 1.2.2.

Commercial hollow fiber polymer membranes are often made by an air gap spinning process with the following steps, illustrated by the schematic shown in Figure 1.2:

1. Preparing a homogeneous polymer solution
2. Forming the solution into a hollow fiber shape
3. Inducing phase separation to yield polymer-lean and polymer-rich domains
4. Solidifying the polymer-rich phase
5. Removing the polymer-lean phase to yield a micro- or nano-porous structure

For a typical dry–wet or air gap spinning process, the extruded hollow fiber spinline, in this case the nascent membrane, cools as it passes through the air gap, and some solvent is lost via evaporation. Moreover, the membrane spinline is elongated within the air gap because the take-up velocity is usually greater than the linear extrusion velocity, and the fiber is thus subjected to *draw-down*. In general, elongation stops upon entering the liquid medium as rapid interchange of components and/or rapid cooling lead directly to phase separation and fiber solidification, corresponding to a drastic increase in system viscosity. The last step, removal of the polymer-lean phase, is often a post-spinning operation.

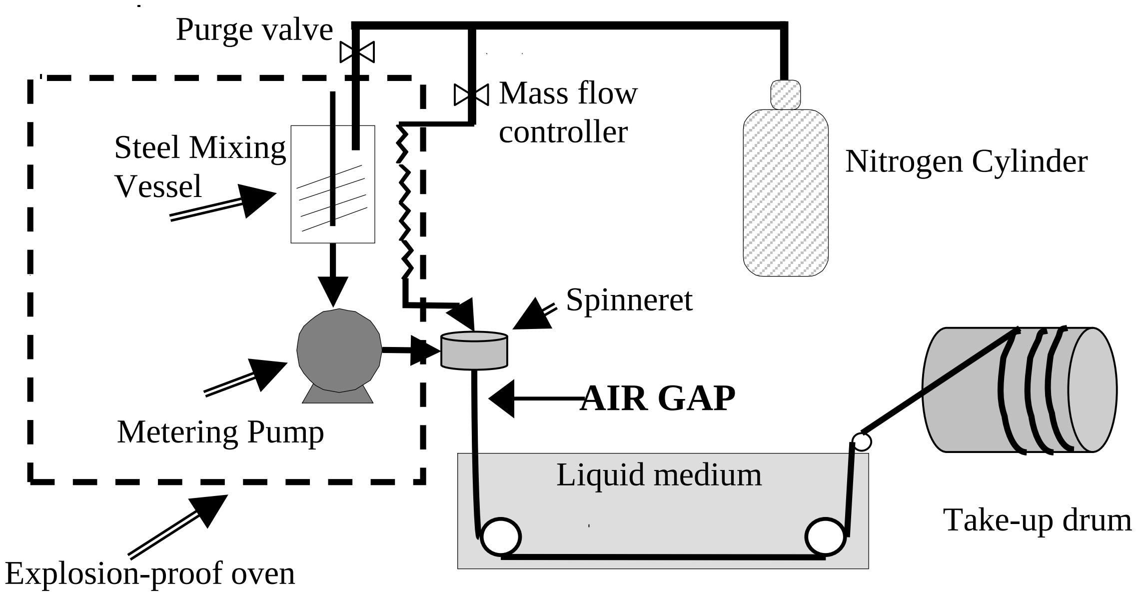

Figure 1.2 Typical Hollow Fiber Spinning Process

1.2.2 Development of Membrane Microstructure

There are two general mechanisms for phase separation during the membrane formation process: phase inversion and thermally induced phase separation (TIPS). With phase inversion, phase separation is induced by component interchange (exchange of a non-solvent for the solvent used to prepare the polymer solution) or a drying process (evaporation of solvent until phase separation and solidification occur). Both phase inversion schemes are mass transfer-based processes that have been traditionally used to make hollow fiber membranes from glassy polymers [12, 14]. In TIPS, phase separation is induced by cooling the polymer solution, and as such provides a method of making membranes from high-performance semi-crystalline polymers that are difficult to process at ambient temperatures. In addition, since heat transfer is easier to control than the multi-component mass transfer often involved with phase inversion processes, the TIPS process creates membranes more reproducibly and with fewer defects [15-17].

Regardless of the method of induction, phase separation marks the point at which the initially homogeneous solution used for membrane formation evolves into diluent-rich droplets dispersed in a viscous polymer-rich matrix, and as time passes, the diluent-rich droplet domains grow. The sizes of the diluent-rich domains in the phase-separated liquid structure relate directly to the pore sizes in the final membrane; thus, control of factors that affect the size of these domains during the spinning process before phase separation occurs is paramount to controlling the evolution of the membrane microstructure (pore size, pore size distribution, porosity, and anisotropy or gradation in pore size over the membrane cross-section). Anisotropy is of particular interest in many hollow fiber spinning applications: pore size gradients facilitate micro- and ultrafiltration by reducing internal pore blocking and thickness of the discriminating layer, thus improving permeability and throughput. Membranes that possess a pore size gradient across the membrane thickness can be characterized by the extent of anisotropy, the fraction of the membrane cross-section containing a pore size gradient [18].

Previous research, both theoretical and experimental, has shown that regardless of the phase separation mechanism involved, the growth kinetics of diluent-rich domains in the phase-separated liquid structure, and thus the membrane structure development kinetics, depend on the local temperature and local concentration [19-24]. In particular, the presence of concentration and cooling rate gradients at the time of phase separation has been shown to result in anisotropic membrane structures [25-28]. Thus, characterizing hollow fiber spinning concentration and temperature prior to phase separation is paramount to controlling membrane anisotropy.

In the air gap region during spinning, evaporation, cooling, and elongation of the filament combine to control the concentration and temperature profiles that develop in the nascent membrane prior to phase separation: the extent of evaporation and cooling directly determine the concentration gradients and temperature profiles that evolve in the spinline, and the elongation of the filament changes its dimensions, thus affecting the evaporation and cooling activity. In light of these considerations, the ability to model accurately the evaporation, cooling, and elongation occurring within the air gap prior to phase separation is crucial to the control of any hollow fiber spinning process, especially in terms of hollow fiber membrane development work.

This research strives to achieve this goal through rigorously modeling the heat–mass–momentum transport phenomena of the hollow fiber spinning process in the air gap up to the point of phase separation. Moreover, since TIPS spinning processes provide the opportunity for evaporation, cooling, and elongation to occur in the air gap during a spinning process [29], hollow fiber membranes formed via TIPS are used to challenge the spinning model developed in the course of this work.

1.2.3 Summary of Existing Membrane Formation and Spinning Literature

Several general surveys exist that discuss the history and development of membrane technology and the specifics of membrane structure and filtration transport, including the hollow fiber membrane configuration and general topics related to spinning operations [4, 18, 30-32]. In terms of published work in journals concerning the study of spinning and membrane formation, literature relates to both pure polymer melts and polymer solutions for creation of flat sheets, solid fibers, and hollow fibers [33-37].

Tan [38], Tsay [39-41], Shojaie [42-44] and coworkers present work related to modeling of flat sheet membrane formation via evaporative casting, where solvent evaporates from a polymer solution film cast on a solid support. Such flat sheet phase inversion modeling efforts center on mass balances to calculate concentration profiles across the membrane thickness as solvent evaporation occurs. Additional flat sheet membrane modeling efforts have been reported by Matsuyama [45] and Atkinson [26-28] for TIPS flat sheet membrane formation. These TIPS flat sheet models include both mass and energy balances to calculate concentration and temperature profiles across the membrane as functions of evaporation time, initial polymer concentration, sample temperature, atmospheric temperature, cooling rate, polymer molecular weight, and convection conditions above the membrane, and the authors have presented experimental results to support model predictions of the concentration profiles. However, these flat sheet modeling efforts cannot be directly applied to model properly hollow fiber spinning, even with a conversion to the proper geometry. Flat sheet models neglect momentum transfer and hollow fiber dimensional changes due to draw-down cannot be considered.

The textile industry spins solid fibers by extruding a polymer–solvent solution and allowing solvent to evaporate from the solid fiber to cause polymer solidification [46], a process similar to the evaporative casting process for flat sheets. Ohzawa [47, 48], Simon [49, 50], Chandler [51], Gou [52] and coworkers are responsible for some existing solid fiber transport models of solution spinning; however, these models are simplified to predict average concentration values over the fiber cross-section, supplemented in some cases with a separate calculation of the surface concentration, but otherwise unable to predict radial concentration gradients. Brazinsky [53] presents a model that includes radial concentration variation for spinning solid fibers, but no experimental data is given to support the concentration predictions. Finally, Tsai [54] developed a model to calculate radial concentration gradients for the optical fiber spinning process, but it ignores changes in the filament diameter, and no experimental comparison is made to validate model predictions.

In terms of previous hollow fiber spinning model efforts for solution spinning, existing work by Castellari [55] and coworkers focuses on membrane formation via phase inversion, but neglects mass transfer into the fiber lumen without justification; in addition, solvent evaporation is described empirically. Existing models for hollow fiber membranes made via the TIPS process such as the work of Berghmans [56] and Batarseh [25, 57, 58] focus on the heat and mass transfer for the spinning process, with some predictions of radial concentration gradients. However, these models neglect momentum transfer; thus, hollow fiber dimensional changes due to draw-down cannot be considered.

Discussed in the literature by Kase [34], Matovich [59], Denn [60], and coworkers, the thin filament analysis (TFA) is a widely accepted approximate analysis of solid fiber spinning of nonvolatile pure polymer melts based on the assumption of a small fiber diameter relative to draw zone length. The TFA for fiber spinning focuses on the spinning *draw zone*, where the fiber is drawn via uniaxial extension to the desired size through a quench medium (often an air gap) prior to phase separation and solidification. The TFA involves radial averaging of the axisymmetric conservation of mass, energy, and momentum equations. The final equations predict the variation of fiber inner and outer diameters, velocity, stress, and temperature with axial distance in the draw zone.

The TFA has been extended in separate efforts by Freeman *et al.* [33], Lipscomb [61], and Chung and coworkers [62] to model hollow fiber spinning. There are discrepancies among these hollow fiber TFA modeling efforts, most notably with the treatment of the core gas pressure for spinning a hollow fiber using a core gas. Freeman *et al.*treat the core gas pressure as a constant, while Chung *et al.* neglect core gas pressure profiles; in fact, the equations presented by Chung *et al.* represent the TFA for spinning with core liquids, but they are derived in an *ad hoc* fashion: the viscous force equations for the clad and core are coupled using a drag coefficient. Furthermore, Chung *et al.*include some mass transfer aspects with the description of solvent phase inversion-type mass transfer to an aqueous lumen liquid, but no solvent loss is allowed to occur at the outer radius due to evaporation. Lipscomb argues that the core gas pressure changes are essential to proper prediction of spinline variables, rigorously calculating the core gas pressure profile throughout the draw zone to allow a constant core gas mass flow rate. However, the analysis neglects the effects of surface tension. Furthermore, none of these existing TFA models of fiber spinning methodically considers spinline concentration changes. Thus, two deficiencies of the current TFA for hollow fiber spinning are failure to consider surface tension effects and failure to account for concentration changes due to evaporation of volatile components. Both omissions are concerns when applying the analysis to solution spinning, especially for modeling hollow fiber membrane spinning processes.

Commercial fluid flow modeling software packages such as FLUENT, FIDAP, POLYFLOW and FEMLAB are two- and three-dimensional (2D and 3D) approaches that can hypothetically be applied to fiber spinning processes. However, various complications arise with these options, including difficulty with specifying the free surface of the fiber to define the fiber–air interface. Modeling hollow fiber spinning in 2D and 3D domains is the focus of concurrent work at The University of Toledo as discussed in section 1.3.

This research addresses the shortcomings of existing fiber spinning models, especially in terms of applying them to the hollow fiber membrane spinning process. Specifically, the work described herein extends the thin filament analysis (TFA) for hollow fiber spinning published by Lipscomb [61], incorporating surface tension and evaporative cooling effects and modeling concentration changes in boundary layers at the fiber outer wall to predict membrane extent of anisotropy. In addition, model predictions are compared with in-line experimental spinning measurements of fiber outer diameter and axial velocity profiles, along with measured membrane extent of anisotropy in the spun hollow fiber membranes.

1.3 Significance of This Work

This research is the first systematic and fundamental study to characterize and model the impact of system physical properties and processing parameters on the heat, mass, and momentum transfer occurring during the hollow fiber spinning process as it relates to the formation of hollow fiber membranes. The major contribution of this research is a fully-coupled model capable of describing the transport phenomena occurring in an evolving hollow fiber membrane during a spinning process. The model can be used to tailor both membrane micro- and macrostructure through prediction of hollow fiber dimensions (inner and outer diameters) and hollow fiber membrane extent of anisotropy. The model, applicable up to the point of phase separation, can be used for both solid fibers and hollow fibers with core gases or liquids; furthermore, the model can be applied to any hollow fiber spinning process for which material properties (such as viscosity and density) and processing conditions (such as spinning temperature and take-up velocity) are known.

This project has been conducted concurrently with research at The University of Toledo. The work presented here ties in with prior fiber spinning work at both UT−Austin and U. Toledo, including modeling and experimental measurements for the steady-state melt hollow fiber spinning process [61], spinning sensitivity studies [61, 63], and spinning instabilities [63] as well as fiber spinning and membrane microstructure development investigations [19, 64].

Future efforts will relate the product of the research reported here to the phase separation kinetics that control the membrane microstructure development. The ultimate long-term goal is a complete model that relates hollow fiber membrane macrostructure (inner and outer diameters, and thus wall thickness) and microstructure (porosity, pore size, pore size distribution, and anisotropy) to spinning system physical properties and processing conditions for hollow fiber membrane spinning.

1.4 Structure of the Dissertation

The research objectives were accomplished using the following strategy:

1. Developing a fully coupled transport model of the hollow fiber spinning process as discussed in Chapters 2 and 3, in which the existing thin filament analysis for hollow fiber spinning [61] was modified to include the effects of surface tension and evaporative cooling and combined with a boundary layer analysis to predict membrane extent of anisotropy through modeling of concentration gradients
2. Performing sensitivity studies on the model to gauge the effects of process variables and physical parameters on the model predictions as included in Chapters 2 and 3
3. Collecting necessary physical property data for a system of interest for combined use with the model and experiments to verify model results as discussed in Chapter 4
4. Completing a parametric set of spinning experiments to validate model predictions as outlined in Chapter 4, with fibers spun using a Leistritz bench-scale twin-screw extruder setup
5. Comparing experimental results for spinline outer diameter profiles, axial velocity profiles, and membrane extent of anisotropy to predictions given by the model, drawing conclusions about model applicability, with results and discussion of results in Chapter 5, followed by conclusions and recommendations for future work in Chapter 6.

Appendix A presents the MATLAB program used for solution of the model, spinning equipment details, sample calculations, and details of some procedures and results summarized in the body of the dissertation. Appendix B contains a detailed derivation of the existing TFA for fiber spinning [61] along with additional details for the model derivation in the present research.

1.5 References

1. W.S.W. Ho, Recent developments and applications for hollow-fiber membranes, Journal of the Chinese Institute of Chemical Engineers, 34 (2003) 75-89.
2. A. Gabelman and S.T. Hwang, Hollow fiber membrane contactors, J. Membr. Sci., 159 (1999) 61-106.
3. A. Ziabicki, Fundamentals of fibre formation, John Wiley, New York, 1976.
4. M.C. Porter, Handbook of Industrial Membrane Technology, Noyes Publishing, Park Ridge, NJ, 1990. pages 604.
5. S.A. McKelvey, D.T. Clausi, and W.J. Koros, A guide to establishing hollow fiber macroscopic properties for membrane applications, J. Membr. Sci., 124 (1997) 223-232.

6. C.V. Kopp, R.J.W. Streeton, and P.S. Khoo, Hollow fibre membrane extrusion, US Patent 5,395,570, 1995.
7. H. Sun, K.B. Rhee, T. Kitano, and S.I. Mah, HDPE hollow fiber membrane via thermally induced phase separation II. Factors affecting the water permeability of the membrane, J. Appl. Polym. Sci., 75 (2000) 1235-1242.
8. A.D. Rovère, B.P. Grady, and R.L. Shambaugh, The influence of processing parameters on the properties of melt-spun polypropylene hollow fibers, J. Appl. Polym. Sci., 83 (2002) 1759-1772.
9. I.M. Wienk, F.H.A. Olde Scholtenhuis, T. van den Boomgaard, and C.A. Smolders, Spinning of hollow fiber ultrafiltration membranes from a polymer blend, J. Membr. Sci., 106 (1995) 233-243.
10. A. Idris, A.F. Ismail, M.Y. Noordin, and S.J. Shilton, Optimization of cellulose acetate hollow fiber reverse osmosis membrane production using Taguchi method, J. Membr. Sci., 205 (2002) 223-237.
11. T.H. Oh, M.S. Lee, S.Y. Kim, and H.J. Shim, Studies on melt-spinning process of hollow fibers, J. Appl. Polym. Sci., 68 (1998) 1209-1217.
12. I. Cabasso, Membranes, in: J.I. Kroschwitz (Ed.), Encyclopedia of Polymer Science and Engineering, 9, 2nd ed., John Wiley & Sons, New York, 1987.
13. S.G. Li, G.H. Koops, M.H.V. Mulder, T. Vandenboomgaard, and C.A. Smolders, Wet Spinning of Integrally Skinned Hollow-Fiber Membranes by a Modified Dual-Bath Coagulation Method Using a Triple Orifice Spinneret, J. Membr. Sci., 94 (1994) 329-340.
14. R.E. Kesting, Phase inversion membranes, in: D.R. Lloyd (Ed.), Materials Science of Synthetic Membranes, ACS Symposium Series, 269, ACS Press, Washington, DC, 1985, pp. 131-163.
15. A.J. Castro, Methods for making microporous products, US Patent 4,247,498, 1981.
16. D.R. Lloyd, J.W. Barlow, and K.E. Kinzer, Microporous membrane formation via thermally-induced phase separation, in: K.K. Sirkar and D.R. Lloyd (Eds.), New Membrane Materials and Processes for Separation, AIChE Symposium Series 261, New York, 1988.
17. Y. Liu, G.H. Koops, and H. Strathmann, Characterization of morphology controlled polyethersulfone hollow fiber membranes by the addition of polyethylene glycol to the dope and bore liquid solution, J. Membr. Sci., 223 (2003) 187-199.
18. M.H.V. Mulder, Basic principles of membrane technology, Kluwer Academic Press, Dordrecht, 1991.
19. D.S. Martula, Coalescence-induced coalescence, Dissertation, The University of Texas at Austin, 2000.
20. I.C. Kim and K.H. Lee, Effect of poly(ethylene glycol) 200 on the formation of a polyetherimide asymmetric membrane and its performance in aqueous solvent mixture permeation, J. Membr. Sci., 230 (2004) 183-188.
21. R. Mahendran, R. Malaisamy, and D. Mohan, Preparation, characterization and effect of annealing on performance of cellulose acetate/sulfonated polysulfone and cellulose acetate/epoxy resin blend ultrafiltration membranes, European Polym. J., 40 (2004) 623-633.

22. S.Y. Kim, T. Kanamori, Y. Noumi, P.C. Wang, and T. Shinbo, Preparation of porous poly(D,L-lactide) and poly(D,L-lactide-co-glycolide) membranes by a phase inversion process and investigation of their morphological changes as cell culture scaffolds, J. Appl. Polym. Sci., 92 (2004) 2082-2092.
23. G. Arthanareeswaran, K. Srinivasan, R. Mahendran, D. Mohan, M. Rajendran, and V. Mohan, Studies on cellulose acetate and sulfonated poly(ether ether ketone) blend ultrafiltration membranes, European Polym. J., 40 (2004) 751-762.
24. S. Doi and K. Hamanaka, Pore-Size Control Technique in the Spinning of Polysulfone Hollow Fiber Ultrafiltration Membranes, Desalination, 80 (1991) 167-180.
25. M.T. Batarseh, Formation of anisotropic hollow fiber membranes via TIPS, Dissertation, The University of Texas at Austin, 1999.
26. P.M. Atkinson, Formation of anisotropic flat sheet membranes via evaporative TIPS, Dissertation, The University of Texas at Austin, 1999.
27. P.M. Atkinson and D.R. Lloyd, Anisotropic flat sheet membrane formation via TIPS: Thermal effects., J. Membr. Sci., 171 (2000) 1-18.
28. P.M. Atkinson and D.R. Lloyd, Anisotropic flat sheet membrane formation via TIPS: Forced convection and molecular weight effects, J. Membr. Sci., 175 (2000) 225-238.
29. M.J.H. Bulters and H.E.H. Meijer, Analogy between the modelling of pullout in solution spinning and the prediction of the vortex size in contraction flows, Journal of Non-Newtonian Fluid Mechanics, 38 (1990) 43-80.
30. D.R. Lloyd, Materials Science of Synthetic Membranes, ACS Press, Washington, DC, 1985. pages 269.
31. K. Scott, Handbook of Industrial Membranes, 1st ed, Elsevier Science Publishers, Ltd., 1995.
32. W.S.W. Ho and K.K. Sirkar, Membrane Handbook, Van Nostrand Reinhold, New York, 1992. pages 954.
33. B.D. Freeman, M.M. Denn, R. Keunings, G.E. Molau, and J. Ramos, Profile development in drawn hollow tubes, Journal of Polymer Engineering, 6 (1986) 171-186.
34. S. Kase and T. Matsuo, Studies on melt spinning. II. Steady-state and transient solutions of fundamental equations compared with experimental results, J. Appl. Polym. Sci., 11 (1967) 251-287.
35. A.K. Doufas and A.J. McHugh, Two-dimensional simulation of melt spinning with a microstructural model for flow-induced crystallization, J. Rheol., 45 (2001) 855-879.
36. T.C. Hagen, Elongational flows in polymer processing, PhD, Virginia Polytechnic Institute and State University, 1998.
37. A.D. Rovère and R.L. Shambaugh, Melt-Spun Hollow Fibers: Modeling and Experiments, Polym. Eng. Sci., 41 (2001) 1206-1219.
38. L. Tan, W.B. Krantz, A.R. Greenberg, and R.L. Sani, Studies of convective transport in evaporative casting of dense polymer films, J. Membr. Sci., 108 (1995) 245-255.
39. C.S. Tsay and A.J. McHugh, Mass transfer dynamics of the evaporation step in membrane formation by phase inversion, J. Membr. Sci., 64 (1991) 81-92.
40. C.S. Tsay and A.J. McHugh, The combined effects of evaporation and quench steps on asymmetric membrane formation by phase inversion, Journal of Polymer Science: Part B: Polymer Physics, 29 (1991) 1261-1270.

41. C.S. Tsay and A.J. McHugh, Mass transfer modeling of asymmetric membrane formation by phase inversion, Journal of Polymer Science: Part B: Polymer Physics, 28 (1990) 1327-1365.
42. S.S. Shojaie, W.B. Krantz, and A.R. Greenberg, Development and validation of a model for the formation of evaporatively cast polymeric films, Journal of Materials Processing and Manufacturing Science, 1 (1992) 181-194.
43. S.S. Shojaie, W.B. Krantz, and A.R. Greenberg, Dense polymer film and membrane formation via the dry-cast process, Part I. Model development, J. Membr. Sci., 94 (1994) 255-280.
44. S.S. Shojaie, W.B. Krantz, and A.R. Greenberg, Dense polymer film and membrane formation via the dry-cast process, Part II. Model validation and morphological studies, J. Membr. Sci., 94 (1994) 281-298.
45. H. Matsuyama, S. Berghmans, and D.R. Lloyd, Formation of anisotropic membranes via thermally induced phase separation, Polymer, 40 (1999) 2289-2301.
46. A.K. Agrawal and R. Bhalla, Advances in the production of poly(lactic acid) fibers. A review, Journal of Macromolecular Science-Polymer Reviews, C43 (2003) 479-503.
47. Y. Ohzawa, Y. Nagano, and T. Matsuo, Studies on dry spinning. I. Fundamental equations, J. Appl. Polym. Sci., 13 (1969) 257-283.
48. Y. Ohzawa and Y. Nagano, Studies on dry spinning. II. Numerical solutions for some polymer-solvent systems based on the assumption that drying is controlled by boundary-layer mass transfer, J. Appl. Polym. Sci., 14 (1970) 1879-1899.
49. V. Simon, The temperature of fibers during air-gap wet spinning: Cooling by convection and evaporation, International Journal of Heat and Mass Transfer, 37 (1994) 1133-1142.
50. V. Simon, Analysis of fiber formation during air-gap wet spinning, AIChE J., 41 (1995) 1281-1294.
51. K.W. Chandler, J. Peddieson, S.A. Idem, and S.G. Rochelle, An improved 1D fiber dry spinning mass transfer model, Mechanics Research Communications, 29 (2002) 351-357.
52. Z.M. Gou and A.J. McHugh, A comparison of Newtonian and viscoelastic constitutive models for dry spinning of polymer fibers, J. Appl. Polym. Sci., 87 (2003) 2136-2145.
53. I. Brazinsky, A.G. Williams, and H.L. LaNieve, The dry spinning process: comparison of theory with experiment, Polym. Eng. Sci., 15 (1975) 834-841.
54. C.-C. Tsai, T.- J. Liu, Y.- H. Chang, and W.T.W. Tseng, Numerical simulation of an optical fiber-forming process, Chem. Eng. Sci., 52 (1997) 221-235.
55. C. Castellari, R. Francesconi, S. Ottani, F. Comelli, and G. Pezzin, Latent skin in asymmetric Loeb-type hollow fiber membrane, Polym. Eng. Sci., 28 (1988) 113-119.
56. S. Berghmans, H. Berghmans, and H.E.H. Meijer, Spinning of hollow porous fibres via the TIPS mechanism, J. Membr. Sci., 116 (1996) 171-189.
57. M.T. Batarseh, H.A. Balasubramanian, D.R. Lloyd, G.G. Lipscomb, and J.D. Stiehl, Anisotropic hollow fiber membrane formation. I. Prediction of concentration profiles., In preparation (2004).
58. M.T. Batarseh, H.A. Balasubramanian, D.R. Lloyd, G.G. Lipscomb, and J.D. Stiehl, Anisotropic hollow fiber membrane formation. II. Prediction of cooling rate profiles., In preparation (2004).
59. M.A. Matovich and J.R.A. Pearson, Spinning a Molten Threadline. Steady-State Isothermal Viscous Flows, Ind. Eng. Chem. Fundam., 8 (1969) 512-520.

60. M.M. Denn, Continuous drawing of liquids to form fibers, Ann. Rev. Fluid Mech., 12 (1980) 365-387.
61. G.G. Lipscomb, The melt hollow fiber spinning process: Steady-state behavior, sensitivity and stability, Polymers for Advanced Technologies, 5 (1994) 745-758.
62. T.-S. Chung, Z.-L. Xu, and W. Lin, Fundamental understanding of the effect of air-gap distance on the fabrication of hollow fiber membranes, J. Appl. Polym. Sci., 72 (1999) 379-395.
63. B. Ashman, Stability of Hollow Fiber Spinning, Master of Science in Chemical Engineering, University of Toledo, 1998.
64. K.S. McGuire, Membrane formation via liquid-liquid thermally induced phase separation, Dissertation, The University of Texas at Austin, 1995.

Chapter 2. Modeling the Effects of Surface Tension and Evaporative Cooling in Hollow Fiber Spinning

2.1 Motivation for Modeling Surface Tension Effects

Surface tension has the potential to affect significantly the evolution of hollow fiber structure during a spinning process. Quantifying the tendency of a substance to minimize its surface area to volume ratio, significant surface tension can affect the spinline dimensions (inner and outer diameters) in a hollow fiber spinning process. In addition to this intuitive relevance to the spinning process, existing literature indicates that surface tension plays a part in the occurrence of spinning instabilities such as draw resonance [1-4].

Draw resonance, a spinning instability extensively discussed in the literature, is a periodic spinline diameter fluctuation that is most often attributed to spinning above a critical draw ratio (ratio of spinline take-up velocity to extrusion velocity), which is approximately 20 for isothermal Newtonian fluid spinning. Figure 2.1 shows a spun hollow fiber with non-uniform diameter resulting from the occurrence of draw resonance. Such non-uniformity is detrimental to both fiber properties and performance characterization: smaller diameter sections result in a weaker fiber structure regardless of fiber application, and non-uniform diameter makes flux quantities for hollow fiber membranes unpredictable. Several spinning stability studies have shown surface tension to be a factor in terms of predicting critical conditions for the onset of fiber non-uniformity caused by draw resonance [1, 5].

Specifically, studies characterizing the onset of spinning instability in terms of processing conditions and spinning system physical properties show that surface tension plays a significant and quantifiable role. Existing theoretical and experimental work for solid fiber spinning interprets the destabilizing effects of surface tension on the process by changing the magnitude of surface tension forces relative to viscous forces as set by the ratio of the Reynolds number *Re* to the Weber number *We*; $\frac{\mathrm{Re}}{We} = \frac{\gamma}{\bar{v}\eta_o}$ is the inverse of the Capillary number *Ca*, where γ = filament surface tension, $\bar{v}$ = axial velocity of the filament, and η_o = filament viscosity. Results are used to gauge the effects of surface tension on the conditions for which the spinning process becomes unstable, and findings show a significant difference in unstable conditions for low *Re/We* (viscous forces dominant) versus high *Re/We* (surface tension forces dominant). These observations for solid fiber spinning presumably extend to hollow fiber spinning operations; thus, the work discussed here modeling the effects of surface tension for the hollow fiber spinning process is an important precursor to characterizing hollow fiber spinning instability.

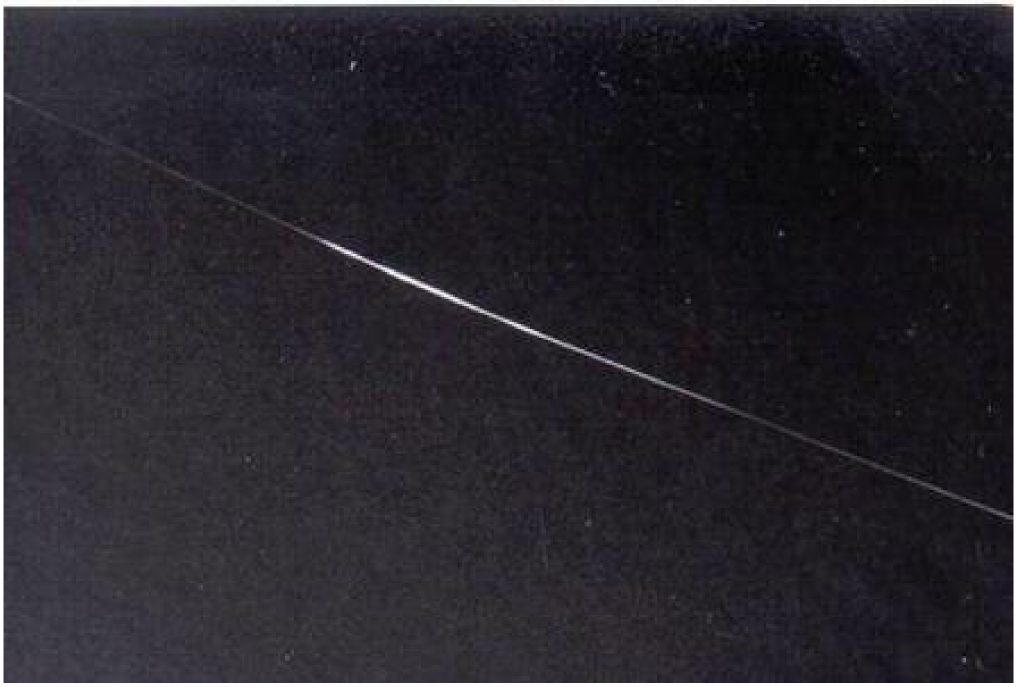

Figure 2.1 Effect of Draw Resonance on Fiber Structure: Fiber has a periodic diameter fluctuation (thin section, thick section, then thin section again) resulting from draw resonance occurring during spinning

2.2 Outline of Chapter 2

As mentioned in Chapter 1, the thin filament analysis (TFA) is a widely accepted approximate analysis of fiber spinning, but the existing work for hollow fibers neglects the effects of surface tension and does not properly account for any type of phase change [6-10]. In this chapter, the TFA for hollow fiber spinning has been modified to include both surface tension effects and evaporative cooling effects; the latter is an important factor in determining concentration and temperature profiles for solution spinning, especially for high spinning temperatures and/or volatile diluents. Improving the existing TFA for fiber spinning is an important first step toward accomplishing the goal of this research: creating a model that can be used to tailor hollow fibers, including membranes, for desired applications.

Background of the TFA as it relates to hollow fiber spinning is discussed briefly here, followed by a list of assumptions pertaining to this analysis. The equations of continuity, core gas pressure, and the melt spinning energy balance are unchanged by surface tension effects; all are presented as found in the existing literature [9]. A modified version of the energy balance accounting for evaporative cooling effects in solution spinning is then described. Derivation of the momentum and stress balances to include surface tension effects follows.

The analysis here is shown to reduce to the existing analysis in the absence of surface tension and evaporative cooling, and results are given to illustrate the effects of surface tension on melt spinning of poly(ethylene terephthalate), PET. In addition, sensitivity studies for a steady-state, ideal gas core, Newtonian clad PE–dodecanol spin are used to gauge the importance of surface tension and the effects of evaporative cooling for modeling spinline variables in typical hollow fiber membrane spinning operations. Differences in predictions for PET melt spinning and PE–dodecanol membrane spinning are discussed as they relate to the fundamental differences in the processes: the PET operation is representative of a high-speed industrial-scale spin for a nonvolatile melt, while the PE–dodecanol results represent low-speed, laboratory-scale spinning of a volatile solution.

2.3 Equation Derivation

Since the typical fiber spinning process represented by Figure 1.2 involves molecular rearrangement from shear flow within the spinneret to elongational flow through the draw zone followed by phase separation and/or solidification, detailed analysis of the process rheology in its entirety is a daunting task. The TFA for fiber spinning described here focuses only on the *draw zone*, where the fiber is drawn via uniaxial extension to the desired size through an air gap prior to the occurrence of phase separation and/or solidification. Furthermore, the present analysis applies to both solid and hollow fibers and can be used for co-extrusion systems provided the thin filament assumption defined in section 2.3.1 is not violated.

2.3.1 Model Assumptions

The following assumptions govern the analysis in the present work:

1. The ratio of fiber radius to draw zone length, R_o/L, is small: this is known as the "thin filament" assumption.
2. The fiber is axisymmetric with respect to all dependent variables: using a cylindrical coordinate system, there is no angular dependence.
3. Flow kinematics in the draw zone are purely elongational: the axial velocity component is independent of the radial coordinate.
4. All material properties are constant over the cross-section for a given axial position.
5. Both core and clad are Newtonian fluids.
6. The core fluid is an ideal gas.
7. The effects of air drag and gravity are negligible.
8. Inertial and shear viscous terms are negligible in the radial conservation of momentum equation.
9. Radial convection, axial conduction, viscous dissipation, and radiation are negligible in the energy balance.
10. The cross-sectional average temperatures in the core and clad are equal.
11. Density, heat of vaporization, and surface tension of the clad and heat capacities of both core and clad are constant.
12. Core density-related energy changes are negligible: due to the dependence of internal energy on a fluid's specific volume, changes in core gas density, modeled here as a function of axial position, produce changes in internal energy. However, these effects are neglected in the energy balance relative to the axial convection and radial conduction

terms retained in the energy equation. For sufficiently small core pressure and temperature changes, this assumption is justified.

13. Phase separation or transition other than diluent evaporation does not occur in the draw zone.

The assumption of constant material properties (clad density and heat of vaporization, heat capacities, and surface tension) is justified by the insignificant (generally less than 10%) change in these quantities over a normal spinning temperature range [11]. The Newtonian fluid assumption for the clad is made here for practicality: especially in solution spinning with low polymer content and low extension rates, operation is in the upper Newtonian plateau, and non-Newtonian effects are not expected. If warranted, the present analysis can be extended to include non-Newtonian effects through incorporation of an alternative fluid constitutive equation, as has been explored in previous work [12, 13]. Similarly, the ideal gas core case represented here is applicable to a number of industrial and academic spinning endeavors; however, the analysis here can also be systematically applied to model spinning with non-ideal gases and core liquids.

Per assumption (10), radial temperature variation is not considered here as previous work has shown that a typical polymer spinline cross-section cools uniformly during the spinning process [14]; however, some processes, such as glass spinning for fiber optics, operate in excess of 500 K, have significant radiation effects, and may develop significant radial temperature gradients [15].

Assumption (13) emphasizes that the model is applicable up to the point of phase separation. Concentration changes prior to phase separation, which are likely to occur during solution spinning, are modeled in detail in Chapter 3; in addition, diluent evaporation is discussed briefly in this chapter as it relates to evaporative cooling and the resulting temperature predictions of the TFA. Previous work has shown that concentration changes, and thus the corresponding changes in material properties such as clad viscosity, are confined to a thin boundary region in the spinline cross-section at the outer radius [14], and material properties are presumed constant over the spinline cross-section as stated in assumption (4). Furthermore, assumptions (7), (9), and (12) can be justified based on order-of-magnitude calculations and previous experimental evidence showing that these effects are negligible [9, 14]; representative calculations are shown in Appendix A.

2.3.2 Model Development Including Evaporative Cooling and Surface Tension

The TFA for hollow fiber spinning involves radial averaging of the axisymmetric (that is, no angular dependence over the spinline cross-section in cylindrical coordinates) conservation of mass, momentum, and energy equations. The final equations predict the variation of fiber inner and outer diameters, velocity, stress, and temperature with axial distance in the draw zone based on the assumptions listed in section 2.3.1. The equation of continuity, the core gas pressure dependence (ideal gas law), and the energy balance for melt spinning are presented here without derivation as they are found in the existing literature [9]. Detailed derivation of the equations is given in Appendix B.

At steady-state, the thin filament continuity expression for hollow fiber spinning appears in equation (2.1), where R_o and R_i are the spinline outer and inner radii, $\bar{v}$ is the spinline axial velocity (constant over the spinline cross-section), ρ_o and ρ_i represent clad and core densities, and w_o and w_i are the mass flow rates of clad and core. Spinline radii and axial velocity and core gas density are functions of axial position z, while clad density and both core and clad mass flow rates are constant.

$$\left(\frac{R_o}{R_i}\right)^2 = R_o^2\left(\frac{\pi \bar{v} \rho_i}{w_i}\right) = 1 + \frac{\rho_i}{\rho_o}\frac{w_o}{w_i} \qquad (2.1)$$

With the assumption of an ideal gas core, the ideal gas law, shown in equation (2.2), governs the relationship between core gas density, core gas gauge pressure $\overline{p_i}$, and the spinline temperature $\overline{T}$ (like axial velocity, constant over the spinline cross-section); all of these quantities are functions of axial position in the draw zone. In equation (2.2), p_{atm} is the ambient air pressure, MW_i is the core gas molecular weight, and R_g is the universal gas constant.

$$\rho_i = \frac{\left(\overline{p_i} + p_{atm}\right) MW_i}{R_g \overline{T}} \qquad (2.2)$$

If no phase transition is allowed, an energy balance for the core and clad regions leads to equation (2.3). In this expression, C_{po} and C_{pi} are the clad and core specific heat capacities, z is the axial position, T_q is the temperature of the draw zone quench medium (the air gap region), and h is the convective heat transfer coefficient. This is the TFA energy balance in the existing literature, used to predict temperature profiles for melt spinning [9].

$$\left(w_o C_{po} + w_i C_{pi}\right)\frac{d\overline{T}}{dz} = \left(T_q - \overline{T}\right)\left(2\pi R_o h\right) \qquad (2.3)$$

However, equation (2.3) can be modified to estimate evaporative cooling effects on the spinline temperature profile. This is relevant to solution spinning, especially at high temperature and/or when using volatile diluents. In order to account for evaporative cooling effects in the TFA for fiber spinning, the energy balance's boundary condition defining the radial heat flux at the clad–air quench interface, $-k_o \left.\frac{d\overline{T}}{dr}\right|_{Ro}$, must be modified to include both the convective heat transfer to the quench air and the evaporative cooling effects. In this expression, k_o is the thermal conductivity of the clad, and r is the radial direction.

Presented here for clarity, the general forms of the energy balance and the boundary condition to be modified are given as equations (2.4) and (2.5).

$$\left(w_o C_{po} + w_i C_{pi}\right)\frac{d\overline{T}}{dz} = 2\pi R_o k_o \left.\frac{d\overline{T}}{dr}\right|_{Ro} \qquad (2.4)$$

$$-k_o \left.\frac{d\overline{T}}{dr}\right|_{Ro} = h\left(T\big|_{Ro} - T_q\right) \qquad (2.5)$$

Evaporative cooling for solution spinning is due to the energy release that accompanies diluent evaporation in a *boundary layer* that constitutes a relatively small portion of the fiber cross-section extending inward from the clad–air quench interface at the spinline outer radius. The boundary layer concept is described more fully in Chapter 3; for the purposes of modeling evaporative cooling effects here, it is sufficient to say that the boundary layer is the only portion of the spinline cross-section that changes composition during spinning due to diluent loss through evaporation and diffusion. Outside of the boundary layer, solution concentration is considered constant and equal to that of the initial spinning solution.

To estimate the evaporative cooling term, it is necessary to calculate the amount of diluent that is lost through evaporation during spinning. This is done by calculating the rate of diluent diffusive mass flux out of the fiber wall through the boundary layer at the outer radius, $D\frac{\partial C_d}{\partial r}\Big|_{Ro}$, as given by equation (2.6).

$$D\frac{\partial C_d}{\partial r}\bigg|_{Ro} = \rho_d^0\left(\phi_d\big|_{Ro} - \phi_d^0\right)\left(\frac{D\bar{v}}{\pi\, z}\right)^{1/2} \quad (2.6)$$

In equation (2.6), which is derived explicitly in section 3.2.1, *D* represents the mutual diffusion coefficient of the solution, assumed constant and equal to its value at the spinning temperature T_0 and initial solution composition at $z = 0$; C_d is the mass concentration of diluent in the solution, a function of both *r* and *z*; ρ_d^0 is the density of pure liquid diluent at the spinning temperature T_0; $\phi_d\big|_{Ro}$ is the diluent volume fraction in the spinline at the outer radius, a function of *z*, determined using equation (3.16) as discussed in section 3.2.1; and ϕ_d^0 is the initial volume fraction of diluent in the spinning solution. The diffusion coefficient is calculated using the Zielinski–Duda predictive correlation as described in section 4.1.4.

To convert the quantity in equation (2.6) to an energy flux for updating the boundary condition shown in equation (2.5) to include evaporative cooling effects, equation (2.6) is multiplied by the diluent heat of vaporization per unit mass, $\Delta\hat{H}_{vap}^{d}$, resulting in equation (2.7). The diluent heat of vaporization is assumed constant and equal to its value at the initial spinning temperature; it is calculated using the published correlation for pure diluent [16].

$$rate\ of\ energy\ loss\ via\ evaporation\big|_{Ro} = \Delta\hat{H}_{vap}^{d}\left[\rho_d^0\left(\phi_d\big|_{Ro} - \phi_d^0\right)\left(\frac{D\bar{v}}{\pi\, z}\right)^{1/2}\right] \quad (2.7)$$

The boundary condition describing radial heat flux at the clad–air quench interface is then described by equation (2.8): the energy conducted in the radial direction at R_o is equal to the sum of the heat lost due to convection into the quench air and the heat lost via evaporative cooling. Applying this equation to the general TFA energy balance of equation (2.4) results in the energy balance given by (2.9), used here to model the axial temperature profile for simulations of solution spinning for hollow fiber membranes.

$$-k_o \frac{d\bar{T}}{dr}\bigg|_{Ro} = h\left(T\big|_{Ro} - T_q\right) + \Delta\hat{H}^{d}_{vap}\left[\rho^{0}_{d}\left(\phi_d\big|_{Ro} - \phi^{0}_{d}\right)\left(\frac{D\bar{v}}{\pi z}\right)^{1/2}\right] \quad (2.8)$$

$$\left(w_o C_{po} + w_i C_{pi}\right)\frac{d\bar{T}}{dz} = 2\pi R_o\left\{h\left(T_q - \bar{T}\right) + \Delta\hat{H}^{d}_{vap}\left[\rho^{0}_{d}\left(\phi_d\big|_{Ro} - \phi^{0}_{d}\right)\left(\frac{D\bar{v}}{\pi z}\right)^{1/2}\right]\right\} \quad (2.9)$$

Surface tension considerations directly affect the derivation of the momentum balance for the hollow fiber spinning process. To consider surface tension effects, the boundary conditions describing stress at the core–clad and clad–air quench interfaces must be carefully formulated. At the inner radius R_i, continuity of the forces at the core–clad interface requires the general expressions (2.10) and (2.11) to hold.

$$\left[\sigma_o \bullet \left(-n_i^{\perp}\right) \bullet n_i^{\perp} + \sigma_i \bullet n_i^{\perp} \bullet n_i^{\perp} = \gamma\left(\nabla \bullet n_i^{\perp}\right)\right]\Big|_{Ri} \quad (2.10)$$

$$\left[\sigma_o \bullet n_i^{\perp} \bullet n_i^{ll} = \sigma_i \bullet n_i^{\perp} \bullet n_i^{ll}\right]\Big|_{Ri} \quad (2.11)$$

In equations (2.10) and (2.11), evaluated at the core–clad interface position at R_i, γ is the clad surface tension, σ_o and σ_i represent the total stress tensors associated with the clad and the core, and $n_i^{\perp}$ and n_i^{ll} are unit normal and tangent vectors. Refer to Figure 2.2, a schematic of the extruding spinline.

Equation (2.10) represents the normal stress balance at the inner radius: the total normal stress exerted by the clad on the core combines with the total normal stress exerted by the core on the clad to give the net stress arising from the interfacial tension between the core and the clad. For an ideal gas core fluid, the interfacial tension at the gas–liquid interface at the inner radius R_i is the clad surface tension. Equation (2.11) is the tangential stress balance at the core–clad interface, which is not affected by surface tension.

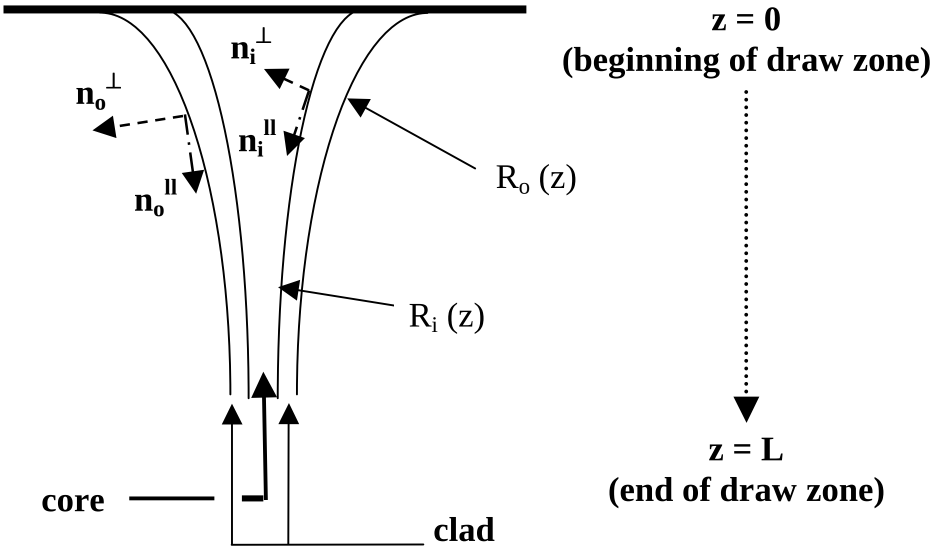

Figure 2.2 Schematic of a Hollow Fiber During Extrusion

The unit normal vector $n_i^{\perp}$ is defined in equation (2.12) for $(R_o/L)^2 << 1$ (the thin filament assumption); the unit tangent vector is defined in (2.13).

$$\left(n_{ir}^{\perp}, n_{iz}^{\perp}\right) = \left(-1, \frac{dR_i}{dz}\right) \qquad (2.12)$$

$$\left(n_{ir}^{ll}, n_{iz}^{ll}\right) = \left(\frac{dR_i}{dz}, 1\right) \qquad (2.13)$$

In (2.12) and (2.13), *r* represents the radial direction and *z* the axial direction. Returning to (2.10) and (2.11), substituting for $n_i^{\perp}$ and n_i^{ll} for a symmetric stress tensor and rearranging results in (2.14) for the normal stress balance and (2.15) for the tangential stress balance at the core–clad interface R_i.

$$\left[\sigma_{rr}^{o} - 2\left(\frac{dR_i}{dz}\right)\sigma_{rz}^{o} = \sigma_{rr}^{i} - 2\left(\frac{dR_i}{dz}\right)\sigma_{rz}^{i} + \frac{\gamma}{R_i}\right]\Bigg|_{Ri} \qquad (2.14)$$

$$\left[-\left(\frac{dR_i}{dz}\right)\sigma^{o}_{rr}-\sigma^{o}_{rz}+\left(\frac{dR_i}{dz}\right)\sigma^{o}_{zz}=-\left(\frac{dR_i}{dz}\right)\sigma^{i}_{rr}-\sigma^{i}_{rz}+\left(\frac{dR_i}{dz}\right)\sigma^{i}_{zz}\right]\Bigg|_{Ri} \quad (2.15)$$

In (2.14) and (2.15), the σ^{o}_{jk} and σ^{i}_{jk} terms are the clad and core total stress tensor components. The next step is to substitute for the components of the core stress tensor using the definition, $\sigma^{i}_{jk}=\tau^{i}_{jk}-pI$, where τ^{i}_{jk} terms represent the components of the core deviatoric stress tensor, p is the core pressure $\overline{p_i}$, and I is the identity tensor, resulting in (2.16) and (2.17).

$$\left[\sigma^{o}_{rr}-2\left(\frac{dR_i}{dz}\right)\sigma^{o}_{rz}=\tau^{i}_{rr}-\overline{p_i}-2\left(\frac{dR_i}{dz}\right)\tau^{i}_{rz}+\frac{\gamma}{R_i}\right]\Bigg|_{Ri} \quad (2.16)$$

$$\left[-\left(\frac{dR_i}{dz}\right)\sigma^{o}_{rr}-\sigma^{o}_{rz}+\left(\frac{dR_i}{dz}\right)\sigma^{o}_{zz}=-\left(\frac{dR_i}{dz}\right)\left(\tau^{i}_{rr}\right)-\tau^{i}_{rz}+\left(\frac{dR_i}{dz}\right)\left(\tau^{i}_{zz}\right)\right]\Bigg|_{Ri} \quad (2.17)$$

Assuming a Newtonian ideal gas core with τ^{i}_{jk} directly proportional to core gas viscosity η_i, where $\eta_i << 1$, equations (2.16) and (2.17) can be further simplified to (2.18) and (2.19).

$$\left[\sigma^{o}_{rr}-2\left(\frac{dR_i}{dz}\right)\sigma^{o}_{rz}=-\overline{p_i}+\frac{\gamma}{R_i}\right]\Bigg|_{Ri} \quad (2.18)$$

$$\left[-\left(\frac{dR_i}{dz}\right)\sigma^{o}_{rr}-\sigma^{o}_{rz}+\left(\frac{dR_i}{dz}\right)\sigma^{o}_{zz}=0\right]\Bigg|_{Ri} \quad (2.19)$$

Finally, modifying (2.18) by substitution for σ^{o}_{rz} using the result from the tangential stress balance in (2.19), neglecting terms that scale as $(R_o/L)^2<<1$, and rearranging gives (2.20) and (2.21), the final forms of the normal and tangential stress balances at the core–clad interface $r = R_i$, including surface tension effects.

$$\left[\sigma^{o}_{rr}=-\overline{p_i}+\frac{\gamma}{R_i}\right]\Bigg|_{Ri} \quad (2.20)$$

$$\left[\sigma^{o}_{rz}=\frac{dR_i}{dz}\left(\sigma^{o}_{zz}-\sigma^{o}_{rr}\right)\right]\Bigg|_{Ri} \quad (2.21)$$

A similar process is necessary to derive the normal and tangential stress balances for the clad–air quench interface at $r = R_o$. The basic forms for these balances are equations (2.22) and (2.23).

$$\left[\sigma_o \bullet \left(-n_o^{\perp}\right) \bullet n_o^{\perp} = \gamma\left(\nabla \bullet n_o^{\perp}\right)\right]\Big|_{Ro} \qquad (2.22)$$

$$\left[\sigma_o \bullet n_o^{\perp} \bullet n_o^{ll} = 0\right]\Big|_{Ro} \qquad (2.23)$$

Equation (2.22) represents the normal force balance at the outer radius: with negligible air drag, the total normal force exerted by the clad on the surrounding air gives the net stress arising from the surface tension of the clad. Equation (2.23), the tangential stress balance, is not affected by surface tension. Again referring to Figure 2.2, $n_o^{\perp}$ and n_o^{ll} are the unit outward normal and unit tangent vectors at $r = R_o$, defined in equations (2.24) and (2.25).

$$\left(n_{or}^{\perp}, n_{oz}^{\perp}\right) = \left(1, -\frac{dR_o}{dz}\right) \qquad (2.24)$$

$$\left(n_{oz}^{ll}, n_{or}^{ll}\right) = \left(\frac{dR_o}{dz}, 1\right) \qquad (2.25)$$

F o r -f a l u s i y d m md ee tf ri in

(R_o/)^2, L e q u a t i o o n f s t (h 2e .

s t r e–a s i s r r_o, b q i = a u n l e c R a n l n cu c hd e i s

$$\left[\sigma_{rz}^{o} = \frac{dR_o}{dz}\left(\sigma_{zz}^{o} - \sigma_{zr}^{o}\right)\right]\Big|_{r=R_o} \qquad (2.26)$$

$$\left(\sigma_{rr}^{o} = -\frac{\gamma}{R_o}\right)\Big|_{R_o} \qquad (2.27)$$

C o m b i n i n g. 2 t6 h) e,

w i t h a g [e , 1n-a 7e rv]r æ a d l ia

N e w t -s o e n a c i s t a, i n o y n i c a d l h a d l a

m o r e d e t a i l e d

$$\frac{d}{dz}\left[(w_o + w_i)\bar{v}\right] = \frac{d}{dz}\left[2\eta_o A_o \frac{d\bar{v}}{dz} - A_o \bar{p} - A_i \bar{p_i}\right] + 2\pi\gamma\left[\frac{dR_o}{dz} + \frac{dR_i}{dz}\right] \qquad (2.28)$$

In equation (2.28), A_o and A_i represent clad and core cross-sectional areas, η_o is the clad viscosity, and $\bar{p}$ is the radial-average pressure associated with the clad at a particular axial position z, which cannot be determined through direct experimental measurement. This term must be expressed alternatively, which can be done using results from the radial momentum balance as shown below.

A radial momentum balance on the clad, derived following a procedure similar to that used above for considering the axial component of momentum, results in equation (2.29), which gives the necessary expression for the radial-average clad pressure. The details of the derivation appear in Appendix B. Combining equations (2.28) and (2.29) results in equation (2.30), the TFA momentum balance including surface tension.

$$-A_o\bar{p} = \eta_o A_o\left(\frac{d\bar{v}}{dz}\right) + A_i\bar{p_i} - \pi\gamma\left(R_o + R_i\right) \qquad (2.29)$$

$$\frac{d}{dz}\left[(w_o + w_i)\bar{v}\right] = \frac{d}{dz}\left[3\pi\left(R_o^2 - R_i^2\right)\eta_o\frac{d\bar{v}}{dz}\right] + \pi\gamma\left[\frac{dR_o}{dz} + \frac{dR_i}{dz}\right] \qquad (2.30)$$

A coupled set of four independent equations has been presented, consisting of equations (2.1), (2.2), (2.3) or (2.9), and (2.30). The TFA for the hollow fiber spinning process is designed to predict the variation of five spinline variables: clad inner radius, clad outer radius, temperature, velocity, and stress (core gas density or pressure), all as functions of axial position in the draw zone. Therefore, one more relationship, shown in equation (2.31), is necessary to characterize the variation of core gas density with axial position. This expression results from calculating σ_{rr}^{o} for an incompressible Newtonian clad and combining the result with the interfacial stress balances given above in equations (2.20), (2.21), (2.26), and (2.27). Refer to section B.4 for details of the derivation.

$$\bar{v}\frac{d\rho_i}{dz} = \left(1 + \frac{\rho_o w_i}{\rho_i w_o}\right)\left[\gamma\left(\frac{1}{R_i} + \frac{1}{R_o}\right) - \left(\frac{\rho_i\bar{p}_i}{\eta_o}\right)\right] \qquad (2.31)$$

Boundary conditions for analysis of the fiber spinning process are conditions at the beginning ($z = 0$) and end ($z = L$) of the draw zone. At the beginning of the draw zone, the initial clad cross-sectional area A_o^0 is set by continuity, equation (2.1), using the set values of constant clad and core mass flow rates, w_o and w_i, clad density ρ_o, initial core gas density ρ_i^0 [calculated using the ideal gas law in equation (2.2) with set values of spinning temperature $\overline{T^0}$ and initial core gas gauge pressure $\overline{p_i^0}$], and either the initial outer radius R_o^0 or the extrusion velocity $\overline{v^0}$. Generally, the outer radius is set either as that of the spinneret or the spinline outer radius at the point of maximum die swell, and then both the initial inner radius R_i^0 (and as a result, the initial clad cross-sectional area A_o^0) and the extrusion velocity are set by continuity. At the end of the draw zone, the final spinline velocity $\overline{v^L}$ equals the velocity of the take-up wheel contacting the filament, and the fifth necessary boundary condition corresponds either to a set draw zone length L or the point where the spinline reaches a desired final temperature $\overline{T^L}$. The TFA equation set derived in this section and the corresponding boundary conditions are summarized in (2.32), with the boundary conditions listed as the last two lines.

$$
\begin{gathered}
\left(\frac{R_o}{R_i}\right)^2 = R_o^2\left(\frac{\pi\bar{v}\rho_i}{w_i}\right) = 1 + \frac{\rho_i}{\rho_o}\frac{w_o}{w_i} \qquad \mathbf{(2.1)} \\
\rho_i = \frac{\left(\overline{p_i} + p_{atm}\right) MW_i}{R_g \overline{T}} \qquad \mathbf{(2.2)} \\
\left(w_o C_{po} + w_i C_{pi}\right)\frac{d\overline{T}}{dz} = \left(T_q - \overline{T}\right)\left(2\pi R_o h\right) \qquad \mathbf{(2.3)} \\
\left(w_o C_{po} + w_i C_{pi}\right)\frac{d\overline{T}}{dz} = 2\pi R_o \left\{ h\left(T_q - \overline{T}\right) + \Delta\hat{H}_{vap}^{d}\left[\rho_d^0\left(\phi_d\big|_{Ro} - \phi_d^0\right)\left(\frac{D\bar{v}}{\pi z}\right)^{1/2}\right]\right\} \qquad \mathbf{(2.9)} \\
\frac{d}{dz}\left[\left(w_o + w_i\right)\bar{v}\right] = \frac{d}{dz}\left[3\pi\left(R_o^2 - R_i^2\right)\eta_o\frac{d\bar{v}}{dz}\right] + \pi\gamma\left[\frac{dR_o}{dz} + \frac{dR_i}{dz}\right] \qquad \mathbf{(2.30)} \\
\bar{v}\frac{d\rho_i}{dz} = \left(1 + \frac{\rho_o w_i}{\rho_i w_o}\right)\left[\gamma\left(\frac{1}{R_i} + \frac{1}{R_o}\right) - \left(\frac{\rho_i\overline{p_i}}{\eta_o}\right)\right] \qquad \mathbf{(2.31)} \\
At\ z = 0: \quad R_o = R_o^0\ or\ \bar{v} = \overline{v^0};\ \overline{T} = \overline{T^0};\ \overline{p_i} = \overline{p_i^0} \\
At\ z = L: \quad \bar{v} = \overline{v^L};\ \overline{T} = \overline{T^L}\ or\ L = known
\end{gathered}
\tag{2.32}
$$

2.3.3 Equation Solution Procedure

Equations (2.1), (2.2), (2.3) or (2.9), (2.30), and (2.31), subject to the boundary conditions in (2.32), characterize the hollow fiber spinning process using the thin filament analysis approach, accounting for surface tension effects; evaporative cooling is included when using the energy balance of (2.9) rather than (2.3) with boundary condition (2.8) rather than (2.5). MATLAB 6.1 was used to simulate typical fiber spinning conditions, employing a shooting method to solve for the initial velocity derivative with respect to axial position, $\left.\left(\frac{d\bar{v}}{dz}\right)\right|_{z=0}$, changing this quantity until the calculated spinline axial velocity at the end of the draw zone matches the known value $\overline{v^{L}}$. The differential equation set was solved numerically by invoking a 4th – order Runge–Kutta solution scheme using the *ode45* command. Relative tolerance (*RelTol*) and absolute tolerance (*AbsTol*) were both set to 10^{-8}, with a convergence criterion of 10^{-6} for the calculation of the initial velocity derivative.

In addition, to account for evaporative cooling effects using equation (2.9), the diluent concentration at the outer radius must be supplied to the program as a function of axial position; these values are unknown *a priori* and so must be assumed initially to calculate the temperature profile with the modeling efforts described here. As discussed in Chapter 3, the TFA simulation results using the assumed concentrations are then used to calculate the actual concentration values corresponding to the data, repeating the process until the model-predicted results for consecutive iterations agree within 1%.

2.4 Process Sensitivity Studies

2.4.1 Reduction to Prior Work: Melt Spinning

Setting surface tension to zero in the equations derived here reduces the problem to that of the existing published TFA hollow fiber spinning model. When surface tension effects are neglected, the momentum balance and the stress balance in equations (2.30) and (2.31) collapse to the relationships from the previous published analysis [9] as shown in (2.33) and (2.34). With nonvolatile melts, evaporative cooling is not a factor, and the energy balance of (2.3) applies as in the existing analysis. In addition, setting the clad inner radius and core mass flow rate to zero recovers the solid fiber case, and these results can be compared to results from published solid fiber modeling efforts.

$$\frac{d}{dz}\left[(w_o + w_i)\bar{v}\right] = \frac{d}{dz}\left[3A_o\eta_o\frac{d\bar{v}}{dz}\right] \qquad (2.33)$$

$$\bar{v}\frac{d\rho_i}{dz} = -\left(\frac{\rho_i\overline{p_i}}{\eta_o}\right)\left(1+\frac{\rho_o w_i}{\rho_i w_o}\right) \qquad (2.34)$$

To explore the effects of surface tension on predictions of the thin filament analysis of hollow fiber melt spinning, simulations of the TFA model modified to include surface tension effects were compared to results predicted in the absence of surface tension using typical hollow fiber spinning conditions for the manufacture of poly (ethylene terephthalate), PET, fibers [9-11]. The PET spinning process conditions appear in Table 2.1, and the PET spinning system physical properties are given in Table 2.2.

The Newtonian clad shear viscosity of the nonvolatile PET melt is assumed to obey an Arrhenius-type temperature dependence as given in (2.35), where η_o^0 represents the pre-exponential factor and E_o is the viscosity activation energy for the temperature dependence. Values defining these parameters and thus the viscosity temperature dependence are included in Table 2.2.

$$\eta_o = \eta_o^0 \exp\left(\frac{E_o}{R_g\bar{T}}\right) \qquad (2.35)$$

Furthermore, the heat transfer coefficient h (W/m^2/K) used here is taken from the literature result for cross-flow cooling [6] as shown in equation (2.36). This relationship incorporates quench fluid thermal conductivity k_q (W/m/K), density ρ_q (kg/m^3), viscosity η_q (Pa-s), and velocity v_q (m/s) normal to the fiber axis, with all physical properties evaluated at the quench fluid temperature T_q (K). The physical properties for the quench fluid correspond to the values for air [16] as given in equations (2.37) to (2.39).

$$h = 0.42\left(\frac{k_q}{2R_o}\right)\left(\frac{2\rho_q \bar{v} R_o}{\eta_q}\right)^{1/3}\left[1+\left(\frac{8v_q}{\bar{v}}\right)^2\right]^{1/6} \qquad (2.36)$$

$$k_q = \left(6.56\times10^{-5}\right)\exp\left\{0.9\log\left[1.8\left(T_q - 273.15\right)-32\right]\right\}+\left(2.3\times10^{-2}\right) \qquad (2.37)$$

$$\rho_q = \frac{637.45}{460+1.8\left(T_q-273.15\right)+32} \qquad (2.38)$$

$$\eta_q = \left(2.5\times10^{-8}\right)\left[1.8\,(T_q-273.15)+32\right]-\left(1\times10^{-7}\right)\left[1.8\,(T_q-273.15)+32\right]^4+\left(1.65\times10^{-5}\right) \qquad (2.39)$$

Table 2.1 PET Spinning Process Conditions for Sensitivity Studies

Condition	Value
R_i^0 = initial clad inner radius	0.6 mm
R_o^0 = initial clad outer radius	1.0 mm
$\bar{v}^0$ = extrusion velocity	0.00338 m/s
$\bar{T}^0$ = spinning temperature	568 K
$\bar{p}_i^0$ = initial core gas gauge pressure	27 Pa
$\bar{v}^L$ = take-up velocity	14.0 m/s
$\bar{T}^L$ = filament temperature at end of draw zone	343 K
T_q = quench fluid temperature	303 K
v_q = quench fluid velocity normal to fiber axis	0.2 m/s
w_i = core gas mass flow rate	2.29 x 10^{-9} kg/s
w_o = clad mass flow rate	6.80 x 10^{-6} kg/s
p_{atm} = ambient air pressure	1.01 x 10^5 Pa

Table 2.2 PET System Material Properties for Sensitivity Studies

Property	Value
ρ_o = clad density, assumed constant	1000 kg/m^3
η_o^0 = pre-exponential factor for clad shear viscosity dependence on temperature	0.00121 Pa·s
E_o / R_g = Ratio of activation energy for clad shear viscosity temperature dependence to the universal gas constant	6802 K
C_{pi} = core gas specific heat capacity, assumed constant	1046 J/kg-K
C_{po} = clad specific heat capacity, assumed constant	1674 J/kg-K
MW_i = core gas molecular weight	28.0 kg/kmol
γ = clad surface tension	32.9 dynes/cm

In these simulations of PET spinning, the final filament temperature $\overline{T^{L}}$ is specified; the calculated draw zone length L required for the filament to reach this temperature per the TFA energy balance of equation (2.3) is 22 cm. It should be noted that the initial outer and inner radii are not specified independently, but calculated from the continuity equation given by (2.1) using the specified extrusion velocity, clad density, core density (calculated from the ideal gas law using the specified initial core gas pressure, spinning temperature, and core gas molecular weight), and core and clad mass flow rates. Surface tension values used in the spinning simulations in this section are zero and 32.9 dynes/cm; as stated above, the zero surface tension case reduces the model to the existing published TFA, and the results for PET fiber spinning and zero surface tension are identical to those published previously [9]. The PET surface tension value of 32.9 dynes/cm, assumed constant over the entire draw zone as stated in section 2.3.1, was taken from the literature as an estimate of the surface tension at the spinning temperature [11]. Figures 2.3 through 2.9, discussed below, show the variation of outer radius, axial velocity, temperature, axial viscous stress, core gas pressure and density, and the outer to inner fiber diameter ratio throughout the draw zone with and without surface tension effects for PET melt spinning.

As seen in Figure 2.3, the spinline outer radius initially decreases exponentially, then approaches its final value asymptotically. The semi-log plot in Figure 2.4 shows the analogous exponential increase and asymptotic transition of the velocity. The asymptotic behavior for both profiles is a consequence of the change in viscosity with spinline cooling.

Figures 2.3 and 2.4 show that the spinline outer radius and axial velocity profiles, and the final asymptotic values of these variables, are not significantly affected by surface tension. These results emphasize the effect of spinline cooling and the dominance of viscous effects over surface tension effects for the typical PET hollow fiber spinning conditions represented here.

The spinline temperature profile is even less sensitive to surface tension than the outer radius and velocity profiles: Figure 2.5 shows that temperature profiles with and without surface tension are less than 1% different throughout the draw zone. This result reflects the fact that the only link of spinline temperature to surface tension is the variation of the spinline outer radius and its role in the convective heat transfer term defined in equation (2.36).

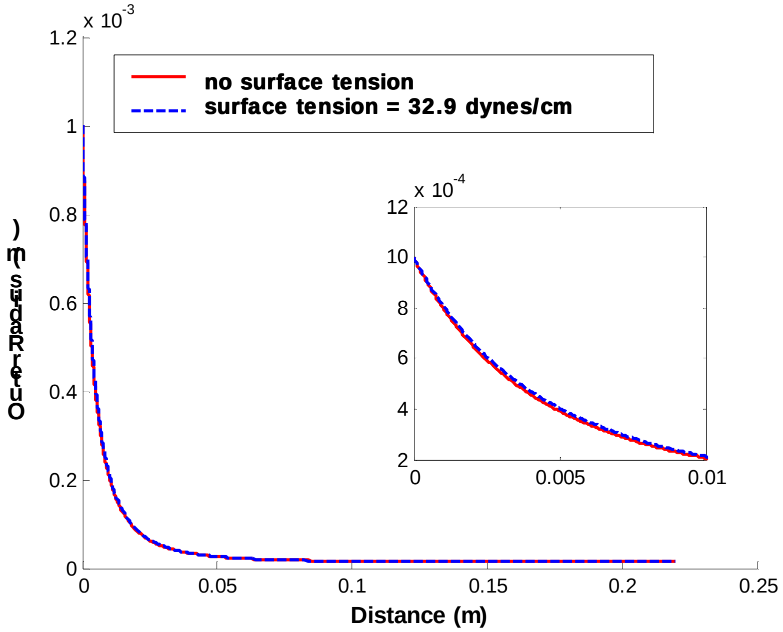

Figure 2.3 PET Spinline Outer Radius Profile

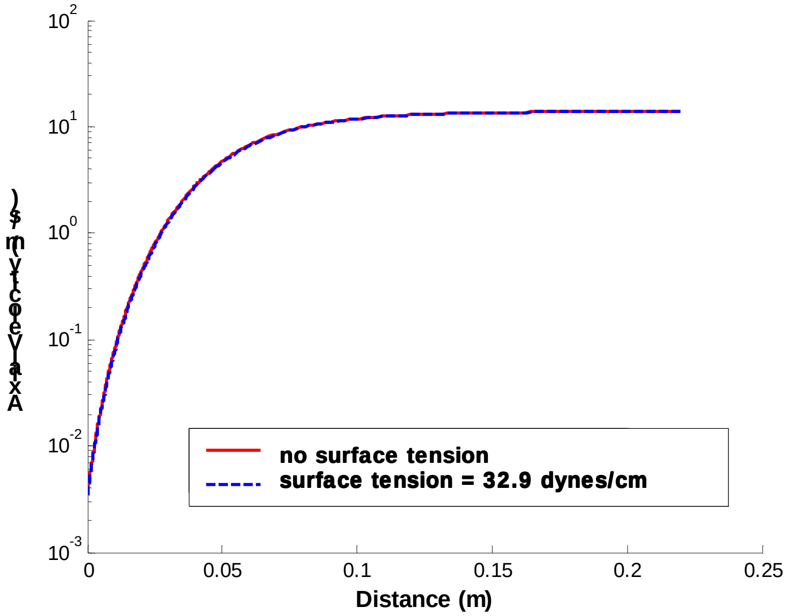

Figure 2.4 PET Spinline Velocity Profile

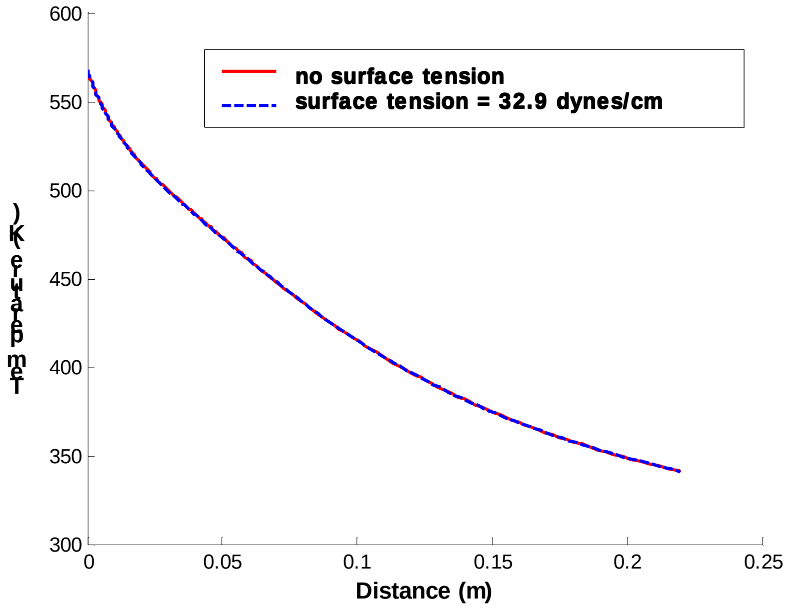

Figure 2.5 PET Spinline Temperature Profile

The spinline axial viscous stress τ_{zz} is calculated by definition for a Newtonian fluid as given by equation (2.40). Resulting axial viscous stress profiles for zero and 32.9 dynes/cm are shown in Figure 2.6.

$$\tau_{zz} = \frac{2}{3}\rho_o \left[\left(\frac{w_o + w_i}{w_o} \right) \left(\bar{v}^2 - \bar{v} \cdot \overline{v^0} \right) + \frac{3\eta_o^0 \bar{v} \left(\frac{d\bar{v}}{dz} \right) \Big|_{z=0}}{\rho_o \overline{v^0}} - \frac{\pi \bar{v} \gamma \left(R_o + R_i - R_o^0 - R_i^0 \right)}{w_o} \right] \qquad (2.40)$$

The predicted monotonically increasing stress trends for both cases are nearly identical, with the case involving surface tension creating slightly higher axial viscous stresses beginning approximately halfway through the draw zone. Because the radii decrease throughout the draw zone, the surface tension term in equation (2.40) always adds to the calculated viscous stress, with the contribution of this term increasing as the axial velocity increases. Since the axial viscous stress in the spinline correlates with molecular orientation [9], and thus final fiber macroscopic properties such as ductility, any fluctuations in this quantity can affect the performance and usefulness of the fibers. In particular, in-line measurement of the spinline tension, defined by the product of the axial viscous stress and the spinline cross-sectional area, can be used to detect spinning instabilities [18-20]. Thus, the analysis described herein can supplement future experimental work on spinning instabilities, forecasting process conditions for which the predicted axial viscous stress profile shows anomalies that could lead to unstable spinning.

Predicted core gas pressure profiles for PET melt spinning with and without surface tension effects, shown in Figure 2.7, have slightly different trends. With no surface tension, pressure is nearly constant for a brief initial period followed by a sharp decrease along the draw zone; the 32.9 dynes/cm case exhibits a slight initial *increase* to a maximum value, followed by a decrease analogous to the zero surface tension case.

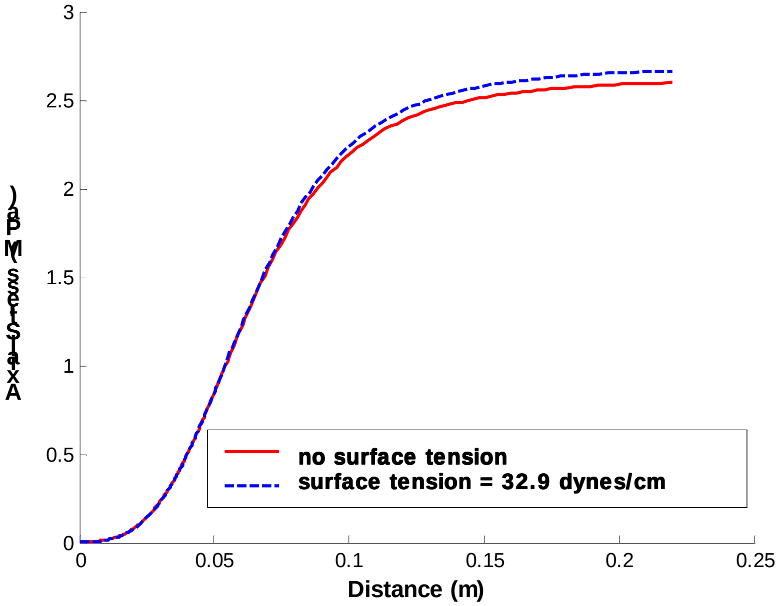

Figure 2.6 PET Spinline Axial Viscous Stress Profile

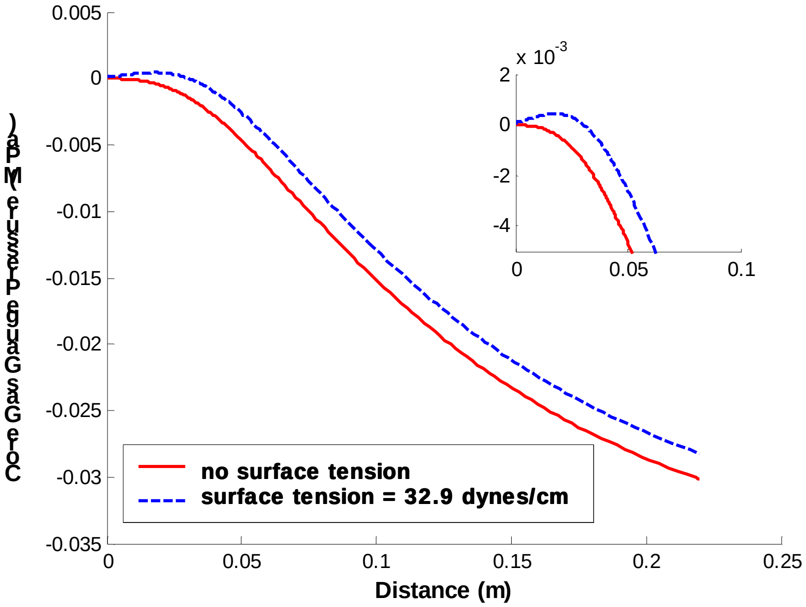

Figure 2.7 PET Spinline Core Gas Pressure Profile

The calculated core gas density profile shown in Figure 2.8 facilitates discussion of the effects of surface tension on core pressure behavior. For ideal gases described by equation (2.2), core gas pressure is directly proportional to core gas density, which is inversely proportional to temperature; therefore, changes in pressure are directly linked to changes in these two variables. Figure 2.8 shows that the core gas density increases along the draw zone, while Figure 2.5 shows that temperature always decreases. Thus, the core gas pressure profile along the draw zone depends on the relative rates of change of core gas density and temperature at a given axial position.

Equation (2.31), which quantifies the effect of surface tension on core gas density, can be solved for the core gas pressure to give equation (2.41).

$$\overline{p_i} = \frac{\eta_o}{\rho_i}\left[\gamma\left(\frac{1}{R_i}+\frac{1}{R_o}\right) - \frac{\bar{v}\dfrac{d\rho_i}{dz}}{\left(1+\dfrac{\rho_o w_i}{\rho_i w_o}\right)}\right] \qquad (2.41)$$

Coupled with the ideal gas law of equation (2.2) and affected by the viscosity, equation (2.41) is temperature-dependent as well. The ratio of spinline viscosity to core gas density, appearing on the right hand side of (2.41), is known always to be positive and always increase along the draw zone per the temperature dependence of spinline viscosity and the results shown in Figures 2.5 and 2.7 for the temperature and core gas density profiles. Thus, equation (2.41) shows that the core gas pressure trend is affected by the remaining two terms on the right hand side: one positive term that is multiplied by surface tension, and one negative term that is multiplied by the velocity. The core pressure profiles given in Figure 2.7 indicate that for the 32.9 dynes/cm case, the positive contribution of the surface tension term in equation (2.41) dominates the negative contribution of the velocity term for the relatively low velocities early in the draw zone, and the core gas pressure initially increases. Farther into the draw zone, the velocity increases dramatically as shown in Figure 2.4; this increase, and its effect on the core gas pressure, is compounded by the increase in core gas density depicted in Figure 2.8. Thus, for the case of 32.9 dynes/cm, the positive surface tension term in equation (2.41) initially dominates the core pressure behavior, causing the brief period of core gas pressure increase observed in Figure

2.7. As velocity and core gas density quickly increase, however, the negative velocity term in (2.41) takes over to produce the monotonic core pressure decrease analogous to the zero surface tension case. The zero surface tension case decreases throughout the draw zone in accordance with equation (2.41) and the predicted velocity and core gas density profiles.

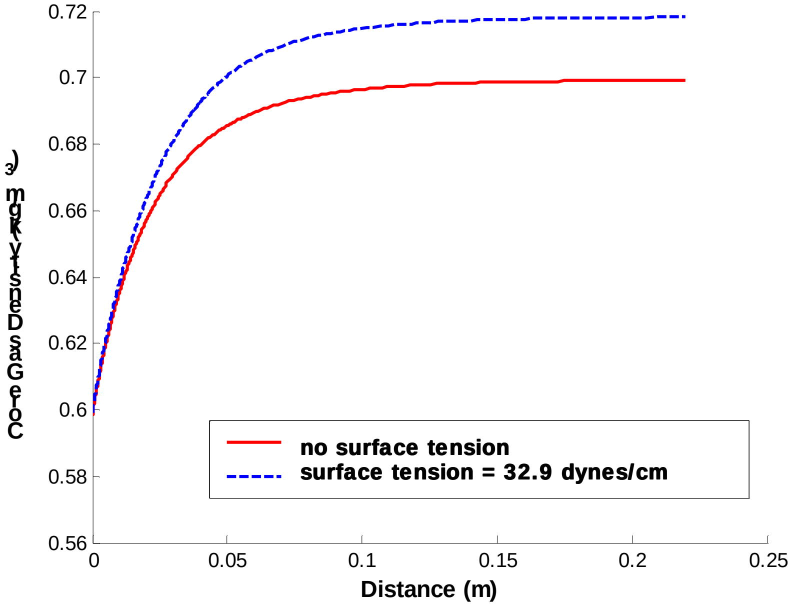

Figure 2.8 PET Spinline Core Gas Density Profile

Moreover, surface tension effects contribute to the increase in the core gas density, with a slightly higher final asymptotic core gas density value for the 32.9 dynes/cm case. Equation (2.34), the zero surface tension counterpart of equation (2.31), can be used to understand this: for zero surface tension, the core gas gauge pressure quickly becomes negative and continues to decrease throughout the draw zone, and the core gas density increases throughout the draw zone as a result. The 32.9 dynes/cm case, per equation (2.31), has the added contribution of the surface tension term affecting the magnitude of the core gas density increase. This term contributes to the change in core gas density throughout the draw zone, and the core gas density values for the 32.9 dynes/cm case are higher.

The profile for the outer to inner spinline diameter ratio, OD/ID, is given in Figure 2.9. This parameter increases exponentially, and then levels off to approach a final asymptotic value. Calculated per the continuity equation, (2.1), the OD/ID ratio is directly proportional to the core gas density and the constant clad density and core and clad mass flow rates. Thus, the profile follows the same trend as the core gas density, increasing throughout the draw zone, with a slightly higher final value for the 32.9 dynes/cm case. Surface tension's illustrated effect on the predicted OD/ID ratio, corresponding to changes in final fiber wall thickness, is a noteworthy result: wall thickness, effectively setting the denier, or weight for a set length of fiber, is an important parameter in terms of the structural integrity of spun fibers.

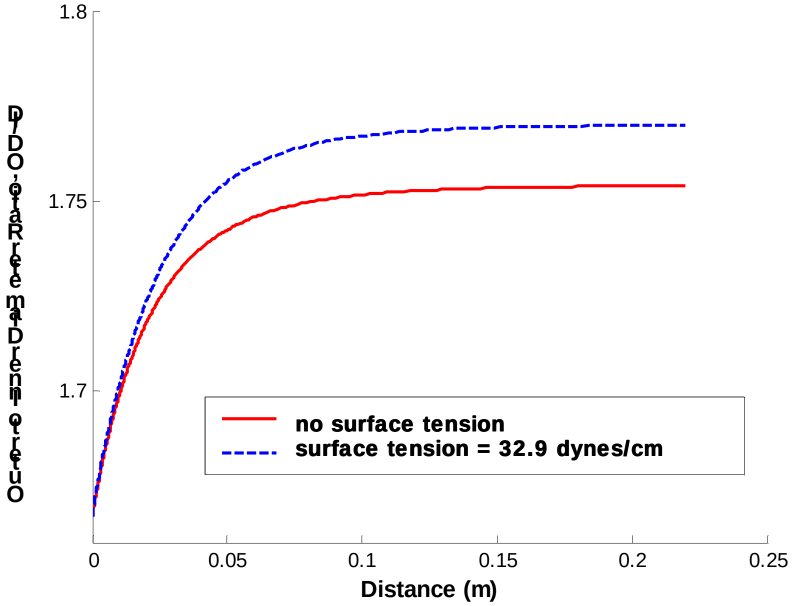

Figure 2.9 PET Spinline OD/ID Profile

2.4.2 Membrane Spinning

The objective of this section is to quantify the effects of surface tension on membrane spinline variables by evaluating their responses to different levels of surface tension during a typical spin. A representative set of membrane spinning conditions and material properties for the polyethylene–dodecanol (PE–dodecanol) system spun with a nitrogen gas core in this research are given in Tables 2.3 and 2.4. Presented in this section are model predictions of spinline variables using these conditions and properties with three levels of surface tension: zero, 30, and 60 dynes/cm. As mentioned above, several fundamental differences in PET melt spinning and PE–dodecanol membrane spinning exist: the PET operation presented above represents a high-speed industrial spin for a nonvolatile melt, while the PE–dodecanol results presented below represent low-speed, laboratory-scale spinning of a volatile solution. As such, PE–dodecanol spinning involves evaporative cooling effects and a much lower draw ratio than PET; furthermore, the PET spin considered in this chapter involves cross-flow air in the air gap, with an initial spinning temperature much higher than that for PE–dodecanol. In addition, the temperature dependence of the spinline viscosity is significantly different for the PET and PE–dodecanol spinning systems: comparing the values given in Tables 2.2 and 2.4, the viscosity activation energy E_o for PET is nearly double that of PE–dodecanol. In light of these fundamental process differences, the model predictions for PET and PE–dodecanol spinning variables can differ significantly. Section 2.4.3 addresses these differences to rationalize the model- predicted behavior for the two systems in terms of the spinning system and process differences.

Like the PET melt spin modeled in section 2.4.1, the simulated PE–dodecanol membrane spinning process is non-isothermal. Furthermore, the heat transfer coefficient for cross-flow cooling represented by equation (2.36) is used for the model simulations in this section, as are the physical properties for the air quench fluid given by equations (2.37) to (2.39). Unlike the PET simulations discussed in section 2.4.1, for the PE–dodecanol trials, the initial outer radius is specified and the extrusion velocity and initial inner radius calculated using continuity, equation (2.1). Additionally, the energy balance that includes evaporative cooling effects, equation (2.9), is used for the solution spinning case in this section.

The system surface tension value of 30 dynes/cm was taken from the literature for pure PE [11] and assumed to represent the surface tension of the PE–dodecanol spinline throughout the draw zone. The higher surface tension value case of 60 dynes/cm is used here for illustrative purposes to gauge a spinline’s general surface tension sensitivity. The heat of vaporization of dodecanol was taken from the literature [16] and set constant to its value at the initial spinning temperature. The pure component densities and heat capacities given in Table 2.4 were taken from the literature [11, 16, 21], with pure component densities set constant to their values at the spinning temperature, and the clad density calculated from these quantities and the volume fractions of each component in the spinning solution. The PE–dodecanol viscosity factors were measured using a concentric cylinder rheometer setup as detailed in section 4.1.3. Figures 2.10 to 2.17, discussed below, show the variation of outer and inner radii, axial velocity, temperature, axial viscous stress, core gas pressure and density, and the outer to inner fiber diameter ratio throughout the draw zone for the three levels of surface tension and the PE–dodecanol hollow fiber membrane spinning process.

Table 2.3 PE–Dodecanol Spinning Process Conditions for Sensitivity Studies

Condition	Value
R_i^0 = initial clad inner radius	6.8 x 10^{-4} m
R_o^0 = initial clad outer radius	2.3 x 10^{-3} m
$\overline{v}^0$ = extrusion velocity	1.74 x 10^{-2} m/s
$\overline{T}^0$ = spinning temperature	413 K
$\overline{p}_i^0$ = initial core gas gauge pressure	58 Pa
$\overline{v}^L$ = take-up velocity	35 m/min
L = draw zone length	0.20 m
T_q = quench fluid temperature	298 K
v_q = quench fluid velocity normal to fiber axis	0 m/s
w_i = core gas mass flow rate	2.08 x 10^{-8} kg/s
w_o = clad mass flow rate	2.00 x 10^{-4} kg/s
p_{atm} = ambient air pressure	101325 Pa

Table 2.4 PE–Dodecanol System Material Properties for Sensitivity Studies

Property	Value
ρ_d^0 = dodecanol density, assumed constant	747 kg/m^3
ρ_p^0 = PE density, assumed constant	785 kg/m^3
ρ_o = clad density, assumed constant	758 kg/m^3
η_o^0 = pre-exponential factor for clad shear viscosity dependence on temperature	6.07 x 10^{-3} Pas
E_o / R = Ratio of activation energy for clad shear viscosity temperature dependence to the gas constant	3681 K
$\Delta\hat{H}_{vap}^{d}$ = diluent heat of vaporization at T^0	3.89 x 10^5 J/kg
C_{pi} = core gas specific heat capacity, assumed constant	1046 J/kg-K
C_{po} = clad specific heat capacity, assumed constant	2134 J/kg-K
ϕ_d^0 = volume fraction of dodecanol in spinning solution	0.71
D = mutual diffusion coefficient calculated at T^0 and ϕ_d^0	7.20 x 10^{-12} m^2/s
MW_i = core gas molecular weight	28.0 kg/kmol
γ = clad surface tension	30 dynes/cm

Figures 2.10 and 2.11 show that the PE–dodecanol spinline outer and inner radii decrease exponentially throughout the draw zone. Unlike the PET results in Figure 2.3, a significant difference exists in the predicted radii at a given axial position for the three levels of surface tension and the PE–dodecanol spin conditions for most of the draw zone. In this region, the predicted radius at a given axial position increases on the order of 10% for each increase in surface tension level. However, the final values of the radii for each level of surface tension are nearly identical, which is addressed below with the discussion of the spinline core gas density profile.

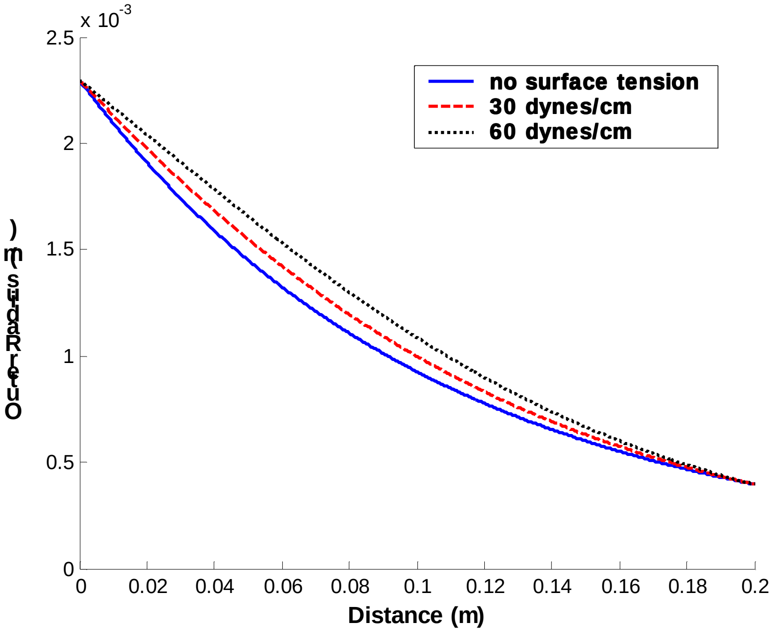

Figure 2.10 PE–Dodecanol Spinline Outer Radius Profile

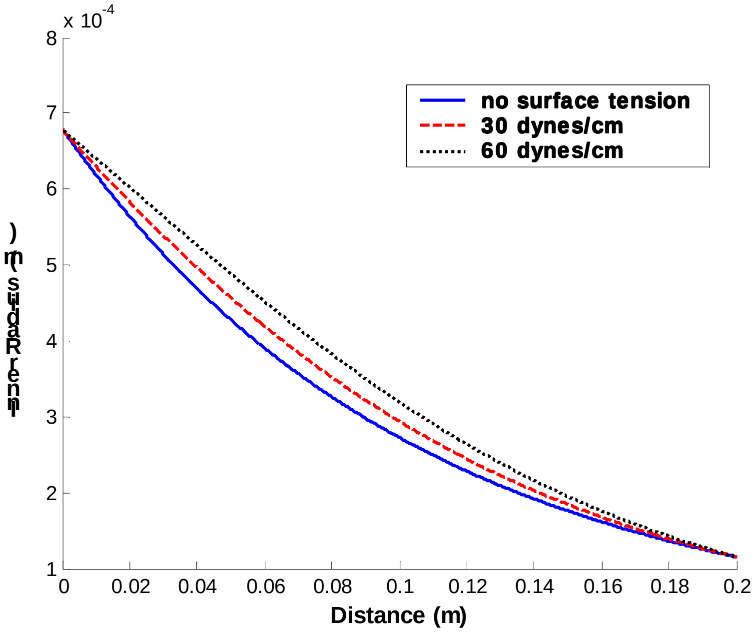

Figure 2.11 PE–Dodecanol Spinline Inner Radius Profile

Figure 2.12 shows a semi-log plot of the predicted velocity profiles for PE–dodecanol spinning, with the exponential increase of the velocity to the final take-up value continuing through the entire draw zone. These results complement the radii profiles of Figures 2.10 and 2.11: causing the spinline to minimize its surface area to volume ratio, both the inner and outer radii profiles are shifted to higher values throughout the draw zone as surface tension increases, resulting in an increase in spinline cross-sectional area at a given axial position. Per the uniaxial extension assumption in section 2.3.1, the axial velocity of the spinline is the same over the spinline cross-section at a given axial position. Thus, at a given axial position, for higher values of spinline cross-sectional area resulting from higher surface tension, the calculated axial velocity is lower to conserve momentum as established by equation (2.30)—the more gradual decreases in radius for higher surface tension correspond to more gradual increases in the predicted axial velocity.

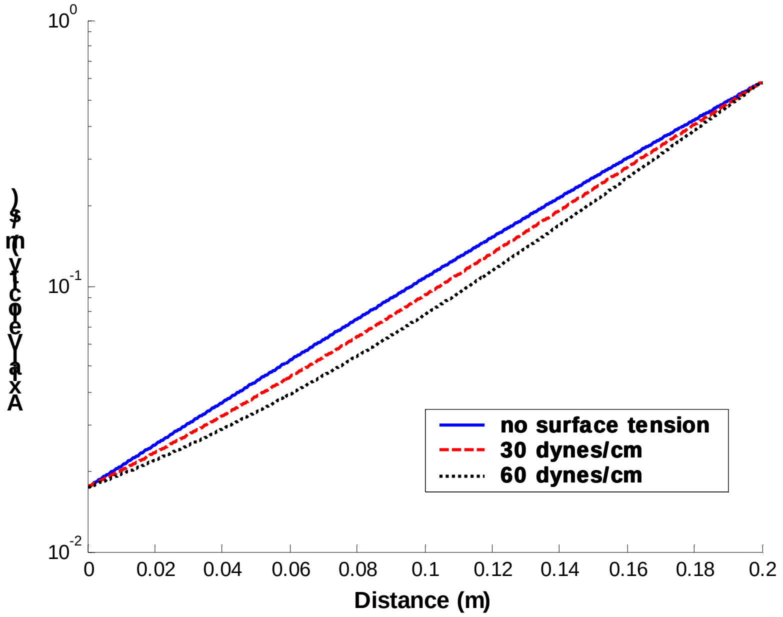

Figure 2.12 PE–Dodecanol Spinline Velocity Profile

Temperature profile predictions for PE–dodecanol spinning appear in Figure 2.13. In addition to results for typical PE–dodecanol spinning with different levels of surface tension,

Figure 2.13 includes additional data to illustrate the contribution of evaporative cooling effects. Focusing first on the three profiles for zero, 30, and 60 dynes/cm with all other spinning conditions represented in Tables 2.3 and 2.4, results in Figure 2.13 show that the temperature profile is not very sensitive to surface tension: final predicted spinline temperatures are about 1 K higher for each level of increase in surface tension. This is intuitively expected: higher surface tension leads to higher spinline cross-sectional area and lower axial velocity as discussed above, and this decreases the heat transfer rate, even if only slightly. Heat transfer rate as a function of surface tension can be quantified through the variation of the convective heat transfer coefficient with outer radius per equation (2.36): as outer radius increases, the heat transfer coefficient decreases.

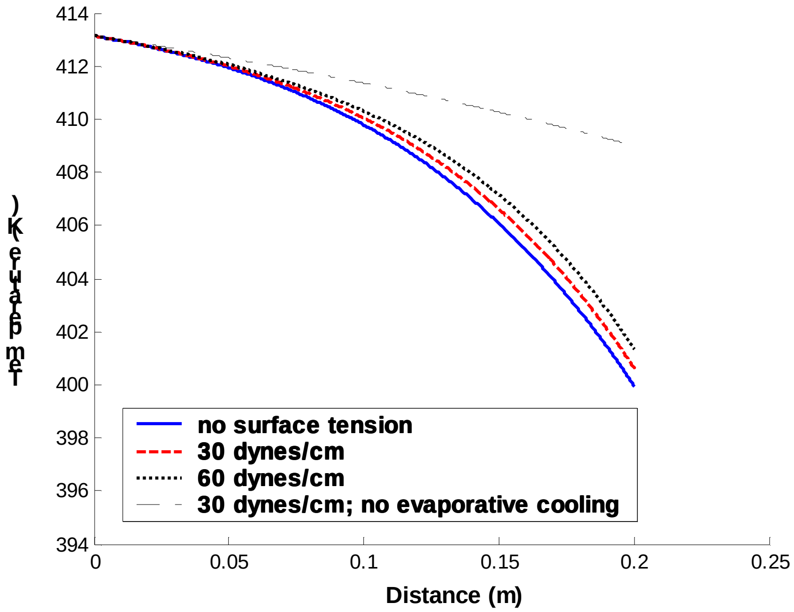

Figure 2.13 PE–Dodecanol Spinline Temperature Profile

In addition to the three predicted temperature profiles for different levels of surface tension, Figure 2.13 presents another data set to examine the specifics of evaporative cooling. This additional profile, the fourth legend entry in Figure 2.13, is for a surface tension of 30 dynes/cm, and this case represents the predicted temperature profile if evaporative cooling effects are neglected. For this case, only convective heat transfer occurs at the outer radius, and the melt spinning energy balance of equation (2.3) applies. This produces an approximately linear temperature drop of about 4 K compared to the approximately 12 K temperature drop for 30 dynes/cm including evaporative cooling.

The PE–dodecanol axial viscous stress profile predictions appear in Figure 2.14. Per equation (2.40), the axial viscous stress values depend on the velocity, the velocity derivative with respect to *z* at the beginning of the draw zone, and the surface tension. Results shown here indicate that for the majority of the draw zone, the differences in the velocity profile for the three levels of surface tension produce lower axial viscous stresses for higher surface tension.

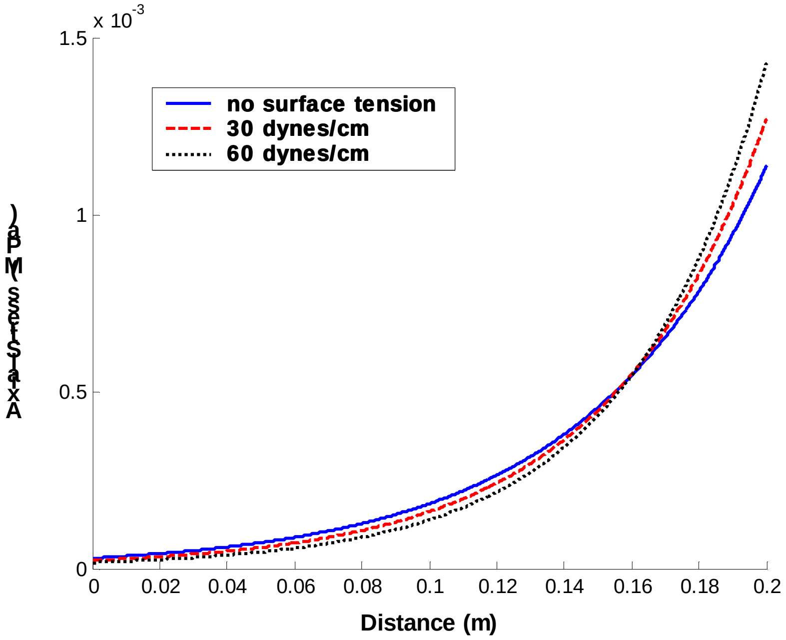

Figure 2.14 PE–Dodecanol Spinline Axial Viscous Stress Profile

However, near the end of the draw zone, as velocities for the three cases converge to the identical take-up velocity set as a required boundary condition for all cases, the surface tension term in equation (2.40) becomes more important in the calculation of the stress, slightly increasing the axial stresses for the 30 and 60 dynes/cm cases in this region. As discussed in section 2.4.1, changes in the axial viscous stress profile correspond to changes in spinline tension, a quantity often used to detect spinning instabilities. Stress profile differences for different ranges of membrane spinning conditions and the different values of spinline tension that result relate to future hollow fiber membrane spinning instability studies and the role of surface tension.

PE–dodecanol core gas pressure profiles are presented in Figure 2.15. In order to simulate a consistent set of conditions while only varying the surface tension level, the initial core gas gauge pressure $\overline{p_i}$ was set to the same value, 58 Pa, for all cases in this section. However, as the pressure profile predictions in Figure 2.15 show, both the zero and 60 dynes/cm cases result in nearly instantaneous changes to different values. The input value of 58 Pa was based on the order of magnitude of the published value of 27 Pa for PET spinning used in section 2.4.1, confirmed by laboratory spinning experience here: for the typical spinning operations using a core gas for membrane spinning in this research, the gas input rate is too small to produce a significant (relative to P_{atm}) initial core gas gauge pressure. For the zero and 60 dynes/cm cases, the interactions among the various other spinning parameters at the beginning of the draw zone influence the required initial pressure value—the initial pressure is not a readily variable parameter. The discussion here disregards this immediate pressure change, which is very small relative to the ambient pressure, and instead focuses on the predicted trends in core gas pressure and the differences between the trends for the three levels of surface tension.

The zero surface tension case shown in Figure 2.15 shows that the predicted core gas gauge pressure drops monotonically along the draw zone, becoming negative very early. The 30 and 60 dynes/cm cases show a different trend, increasing monotonically along the draw zone, with a more dramatic increase for the 60 dynes/cm case. Thus, there is a large qualitative difference in the behavior of the cases with and without surface tension.

Like the PET case in section 2.4.1, the discussion of the core pressure profile can be related to the predicted core gas density profile, shown in Figure 2.16. Core gas density results for all three levels of surface tension are comparable, with a less than 3% net change in core gas density over the entire draw zone. Referring to equation (2.41) for the calculation of the core gas gauge pressure, such minor changes in core gas density are overpowered by the surface tension term for the 30 and 60 dynes/cm cases, and the predicted core gas pressure increases throughout the draw zone. For zero surface tension, the core pressure in equation (2.41) depends directly on the core gas density gradient, which, though very gradual, is positive throughout the draw zone.

Thus, for zero surface tension, the predicted core gas gauge pressure decreases everywhere along the draw zone, becoming negative immediately per the sign of the density gradient term in equation (2.41).

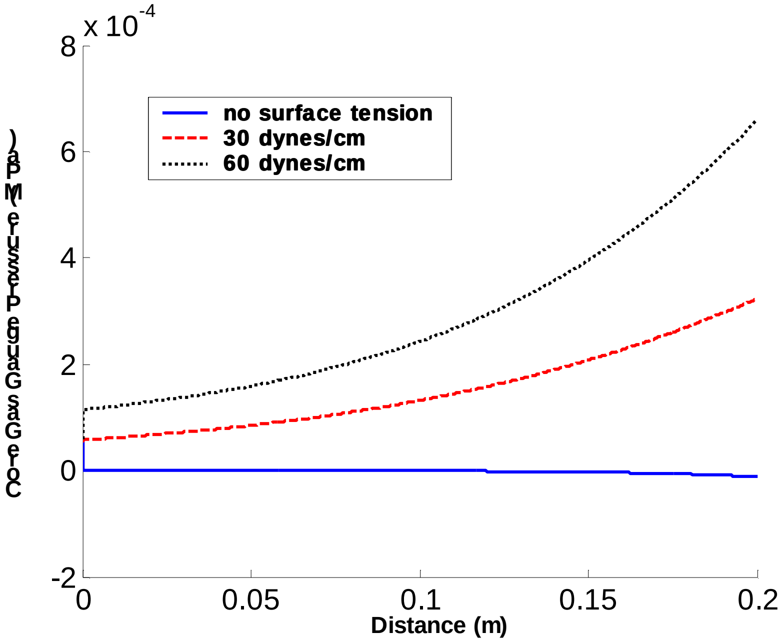

Figure 2.15 PE–Dodecanol Spinline Core Gas Pressure Profile

In addition, the radii profiles of Figures 2.10 and 2.11 show that profiles for all levels of surface tension converge to nearly the same final radius values despite measurable differences in the predicted radii for the majority of the draw zone. This can be attributed to two factors: all cases are bounded with the same take-up velocity as a required boundary condition, and the difference in the final core gas density for the three cases is not significantly different as shown in Figure 2.16. Thus, calculated final inner and outer radii for the three levels of surface tension using continuity, equation (2.1), are nearly identical. Thus, results here show that although the final values of the radii are essentially the same for all levels of surface tension and the conditions simulated here, the approach to the final values is predicted to be significantly different. For some spinning conditions involving high axial stresses (such as higher draw ratios than the draw ratio of 34 considered here for PE–dodecanol) or a stress-sensitive system prone to instability or spinline breakage, the evolution of the radii profiles may be very important: since the spinline tension is the axial stress per unit area, changes in the cross-sectional area profile may affect operational stability.

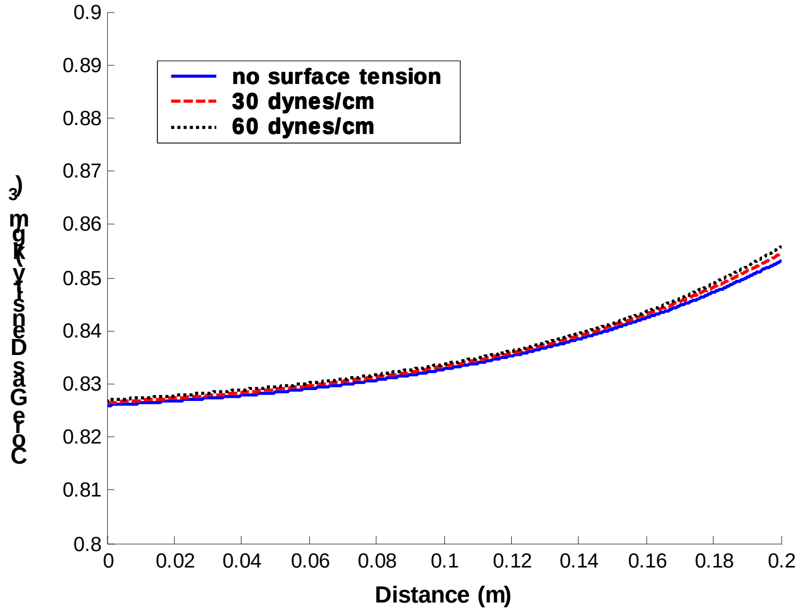

Figure 2.16 PE–Dodecanol Spinline Core Gas Density Profile

Furthermore, the PE–dodecanol OD/ID ratio profile appearing in Figure 2.17 varies directly with core gas density and increases analogously along the draw zone. Like the core gas density, the OD/ID ratio does not change significantly over the draw zone, and results for all three surface tension levels are comparable. Thus, for the PE–dodecanol hollow fiber membrane spinning conditions simulated here, surface tension does not have a significant effect on wall thickness, an important consideration in terms of membrane flux.

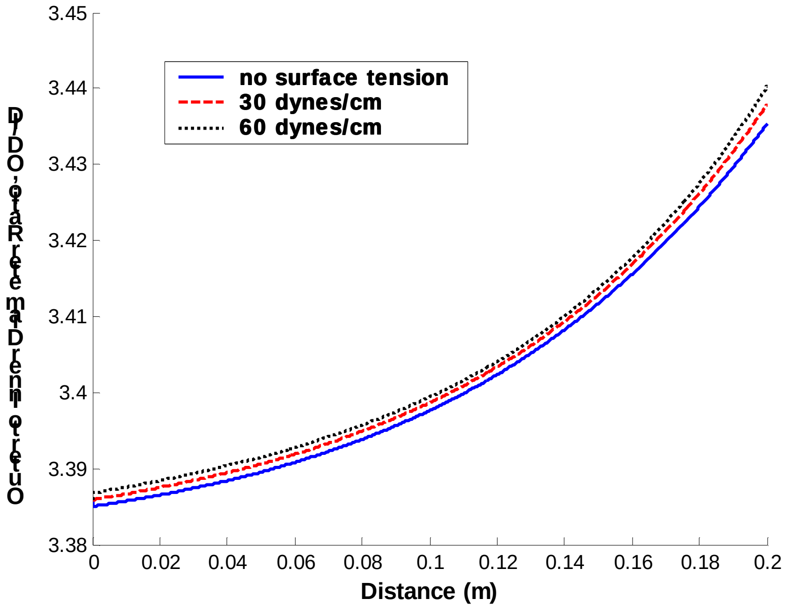

Figure 2.17 PE–Dodecanol Spinline OD/ID Profile

2.4.3 Comparison of Model Predictions for PET and PE–Dodecanol Spinning

Differences between the conditions and physical properties pertinent to PET melt spinning and PE–dodecanol membrane spinning result in significantly different spinline behavior. The PET operation is a high-speed industrial spin with a draw ratio on the order of 4000; PE–dodecanol spinning is done on a laboratory scale using a draw ratio on the order of 30. With a comparable air gap length for both cases, the extremely high draw ratio forces the PET spinline to increase in velocity at a much faster rate than the PE–dodecanol case. This contributes to PET spinline cooling, as does the non-zero air velocity in the air gap, with the net effect being an increase in the convective heat transfer coefficient. The result is a much more dramatic temperature drop over the draw zone for the PET spinline compared to the PE–dodecanol spinline. This is true despite the occurrence of evaporative cooling for the PE–dodecanol solution spinning case: results shown here indicate that although evaporative cooling is more significant than convective heat transfer for the PE–dodecanol, stagnant air gap case modeled here, the rate of cooling cannot compete with that experienced by nonvolatile PET with its high draw ratio and non-zero air velocity.

In addition, the temperature dependence of the spinline viscosity is significantly different for the PET and PE–dodecanol spinning systems. With a viscosity activation energy nearly double that of the 30 wt-% PE–dodecanol solution, PET viscosity is affected more dramatically by changes in temperature. The effect of the different viscosity activation energy is compounded by the much more dramatic temperature decrease for the PET spin. Results show that the PET viscosity increase with axial distance is dramatic enough to force the majority of the spinline attenuation to occur early in the draw zone, and an asymptotic value of spinline outer radius is approached long before the end of the air gap. This contrasts with PE–dodecanol and its exponential increases to final inner and outer radii and axial velocity along the entire draw zone length. Again, these results are linked to the high PET draw ratio, which makes the axial velocity increase with axial distance at a very large rate and thus spurs the temperature decrease and spinline viscosity increase that cause rapid spinline attenuation.

2.5 Summary of Chapter 2

In this chapter, the TFA for hollow fiber spinning was modified to include surface tension and evaporative cooling effects. The results presented here are used to gauge the sensitivity of spinline variables to surface tension for PET industrial melt spinning and PE–dodecanol hollow fiber membrane spinning.

For high-speed PET industrial melt spinning, results show that predicted spinline outer radius, axial velocity, and temperature profiles are insensitive to surface tension, while the predicted axial viscous stress, core gas pressure, core gas density, and the outer to inner diameter ratio (OD/ID) profiles are affected moderately. Surface tension sensitivity studies for low-speed laboratory spinning of PE–dodecanol membranes, however, show measurable differences for predictions of the inner and outer radii, axial velocity, and core gas pressure profiles. For the simulation results presented here, all three levels of surface tension produce the same final inner and outer radii and axial velocity; however, surface tension effects produce differences in the evolution of these profiles, which could be important to spinline stability. In addition, evaporative cooling effects were shown to affect noticeably the predicted temperature profile for PE–dodecanol membrane spinning.

The sensitivity study results presented here illustrate that for low-speed membrane spinning, surface tension plays a significant part in spinline behavior. In contrast, high-speed PET spinning is influenced highly by the very large draw ratio and dramatic spinline axial velocity, temperature, and viscosity changes that result, and viscous effects due to spinline cooling dominate surface tension effects for a typical PET hollow fiber melt spin. These results have possible implications for future spinning instability studies and the ability of surface tension to accelerate or inhibit these occurrences.

2.6 References

1. R.G. D'Andrea and C.B. Weinberger, Effects of surface tension and gravity forces in determining the stability of isothermal fiber spinning, AIChE J., 22 (1976) 923-925.
2. J.C. Chang, M.M. Denn, and F.T. Geyling, Effects of Inertia, Surface-Tension, and Gravity on the Stability of Isothermal Drawing of Newtonian Fluids, Industrial & Engineering Chemistry Fundamentals, 20 (1981) 147-149.
3. T. Hagen, On the effects of spinline cooling and surface tension in fiber spinning, Zeitschrift Fur Angewandte Mathematik Und Mechanik, 82 (2002) 545-558.
4. A.L. Yarin, and P. Gospodinov, Stability loss and sensitivity in hollow fiber drawing, Phys. Fluids, 6 (1994) 1454-1463.
5. J.R.A. Pearson and Y.T. Shah, On the stability of nonisothermal fiber spinning--general case, Ind. Eng. Chem. Fundam., 11 (1972) 150-153.
6. S. Kase and T. Matsuo, Studies on melt spinning. II. Steady-state and transient solutions of fundamental equations compared with experimental results, J. Appl. Polym. Sci., 11 (1967) 251-287.
7. M.M. Denn, Continuous drawing of liquids to form fibers, Ann. Rev. Fluid Mech., 12 (1980) 365-387.
8. M.A. Matovich and J.R.A. Pearson, Spinning a Molten Threadline. Steady-State Isothermal Viscous Flows, Ind. Eng. Chem. Fundam., 8 (1969) 512-520.
9. G.G. Lipscomb, The melt hollow fiber spinning process: Steady-state behavior, sensitivity and stability, Polymers for Advanced Technologies, 5 (1994) 745-758.
10. M.M. Denn, Computational analysis of polymer processing, in: S.M. Richardson (Ed.), Computational analysis of polymer processing, Applied Science Publishers, London, 1983.
11. J. Brandrup, E.H. Immergut, and E.A. Grulke, (Eds.), Polymer Handbook, 4th ed., John Wiley & Sons, New York, 1999.
12. R.J. Fisher and M.M. Denn, Draw resonance in melt spinning, Applied Polymer Symposium, 27 (1975) 103-109.

13. J.C. Hyun, Theory of draw resonance: Part II. Power law and maxwell fluids, AIChE J., 24 (1978) 423-426.
14. M.T. Batarseh, Formation of anisotropic hollow fiber membranes via TIPS, Dissertation, The University of Texas at Austin, 1999.
15. B.T.F. Chung and V. Iyer, Heat transfer from moving fibers in melt spinning process, J. Appl. Polym. Sci., 44 (1992) 663-670.
16. R.L. Rowley, W.V. Wilding, J.L. Oscarson, Y. Yang, R.J. Rowley, T.E. Daubert, and R.P. Danner, DIPPR® Data Compilation of Pure Compound Properties: Design Institute for Physical Property Data, AIChE®, New York, NY (2001).
17. W.M. Deen, Analysis of transport phenomena, Oxford University Press, New York, 1998.
18. J.W. Hill and J.A. Cuculo, An experimental study of threadline dynamics with emphasis on the effect of molecular weight on the elongational viscosity of melt-spun poly(ethylene terephthalate), J. Appl. Polym. Sci., 18 (1974) 2569-2588.
19. C.J.S. Petrie and M.M. Denn, Instabilities in polymer processing, American Institute of Chemical Engineers Journal, 22 (1976) 209-236.
20. R.J. Fisher, and M. M. Denn, Mechanics of nonisothermal polymer melt spinning, AIChE J., 23 (1977) 23-28.
21. J.E. Mark, (Ed.), Physical properties of polymers handbook, AIP Press, Woodbury, N.Y., 1996.

Chapter 3. Modeling Membrane Extent of Anisotropy Including General Membrane Sensitivity Studies

3.1 Motivation and Background for Modeling Concentration Profiles

Due to the general lack of fundamental insight in terms of how the membrane fabrication process relates to the final structure and properties of a given hollow fiber membrane, membrane optimization is currently a trial-and-error process involving costly and time-consuming experimentation [1]. This chapter provides a means to predict membrane extent of anisotropy, and as such is an important precursor to development of a complete model to predict membrane macrostructure (inner and outer diameters, and thus fiber wall thickness) and microstructure (pore size, pore size distribution, porosity, and anisotropy) as functions of spinning conditions and material properties.

Previous efforts to model the membrane microstructure formation process generally involve monitoring the phase separation process, choosing a mechanism by which phase separation occurs and relating that to evolution of the domains representative of the membrane microstructure. However, such analyses are very system-specific, forcing the user to know or somewhat arbitrarily specify the phase separation mechanism and characterize the complicated kinetics of the process [2-10]. In addition, the solution scheme may involve extensive and costly computational time, and there is limited work in the area of hollow fibers [11].

The present research is a general formulation that builds on the thin filament analysis (TFA) model for hollow fiber spinning [12] discussed and updated to include surface tension and evaporative cooling effects as described in Chapter 2. The model development in this chapter involves using the results from simulations of the TFA from Chapter 2 in combination with a boundary layer analysis to model radial concentration gradients that evolve in the spinline during the hollow fiber membrane spinning process. Combined with the axial temperature profile predictions of the TFA, this data is useful because the concentration and temperature at the time of phase separation determine the kinetics involved in the phase separation process. Thus, prediction of concentration gradients and temperature profiles is an important fundamental step toward predicting final membrane structure as a function of spinning system physical parameters and process variables.

Specifically, a concentration gradient leads to a pore size gradient, and in asymmetric or anisotropic hollow fiber membranes, the predicted radial concentration gradients from the present modeling efforts can be used to estimate membrane extent of anisotropy, the fraction of the membrane cross-section exhibiting a pore size gradient [13]. The boundary layer analysis approach for modeling concentration gradients is justified because previous work has shown that for many membranes, pore size gradients, and thus concentration changes, are confined to thin boundary regions in the cross-section extending inward from the fiber outer radius [13-15].

In the cross-section adjacent to the fiber inner radius, experimental results for spinning with a nitrogen gas core indicate that hollow fiber membranes spun under typical conditions possess very limited anisotropy in the cross-section adjacent to the inner wall. Furthermore, saturating the core gas with diluent prior to extrusion has been shown experimentally to eliminate anisotropy at the inner wall completely [16]. Existing efforts to model concentration gradients at the inner wall show that even when spinning typical hollow fiber membranes with an unsaturated (with diluent) ideal gas core, both heat and mass transfer to the lumen are negligible, with the core gas quickly becoming saturated with diluent [14, 17].

Figures 3.1 and 3.2 show scanning electron micrographs (SEMs) of cross-sections of the same typical PE–dodecanol hollow fiber membrane, focusing on the microstructure adjacent to the outer and inner radii, respectively. The radial pore size gradient near the outer radius is evident in Figure 3.1, in contrast to the minimal difference in pore structure observed over the cross-section near the inner radius in Figure 3.2. Thus, in the modeling efforts presented here, only outer wall membrane anisotropy is considered.

The procedure developed herein for modeling concentration gradients requires little computational time and is applicable to hollow fiber membranes spun under a variety of conditions. Another advantage is that knowledge of the phase separation kinetics or even the phase separation mechanism is not required for predicting the membrane extent of anisotropy using the analysis presented here.

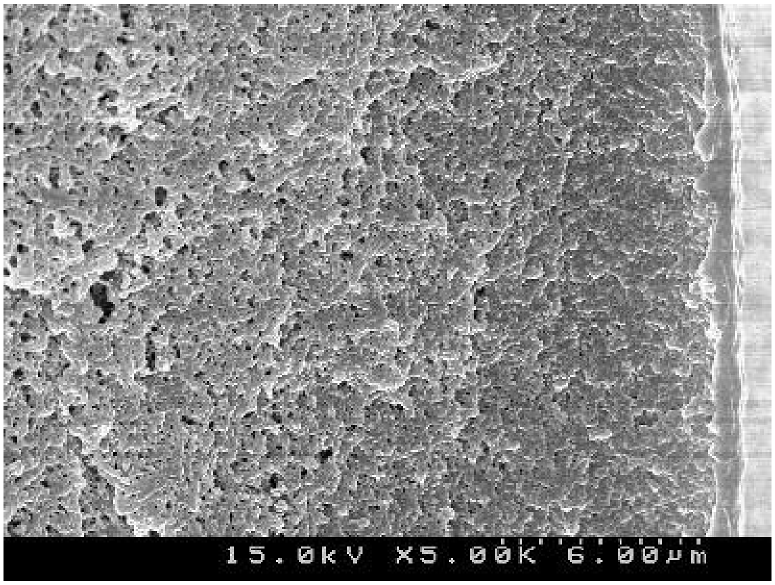

Figure 3.1 Typical PE–Dodecanol Hollow Fiber Membrane Cross-Section SEM: the fiber outer radius appears on the right hand side of the image, and anisotropy is evident

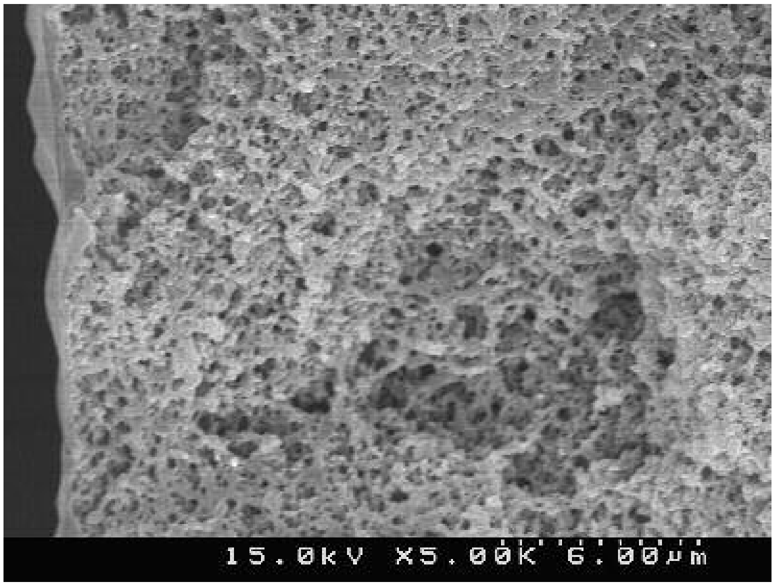

Figure 3.2 Typical PE–Dodecanol Hollow Fiber Membrane Cross-Section SEM: the fiber inner radius appears on the left hand side of the image, and pore structure differences here are minimal

3.2 Equation Development

The starting point for the modeling efforts is the TFA of the hollow fiber spinning process modified to include the effects of surface tension and evaporative cooling as detailed in Chapter 2. The TFA predicts the variation of fiber inner and outer diameters, velocity, stress, and temperature with axial distance in the draw zone. The boundary layer analysis for predicting radial concentration gradients for solution spinning is separate from the TFA in that it can be performed only after obtaining the predicted velocity, clad outer radius, and temperature profiles for the given spinning operation from simulations of the TFA equations. With the predicted spinline velocity, outer radius, and temperature profiles, the diluent concentration in the spinline at the outer radius is calculated as a function of axial position by equating the diluent diffusive flux out of the spinline through the cross-sectional boundary layer to the diluent convective flux into the air gap. The calculated concentration values at the outer radius provide necessary boundary condition data, which is combined with the predicted spinline variable profiles from the TFA to calculate the membrane extent of anisotropy.

As discussed in section 2.3.2, since modeling the effects of evaporative cooling in the TFA for fiber spinning are quantified by calculating the amount of energy lost via diluent evaporation, the heat flux boundary condition applied at the spinline outer radius for the TFA energy balance given by equation (2.9) depends on the diluent diffusive flux through the boundary layer. This calculation requires knowledge of the concentration of diluent in the spinline at the outer radius as a function of axial position, calculated using the methodology described below in section 3.2.1. Thus, incorporating the effects of evaporative cooling makes the concentration and temperature modeling efforts an iterative process: the temperature profile is first calculated using assumed values for the diluent concentration at the outer radius, and simulation results are then used to calculate values of the diluent concentration at the outer radius as functions of axial position. The procedure is repeated until results from consecutive program iterations agree to within 1%.

3.2.1 Boundary Layer Analysis for Modeling Concentration Gradients

For the case of steady-state operation, a binary solution of polymer and diluent, constant mutual diffusion coefficient, constant core and clad densities, negligible axial diffusion, and a thin concentration boundary layer relative to fiber wall thickness, conservation of mass for the diluent gives equation (3.1). In this equation, C_d represents mass concentration of diluent, v_r is the spinline radial velocity, r is radial position, z is axial position, $\bar{v}$ is the spinline axial velocity, and D is the mutual diffusion coefficient. Equation (3.1) describes concentration as a function of position in the boundary layer adjacent to the spinline outer radius.

$$v_r \frac{\partial C_d}{\partial r} + \bar{v} \frac{\partial C_d}{\partial z} = D\left[\frac{1}{r}\frac{\partial}{\partial r}\left(r\frac{\partial C_d}{\partial r}\right)\right] \qquad (3.1)$$

Substituting for the radial velocity term using the continuity equation for cylindrical coordinates [18] and neglecting the effects of curvature due to the assumption of a relatively thin concentration boundary layer produces equation (3.2). Refer to section B.6 for details of the derivation shown here. This result is similar to that for analyzing the case of mass transfer to a flat plate with Schmidt number Sc <<1 (the momentum boundary layer is thin relative to the concentration boundary layer): an extra factor of ½ is the only difference. The solution procedures for the two cases are analogous.

$$-\frac{r}{2}\frac{\partial \bar{v}}{\partial z}\frac{\partial C_d}{\partial r} + \bar{v}\frac{\partial C_d}{\partial z} = D\left(\frac{\partial^2 C_d}{\partial r^2}\right) \qquad (3.2)$$

Defining a new spatial variable, y, in terms of the radial coordinate using equation (3.3) and then converting concentration to a dimensionless value Θ per equation (3.4) converts the diluent concentration expression of (3.2) to equation (3.5), subject to the boundary conditions given in (3.6). In these relationships, C_{d0} is the concentration of diluent in the spinline at the outer radius R_o; and $C_{d\infty}$ is the concentration of diluent in the bulk of the clad cross-section, far from the boundary layer, where concentration is assumed to be uniform and equal to the initial concentration of diluent in the extrudate. See section B.6 for details related to use of the chain rule for differentiation to convert the coordinates.

$$y = R_o - r \qquad (3.3)$$

$$\Theta = \frac{C_d - C_{d0}}{C_{d\infty} - C_{d0}} \qquad (3.4)$$

$$\left(\frac{y}{2}\right)\left(\frac{d\bar{v}}{dz}\right)\left(-\frac{\partial\Theta}{\partial y}\right) + \bar{v}\frac{\partial\Theta}{\partial z} = D\frac{\partial^2\Theta}{\partial y^2} \qquad (3.5)$$

$$\begin{aligned} &BC1: \quad @\, y = 0, \Theta = 0 \\ &BC2: \quad @\, y \to \infty, \Theta = 1 \qquad (3.6) \\ &BC3: \quad @\, z = 0, \Theta = 1 \end{aligned}$$

The second-order partial differential equation given by equation (3.5) is solved using a similarity transform, where the similarity variable η is defined by equation (3.7) in terms of an additional expression *g(z)*, a function of the axial position. Equation (3.8) gives the solution for *g(z)*; using this result to solve for the dimensionless concentration Θ yields equation (3.9).

$$\eta = y \cdot g(z) \qquad (3.7)$$

$$g(z) = \sqrt{\frac{\bar{v}}{4Dz}} \qquad (3.8)$$

$$\theta = erf(\eta) \qquad (3.9)$$

The initial concentration of diluent in the extrudate, $C_{d\infty}$, is a set parameter, equal to the concentration of diluent in the prepared spinning solution; however, the surface concentration at R_o, represented by C_{d0}, depends on the extent of diluent evaporation and must be determined through a mass balance. At the fiber outer radius R_o, diluent evaporates and is swept away by convection into the air gap surrounding the spinline, setting up a radial concentration gradient that spurs diluent diffusion from the bulk of the clad cross-section outward toward R_o. The extent of diluent evaporation, and thus the surface concentration C_{d0}, can vary along the draw zone and must be calculated as a function of axial position. Although necessarily set as a constant value in the first boundary condition given in equation (3.6) for solving equation (3.5) analytically, for spinning conditions under which the concentration variation is minor, accounting for this variation does not compromise the accuracy of the analysis. Future work discussed in Chapter 6 includes determining under which conditions the boundary layer analysis developed here is adequate for predicting concentration profiles during fiber spinning.

The mass balance for determining the surface concentration in the spinline at R_o is established by equating the cross-sectional diffusive flux of diluent through the boundary layer toward the outer radius to the convective flux of diluent away from the fiber into the air gap, as given by equation (3.10).

$$\frac{-D\rho_d^0}{1-\frac{\phi_d|_{Ro}}{\rho}\left(\rho_d^0-\rho_p^0\right)}\frac{\partial\phi_d}{\partial r}\bigg|_{Ro}=k_c\left(\rho_d^g\big|_{Ro}-\rho_d^g\big|_{\infty}\right) \qquad (3.10)$$

In equation (3.10), ρ_d^0 and ρ_p^0 represent the pure diluent and polymer densities, and ρ is the solution density, all assumed constant as stated previously; these quantities are set equal to their known initial values at the beginning of the draw zone as in Chapter 2. Pure component densities are calculated as functions of temperature [19, 20] based on the spinning temperature at the beginning of the draw zone. The solution density is calculated using the volume-weighted pure component densities and the initial spinning solution composition, assuming incompressible clad and diluent. The diluent volume fraction in the spinline is represented by ϕ_d. Note that the denominator (the term with the pure component densities) in the diffusive flux term on the left hand side allows for high rates of radial mass transfer, including the effects of convective mass transfer in the radial direction. Order of magnitude calculations for typical processes suggest that these effects are small.

The convective mass transfer coefficient at the fiber outer wall is k_c, calculated using equation (3.11) following the work of Ohzawa *et al.* [21, 22]. In equation (3.11), T_q is the temperature of the air in the air gap, MW_q is the molecular weight of air (29 kg/kmol), k_q and ρ_q are the air thermal conductivity and density as defined in equations (2.37) and (2.38), and C_{pq} is the air heat capacity, defined by equation (3.12) for the units of J/kg-K [20]. The heat transfer coefficient h is defined from the literature for cross-flow cooling as given by equation (2.36). Finally, D_{d-air} is the diffusion coefficient for diluent into air as defined by the Fuller equation for diffusion of gases [23] given in units of m^2/s by equation (3.13).

$$k_c=\frac{R_gT_q}{p_{atm}}\left(\frac{\rho_qD_{d-air}}{k_qC_{pq}}\right)^{1/2}\frac{h}{MW_q} \qquad (3.11)$$

$$C_{pq} = \left\{ 28958 + 9390.0 \left[\frac{\left(\dfrac{3012.0}{T_q} \right)}{\sinh\left(\dfrac{3012.0}{T_q} \right)} \right]^2 + 7580.0 \left[\frac{\left(\dfrac{1484.0}{T_q} \right)}{\cosh\left(\dfrac{1484.0}{T_q} \right)} \right]^2 \right\} \frac{1}{MW_q} \tag{3.12}$$

$$D_{d-air} = \frac{1.0 \times 10^{-9}\, T_q^{1.75}}{p_{atm} \left[\left(\sum v_{atom} \right)_{air}^{1/3} + \left(\sum v_{atom} \right)_{d}^{1/3} \right]^2} \left(\frac{1}{MW_q} + \frac{1}{M_d} \right)^{1/2} \tag{3.13}$$

In equation (3.13), the ambient air pressure, p_{atm}, must have units of atmospheres; the $\sum v_{atom}$ terms are diffusion volumes (the sum of the atomic volume of all the atoms for a molecule of air or diluent) [23]; and M_d is the diluent molecular weight.

Returning to define the remaining terms in equation (3.10), the diluent concentration in the air far from the spinline, $\rho_d^g\big|_{\infty}$, is zero; $\rho_d^g\big|_{Ro}$, the diluent concentration in the air adjacent to the spinline surface at the outer radius R_o, is calculated using the Flory–Huggins theory to describe the diluent activity in the spinline, with the assumptions of thermodynamic equilibrium of the diluent at the clad–air quench interface and the surrounding ambient air in the air gap being an ideal gas [14]. This gives equation (3.14) for $\rho_d^g\big|_{Ro}$. In equation (3.14), P_d^0 represents the diluent vapor pressure; M_d is the diluent molecular weight; R_g is the universal gas constant; and χ is the Flory–Huggins interaction parameter, determined as a function of temperature for the PE–dodecanol system as discussed in section 4.1.2.

$$\rho_d^g\Big|_{Ro} = \frac{P_d^0 M_d}{R_g \bar{T}} \phi_d\big|_{Ro} \exp\left[1 - \phi_d\big|_{Ro} + \chi \left(1 - \phi_d\big|_{Ro} \right)^2 \right] \tag{3.14}$$

Converting concentration of diluent to volume fraction of diluent using $C_d = \phi_d \rho_d^0$, it follows that the radial variation of diluent volume fraction can be expressed by equation (3.15), where ϕ_d^0 represents the diluent volume fraction in the initial spinning solution.

$$\left.\frac{\partial \phi_d}{\partial r}\right|_{Ro} = \frac{\left(C_{d0} - C_{d\infty}\right)}{\rho_d^0}\sqrt{\frac{\bar{v}}{\pi D z}} = \left(\phi_d\big|_{Ro} - \phi_d^0\right)\sqrt{\frac{\bar{v}}{\pi D z}} \tag{3.15}$$

Combining equations (3.10), (3.14), and (3.15) gives equation (3.16), which is used to determine the diluent concentration (volume fraction of diluent, ϕ_d) in the spinline at the outer radius R_o.

$$\frac{-\rho_d^0}{1 - \frac{\phi_d|_{Ro}}{\rho}\left(\rho_d^0 - \rho_p^0\right)}\left(\phi_d\big|_{Ro} - \phi_d^0\right)\sqrt{\frac{D\bar{v}}{\pi z}} = k_c\left\{\frac{P_d^0 M_d}{R_g \bar{\bar{T}}}\phi_d\big|_{Ro}\exp\left[1 - \phi_d\big|_{Ro} + \chi\left(1 - \phi_d\big|_{Ro}\right)^2\right]\right\} \tag{3.16}$$

3.2.2 Concentration Gradients: Method of Solution

The boundary layer analysis at the fiber outer wall described in section 3.2.1 is used to predict radial concentration gradients in the spinline as a function of axial position in the draw zone. The calculation procedure involves several steps; first, simulations of the TFA model including surface tension and evaporative cooling effects with assumed values of diluent concentration at the outer radius are used to determine the spinline axial velocity, outer radius, and temperature profiles for a given spinning operation. Next, results from these simulations of the modified TFA model are used to calculate the concentration of diluent in the spinline at the outer radius (the surface concentration C_{d0}) as a function of axial position using equation (3.16). Calculated outer radius concentration values are then input to the model, and the simulation is repeated to obtain new temperature and other spinline variable profiles. This iterative procedure is repeated until results from consecutive iterations agree within 1%. Results from the TFA simulations are then used with equations (3.3), (3.7), and (3.8) to calculate the similarity variable η as a function of both radial and axial position. Finally, dimensionless concentration Θ is obtained using equation (3.9) and converted to the desired dimensional concentration, C_d, using equation (3.4) with the calculated surface and known bulk concentration values C_{d0} and $C_{d\infty}$.

All calculations were performed using MATLAB 6.1, with the TFA simulations conducted as described in section 2.3.3 and the diluent concentration at R_o calculated by solving equation (3.16) using the *fsolve* command (*MaxIter* = 4000, *MaxFunEvals* = 20000, *TolFun* = 1 x 10^{-10}, *TolX* = 1 x 10^{-10}).

3.3 Membrane Spinning: General Sensitivity Studies

This section is divided into segments, each discussing the response of the predicted PE–dodecanol spinline temperature, axial viscous stress, and outer to inner diameter ratio (OD/ID) to different levels of a specific spinline process parameter. In addition, effects on membrane extent of anisotropy are discussed collectively in a following section. Sensitivity to initial spinning temperature, draw ratio (ratio of take-up velocity to linear extrusion velocity), core gas flow rate, clad viscosity, air gap temperature, velocity of the air in the air gap, air gap length, and diffusion coefficient are presented. Only one process parameter is varied per sensitivity study; the other spinning conditions for that section correspond to the "base case" experimental conditions and system physical properties given in Tables 2.3 and 2.4, which are representative of typical laboratory-scale spinning of the PE–dodecanol system. Moreover, many of the spinning process parameters varied here for the sensitivity studies were also varied experimentally in this research, with the results presented and discussed in Chapters 4 and 5.

3.3.1 Sensitivity to Spinning Temperature

Depending on the volatility of the diluent and the temperature dependence of the solution viscosity, the initial spinning temperature $\overline{T}^{0}$ potentially affects the extent of evaporation and rate of elongation in the air gap. In addition, the diffusion coefficient of the polymer–diluent solution, appearing in both the evaporative cooling term of the energy balance in equation (2.9) and the concentration boundary layer analysis of section 3.2.1, varies with the initial spinning temperature, as does the diluent heat of vaporization. These factors, combined with the effect of initial temperature on the extent of spinline cooling, suggest that selection of $\overline{T}^{0}$ could be important to concentration and temperature profiles for a hollow fiber membrane spinline. The spinning temperature is dictated in part by the temperature required to maintain a homogeneous spinning solution for extrusion into the air gap; in addition, energy considerations for a process make lower operating temperatures more favorable. Thus, $\overline{T}^{0}$ can only be varied over a limited range for a given process; however, the considerations listed above warrant examining the sensitivity of spinline variables to spinning temperature.

Simulations for three possible spinning temperatures for the PE–dodecanol system, 393 K, 413 K, and 433 K, were performed here. These spinning temperatures correspond to diffusion coefficients of 2.29 x 10^{-12}, 7.21 x 10^{-12}, and 1.45 x 10^{-11} m^2/s, respectively, all predicted using the Zielinski–Duda formulation as discussed in section 4.1.4. Diluent heat of vaporization values are 4.06, 3.89, and 3.72 x 10^5 J/kg, calculated for each spinning temperature using the published correlation for dodecanol [20]. Solution density was also calculated for each spinning temperature using published correlations for pure polymer and diluent [19, 20]. All other spinning conditions and system material properties are given in Tables 2.3 and 2.4.

The predicted spinline temperature profiles, given in Figure 3.3, have nearly identical trends, but they are offset by the difference in initial spinning temperature. Thus, lower initial spinning temperatures correspond to lower temperatures throughout the draw zone. If a specific final filament temperature at the end of the draw zone is desired, the air gap must be lengthened for higher spinning temperatures or shortened for lower spinning temperatures.

The predicted OD/ID profiles shown in Figure 3.4, although offset from each other per equation (2.1) due to the differences in core gas density and inner radius corresponding to the spinning temperature difference, are not significantly different. The axial viscous stress profiles, shown in Figure 3.5, show a bit more variation because lower initial spinning temperature corresponds to higher viscosities everywhere in the spinline, resulting in higher stresses.

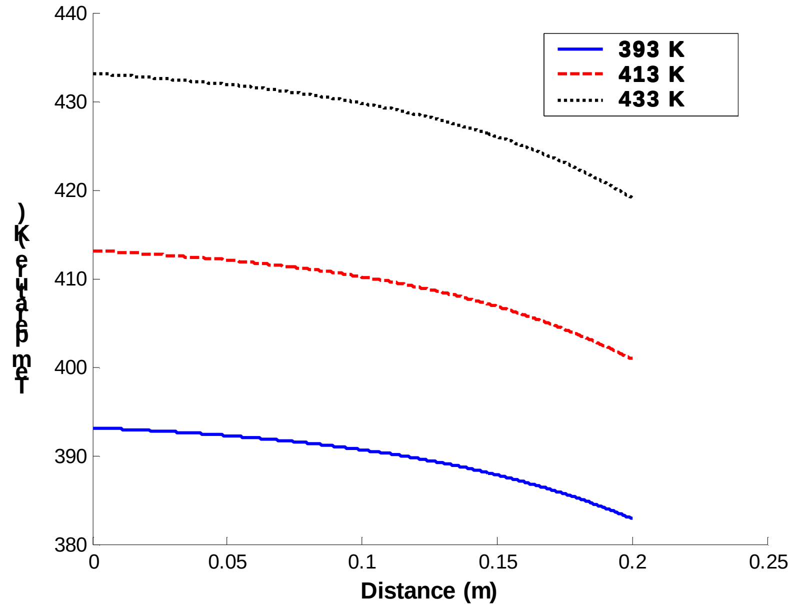

Figure 3.3 Sensitivity of Membrane Temperature Profile to Spinning Temperature

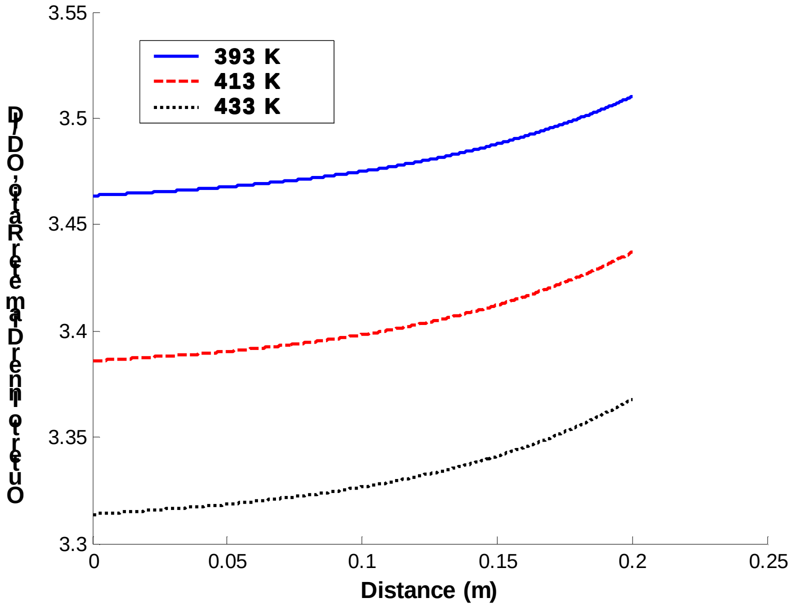

Figure 3.4 Sensitivity of Membrane OD/ID Profile to Spinning Temperature

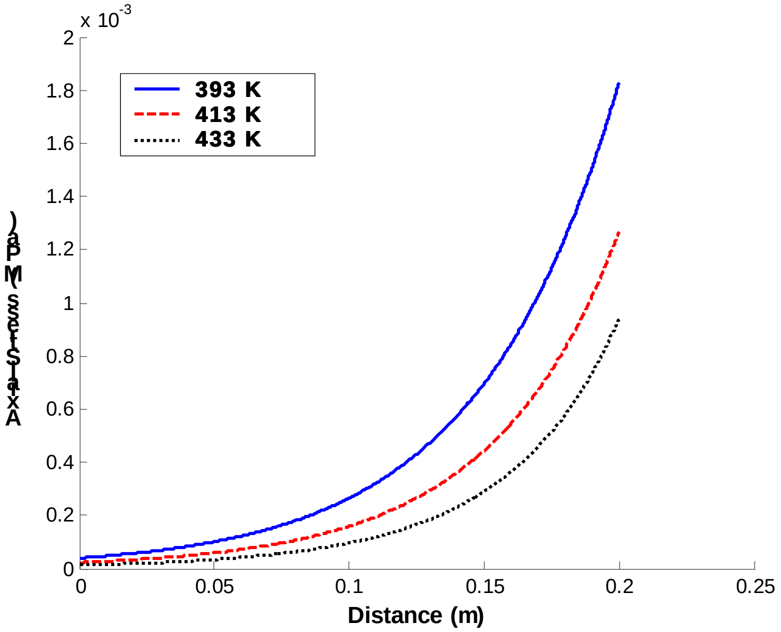

Figure 3.5 Sensitivity of Membrane Axial Viscous Stress to Spinning Temperature

3.3.2 Sensitivity to Draw Ratio

Setting the draw ratio (again, the ratio of spinline take-up velocity to linear extrusion velocity) is highly dependent on system behavior and spinning stability. Numerous studies have involved correlating the draw resonance instability discussed briefly in Chapter 2 with spinning above a critical draw ratio, which is approximately 20 for isothermal spinning of Newtonian fluids and higher for conditions involving spinline cooling, such as those studied in this research; that is, spinline cooling has a stabilizing effect and extends the range of useable draw ratios [24]. However, a critical draw ratio for membrane spinning exists in general as observed experimentally in this research, and this limits the range of feasible draw ratios for some spinning processes. Experiments using the spinning conditions and the physical properties of the dodecanol system as given in Tables 2.3 and 2.4 resulted in the fiber pooling on the water bath surface for too low of a draw ratio (generally less than 24) and instability (non-uniform fibers produced, characterized by diameter fluctuation at a given axial position with time) or filament breakage for a draw ratio that is too high (generally above 35). However, through manipulation of the take-up velocity, draw ratios of 24, 29, and 34 were possible experimentally and were used for the sensitivity modeling in this section; these draw ratios correspond to take-up velocities of 25.0, 30.0, and 35.0 m/min. The spinning temperature for these sensitivity studies is 393 ± 1 K, the same as that used experimentally for the draw ratio sensitivity studies discussed in Chapters 4 and 5; densities, diffusion coefficient, and diluent heat of vaporization are calculated based on this temperature. The linear extrusion velocity, the same for all the draw ratios used in this section, and other spinning conditions and physical parameters are listed in Tables 2.3 and 2.4.

Results show that this range of draw ratios does not produce a significant difference in temperature profiles as illustrated by Figure 3.6. The three draw ratio cases end with temperatures less than one degree apart. This is a result of the minor changes in convective heat transfer coefficient, set by equation (2.36), which result chiefly from the changes in the velocity profile for the different draw ratios used here. Higher velocities mean more convective heat transfer to the air gap, but the difference in velocities tested here is not significant enough to affect drastically this quantity or the temperature profile that results.

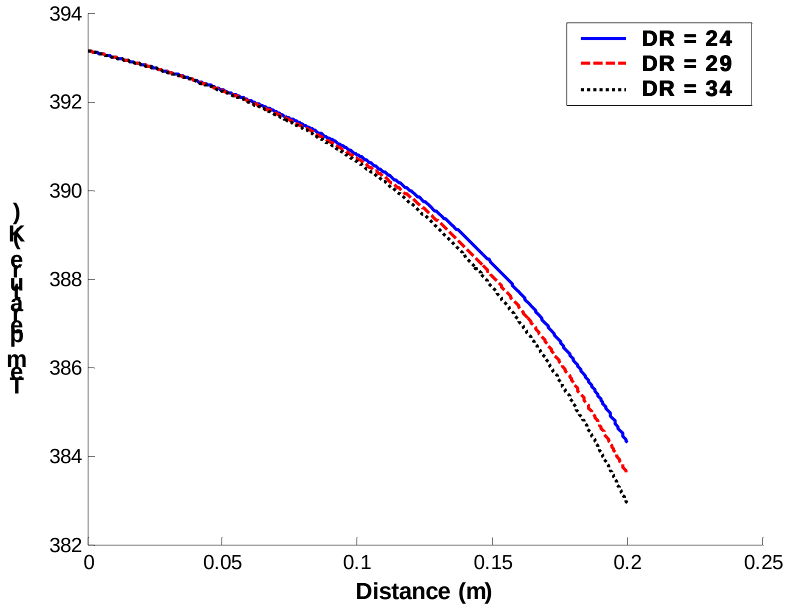

Figure 3.6 Sensitivity of Membrane Temperature Profile to Draw Ratio

The OD/ID profiles presented in Figure 3.7 reflect the insignificant changes in temperature discussed above. Although the *y*-axis scale of Figure 3.7 shows that the OD/ID values increase along the spinline, this increase is not significant. Values of OD/ID for the three draw ratios used in the simulations are not significantly different anywhere in the draw zone, following from the insignificant difference in core gas density between the three cases.

Figure 3.8 shows the spinline axial viscous stress profiles as functions of draw ratio. Stresses increase for higher draw ratios as expected; however, the stress profiles follow the same trend throughout the draw zone, and it is difficult to make a conclusion about the significance of the difference in magnitude predicted here.

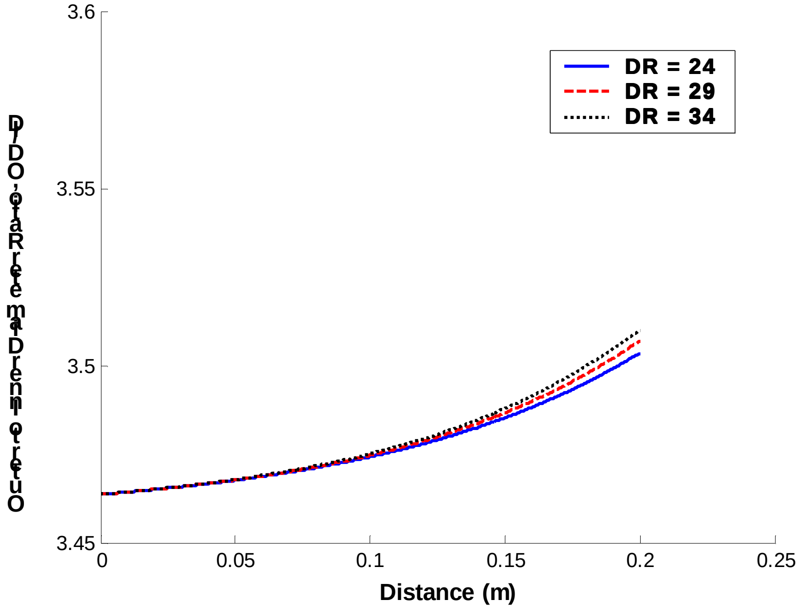

Figure 3.7 Sensitivity of Membrane OD/ID Profile to Draw Ratio

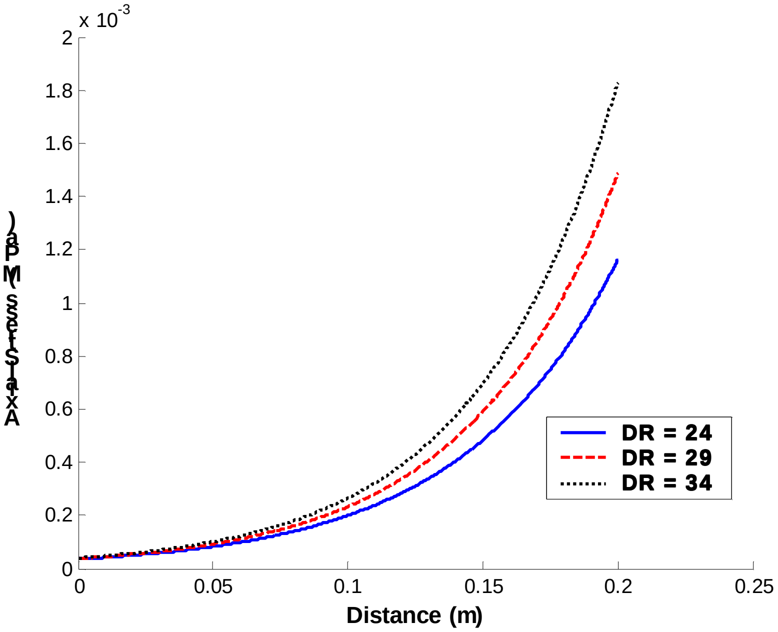

Figure 3.8 Sensitivity of Membrane Axial Viscous Stress to Draw Ratio

3.3.3 Sensitivity to Core Gas Flow Rate

Core gas flow rate plays a major role in determining the spinline inner radius per equation (2.1). This is evident in the results shown here, where three different core gas mass flow rates, corresponding to 1.00, 3.00, and 5.00 SCCM volumetric flows, are compared. Volumetric flow rates are specified by the gas flow controller for display simplicity: the core gas mass flow rate, constant throughout the draw zone, is calculated as shown in Appendix A using the ideal gas law in equation (2.2) with the set volumetric flow rate and standard temperature and pressure conditions of 273 K and 1 atm. All other spinning conditions and physical properties are given in Tables 2.3 and 2.4.

The temperature profiles in Figure 3.9 for the three core flows are virtually identical; the core gas heat capacity is small relative to that of the core, and changes in inner radius do not significantly alter the heat transfer occurring during spinning. Similarly, the predicted axial viscous stress profiles for the three core flow rates, given in Figure 3.10, nearly coincide: although both core flow rate and inner radius are factors in calculating the axial viscous stress per equation (2.40), the stress is not sensitive to either quantity for the range of core gas flows used here.

However, there is a significant difference in the predicted OD/ID profiles for all three core flow rates used here. Illustrated in Figure 3.11, the final OD/ID ratios decrease from about 3.4 to 2.1 to 1.75 as core gas flow rate increases from 1.00 to 5.00 SCCM. Thus, core gas mass flow rate is a key factor in setting hollow fiber membrane wall thickness. This is quantified by the continuity equation in (2.1).

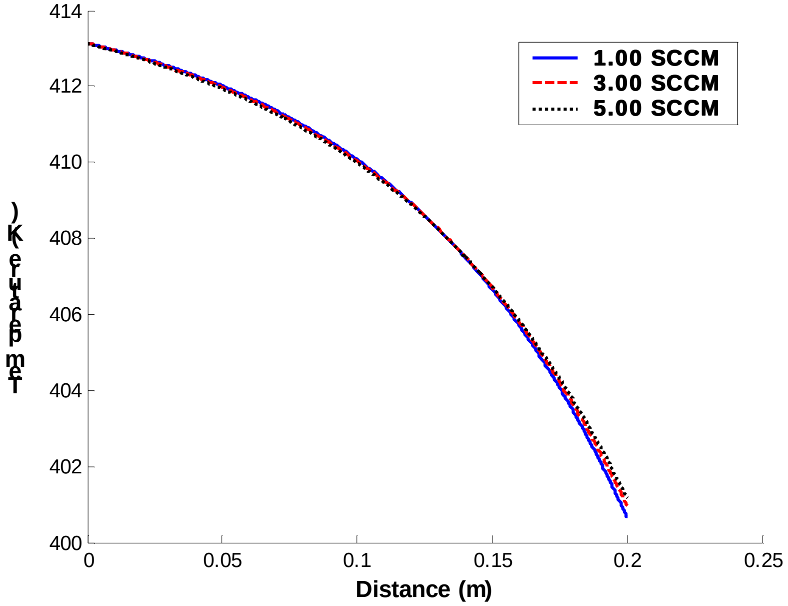

Figure 3.9 Sensitivity of Membrane Temperature Profile to Core Flow Rate

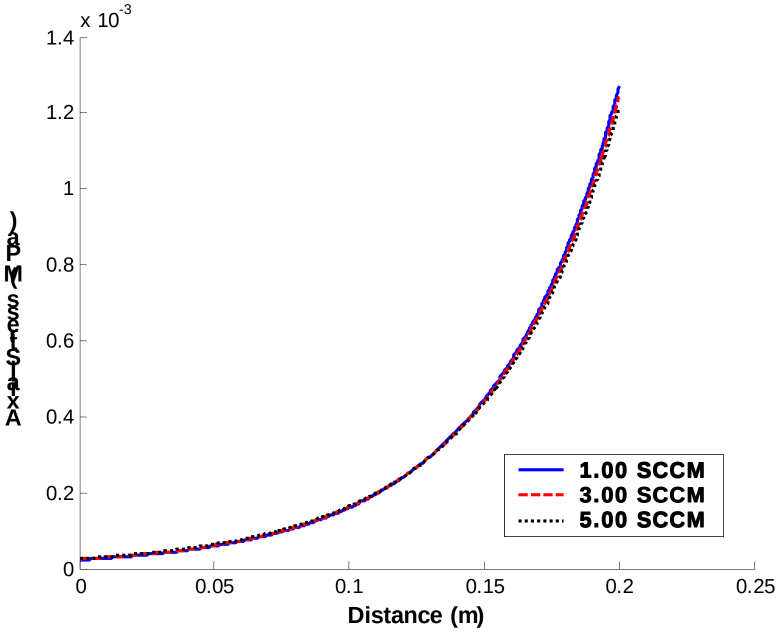

Figure 3.10 Sensitivity of Membrane Axial Viscous Stress Profile to Core Flow Rate

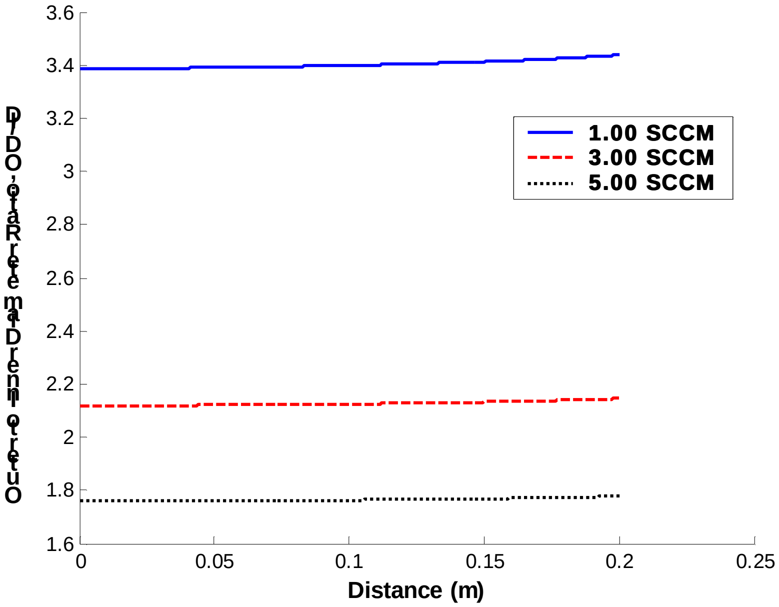

Figure 3.11 Sensitivity of Membrane OD/ID Profile to Core Flow Rate

3.3.4 Sensitivity to Clad Viscosity

The Newtonian clad viscosity is assumed to obey an Arrhenius temperature dependence given by equation (2.35). This section examines the sensitivity of the spinline to the value of the clad viscosity activation energy, E_o, which determines the sensitivity of the viscosity to changes in temperature. TFA model predictions for E_o = 7309 cal/mol, the value measured for 30 wt-% PE–dodecanol as discussed in section 4.1.3, are contrasted with results for doubling this value to 14617 cal/mol. In order to retain the proper order of magnitude of calculated system viscosity, the viscosity pre-factor, η_o, was also adjusted to a value of 8.18×10^{-7} Pa s, which produces the experimentally measured value of viscosity (see section 4.1.3) using the doubled activation energy at the spinning temperature of 413 K. All other spinning conditions and system properties are outlined in Tables 2.3 and 2.4.

Doubling the viscosity activation energy results in a stronger dependence of viscosity on temperature: for the higher E_o of 14617 cal/mol, viscosity increases earlier in the spinline, and this translates to a greater extent of draw-down earlier in the spinline. However, for the spinning conditions used here, this difference in draw-down is not enough to alter significantly the convective heat transfer coefficient or the temperature profile prediction as shown in Figure 3.12: final temperatures for the two cases are only about 1 K different. Moreover, the predicted OD/ID profiles given in Figure 3.13 show final values that are not significantly different for the two cases of viscosity activation energy. Both cases show that the OD/ID ratio increases throughout the draw zone.

The axial viscous stress profiles presented in Figure 3.14 are only slightly different as well: the higher spinline viscosities for the 14617 cal/mol case create higher spinline stresses over a majority of the draw zone. However, because the temperature profile predictions are so similar for the two cases examined here, the viscosity values are at most 3% different, and the difference in predicted viscous stress for the two cases is not dramatic.

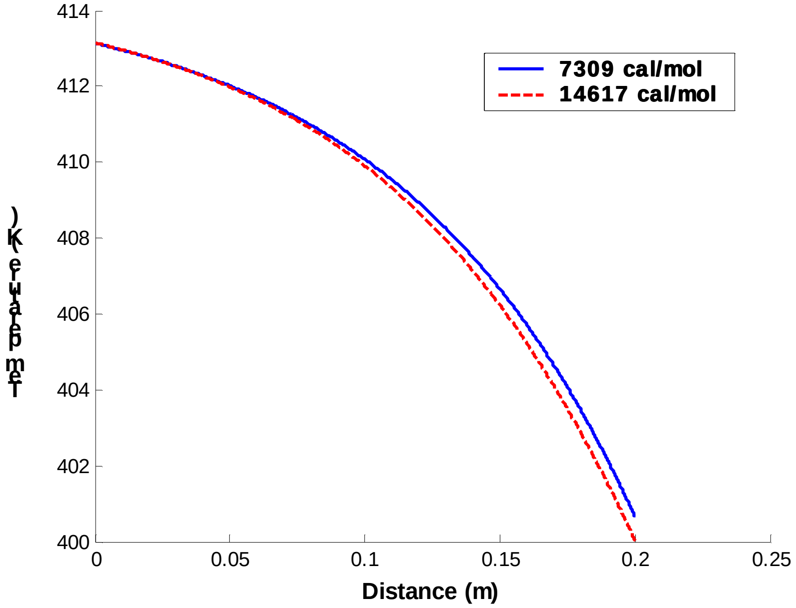

Figure 3.12 Sensitivity of Membrane Temperature Profile to Viscosity Activation Energy

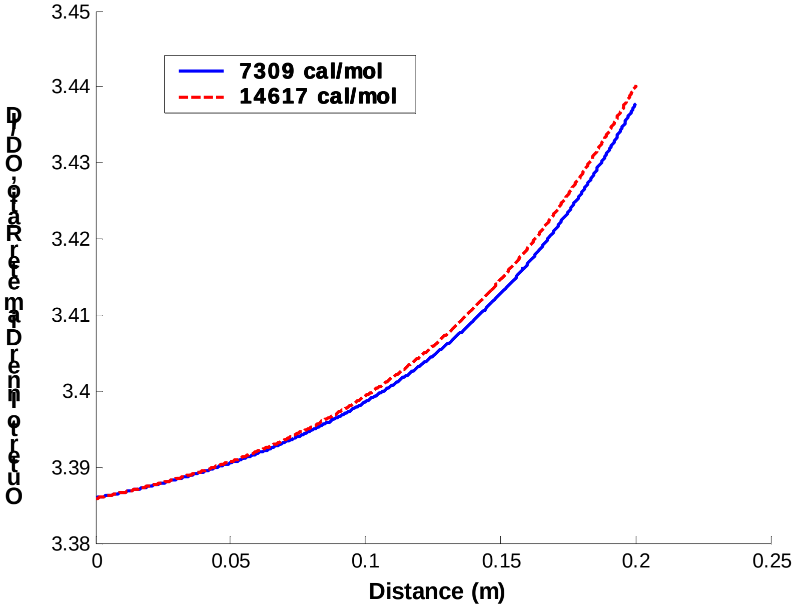

Figure 3.13 Sensitivity of Membrane OD/ID Profile to Viscosity Activation Energy

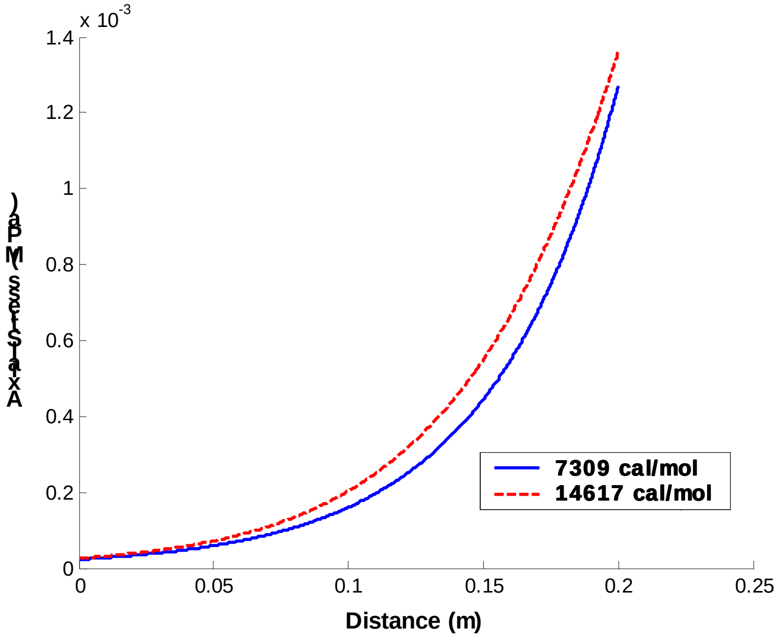

Figure 3.14 Sensitivity of Membrane Axial Viscous Stress Profile to Viscosity Activation Energy

3.3.5 Sensitivity to Air Gap Temperature

In this section, the air gap temperature, T_q, was varied; all cases correspond to stagnant air ($v_q = 0$). All other spinning conditions and physical properties are given in Tables 2.3 and 2.4. Results show that the spinning process is insensitive to air gap temperature over a 20 K change: the most noticeable effect is the approximately 1 K difference in final temperature seen in Figure 3.15 for the three cases of 288 K, 298 K, and 308 K for T_q. The OD/ID ratios have only slightly different final values as shown in Figure 3.16, and axial viscous stresses shown in Figure 3.17 agree within 2% over the entire draw zone.

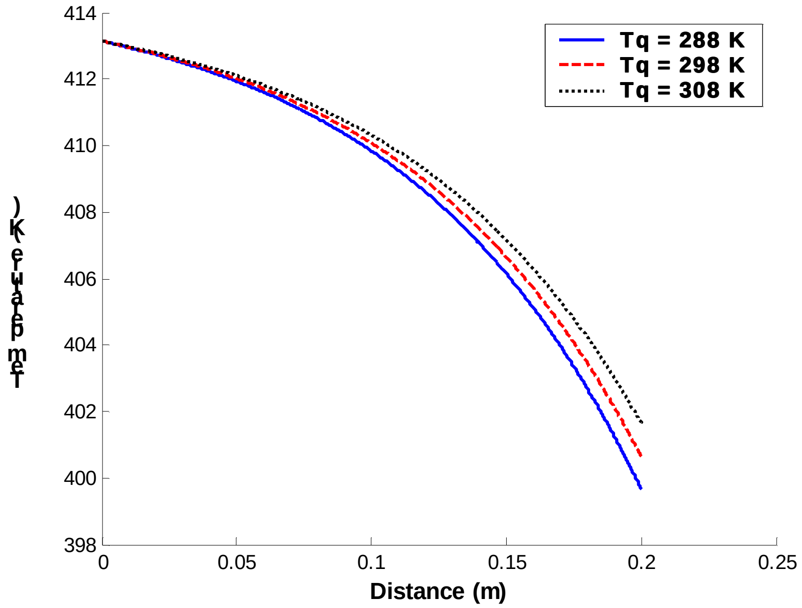

Figure 3.15 Sensitivity of Membrane Temperature Profile to Air Gap Temperature

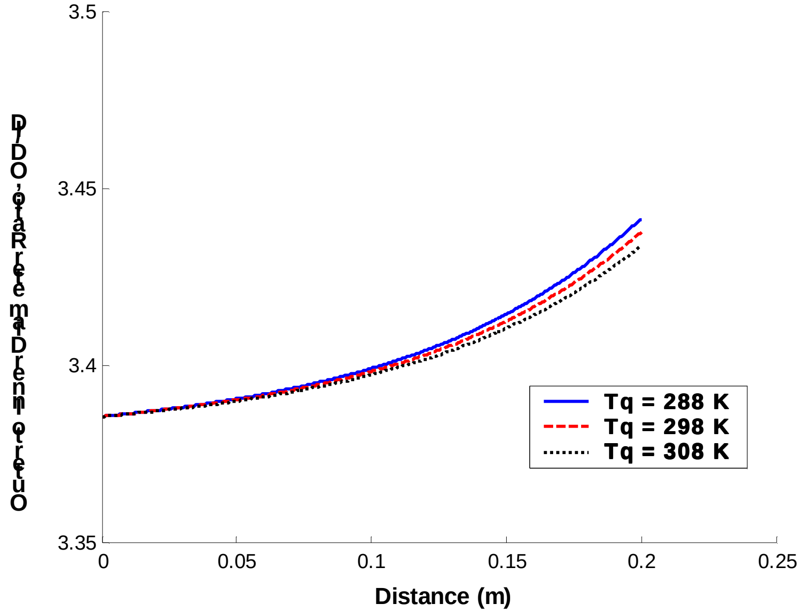

Figure 3.16 Sensitivity of Membrane OD/ID Profile to Air Gap Temperature

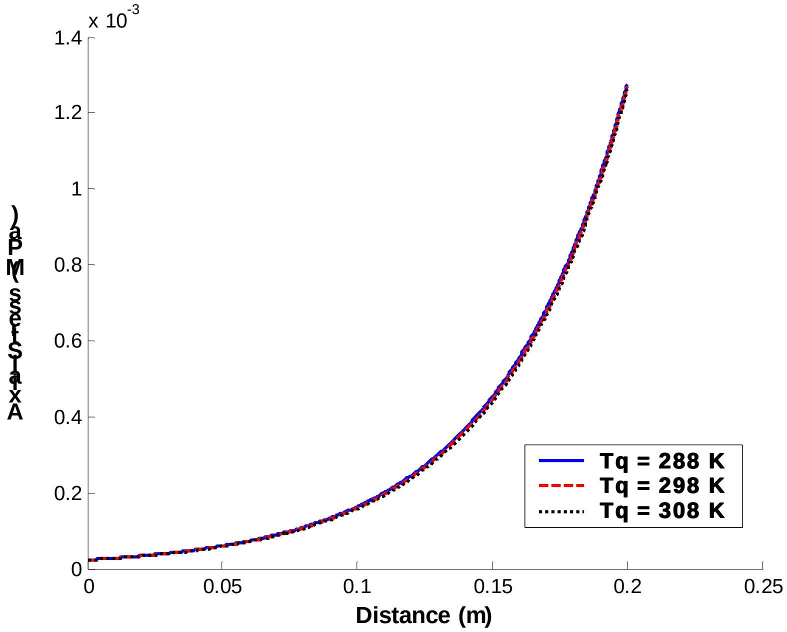

Figure 3.17 Sensitivity of Membrane Axial Viscous Stress Profile to Air Gap Temperature

3.3.6 Sensitivity to Velocity of Air in Air Gap

The convective heat transfer coefficient correlation of equation (2.36) is taken from the literature result for cross-flow cooling [25], and in this section, the sensitivity of predicted spinline variables to velocity of the air in the air gap is examined using cross-flow air velocities of 0, 0.2, and 1.0 m/s for v_q. All other spinning conditions and physical properties for these simulations are given in Tables 2.3 and 2.4. The air velocity is a parameter readily varied in practice. Furthermore, although all results shown here represent cross-flow air, the correlation for the convective heat transfer coefficient are easily modified to simulate co- and counter-current air flow in the air gap.

The temperature profile predictions shown in Figure 3.18 show significant differences between the three cases: the 0.2 m/s case has a final temperature of 388 K, 13 K cooler than the stagnant air result, and the 1.0 m/s v_q is 16 K cooler with a final value of 372 K.

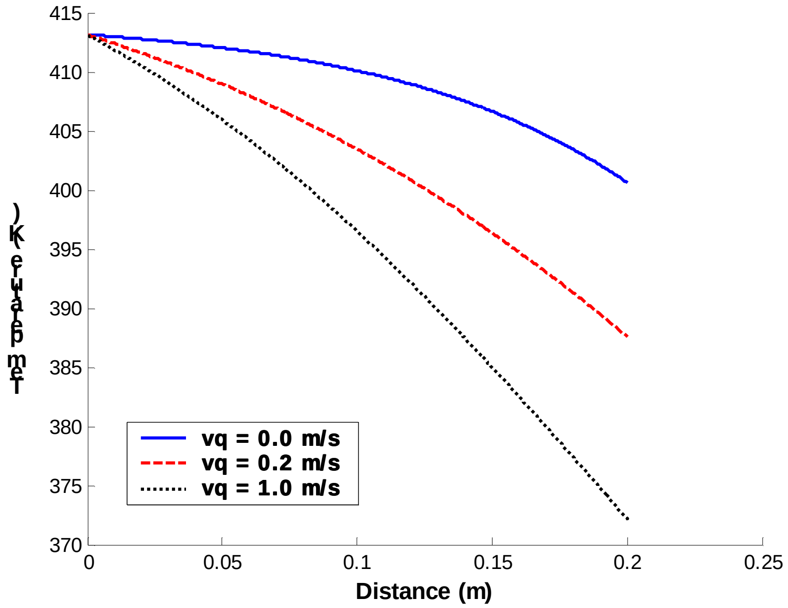

Figure 3.18 Sensitivity of Membrane Temperature Profile to Air Velocity

The OD/ID profiles in Figure 3.19 are also measurably different: final values progress as 3.4 to 3.5 to 3.6 as the air velocity increases. This correlates with the increase in core gas density with decreasing temperature.

However, the axial viscous stress profiles shown in Figure 3.20 are only slightly different for the three cases of air velocity. The dominant terms in the calculation of the axial viscous stress are the velocity and the viscosity. The change in air velocity does not dramatically affect the predicted spinline velocity profile, and even with the more drastic temperature drop for higher air velocity, the viscosity temperature dependence given by the parameters in Table 2.4 is such that the viscosity does not change dramatically through the draw zone. Thus, the axial viscous stress profiles predicted for the three air velocities are not significantly different.

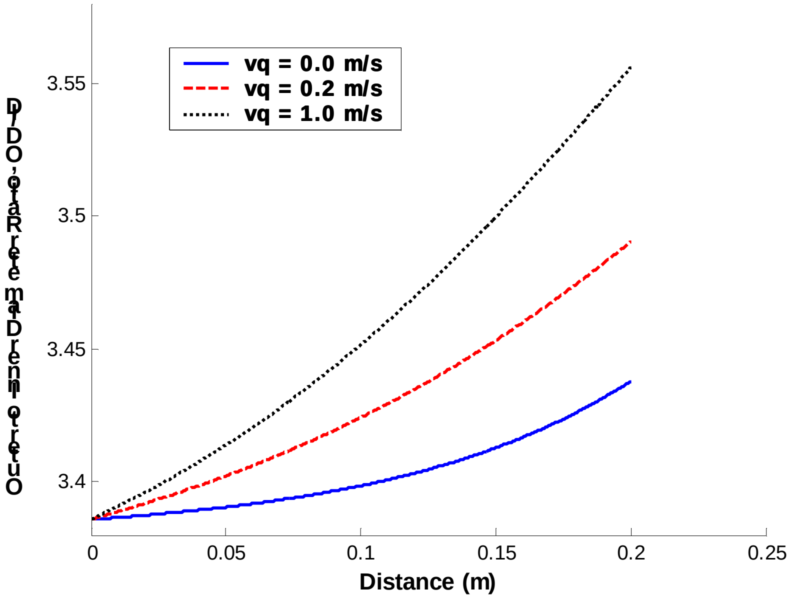

Figure 3.19 Sensitivity of Membrane OD/ID Profile to Air Velocity

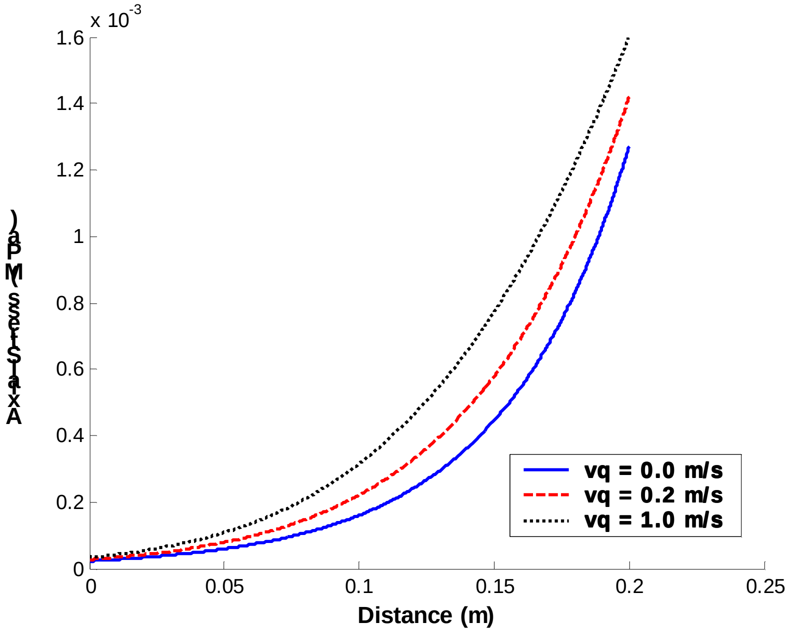

Figure 3.20 Sensitivity of Membrane Axial Viscous Stress Profile to Air Velocity

3.3.7 Sensitivity to Air Gap Length

This section quantifies the response of spinline variables to differences in air gap length, with values of 0.05, 0.10, and 0.20 m examined. All other spinning conditions and system physical properties for this section are described in Tables 2.3 and 2.4. Figure 3.21 presents predicted temperature profiles for the three air gap length cases. A higher air gap residence time leads to a more dramatic spinline temperature drop, resulting in a final temperature of 400 K for the 0.20 m air gap versus 410 K and 406 K for 0.05 and 0.10 m, respectively. The more extensive temperature drop for the longer air gaps results in a slight net increase in the OD/ID ratio along the draw zone, again resulting from the higher core gas density at lower spinline temperatures. Figure 3.22 illustrates this result.

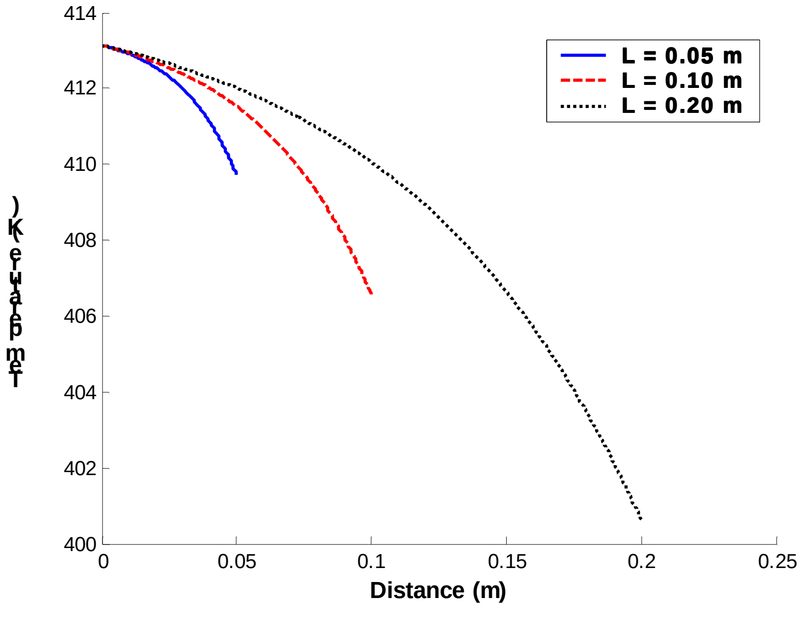

Figure 3.21 Sensitivity of Membrane Temperature Profile to Air Gap Length

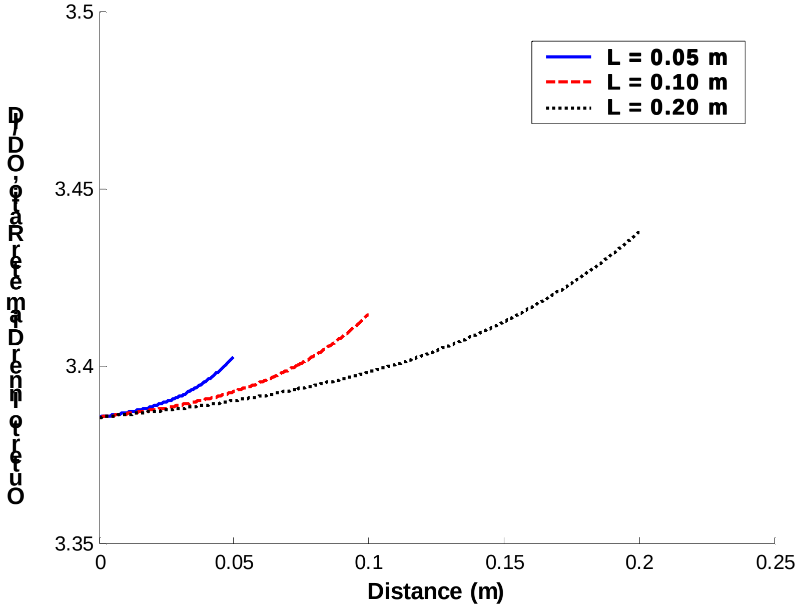

Figure 3.22 Sensitivity of Membrane OD/ID Profile to Air Gap Length

Results for the predicted axial viscous stress profiles, given in Figure 3.23, show that the 0.20 m air gap case corresponds to a more gradual increase in stress values along the draw zone than the other two cases. Referring to equation (2.40), the axial stress behavior for these cases appears to be dominated by the magnitude of the spinline axial velocity: because all three cases in this section use the same draw ratio, the longer air gap cases exhibit slower changes in axial velocity along the draw zone. As a result, the calculated viscous stresses are lower at a given axial position.

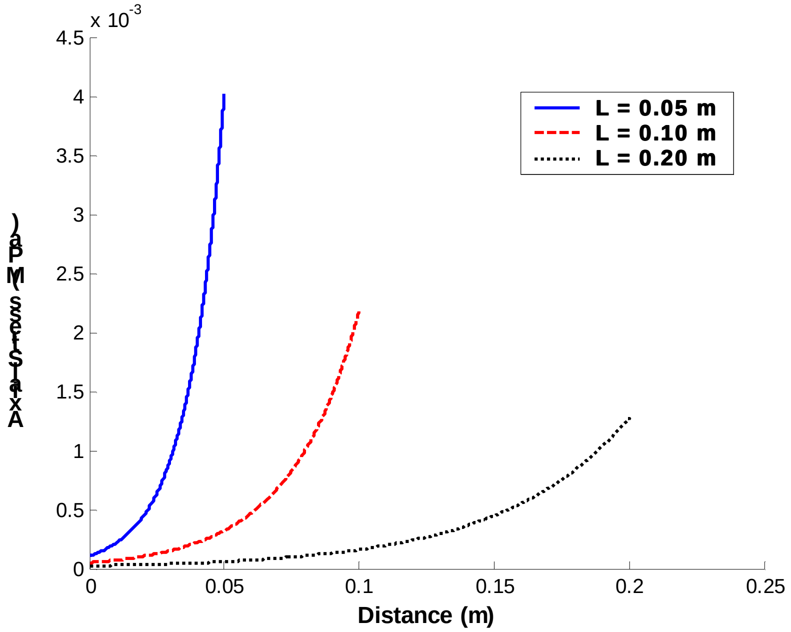

Figure 3.23 Sensitivity of Membrane Axial Viscous Stress Profile to Air Gap Length

3.3.8 Sensitivity to Diffusion Coefficient

This section illustrates the response of spinline variables to differences in diffusion coefficient. For the simulations in the preceding sensitivity studies, the diffusion coefficient is set equal to its value at the initial spinning temperature and concentration per the Zielinski–Duda predictive formulation as described in section 4.1.4. In this section, however, spinning conditions and system physical properties except for diffusion coefficient are listed in Tables 2.3 and 2.4; diffusion coefficient is increased by a factor of five and a factor of ten to produce values of 7.21 x 10^{-12}, 3.61 x 10^{-11}, and 7.21 x $^{-11}$ m^2/s for the simulations represented in this section. Although the spinning temperature sensitivity studies detailed in section 3.3.1 involve some level of change in the system diffusion coefficient, it is useful to examine the effect of this parameter individually, with all of the simulation results presented in this section corresponding to a spinning temperature of 413 K.

As shown in Figures 3.24, 3.25, and 3.26, none of the spinline variable profiles is sensitive to diffusion coefficient when this parameter is varied independently. Through the evaporative cooling effects in the energy balance of equation (2.9), the diffusion coefficient enters to affect the temperature profile calculation directly. Through the effect of the calculated temperature on spinline viscosity, diffusion coefficient has an indirect effect on calculation of the OD/ID and axial viscous stress profiles. However, the range of diffusion coefficient values examined here predicts virtually the same profiles for all three of these spinline variables.

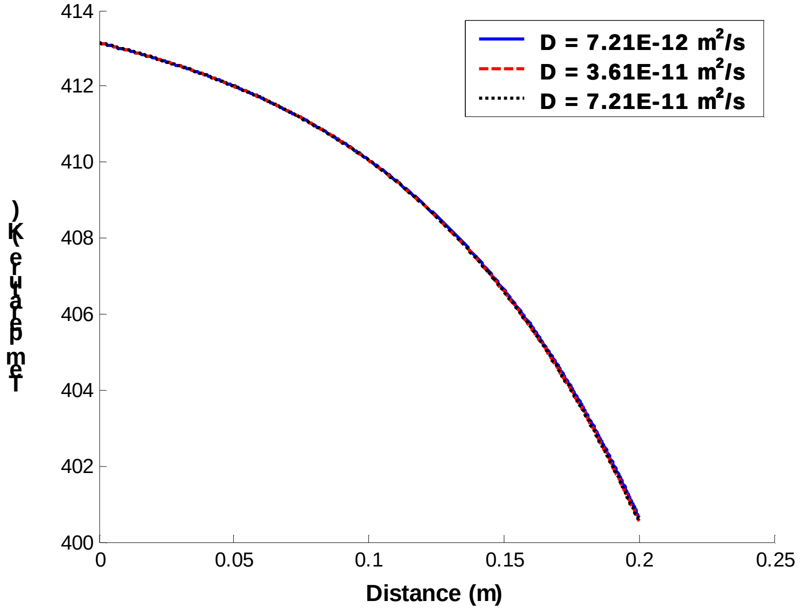

Figure 3.24 Sensitivity of Membrane Temperature Profile to Diffusion Coefficient

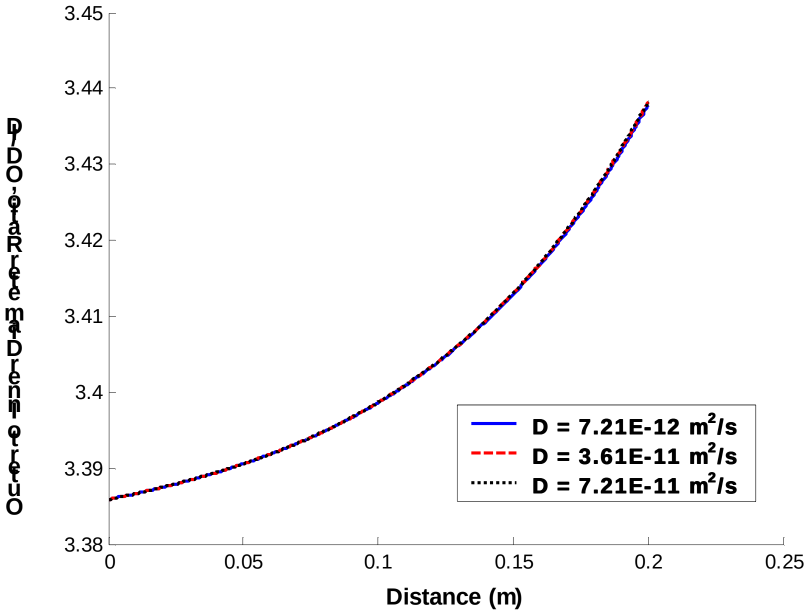

Figure 3.25 Sensitivity of Membrane OD/ID Profile to Diffusion Coefficient

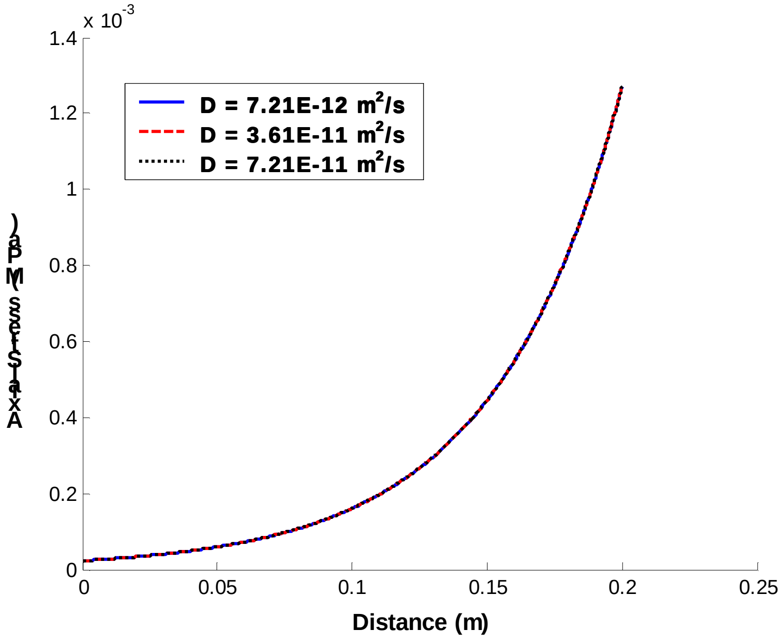

Figure 3.26 Sensitivity of Membrane Axial Stress Profile to Diffusion Coefficient

3.3.9 Sensitivity of Membrane Extent of Anisotropy

Predictions for membrane extent of anisotropy as related to the preceding spinning sensitivity studies are summarized here. Representing the major thrust of this research, modeling membrane anisotropy as a function of spinning conditions and system physical properties is relevant to general membrane research activity. The modeling efforts presented in this chapter have potential application to the optimization of the membrane research process: predicting membrane extent of anisotropy that results from a given set of spinning parameters reduces the number of experiments necessary for evaluating the use of a particular system to make membranes with desired anisotropy. The net result is an improvement of the trial-and-error approach currently prevalent in the membrane research field.

Membrane anisotropy is calculated using the boundary layer analysis discussed in this chapter. The portion of the membrane cross-section near the outer radius having a diluent concentration less than 95% of the diluent concentration of the initial spinning solution is defined as the anisotropic region. The thickness, in the radial direction, of this anisotropic layer is then divided by the final fiber wall thickness calculated by the modified TFA and multiplied by 100 to express this portion as a percentage. The resulting value is the membrane extent of anisotropy reported here.

With regard to the membrane spinning temperature sensitivity studies detailed in section 3.3.1, the lower diluent heat of vaporization and lower diffusion coefficient for lower spinning temperatures lead to differences in extent of diluent evaporation. Thus, a difference in membrane extent of anisotropy is expected for different initial spinning temperatures. For the spinning temperature sensitivity studies, there is a minor difference in the concentration predictions: the extent of anisotropy predicted for 433 K, the highest spinning temperature, is 3%, compared to 2% predicted for the lower temperatures of 393 K and 413 K. Figure 3.27 shows the evolution of the concentration gradients as the spinline passes through the air gap for the 433 K spinning case corresponding to all the conditions listed in Tables 2.3 and 2.4, with the extent of anisotropy determined by the portion of the membrane cross-section possessing a concentration gradient at the end of the air gap. The concentration profiles appear a bit jagged as a consequence of calculating the concentration for only 100 radial divisions of the cross-section; the appearance of Figure 3.27 improves with concentration calculations at additional radial steps.

The predicted membrane extent of anisotropy is 2% for all draw ratios in the sensitivity studies for that parameter in section 3.3.2. Evolution of the concentration gradients throughout the air gap follows a pattern similar to that shown in Figure 3.27. As mentioned in section 3.3.2, the range of feasible draw ratios for laboratory membrane spinning of PE–dodecanol is somewhat limited by spinning stability considerations. For a spinning situation subject to a broader range of draw ratios, larger differences in predicted membrane anisotropy may result.

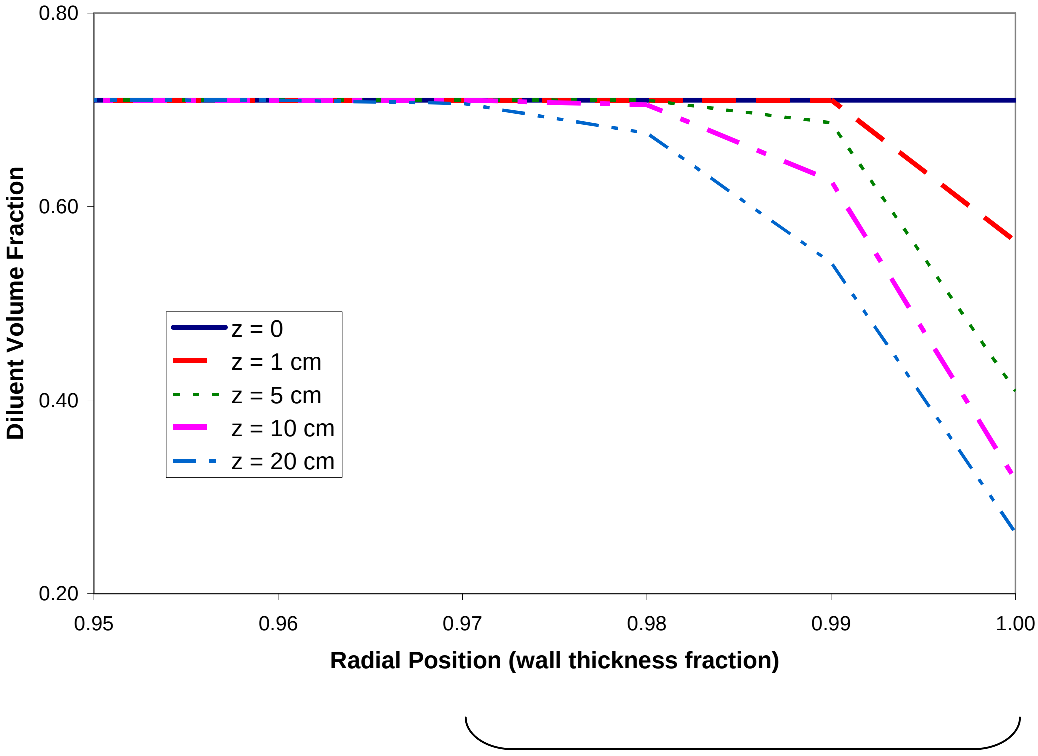

Membrane Extent of Anisotropy = 3%

Figure 3.27 Evolution of Concentration Gradients for Spinning Parameters of Tables 2.3 and 2.4

For the core gas flow rate sensitivity studies in section 3.3.3, predicted membrane extent of anisotropy increases from 2% for 1.00 and 3.00 SCCM to 3% for 5.00 SCCM. This result is spurred by the decrease in wall thickness for higher core flow rates, illustrated by the OD/ID profiles in Figure 3.11 as dictated by the continuity equation given by (2.1): the wall thickness is inversely proportional to the square root of the core gas mass flow rate. The calculated concentration boundary layer, or portion of the membrane cross-section possessing a concentration gradient, represents a larger fraction of the membrane cross-section as the core flow rate increases, resulting in a higher extent of anisotropy in the membrane.

The effects of both viscosity activation energy and air gap temperature, detailed in the sensitivity studies of sections 3.3.4 and 3.3.5, are insignificant in terms of the predicted membrane extent of anisotropy. For all cases, the predicted membrane extent of anisotropy is 2%. The predicted temperature profiles for both of these sensitivity studies, shown in Figures 3.12 and 3.15, are relatively insensitive to both effects—differences in temperature predictions for all cases are very small. Since the initial spinning temperature sensitivity studies of section 3.3.1 produced more significant differences in predictions for both temperature and extent of anisotropy, the very similar temperature predictions for the viscosity activation energy and air gap temperature studies are suspected to be the controlling factors for predicting extent of anisotropy.

Discussed in section 3.5, a limitation of the concentration boundary layer analysis prevents analysis of the concentration profiles for the cases of non-zero air gap velocity considered in section 3.3.6. However, qualitatively speaking, an increase in air gap velocity for the spinning conditions represented in section 3.3.6 produces a more pronounced temperature drop resulting from a higher rate of heat transfer throughout the draw zone. The higher heat transfer rate results from an increase in the convective heat transfer coefficient as calculated by equation (2.36). The difference in predicted temperature between cases with different air gap velocity creates a difference in diluent volatility along the spinline, thus affecting diluent evaporation rate at the spinline outer radius. The net result in terms of the concentration profiles for different air gap velocity is a discrepancy between the actual values of the concentration at specific points in the cross-sectional concentration boundary layer, which affects the evaporation and diffusion rates and in turn affects the membrane extent of anisotropy. Specifically, higher air gap velocity corresponds to higher heat transfer rate, and thus more rapid cooling of the spinline.

This decreases the extent of diluent evaporation, changing the magnitude of the concentration gradient over the cross-sectional spinline concentration boundary layer at the clad–air quench interface.

The predicted concentration profiles for the air gap length sensitivity studies in section 3.3.7 show that the longer air gaps of 0.10 and 0.20 m, corresponding to more time for diluent evaporation, produce a slightly higher membrane extent of anisotropy of 2%, compared to 1% for the shortest air gap of 0.05 m. This increased extent of diluent evaporation happens despite diminishing diluent evaporation rate due to higher extents of spinline cooling for longer air gaps and the resulting effects on the diluent vapor pressure at the clad–air quench interface.

Although the PE–dodecanol system diffusion coefficient sensitivity studies in section 3.3.8 show practically no change in predicted temperature, OD/ID, or axial stress profiles for the diffusion coefficients examined here, extent of anisotropy increases from 2% to 4% to 5% for each half-order of magnitude increase in diffusion coefficient. As the diffusion coefficient increases, the radial concentration gradient must lessen per equation (3.15); a higher diffusion coefficient means more facilitated diffusive transport of diluent through the solution. However, since the diffusive flux increases, the convective flux must increase to maintain equilibrium at the clad–air quench interface per equation (3.16). Thus, more diluent is lost via evaporation, and although the radial concentration gradient is more gradual over the predicted boundary layer, the predicted boundary layer thickness increases, and a greater membrane extent of anisotropy exists for higher diffusion coefficient values.

Table 3.1 summarizes the extent of anisotropy predicted for all of the sensitivity studies here. Results show that the predicted membrane extent of anisotropy increases for increasing spinning temperature, core gas flow rate, air gap length, and diffusion coefficient.

3.4 Comparison to Predictions of Existing Fiber Spinning Models

As detailed in section 1.2.3, a variety of spinning models exist in the literature, involving different sets of assumptions and applying to different spinning situations. In terms of predicting spinline radius, temperature, velocity, and core gas pressure profiles for hollow fiber air gap spinning, the published TFA contrasts with the model used in this research in that it neglects surface tension and evaporative cooling effects as discussed in Chapter 2. Comparison of these spinline variable predictions of the model developed here with predictions of the previously published TFA for fiber spinning is given in section 2.4.1.

Table 3.1 Predicted Extent of Anisotropy Values for Sensitivity Studies

Sensitivity Study	**Spinning Parameter Value**	**Predicted Membrane Extent of Anisotropy (%)**
Spinning Temperature (K)	393	2
	413	2
	433	3
Draw Ratio	24	2
	29	2
	34	2
Core Gas Flow Rate (SCCM)	1.00	2
	3.00	3
	5.00	3
Viscosity Activation Energy (cal/mol)	7309	2
	14617	2
Air Gap Temperature (K)	288	2
	298	2
	308	2
Air Gap Length (m)	0.05	1
	0.10	2
	0.20	2
Diffusion Coefficient (m^2/s)	7.21×10^{-12}	2
	3.61×10^{-11}	4
	7.21×10^{-12}	5

Mentioned in section 1.2.3, some existing efforts to model spinline radial concentration gradients that evolve during hollow fiber solution spinning are simplified analyses that neglect momentum transfer [13-15, 26]. In these models, spinline dimensional changes due to draw-down cannot be considered, and the resulting predictions of other spinline variable profiles are subject to the error this non-rigorous modeling introduces. Hence, in terms of spinline variables such as axial viscous stress, meaningful comparisons of predictions of models neglecting momentum transfer and models including it are not possible.

However, the model developed in this research can be applied to model spinning with no draw-down in order to facilitate comparison of the predicted membrane extent of anisotropy values from the boundary layer analysis used here with predictions of an existing analysis neglecting draw-down. Simulations of the modified TFA spinning model developed herein were conducted for the spinning conditions and physical properties given in Table 3.2 for a spin with no draw-down, and the resulting model-predicted temperature profile and the membrane extent of anisotropy were compared to results from an existing analysis neglecting draw-down [13, 14]. Some of the conditions given in Table 3.2, used with the modified TFA simulation efforts discussed here, were treated differently or not at all in the previous modeling efforts neglecting draw-down. These parameters, starred (*) in Table 3.2, include clad density and core and clad heat capacities, which were assumed constant in the modified TFA model but allowed to vary with temperature and concentration in the other model [20, 27]; initial core gas gauge pressure and clad viscosity parameters, which were incorporated in the modified TFA simulations to model the core gas pressure profile but not considered at all in the other model; the diffusion coefficient, which for this research was set constant to its value for the initial spinning temperature and spinning solution composition but allowed to vary with both temperature and concentration in the other model; and the clad surface tension, included in the TFA modeling efforts here but neglected in the existing analysis.

Predicted temperature profiles compare very well quantitatively, with the modified TFA analysis predicting a 25 K temperature drop axially and the existing analysis predicting a 26 K drop. Similarly, the modified TFA predicted extent of anisotropy is 30%, while the existing analysis predicts approximately 35%. The existing analysis has a minor inconsistency in the calculation of the diluent concentration at the outer radius; future efforts will involve addressing this issue to make more rigorous comparisons. However, the current comparison shows good agreement between the two models, and the model developed here uses a less complex analysis and involves significantly less computational time.

3.5 Limitations of the Concentration Boundary Layer Analysis

The concentration boundary layer analysis used here to predict hollow fiber membrane extent of anisotropy has some inherent limitations. For simulations that involve relatively high rates of heat transfer, such as the non-zero air gap velocity sensitivity studies, non-physical calculated values of the diluent concentration profile at the spinline outer radius result. For these cases, the diluent concentration at the outer radius is predicted initially to decrease as expected, but at some point in the draw zone, the predicted concentration starts to increase. There is no physical stimulus to cause this response during spinning.

High rates of heat transfer lead to high rates of mass transfer due to the dependence of the mass transfer coefficient on the convective heat transfer coefficient per equation (3.11). High heat and mass transfer rates at the clad–air quench interface produce drastic changes in the spinline concentration at the outer radius along the draw zone as diluent evaporates at a very high rate. The analysis in this research assumes a constant concentration at the outer radius throughout the draw zone as required by the concentration expressions in section 3.2.1. For moderate changes in the concentration at the outer radius, however, reasonable predictions of the concentration boundary layer analysis are obtained; for such cases, as discussed in Chapter 5, model- predicted membrane extents of anisotropy compare reasonably with experimentally measured values for hollow fiber membranes.

The example discussed here for a non-zero air velocity in the air gap during spinning predicts the non-physical increase in the diluent concentration at the spinline outer radius. This behavior happens after the predicted outer radius concentration drops from an initial diluent volume fraction of 0.71 to a fraction near 0.30 very early in the draw zone.

Table 3.2 PE–Dodecanol Spinning Process Simulation Conditions for Comparison to Previous Model Predictions
Items that are starred (*) are discussed further in the text

Condition	Value
R_i^0 = initial clad inner radius	2.80×10^{-4} m
R_o^0 = initial clad outer radius	4.24×10^{-4} m
$\overline{v^0}$ = extrusion velocity	10 m/min
v^L = take-up velocity	10 m/min
$\overline{T^0}$ = spinning temperature	420 K
$\overline{p_i^0}$ = initial core gas gauge pressure*	58 Pa
L = draw zone length	0.50 m
T_q = quench fluid temperature	298 K
v_q = quench fluid velocity normal to fiber axis	0 m/s
w_i = core gas mass flow rate	3.34×10^{-8} kg/s
w_o = clad mass flow rate	4.75×10^{-5} kg/s
p_{atm} = ambient air pressure	101325 Pa
ρ_o = clad density, assumed constant*	895 kg/m^3
η_o^0 = pre-exponential factor for clad shear viscosity dependence on temperature*	6.07×10^{-3} Pa·s
E_o / R = Ratio of activation energy for clad shear viscosity temperature dependence to the gas constant*	3681 K
$\Delta\hat{H}_{vap}^{d}$ = diluent heat of vaporization	3.48×10^{5} J/kg
C_{pi} = core gas specific heat capacity, assumed constant*	1047 J/kg-K
C_{po} = clad specific heat capacity, assumed constant*	2538 J/kg-K
ϕ_d^0 = volume fraction of diluent in spinning solution	0.60
D = mutual diffusion coefficient calculated at T^0 and ϕ_d^0 *	5.74×10^{-11} m^2/s
MW_i = core gas molecular weight	28.0
γ = clad surface tension*	30 dynes/cm

One of the initial assumptions of this analysis of the concentration gradients that evolve during hollow fiber spinning is that the diffusion coefficient for the polymer–diluent solution is constant. This assumption is necessary for solving equation (3.1) with the similarity transform method used here. However, as discussed in section 4.1.4, the diffusion coefficient actually varies in a complicated fashion with both solution concentration and temperature. Thus, for high rates of heat transfer, the diffusion coefficient could vary significantly due to the rapid temperature drop. In addition, high rates of heat transfer for some spinning conditions at some axial positions lead to high rates of mass transfer as discussed above. High mass transfer rates produce steep concentration gradients as diluent evaporates very quickly early in the draw zone. This could lead to a drop in the diffusion coefficient as the solution becomes more polymer-concentrated. Not accounting for these concentration- and temperature-induced changes in the diffusion coefficient compromises the analysis of the spinline concentration gradients.

To evaluate the effect of the magnitude of the diffusion coefficient, simulations of a set of spinning conditions invoking high heat and mass transfer rates were used. The conditions correspond to an air gap air velocity of 0.2 m/s for different values of the diffusion coefficient, with other spinning conditions and physical parameters given in Tables 2.3 and 2.4. The actual value of the diffusion coefficient, corresponding to the initial spinning temperature and composition, is 7.21×10^{-12} m^2/s; using this value predicts a non-physical outer radius concentration profile as depicted in Figure 3.28.

If the diffusion coefficient is decreased by about 1.5 orders of magnitude to 1.00×10^{-13} m^2/s, a concentration profile that significantly violates the assumption of constant concentration at the outer radius is still predicted for the spinline outer radius as shown in Figure 3.28 alongside the previous result. This case involves a very dramatic initial decrease to a diluent volume fraction of about 0.03. This predicted value remains constant for the remainder of the draw zone within a 3% margin of error. For this case, the lower diffusion coefficient results in a larger radial concentration gradient per equation (3.15); however, the additional effect is that the diluent radial transport is hindered enough to prevent diluent from diffusing to the outer radius later in the draw zone, and the non-physical increase in the concentration at the outer radius is not predicted.

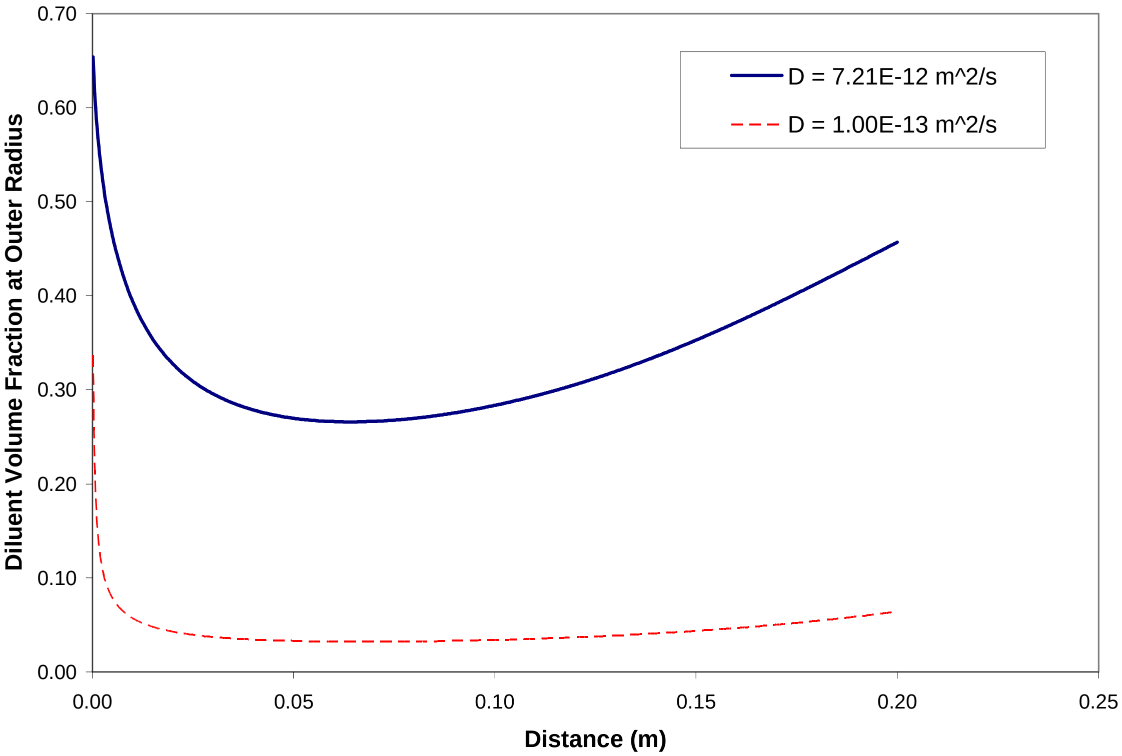

Figure 3.28 Effect of Diffusion Coefficient on the Concentration Profile at the Spinline Outer Radius

However, the fact remains that the assumption of constant outer radius concentration is violated even more substantially than for the previous result: this indicates that although accounting for the concentration and temperature dependence of the diffusion coefficient is a logical step to improve the boundary layer analysis of concentration gradients presented here, this will not eliminate all potential problems with the applicability of this simplified approach to modeling the spinning process, particularly for conditions involving high heat and mass transfer rates.

In addition to neglecting the variation of the diffusion coefficient with concentration and temperature, axial diffusion is neglected in this analysis. Hypothetically, allowing axial diffusion of both heat and mass could alleviate the concentration prediction problems observed here for high heat and mass transfer rates; however, order-of-magnitude calculations for the Peclet numbers, *Pe*, for both heat and mass transfer, included in the Appendix, indicate that axial diffusion is dominated by axial convection for typical spinning operations, and it is omitted from the TFA of fiber spinning for this reason.

3.6 Summary of Chapter 3

This chapter detailed the method for determining concentration gradients to characterize hollow fiber membranes in terms of the predicted extent of anisotropy. The approach models the concentration changes occurring in a relatively thin boundary layer adjacent to the outer radius of the membrane cross-section. The analysis is coupled with the modified TFA of the hollow fiber spinning process detailed in Chapter 2, as the results for the spinline temperature, velocity, and outer radius profiles are needed to do the concentration calculations.

Model results presented here show that the predicted spinline temperature profile is sensitive to the initial spinning temperature, the air gap velocity, and the air gap length. More specifically, the magnitude of the temperature of the filament at the end of the draw zone is influenced most strongly by all three of these factors; the temperature gradient, a measure of the heat transfer rate for the spinline, is most notably affected by the air gap air velocity and affected to a lesser extent by the air gap length.

The results also indicate that the OD/ID ratio, both its evolution along the draw zone and its final value, is most strongly affected by changes in core gas flow rate, and then affected to a lesser degree by initial spinning temperature and air gap velocity. The spinline axial viscous stress is most sensitive to air gap length and also affected to some degree by changes in spinning temperature, draw ratio, and air gap air velocity.

Membrane extent of anisotropy predictions, although 5% or less for all spinning conditions considered here, are most sensitive to initial spinning temperature, core gas mass flow rate, air gap length, and diffusion coefficient, showing an increase in extent of anisotropy for some level of increase in these parameters.

Because the concentration analysis here has limitations causing non-physical predictions of the spinline concentration at the outer radius for some spinning condition sets that induce high heat and mass transfer rates, improvement of this analysis is warranted. Although it is not expected to eradicate the issues of non-physical predictions with modeling some situations, modifying equation (3.1) to include temperature and concentration dependence of the diffusion coefficient is discussed as a recommendation for future work in Chapter 6. Furthermore, experiments performed in this research using the methods outlined in Chapter 4 were used to test the applicability of the model; results are given in Chapter 5.

A product of the analysis here is a method to estimate quickly the extent of anisotropy for typical membrane spinning operations. The membrane spinning cases considered here are practically isothermal, with an approximately 10 K or less temperature drop over the entire draw zone. Moreover, inertial effects are small for the polymer spinline due to the low Reynolds number flows corresponding to a relatively high spinline viscosity. Thus, the boundary layer analysis expression derived here for the concentration at a given position can be used to calculate directly the fraction of the membrane wall possessing a pore size gradient at the end of the draw zone by incorporating the analytical expressions for velocity, outer radius, and core pressure for inertialess, isothermal cases [12]. The pertinent equations appear in (3.17); in this equation set, F represents the total force applied to the core and clad at $z = L$. The calculation involves calculating R_o and R_i at the end of the draw zone, choosing a value of radial position r within the cross-section, and calculating the diluent concentration C_d at this point for $z = L$. Anisotropy exists where diluent concentrations are less than 95% of the diluent concentration in the initial spinning solution, and the final membrane extent of anisotropy is calculated as the fraction of the final calculated membrane wall thickness possessing this concentration difference.

$$
\boxed{
\begin{aligned}
C_d &= \left(C_{d\infty} - C_{d0}\right) erf\left[\left(R_o^L - r\right)\sqrt{\frac{\overline{v}^L}{4DL}} + C_{d0}\right] \\
\overline{v}^L &= \overline{v}^0 \exp\left(\frac{F^L L}{3\eta_o^L A_o^0 \overline{v}^0}\right) \\
R_o^L &= \left[\left(1 + \frac{\rho_i^L w_o}{\rho_o w_i}\right)\left(\frac{w_i}{\pi \overline{v}^L \rho_i}\right)\right]^{1/2} \\
R_i^L &= \left(\frac{w_i}{\pi \overline{v}^L \rho_i^L}\right)^{1/2} \\
\rho_i^L &= \frac{\left(\overline{p_i^L} + p_{atm}\right) MW_i}{R\overline{T}^L} \\
\overline{p_i^L} &= \overline{p_i^o} \exp\left\{\left(\frac{3A_o^0}{F^L}\right)\left(p_{atm} + \frac{\rho_o w_i R\overline{T}^L}{w_o MW_i}\right)\left[\exp\left(-\frac{F^L L}{3\eta_o^L A_o^0 \overline{v}^0}\right) - 1\right]\right\}
\end{aligned}
}
\tag{3.17}
$$

3.7 References

1. A. Idris, A.F. Ismail, M.Y. Noordin, and S.J. Shilton, Optimization of cellulose acetate hollow fiber reverse osmosis membrane production using Taguchi method, J. Membr. Sci., 205 (2002) 223-237.
2. A.A. Alwattari and D.R. Lloyd, Microporous membrane formation via thermally-induced phase separation. VI. Effect of diluent morphology and relative crystallization kinetics on polypropylene membrane structure, J. Membr. Sci., 64 (1991) 55-68.
3. A. Laxminarayan, The kinetics of membrane formation via thermally induced liquid-liquid phase separation, Dissertation, The University of Texas at Austin, 1994.
4. K.S. McGuire, A. Laxminarayan, and D.R. Lloyd, Kinetics of droplet growth in liquid-liquid phase separation of polymer-diluent systems: experimental results, Polymer, 36 (1995) 4951-4960.

5. K.S. McGuire, A. Laxminarayan, D.S. Martula, and D.R. Lloyd, Kinetics of droplet growth in liquid-liquid phase separation of polymer-diluent systems: model development, J. Colloid Int. Sci., 182 (1996) 46-58.
6. D. Beysens, Kinetics and morphology of phase separation in fluids: the role of droplet coalescence, Physica A, 239 (1997) 329-339.
7. J. Alkemper, V.A. Snyder, N. Akaiwa, and P.W. Voorhees, Dynamics of late-stage phase separation: a test of theory, Phys. Rev. Lett., 82 (1999) 2725-2728.
8. D.S. Martula, Coalescence-induced coalescence, Dissertation, The University of Texas at Austin, 2000.
9. D.S. Martula, T. Hasegawa, D.R. Lloyd, and R.T. Bonnecaze, Coalescence-induced coalescence of inviscid droplets in a viscous fluid, J. Colloid Int. Sci., 232 (2000) 241-253.
10. D.S. Martula, R.T. Bonnecaze, and D.R. Lloyd, The effects of viscosity on coalescence-induced coalescence, Int. J. Multiphase Flow, 29 (2003) 1265-1282.
11. G.T. Caneba and D.S. Soong, Polymer membrane formation through the thermal-inversion process. 2. Mathematical modeling of membrane structure formation, Macromolecules, 18 (1985) 2545-2555.
12. G.G. Lipscomb, The melt hollow fiber spinning process: Steady-state behavior, sensitivity and stability, Polymers for Advanced Technologies, 5 (1994) 745-758.
13. M.T. Batarseh, H.A. Balasubramanian, D.R. Lloyd, G.G. Lipscomb, and J.D. Stiehl, Anisotropic hollow fiber membrane formation. I. Prediction of concentration profiles., In preparation (2004).
14. M.T. Batarseh, Formation of anisotropic hollow fiber membranes via TIPS, Dissertation, The University of Texas at Austin, 1999.
15. M.T. Batarseh, H.A. Balasubramanian, D.R. Lloyd, G.G. Lipscomb, and J.D. Stiehl, Anisotropic hollow fiber membrane formation. II. Prediction of cooling rate profiles., In preparation (2004).
16. G.G. Lipscomb, Personal Communication, 2004.
17. J.D. Stiehl, Undergraduate research report, The University of Texas at Austin May 1999.
18. R.B. Bird, W.E. Stewart, and E.N. Lightfoot, Transport Phenomena, John Wiley & Sons, New York, 1960.
19. J.E. Mark, (Ed.), Physical properties of polymers handbook, AIP Press, Woodbury, N.Y., 1996.
20. R.L. Rowley, W.V. Wilding, J.L. Oscarson, Y. Yang, R.J. Rowley, T.E. Daubert, and R.P. Danner, DIPPR® Data Compilation of Pure Compound Properties: Design Institute for Physical Property Data, AIChE®, New York, NY (2001).
21. Y. Ohzawa, Y. Nagano, and T. Matsuo, Studies on dry spinning. I. Fundamental equations, J. Appl. Polym. Sci., 13 (1969) 257-283.
22. Y. Ohzawa and Y. Nagano, Studies on dry spinning. II. Numerical solutions for some polymer-solvent systems based on the assumption that drying is controlled by boundary-layer mass transfer, J. Appl. Polym. Sci., 14 (1970) 1879-1899.
23. A.L. Hines and R.N. Maddox, Mass transfer: fundamentals and applications, PTR Prentice Hall, Englewood Cliffs, 1985.
24. R.J. Fisher and M.M. Denn, Draw resonance in melt spinning, Applied Polymer Symposium, 27 (1975) 103-109.

25. S. Kase and T. Matsuo, Studies on melt spinning. II. Steady-state and transient solutions of fundamental equations compared with experimental results, J. Appl. Polym. Sci., 11 (1967) 251-287.
26. S. Berghmans, H. Berghmans, and H.E.H. Meijer, Spinning of hollow porous fibres via the TIPS mechanism, J. Membr. Sci., 116 (1996) 171-189.
27. J. Brandrup, E.H. Immergut, and E.A. Grulke, (Eds.), Polymer Handbook, 4th ed., John Wiley & Sons, New York, 1999.

Chapter 4. Spinning System Characterization and Spinning Experimental Equipment and Procedure

4.1 System Selection and Characterization

This research strove to illustrate in some detail the sensitivity of membrane extent of anisotropy and various spinline variables to spinning conditions and spinning system physical properties. Thus, a system for which a broad range of spinning conditions could be used to produce a characterizable spinline and hollow fiber membrane structure via a TIPS spinning process was desired. In addition, a suitable system must have known or measurable physical properties and be readily available in adequate quantities, environmentally safe, and cost-effective. With these considerations, several grades of polyethylene, including high, medium, low, and linear low density types from various commercial suppliers, were screened for possible use with various diluents, including several alcohols and ethers. After conducting a number of trial spins and checking the microstructure of the resulting hollow fibers via scanning electron microscopy (SEM), linear low density polyethylene in dodecanol (PE–dodecanol) was chosen as the spinning system for this research.

The polyethylene used is a Dow Affinity linear low density polyethylene, catalog number PL-1840. Characterization of multiple samples (Dow lot numbers OA2101E141, NE2301E141, and OC2901E142) via high-temperature gel permeation chromatography (GPC) produced measurements of the number- and weight-average molecular weights, and thus the sample polydispersity index. A summary of these properties is given in Table 4.1, and detailed GPC results are included in Appendix A. Dodecanol of 98% purity was obtained from Sigma–Aldrich and used as received; its properties are given in Table 4.2.

4.1.1 Determining the PE–Dodecanol Phase Diagram

In-depth interpretation of polymer solution thermodynamics, including detailed work with TIPS, is described in the literature [1-5]. As mentioned in Chapter 1, the kinetics of phase separation, and thus the evolution of membrane microstructure, depend on the phase separation mechanism; thus, establishing the phase diagram is essential for future work to create a model to predict membrane pore size and pore size distribution as functions of processing conditions and material properties. The PE–dodecanol phase diagram appears in Figure 4.1 and was determined as described here.

Table 4.1 Dow Affinity PL-1840 PE Properties

Property	Value	Comments
Melt Index	1.0 g/min	Reported on Dow product sheet as ASTM D 1238 test method result
Density	0.9090 g/cm^3	Reported on Dow product sheet as ASTM D 792 test method result
Melting Point	105.5°C	Reported on Dow product sheet as Dow test method result
Number-Average Molecular Weight	43043	Average value for high-temperature GPC runs for samples from three lots
Weight-Average Molecular Weight	82425	Average value for high-temperature GPC runs for samples from three lots
Polydispersity Index	1.9	Average value for high-temperature GPC runs for samples from three lots

Table 4.2 Dodecanol Properties

Property	Value
Molecular Weight	186.34
Density	0.833 g/cm^3
Melting Point	24–27°C
Boiling Point	260–262°C

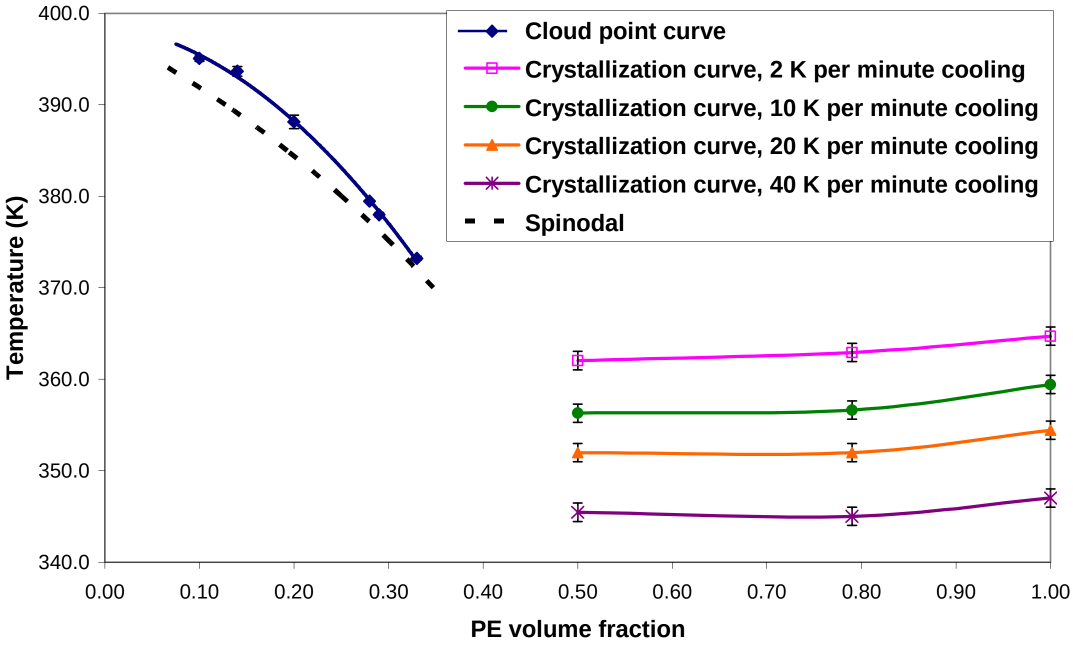

Figure 4.1 PE–Dodecanol Phase Diagram

This system has the capability to phase separate via liquid–liquid TIPS or solid–liquid TIPS, with the liquid–liquid coexistence region defined by the binodal. The experimentally determined cloud point curve is assumed to be representative of the binodal as shown in Figure 4.1. The cloud point curve was determined using optical microscopy, with details of the technique reported elsewhere [6]. In short, uniform polymer–diluent samples were prepared via melting and mixing, then solidified. Small bits of the solid sample were sliced and placed between two glass microscope slides separated by a 100 μm thick Teflon spacer as shown in Figure 4.2; edges of the slide assembly were then sealed with vacuum grease to prevent diluent loss during testing. Using a Linkam hot stage (model HFS-91) and temperature controller (model TMS-91), the PE–dodecanol “sandwiched” samples were heated to a temperature of 423 K and held for 5–10 minutes to ensure homogeneity and erase thermal history [7], then cooled at 10 K/min until liquid–liquid phase separation was observed. The hot stage sample assembly was in-line with a Nikon optical microscope (model Optiphot2-Pol) fitted with a 60x objective lens; video display of the microscope images was made possible through the use of a camera and controller (model MTI CCD-72X). Figure 4.3 shows some representative video images of a sample undergoing liquid–liquid phase separation [8]. Reported cloud point temperatures represent the temperature at which phase separation was observed for samples of a particular composition, and all cloud point values reported in Figure 4.1 are the average of no less than four repeat runs for at least two different samples of a given composition.

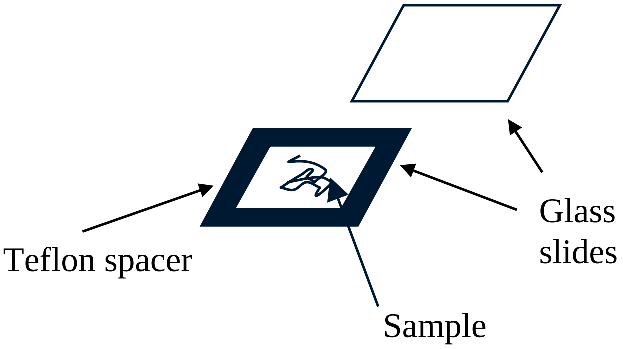

Figure 4.2 Sample Assembly for Determining Cloud Points Via Optical Microscopy

Previous work shows that cloud point measurements are insensitive to cooling rate for rates that are less than or equal to 10 K/min [9]; however, the crystallization curves, which establish the solid–liquid phase separation region for the system, are sensitive to cooling rate as illustrated by the results in Figure 4.1 and discussed in the literature [10]. The crystallization curves were determined using a Perkin–Elmer differential scanning calorimeter (model DSC 7) and thermal analysis controller (TAC 7/DX). Various cooling rates (2, 10, 20, and 40 K/min) were employed, with the reported temperatures corresponding to the peak temperatures of the resulting DSC exotherms. The DSC was calibrated on a regular basis using an Indium standard, and runs were repeated for a given sample and for additional samples of the same composition to ensure measurement reproducibility.

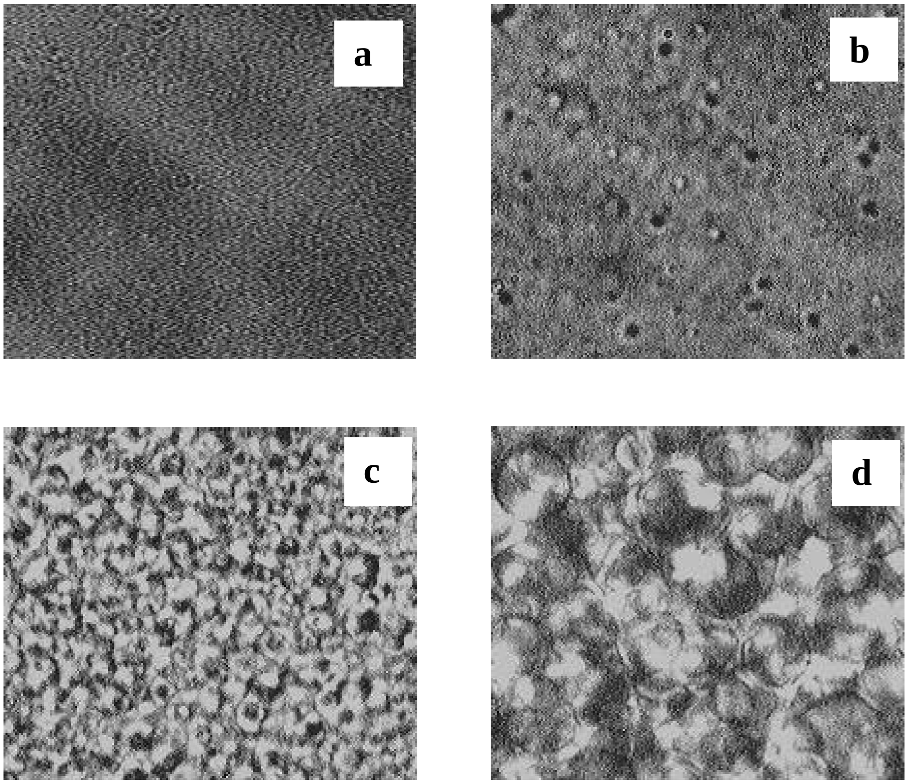

Figure 4.3 Representative Video Images of a Polymer–Diluent Sample Undergoing Liquid–Liquid Phase Separation (time progresses from a–d)

The spinodal, which delineates a metastable region below the binodal that can withstand small concentration fluctuations [3], was calculated using the method of Tompa [11]. Solving for the spinodal polymer volume fraction, ϕ_p, for a particular temperature via equation (4.1) requires the evaluation of the chi interaction parameter, χ, for the system at that temperature; the temperature dependence of chi and the method used to determine this dependence are described in section 4.1.2.

$$\phi_p = \frac{2\chi - 1}{2\chi} \tag{4.1}$$

Hollow fibers spun in the course of this research were generally formed by liquid–liquid TIPS, producing a lacy, interconnected porous membrane structure. The starting mixture for preparing such membranes must have a composition to the right of the critical point (composition and temperature at which spinodal and binodal curves meet) and to the left of the monotectic point (where the binodal and equilibrium crystallization curve meet). The mixture is then heated to a temperature above the binodal to form a homogeneous solution, which is extruded as a hollow fiber. As the spinline cools, it phase separates after passing into the liquid–liquid region below the binodal into a polymer-rich matrix phase with dispersed diluent-rich droplets; the droplet domains grow until the phase-separated mixture reaches the crystallization curve, at which point the polymer-rich matrix solidifies. If the starting solution has a composition to the left of the critical point, liquid–liquid phase separation that occurs after quenching below the binodal forms a diluent-rich matrix phase with dispersed polymer-rich droplets, a mixture lacking the structural integrity of a membrane. If the starting composition is to the right of the monotectic point, the solution solid–liquid phase separates, with polymer crystallizing directly out of the solution after quenching to the crystallization curve. Membranes can be formed via both solid–liquid and liquid–liquid TIPS, resulting in a variety of possible membrane morphologies [2, 3, 5, 12-16].

4.1.2 Determining the PE–Dodecanol Flory–Huggins Interaction Parameter, Chi

Description of the polymer–diluent solution thermodynamics is necessary for use of the boundary layer analysis to predict membrane extent of anisotropy as presented in Chapter 3. Assuming there is no volume change upon mixing of polymer and diluent, the Flory–Huggins theory is applied for this purpose [17]. The interaction parameter, χ, was determined following the strategy of McGuire *et al.* [6], with interaction parameter assumed to be a function of temperature only. This method involves using the Flory–Huggins expressions for polymer chemical potential of the two liquid phases that coexist upon phase separation at the cloud point temperature. These relationships are given in equations (4.2) and (4.3).

$$\left[\left(\phi_2^{\beta}\right)^2 - \left(\phi_2^{\alpha}\right)^2\right]\chi = \ln\left(\frac{1-\phi_2^{\alpha}}{1-\phi_2^{\beta}}\right) + \left(1-\frac{1}{x}\right)\left(\phi_2^{\alpha} - \phi_2^{\beta}\right) \quad (4.2)$$

$$x\left[\left(1-\phi_2^{\beta}\right)^2-\left(1-\phi_2^{\alpha}\right)^2\right]\chi=\ln\left(\frac{\phi_2^{\alpha}}{\phi_2^{\beta}}\right)+\left(x-1\right)\left(\phi_2^{\alpha}-\phi_2^{\beta}\right) \quad (4.3)$$

Here, ϕ_2^{α} and ϕ_2^{β} represent polymer volume fractions in the two phases α and β, and x is the ratio of polymer molar volume to diluent molar volume. The molecular weight of the polyethylene used in this research is high enough such that $x >> 1$, and terms in equations (4.2) and (4.3) that scale with the inverse of the molar volume ratio x were neglected. By simultaneously solving equations (4.2) and (4.3) using the cloud point measurements for PE–dodecanol represented in Figure 4.1 to give values of ϕ_2^{β} at particular temperatures, χ was determined as a function of temperature. The *fsolve* command in MATLAB 6.1 was used to solve the equations via nonlinear least squares, and literature data [6] were reproduced with a relatively low convergence criterion of 1 x 10^{-3}; thus, a higher convergence criterion of 1 x 10^{-9} used in this work provides a more precise correlation for χ with temperature. The result of this calculation for PE–dodecanol, obtained from a linear regression (with a correlation value $R^2 = 0.9937$) to calculated χ values for each cloud point temperature, is given in equation (4.4); units of temperature are Kelvin.

$$\chi=\frac{1392.8}{T}-2.9981 \qquad (4.4)$$

4.1.3 Measuring PE–Dodecanol System Viscosity

The shear viscosity η_o for the PE–dodecanol system is necessary for modeling the momentum transfer for the spinning process. In this research, the spinning solution is assumed to be a Newtonian fluid as discussed in Chapter 2. Since typical fiber spinning operations are non-isothermal, the variation of clad viscosity with temperature must be quantified. To accomplish this, viscosity was assumed to obey an Arrhenius temperature relationship as given by equation (2.35), and measurements of the clad viscosity at different temperatures were used to obtain values of the viscosity pre-factor and the viscosity activation energy.

Viscosity measurements were made using a Paar Physica modular compact rheometer (model MCR300) with a concentric cylinder bob-in-cup configuration (model CC27). In this setup, shown in Figure 4.4 [18], the bob rotates freely on a diffusion air bearing that is coupled with the instrument drive shaft and fed by a continuous stream of filtered, compressed air. Rheology measurements are quantified in the instrument by the amount of torque necessary to turn the shaft at the experimentally prescribed conditions. This apparatus has the ability to examine high-viscosity materials, with the upper measurable viscosity limit (called "near solid" in the instrument manual) set by the maximum torque level sustainable by the bob. Furthermore, sample temperatures up to 423 K can be obtained using the instrument's thermal unit (model TEZ 150P), which operates via the peltier effect, using countercooling via a water stream supplied by a circulation bath (Julabo model F25). In addition, the sample cup contains a volatile solvent trap that prevents evaporation during testing, used here for all PE–dodecanol measurements.

Figure 4.4 Paar–Physica MCR300 Rheometer

PE–dodecanol samples for the rheology tests were prepared using a stirred pot-in-oven setup shown in Figure 4.5. PE and dodecanol were loaded into the pot to form a 30 wt-% PE solution, the initial spinning solution composition for the hollow fiber spinning experiments performed in this research, with a total mass between 150 and 300 grams. The pot, sealed from the atmosphere via silicone O-rings and screw attachments, was then purged with nitrogen gas to avoid polymer degradation, heated to a temperature of 423 K, and held at this temperature for at least 4 hours while constantly stirred by a steel baffle inside the pot. The temperature of 423 K is above the binodal temperature of 378 K corresponding to 30 wt-% PE–dodecanol; thus, a homogeneous solution results under these sample preparation conditions. The baffle was attached to a stirring shaft of ½" diameter, coupled with a motor (Bodine Electric, model 42DSBEPM-E3) and speed controller (Simpson company); a setting of 12 rpm was used for preparing the PE–dodecanol samples. The prepared samples were dispensed into the rheometer sample cup through a ball valve at the bottom of the pot using 10–30 psig of applied nitrogen pressure, with both sample and cup maintained at 423 K.

Figure 4.5 Stirred Pot-in-Oven Setup for Polymer Solution Sample Preparation

PE–dodecanol viscosity values were measured using a log shear rate ramp from 0.001 s^{-1} to 100 s^{-1}, with time for data collection at each shear rate following a log ramp from 1000 seconds to 1 second; ideally, a complete bob revolution should be accomplished for each shear rate measurement. Prior to the shear rate ramp test, the sample was allowed to sit undisturbed for

20–30 minutes to ensure thermal equilibrium with the cup, and the sample was then sheared at 50 s^{-1} to provide a constant initial state for each sample [19]. Measurements were done at 393, 403, and 413 K, with at least three separate trials for each temperature.

A representative plot of the shear viscosity data obtained by the rheometer for 393 K appears in Figure 4.6. As a Newtonian fluid, the polymer solution should exhibit the same viscosity for all shear rates; however, as Figure 4.5 shows, the PE–dodecanol solution viscosity decreases as shear rate increases.

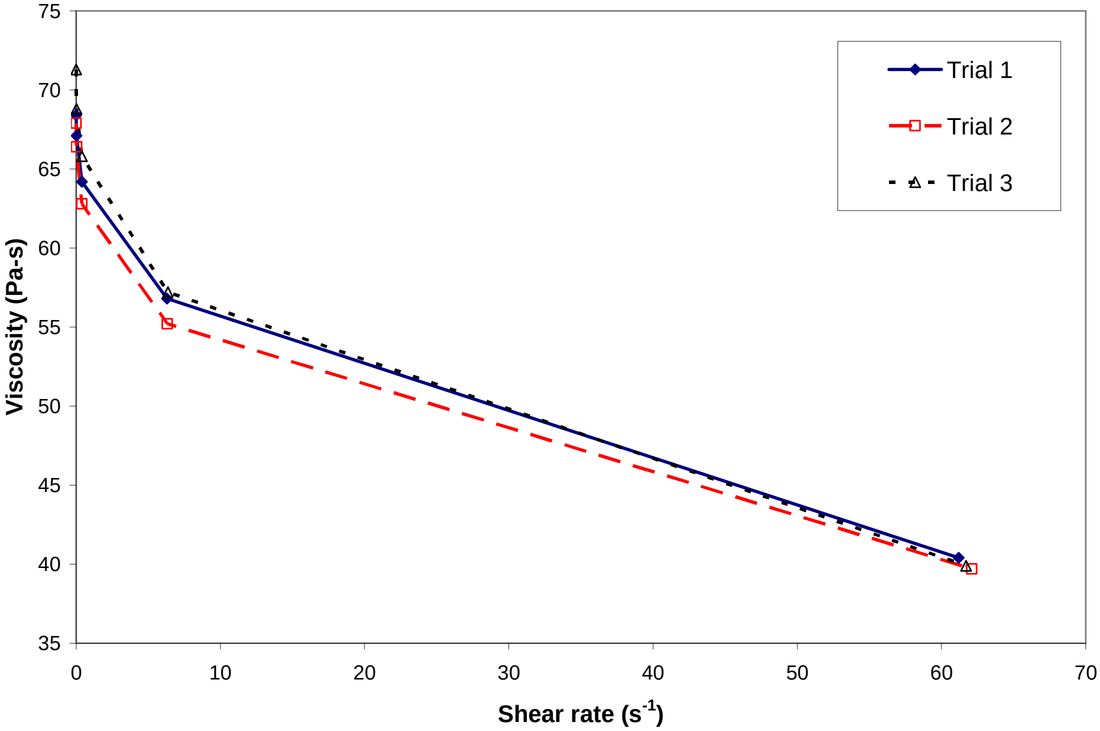

Figure 4.6 PE–Dodecanol Shear Viscosity Data for 393 K

To explore whether the PE–dodecanol viscosity variance with shear rate is significant enough to challenge the Newtonian fluid assumption, sets of measured viscosity values for four different shear rates (0.002, 0.025, 0.399, and 6 s^{-1}) at each of the three temperatures were used with an Arrhenius plot to obtain separate estimates of the viscosity pre-factor and the viscosity activation energy. To do this, viscosity values from all trials for a given shear rate and temperature were averaged and values plotted as a function of inverse temperature on a semi-log plot.

The Arrhenius viscosity plot for PE–dodecanol for the lowest shear rate value of 0.002 s^{-1} appears in Figure 4.7. From this data, the viscosity of the PE–dodecanol spinning solution modeled and spun here varies with temperature according to equation (2.35), where E_o is 3.06 x 10^7 J/kmol, η_o^0 is 6.07 x 10^3 Pa-s, and temperature is in Kelvin. This procedure was repeated for the other shear rate data sets. Calculated values of the pre-factor and viscosity activation energy for all shear rates appear in Table 4.3.

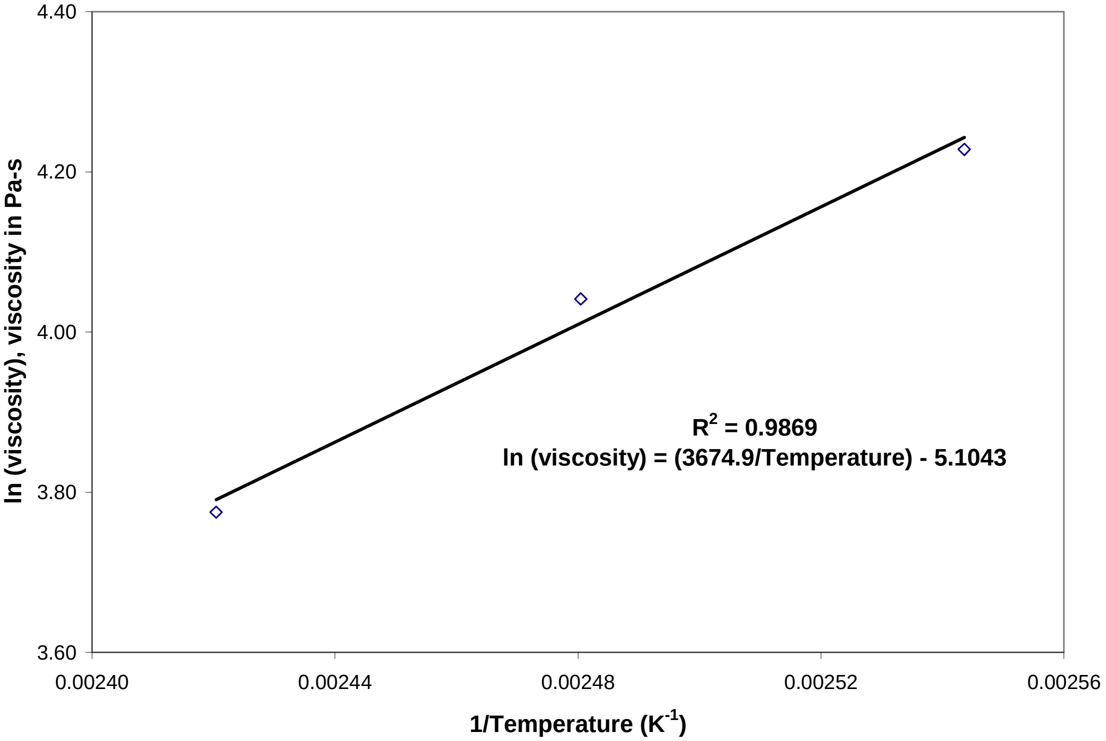

Figure 4.7 PE–Dodecanol Arrhenius Viscosity Plot for 0.002 s^{-1} Shear Rate Data

Table 4.3 PE–Dodecanol Viscosity Measurement Results

Shear Rate (s^{-1})	Pre-factor (Pa-s)	Viscosity Activation Energy (J/kmol)
0.002	6.07×10^{-3}	3.06×10^{7}
0.025	8.74×10^{-3}	2.93×10^{7}
0.399	5.25×10^{-2}	2.33×10^{7}
6	8.28×10^{-2}	2.15×10^{7}

To evaluate the significance of the difference in viscosity results for the different shear rate tests, TFA simulations for the typical PE–dodecanol spinning conditions given in Tables 2.3 and 2.4 were run using each of the different viscosity–temperature relationships established by the reported values in Table 4.3. Results are nearly identical for all of the predicted spinline variable profiles, indicating that the differences in the viscosity measurements reported in Table 4.3 are not significant enough to affect the output of the TFA simulations. Representative of the comparison of the other predicted spinline variables, Figure 4.8 shows the predicted spinline outer radius profiles for all of the viscosity–temperature relationships represented in Table 4.3. As a result, the PE–dodecanol viscosity–temperature function in all other simulations reported here is taken as the 0.002 s^{-1} shear rate result embodied by Figure 4.7.

4.1.4 Determining the PE–Dodecanol Mutual Diffusion Coefficient

A polymer solution's mutual diffusion coefficient *D*, which describes how solvent moves through the homogeneous solution, is most often described as a function of temperature and solution composition. The purely predictive method of Zielinski and Duda [20] was used in this research to determine the PE−dodecanol diffusion coefficient for use with simulations of the TFA model developed here. In addition, experiments involving Fourier transform infrared–attenuated total reflectance (FTIR−ATR) spectroscopy, modeled after the work of Fieldson, Barbari, and Hong [21-23], were performed. Results from the experiments are given in Appendix A.

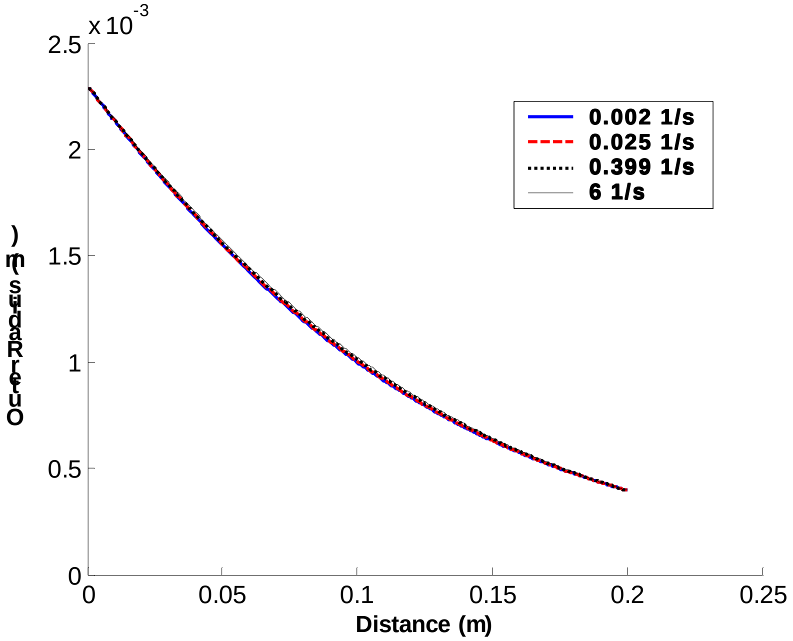

Figure 4.8 PE–Dodecanol Outer Radius Profiles for Viscosity Data of Table 4.3

The Zielinski–Duda purely predictive method for obtaining *D* relies on free volume theory [24]. Free volume theory describes molecular transport in terms of the availability of an intermolecular vacancy close enough to a molecule that possesses sufficient energy to move from its current position to occupy the vacancy; these intermolecular spaces, comprising the “hole” free volume, are continuously rearranged as a result of thermal fluctuations. Analysis of diffusion via the free volume theory, with the assumption of negligible required energy to overcome attractive forces between a candidate molecule and its neighbors, leads to the expression for *D* (cm^2/s) given in equation (4.5).

$$D = D_d^*\left(1-\phi_d\right)^2\left(1-2\chi\phi_d\right) \qquad (4.5)$$

In this expression, ϕ_d represents the diluent volume fraction, and D_d^* , the diluent self-diffusion coefficient, is defined by equation (4.6). Definitions and values of parameters in equation (4.6) for PE–dodecanol are given in Table 4.4 as calculated in the course of this research following the methods detailed by Matsuyama *et al.* [25], with the polymer glass transition temperature T_{gp} taken from the literature [26]. Furthermore, ω_d represents diluent mass fraction, and ω_p represents polymer mass fraction. Figure 4.9 shows the dependence of the PE–dodecanol diffusion coefficient on concentration and temperature as predicted by the Zielinski–Duda formulation.

$$D_d^* = D_{do} \exp\left[\frac{-\left(\omega_d V_d^* + \omega_p \xi V_p^*\right)}{\omega_d \left(\frac{K_{1d}}{\varphi}\right)\left(K_{2d} - T_{gd} + T\right) + \omega_p \left(\frac{K_{1p}}{\varphi}\right)\left(K_{2p} - T_{gp} + T\right)}\right] \tag{4.7}$$

Table 4.4 Zielinski–Duda Diffusion Coefficient Parameters for PE–Dodecanol

Parameter	Definition	Value
D_{do}	Pre-exponential factor	5.30 x 10^{-4}
V_d^*	Specific critical hole free volume of diluent required for a jump	1.024
V_p^*	Specific critical hole free volume of polymer required for a jump	1.034
ξ	Ratio of critical molar volumes for diluent and polymer molar jumping units	2.96
$\frac{K_{1d}}{\varphi}$	(Diluent free volume parameter 1)/(free volume overlap factor)	1.11 x 10^{-3}
$K_{2d} - T_{gd}$	(Diluent free volume parameter 2) – (Diluent glass transition temperature)	–116.951
$\frac{K_{1p}}{\varphi}$	(Polymer free volume parameter 1)/(free volume overlap factor)	4.99 x 10^{-4}
K_{2p}	Polymer free volume parameter 2	251.4
T_{gp}	Polymer glass transition temperature	193

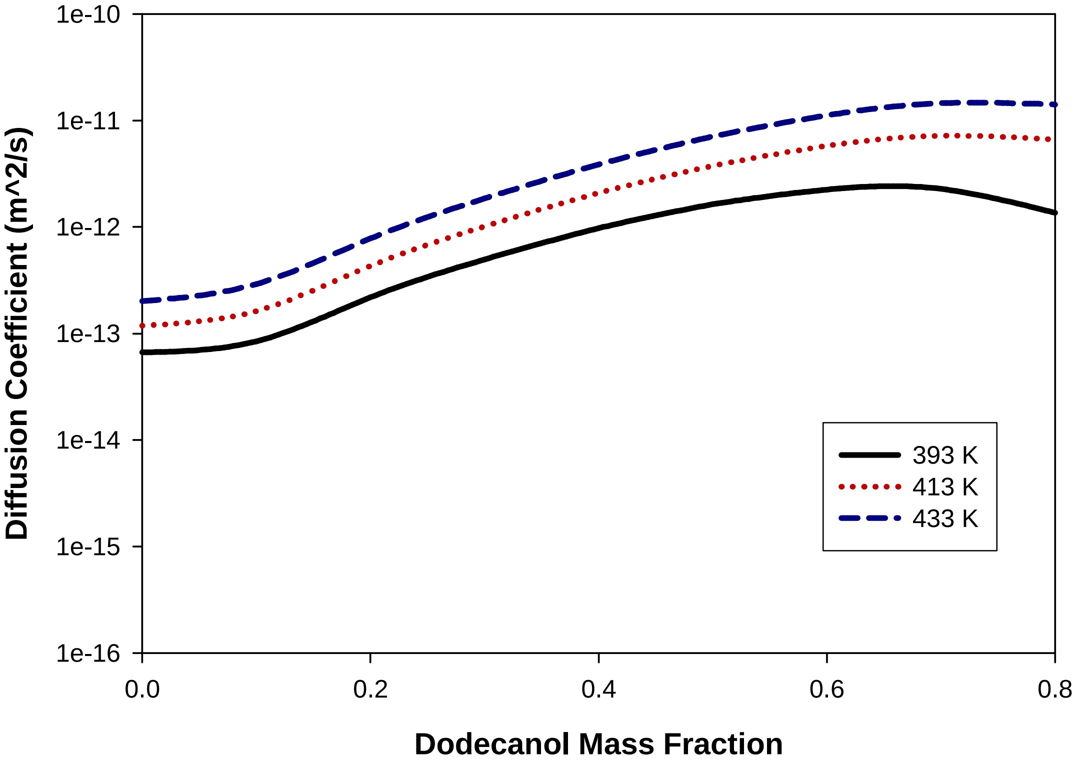

Figure 4.9 Zielinski–Duda Prediction of PE–Dodecanol Diffusion Coefficient

4.1.5 Additional Parameters Taken from the Literature

Physical parameter values for the PE–dodecanol membrane spinning system taken directly from the literature [26-28] are PE and dodecanol pure component densities as functions of temperature; PE, dodecanol, and nitrogen gas pure component heat capacities; PE surface tension, which is assumed to represent the surface tension of the spinline throughout the draw zone as discussed in Chapter 2; and dodecanol heat of vaporization and vapor pressure. All of these parameters are listed in Table 2.4 for a representative set of spinning conditions.

4.2. Spinning Experiment Specifics

4.2.1 Spinning Experimental Procedure

As stated in Chapter 1, hollow fiber membranes spun via the TIPS process were used to validate the model developed in this research. The TIPS process as it is currently practiced is represented by the process schematic shown in Figure 1.2 and can be used to make hollow fiber membranes as follows:

1. A homogeneous solution of the polymer with a high-boiling, low molecular weight diluent or latent solvent is formed by blending at an elevated temperature.
2. This homogeneous solution is extruded through a spinneret as the nascent membrane, which passes through an air gap and then into a quench bath. Through the appropriate choice of diluent and initial polymer concentration [1-3, 29], the solution undergoes liquid–liquid TIPS to form diluent-rich droplets in a polymer-rich liquid matrix. The diluent-rich droplets grow as a function of time.
3. Upon continued cooling, the polymer in the polymer-rich phase crystallizes, which stops the growth of the diluent-rich domains and locks in the membrane microstructure.
4. After polymer crystallization, the diluent is extracted by solvent exchange.
5. The extractant is removed (typically by evaporation), and the spaces previously occupied by the diluent-rich domains become the cells or pores of the membrane.

Spinning experiments were performed in this research using a Leistritz twin-screw extruder (model Micro-18) and attachments as shown in Figure 4.10. The PE–dodecanol spinning process involves high temperatures and produces dodecanol fumes; precautions were taken during spinning to avoid burns and ensure sufficient venting. The standard operating procedure followed for spinning with the twin-screw extrusion setup in this research is included in Appendix A and summarized here. Prior to spinning, set points on the temperature controllers for the diluent feeder, the extruder barrels, the exit melt pump and connecting tubing, and the spinneret must be adjusted and sufficient time allowed for the equipment to heat; for PE–

dodecanol spinning, temperatures were on the order of 413 K, and the system usually heated within a span of one hour.

Figure 4.10 Leistritz Twin-Screw Extrusion Setup

Hollow fibers were spun on a continuous basis using separate feeders for polymer (K-Tron Soder Model K2MVT20), shown in Figure 4.11, and diluent (Leistritz-designed using Zenith model H-9000, 0.6 cm^3/revolution pump and ZeDrive 2000 DC Motor Speed Controller), shown in Figure 4.12. Feeders were calibrated with PE and dodecanol, respectively, to quantify mass flow rate as a function of machine setting. Calibration curves for both feeders appear in Appendix A.

To control precisely the flow rate of the spinning solution to the spinneret, the extruder exit is followed by an external high-temperature melt pump assembly (Leistritz-designed using a Zenith custom metering system providing a flow of 0.297 cm^3/revolution, controlled using a ZeDrive 2000 DC Motor Speed Controller) shown in Figure 4.13. As it was dispensed by the melt pump, the polymer solution was co-extruded through a spinneret with nitrogen gas to form hollow fibers; nitrogen flow was controlled by a Millipore mass flow assembly (control valve model FC260V; digital controller LR250) shown in Figure 4.14, with the gas flow rate indicated in SCCM. Figure 4.15 shows the spinneret used in this research.

Figure 4.11 K-Tron Polymer Feeder

Figure 4.12 Leistritz Diluent Feeder

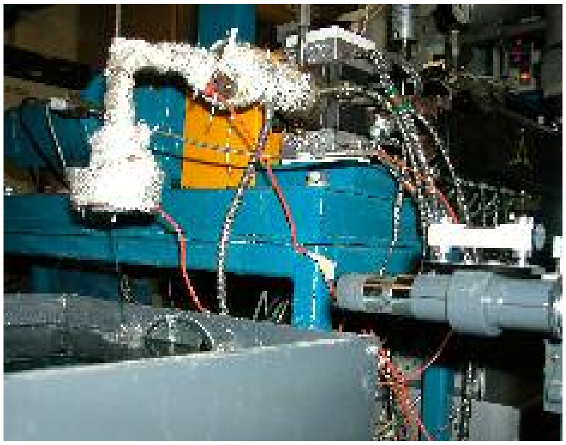

Figure 4.13 Extruder's External Melt Pump Assembly, Spinneret, and Extrusion into the Water Bath

Figure 4.14 Millipore Mass Flow Controller Assembly: (a) gas flow control valve; (b) gas flow controller showing gas throughput in SCCM

Figure 4.15 Spinneret Used with the Leistritz Twin-Screw Extrusion Setup: (a) side view; (b) top view—center inlet port is for core gas flow, and second inlet port is for polymer–diluent solution; (c) plate at left fits into bottom of spinneret, and needle (for core gas flow) fits into the center of the spinneret so that the needle tip extends through the plate orifice

The spinline then passed through an air gap followed by a water quench bath, in which the nascent membrane was guided under a motor-driven roller, all appearing in Figure 4.16. The water bath and driven roller assembly were designed and built in-house (Dayton DC motor model 4Z726A). Upon exiting the bath edge, the fiber passed over an idle roller to diminish drag before take-up on a fiber winder (Randcastle). Both the driven roller in the water bath and the Randcastle fiber winder were calibrated using a tachometer; speeds for both were linear functions of the digitally displayed control motor rpm, and the two devices were set for the same speed during spinning to avoid cold-drawing the fiber spinline. Calibration curves for both rollers are given in Appendix A.

Figure 4.16 Quench Bath and Fiber Take-up Following the Spinneret

Extraction of the dodecanol in the hollow fibers, necessary for analysis of the microstructure via scanning electron microscopy (SEM), took place after spinning was complete by immersing the spools of collected fiber in tubs of methanol or isopropanol, with immersions in four fresh baths of solvent for each roll and a minimum time spent in each bath of four hours. Fibers were then freeze-fractured in liquid nitrogen to obtain crisp cross-sections and mounted on SEM stages using double-sided carbon tape. The sample stage assemblies were then dried under vacuum for at least two hours prior to sputter coating with gold/palladium using an Electron Microscopy Sciences coater (model K575), with a coating time of 40–80 seconds at maximum deposition.

4.2.2 In-line Spinning Instrumentation

An X–Z axis videoscope (Titan Tool Supply, Inc.) was used to experimentally determine spinline outer diameter and axial velocity as functions of axial position. The instrument provided the ability to measure spinline diameter within 90 μm, with an on-screen field of view (FOV) of approximately 1.0 x 0.8 cm. The videoscope setup consisted of positioning the eyetube at a working distance of 8.75 ± 0.25 inches from the spinline and selecting the working height for a particular measurement. For spinline measurements at each height, after leveling the instrument, video was taken of a stainless steel ruler placed flush with the bottom of the spinneret; with its finest measurement of 1/64 of an inch, the ruler was used to keep track of the absolute distance from the spinneret, which varied as the videoscope height was changed to take spinline measurements throughout the draw zone. Recorded video images of the stainless steel ruler were also used to calibrate the on-screen distance markers, resulting in a measurement of 170 μm per on-screen tick mark. The validity of this spatial calibration was confirmed by observing videoscope images of objects of known diameter, including a glass stirring rod.

The videoscope was interfaced with a computer to collect video footage using StreamPix 3.6.0 software (NorPix, 2002), and recordings made use of supplemental light from a variable-brightness illuminator (Titan Tool Supply, Inc., model FO-150). Outer diameter was obtained through direct observation of images, with the ability to save each frame from streaming video (30 frames per second) in digital image file format (such as *.jpeg*, *.tiff*, or *.bmp*). Spinline axial velocity was obtained by tracking particular areas of the moving fiber over a set of consecutive frames, calculating the axial velocity at a given axial position using the observed movement of a marker over a very small (less than 1 mm) spinline distance. Bits of polyethylene powder, assumed too small to affect spinline behavior, were used as the markers for velocity measurements: a small amount of powder was thrown on the moving spinline while video footage was collected.

An infrared (IR) camera (Mikron model TH5104) was evaluated for use in determining spinline surface temperature profiles. Outfitted with a 250 μm close-up lens requiring manual focus, with a working distance of two inches, the instrument has the capability to detect radiation in the 3.0–5.3 μm spectral range. A number of procedures were performed during the evaluation process for the IR camera, including measurements of pure dodecanol samples, pure PE samples, and PE–dodecanol solution samples; these are detailed further in Appendix A. Unfortunately, properties of the PE–dodecanol spinning system make this IR camera inadequate for temperature measurements of the spinline. Specifically, PE transmits IR radiation for all of the wavelengths detected by the camera, and the spinline is in general too thin to overcome this effect. IR camera use is discussed more extensively in Chapter 6.

4.2.3 Experimental Design

In this research, the experiments performed to validate and refine modeling efforts were chosen to gauge the sensitivity of the measurable variables (spinline outer diameter, spinline axial velocity, and membrane extent of anisotropy) to particular processing variables. Three levels each of spinning temperature, draw ratio, core gas flow rate, and air gap length were selected based on values feasible for use in spinning the PE–dodecanol system examined here, resulting in a parametric set of spinning experiments. Starting solutions for the bulk of the spinning experiments were 30 wt-% PE; additional trials were attempted using 40 wt-% PE spinning solutions. A complete list of the performed experiments appears in Table 4.5, and the values of other spinning quantities not varied during the experiments appear in Table 4.6.

Table 4.5 PE–Dodecanol Spinning Experiments for Membrane Sensitivity Studies

Condition Set	Spinning Temperature (± 1 K)	Draw Ratio	Core Gas Flow Rate (SCCM)	Air Gap Length (± 0.5 cm except where noted)	Spinning Solution Composition (wt-% PE)
1	393	24	1.00	20.0	30
2	393	29	1.00	20.0	30
3	393	34	1.00	20.0	30
4	413	34	1.00	20.0	30
5	413	34	3.00	20.0	30
6	413	34	5.00	20.0	30
7	413	34	1.00	10.0	30
8	413	29	1.00	10.0	40
9	413	34	1.00	10.0	40
10	413	24	1.00	0.5 ± 0.2	30
11	413	29	1.00	0.5 ± 0.2	30
12	413	34	1.00	0.5 ± 0.2	30
13	433	34	1.00	20.0	30

Table 4.6 PE–Dodecanol Spinning Conditions Constant for Spinning Experiments

Condition	Value
R_i^0 = initial clad inner radius	6.8×10^{-4} m
R_o^0 = initial clad outer radius	2.3×10^{-3} m
$\overline{v^0}$ = extrusion velocity	1.74×10^{-2} m/s
$\overline{p_i^0}$ = initial core gas gauge pressure	58 Pa
T_q = quench fluid temperature	298 K
v_q = quench fluid velocity normal to fiber axis	0 m/s
w_o = clad mass flow rate	2.00×10^{-4} kg/s
p_{atm} = ambient air pressure	101325 Pa

4.3 References

1. D.R. Lloyd, J.W. Barlow, and K.E. Kinzer, Microporous membrane formation via thermally-induced phase separation, in: K.K. Sirkar and D.R. Lloyd (Eds.), New Membrane Materials and Processes for Separation, AIChE Symposium Series 261, New York, 1988.
2. D.R. Lloyd, K.E. Kinzer, and H.S. Tseng, Microporous membrane formation via thermally-induced phase separation. I. Solid-liquid phase separation, J. Membr. Sci., 52 (1990) 239-261.
3. D.R. Lloyd, S.S. Kim, and K.E. Kinzer, Microporous membrane formation via thermally-induced phase separation. II. Liquid-liquid phase separation, J. Membr. Sci., 64 (1991) 1-11.
4. A. Nakajima, H. Fujiwara, and F. Hamada, Phase relationships and thermodynamic interactions in linear polyethylene-diluent systems, Journal of Polymer Science: Part A-2, 4 (1966) 507-518.
5. S.S. Kim and D.R. Lloyd, Microporous membrane formation via thermally-induced phase separation. III. Effect of thermodynamic interactions on the structure of isotactic polypropylene membranes, J. Membr. Sci., 64 (1991) 13-29.
6. K.S. McGuire, A. Laxminarayan, and D.R. Lloyd, A simple method of extrapolating the co-existence curve and predicting the melting point depression curve cloud point data for polymer-diluent systems., Polymer, 35 (1994) 4404-4407.
7. G.B.A. Lim, Effects of nucleating agent on thermally induced phase separation membrane formation, Dissertation, The University of Texas at Austin, 1990.
8. W. Yave, Personal Communication, 2004.

9. I.C. Sanchez, Encyclopedia of Physical Science and Technology, Academic Press, Inc., 1992. pages 153.
10. H. Matsuyama, S. Berghmans, M.T. Batarseh, and D.R. Lloyd, Effects of thermal history on anisotropic and asymmetric membranes formed by thermally induced phase separation, J. Membr. Sci., 142 (1998) 27-42.
11. H. Tompa, Polymer Solutions, Butterworths, London, 1956. pages 325.
12. A.A. Alwattari and D.R. Lloyd, Microporous membrane formation via thermally-induced phase separation. VI. Effect of diluent morphology and relative crystallization kinetics on polypropylene membrane structure, J. Membr. Sci., 64 (1991) 55-68.
13. L.-P. Cheng, Mechanism Of Microporous Membrane Formation By Precipitation Of Semicrystalline Polymers (Polyamides), Ph.D., Columbia University, New York, 1993.
14. S.S. Kim, G.B.A. Lim, A.A. Alwattari, Y.F. Wang, and D.R. Lloyd, Microporous membrane formation via thermally-induced phase separation. V. Effect of diluent mobility and crystallization on the structure of isotactic polypropylene membranes, J. Membr. Sci., 64 (1991) 41-53.
15. G.B.A. Lim, S.S. Kim, Q. Ye, Y.F. Wang, and D.R. Lloyd, Microporous membrane formation via thermally-induced phase separation. IV. Effect of isotactic polypropylene crystallization kinetics on membrane structure, J. Membr. Sci., 64 (1991) 31-40.
16. K.S. McGuire, D.R. Lloyd, and G.B.A. Lim, Microporous membrane formation via thermally-induced phase separation. VII. Effect of dilution, cooling rate, and nucleating agent addition on morphology, J. Membr. Sci., 79 (1993) 27-34.
17. P.J. Flory, Principles of polymer chemistry, Cornell University Press, 1953.
18. University of Fribourg, http://www.unifr.ch/physics/mm/faci/mcr300.html, (2004).
19. D.S. Martula, Coalescence-induced coalescence, Dissertation, The University of Texas at Austin, 2000.
20. J.M. Zielinski and J.L. Duda, Predicting Polymer/Solvent Diffusion Coefficients Using Free-Volume Theory, AIChE J., 38 (1992) 405-415.
21. G.T. Fieldson and T.A. Barbari, The Use of Ftir-Atr Spectroscopy to Characterize Penetrant Diffusion in Polymers, Polymer, 34 (1993) 1146-1153.
22. S.U. Hong, T.A. Barbari, and J.M. Sloan, Diffusion of methyl ethyl ketone in polyisobutylene: Comparison of spectroscopic and gravimetric techniques, Journal of Polymer Science Part B-Polymer Physics, 35 (1997) 1261-1267.
23. S.U. Hong and T.A. Barbari, Transport of toluene/methyl ethyl ketone mixtures polyisobutylene, Journal of Polymer Science Part B-Polymer Physics, 39 (2001) 908-914.
24. J.S. Vrentas and J.L. Duda, Diffusion in Polymer-Solvent Systems. I. Reexamination of the Free-Volume Theory, Journal of Polymer Science: Polymer Physics Edition, 15 (1977) 403-416.
25. H. Matsuyama, S. Berghmans, and D.R. Lloyd, Formation of anisotropic membranes via thermally induced phase separation, Polymer, 40 (1999) 2289-2301.
26. J. Brandrup, E.H. Immergut, and E.A. Grulke, (Eds.), Polymer Handbook, 4th ed., John Wiley & Sons, New York, 1999.
27. R.L. Rowley, W.V. Wilding, J.L. Oscarson, Y. Yang, R.J. Rowley, T.E. Daubert, and R.P. Danner, DIPPR® Data Compilation of Pure Compound Properties: Design Institute for Physical Property Data, AIChE®, New York, NY (2001).

28. J.E. Mark, (Ed.), Physical properties of polymers handbook, AIP Press, Woodbury, N.Y., 1996.
29. A.J. Castro, Methods for making microporous products, US Patent 4,247,498, 1981.

Chapter 5. Results and Discussion: Comparison of Experimental Results and Model Predictions

5.1 Introduction

The main goal of this research is to create a model that predicts spinline variables, in particular concentration and temperature, based on system material properties and processing conditions. In order to validate the model and also gauge the experimental sensitivity of measurable spinline variables, PE–dodecanol spinning experiments were conducted via twin-screw extrusion as outlined in Chapter 4. Direct measurements of spinline outer diameter and axial velocity, both functions of axial position, were taken during spinning; the experimental results are compared here with model predictions for these spinline variables.

In addition, fiber outer to inner diameter ratio (OD/ID) and membrane extent of anisotropy were experimentally determined post-spinning by examining hollow fiber membrane cross-sections using scanning electron microscopy (SEM). The fraction of the membrane wall containing a pore size gradient was measured and compared to model predictions resulting from the boundary layer analysis described in Chapter 3; OD/ID results were compared to model predictions as well. Surface tension effects and the effects of evaporative cooling, incorporated to create the modified TFA of hollow fiber spinning as discussed in Chapter 2, were included in all model simulations reported in this chapter.

5.2 General Spinning Results

All of the spinning experiments outlined in Table 4.5 were attempted with the PE–dodecanol spinning system using the twin-screw extrusion apparatus described in section 4.2.1. In-line measurements of the spinline outer diameter and axial velocity, both functions of axial position, were taken using the instrumentation and procedure detailed in section 4.2.2. Condition sets 1–3 in Table 4.5 were performed to gauge the sensitivity of spinline variables and membrane extent of anisotropy to draw ratio, spinning using draw ratios of 24, 29, and 34. These numbers correspond to the linear extrusion velocity given in Table 2.3 and take-up velocities of 25, 30, and 35 m/min. The draw ratio sensitivity trials were successfully completed with no problems.

Condition sets 4–6 in Table 4.5 correspond to core gas flow rate sensitivity studies, using core gas flow rates of 1.00, 3.00, and 5.00 SCCM as regulated by the core gas mass flow controller. These experiments were also performed successfully. In addition, trial 13, corresponding to a spinning temperature of 433 K, proved successful. Its results are compared to results for 413 K and 393 K in trials 4 and 3, respectively, to illustrate the sensitivity of the measured results to initial spinning temperature.

Air gap sensitivity studies were to be represented by trials 4, 7, and 12 in Table 4.5, representing air gaps of 20.0 ± 0.5, 10.0 ± 0.5, and 0.5 ± 0.2 cm. However, problems were encountered with all experiments using the shortest air gap, represented in trials 10–12. For trial 12, fibers appeared smooth during collection on the take-up drum, but upon stopping the spin and examining the fiber structure more closely, the cross-section of the entire length of fiber was flattened, with the inner walls of the cross-section (the lumen walls corresponding to the inner radius) nearly touching. This is presumably due to the low extent of spinline cooling experienced for the very short air gap, causing the spinline to flatten upon contact with the motor-driven roller in the water quench bath.

Although the spinline is assumed to experience an iso-enthalpic transition to an undeformable solid upon entering the water quench bath, for the high spinning temperature and the near-wet spin attempted here, this assumption is questionable. If the spinline did not cool sufficiently during its short air gap residence time, its temperature upon reaching the motor-driven roller in the bath may have been high enough to impart some malleability to the threadline, allowing it to deform by flattening as it passed around the roller and out of the bath to be taken up on the fiber winder. The structure of the resulting fiber membranes forces a tremendous required pressure drop for flow through the lumen over the fiber length, making them impractical for application.

In response to the poor structure of trial 12 that could have resulted from too short of an air gap residence time, the draw ratio of trial 12 was decreased from its value of 34 by decreasing the take-up rate, thus giving the spinline a bit more of an opportunity to cool before water quench bath entry. However, the resulting fibers for draw ratios of 29 (trial 11) and 24 (trial 10) were also practically solid with no lumen. Thus, these fibers were discarded and not analyzed further. The air gap sensitivity study was limited to the 10.0 and 20.0 ± 0.5 cm lengths used for trials 7 and 4.

Two attempts were made to spin fibers of 40 wt-% PE–dodecanol, with conditions outlined as trials 8 and 9. The composition of the spinning solution was altered by increasing the feed rate of polymer relative to that for the diluent, keeping the same total mass flow rate out of the extruder to the external melt pump for feeding to the spinneret. After changing the composition of the feed from 30 wt-% PE–dodecanol to 40 wt-% PE–dodecanol and vice versa, for the total flow rate of 12 g/min and the extruder screw speed of 200 rpm, solution was allowed to flow through the spinneret and be discarded as waste for 10 minutes prior to starting spinline take-up. Unfortunately, the draw ratio of 34 (trial 9) produced flat fibers with practically no lumen; decreasing the draw ratio to 29 (trial 8) did not improve fiber appearance.

Furthermore, on a separate occasion, a more complete parametric study for 40 wt-% PE–dodecanol was attempted, spinning parametrically with a broad range of spinning temperatures, core gas flow rates, air gap lengths, and draw ratios; flat fibers were produced for all experiments. In addition, an undetected problem with the motor-driven take-up roller caused the fiber spinline to undergo cold-draw between this in-bath roller and the take-up winder during all of these detailed studies. The cold-draw could have been partially at fault for the flatness of the resulting fibers, but since runs without this effect produced flat fibers also, this could not be isolated as the only culprit.

During the tests with cold-draw, an additional instrumental problem was experienced: at one point during the test, the extruder exit pressure spiked to 1000 psig, indicative of a plug caused by unmolten polymer or presence of a particulate impurity. The pressure decreased after increasing system temperatures, suggesting that the higher percentage of polymer required higher system temperatures to provide adequate mixing and melting during the residence time in the extruder. However, upon trying to operate at the higher system temperatures, extruder exit pressures remained consistently higher than the usual values for 30 wt-% PE–dodecanol and periodically spiked to values too high for operation, forcing a stop-and-start procedure to try to flow through and clear the extruder exit and try again.

Thus, no further attempts to spin with 40 wt-% PE–dodecanol were made. Although pure PE is extruded industrially on a regular basis, the process for membrane spinning and the transition from the extruder exit to the lower flow rate melt pump and the spinneret may have complicated the situation here, creating too much resistance to the flow of the 40 wt-% PE–dodecanol solution. This is one possible cause of the pressure spike: a very high pressure was needed to push the higher polymer content solution through the small diameter spinneret. In addition, the pressure spike may have been caused by improper solution mixing in the extruder spurred by inadequate settings for temperature, flow rates, and/or screw speed for the 40 wt-% PE–dodecanol trials. This probably led to an extruded solution with a polymer content actually less than even 30 wt-% PE. Such fibers may not have the structural integrity to withstand the draw of the roller and take-up winder, causing the observed flattening of the spinline.

Table 5.1 summarizes the successful spinning experiments performed in this research for model validation and sensitivity studies.

Table 5.1 Successful Spins for Model Validation and Sensitivity Studies

Condition Set	**Spinning Temperature (± 1 K)**	**Draw Ratio**	**Core Gas Flow Rate (SCCM)**	**Air Gap Length (± 0.005 m)**	**Spinning Solution Composition (wt-% PE)**
1	393	24	1.00	0.200	30
2	393	29	1.00	0.200	30
3	393	34	1.00	0.200	30
4	413	34	1.00	0.200	30
5	413	34	3.00	0.200	30
6	413	34	5.00	0.200	30
7	413	34	1.00	0.100	30
8	433	34	1.00	0.200	30

5.3 Spinline Outer Diameter Profiles

Spinline outer diameter measurements were performed for model validation using the following sensitivity studies: effect of spinning temperature; effect of draw ratio; effect of core gas flow rate; and effect of air gap length. Spinline images were collected as detailed in section 4.2.2; Figure 5.1 shows a representative spinline image used for obtaining the spinline diameter. Unfortunately, the inner diameter of the translucent filament could not be clearly discerned in these images and is thus not reported here.

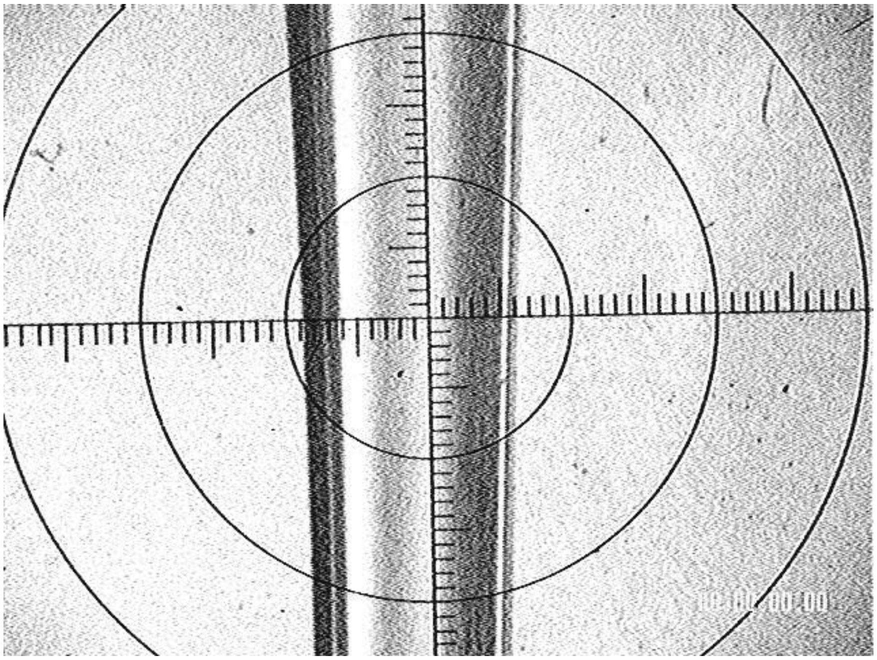

Figure 5.1 Spinline Videoscope Image for Determining Spinline Diameter

5.3.1 Spinning Temperature Sensitivity Studies

Experimental results and modified TFA model predictions for spinline outer diameter profiles for the spinning temperature sensitivity study are presented in Figure 5.2. The three spinning temperatures were 393, 413, and 433 ± 1 K (trials 3, 4, and 8 in Table 5.1). As shown in

Figure 5.2, the modified TFA model-predicted outer diameter profiles for all three temperatures show a much more gradual decrease with axial position than indicated by the experimental measurements. In addition, model predictions show that the lower spinning temperatures should produce a higher degree of draw-down earlier in the spinline, resulting in smaller diameters throughout the draw zone until the final diameter values nearly converge for all three temperatures as dictated by continuity, equation (2.1).

However, throughout the modeled draw zone, the differences in the model predictions of spinline diameter for the three spinning temperature cases are within the margin of error of the videoscope measurements, ± 90 μm. Thus, the diameter differences between the three cases of spinning temperature as predicted with the modified TFA spinning model are undetectable with the current experimental setup. Experimental results agree with this expectation: with the data obtained and the instrumental error of the videoscope, no significant distinction can be made between the data sets obtained experimentally for the three different temperatures.

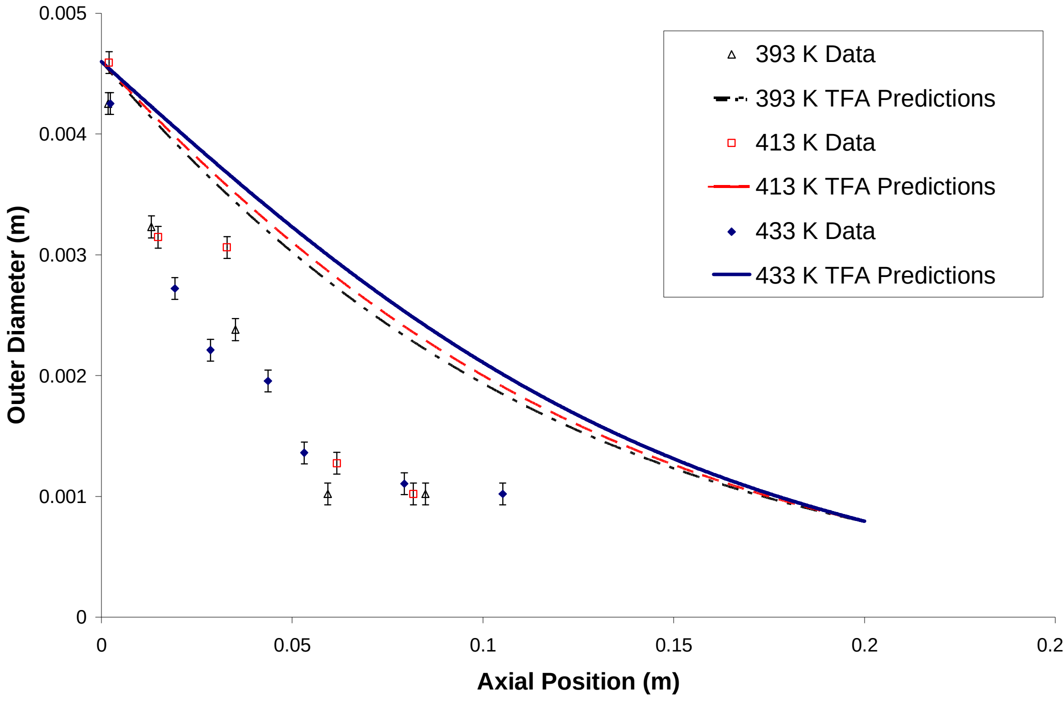

Figure 5.2 Temperature Sensitivity of Spinline Diameter Profile: Comparing model and experimental results for trials 3, 4, and 8 from Table 5.1

Selecting the 413 ± 1 K case corresponding to trial 4 in Table 5.1 as a focus, additional model simulations were performed to examine possible causes of the mismatch between the model and experimental spinline diameter profiles shown in Figure 5.2. The spinline diameter profile is established by continuity as given in equation (2.1), written in terms of the outer radius. Thus, the extent of spinline attenuation in the draw zone depends on the evolution of the axial velocity and core gas density profiles during spinning. Both the velocity variation as given in the momentum balance of equation (2.30) and the core gas density behavior established by equation (2.31) depend on system viscosity.

As a first attempt to try to reconcile the difference between the experimental and predicted diameter profiles shown in Figure 5.2, simulations were performed using a doubled viscosity activation energy of 14617 cal/mol; as in section 3.3.4, the viscosity pre-factor was also adjusted to 8.18 x 10^{-7} Pa-s. Higher viscosity activation energy corresponds to a system whose viscosity is more temperature-sensitive. Thus, the goal of doubling this value for an illustrative simulation was to make the viscosity increase more quickly along the draw zone, resulting in higher elongation rates and more spinline attenuation earlier in the draw zone. However, altering the viscosity temperature dependence in this fashion did not significantly impact the comparison of the model predictions and the experimental results—a large discrepancy remained.

Evaporation of diluent at the clad–air quench interface, which creates the concentration gradient in the cross-sectional boundary layer adjacent to the outer radius as detailed in Chapter 3, results in higher polymer content, and thus higher viscosity for the PE–dodecanol case, in these regions. One of the assumptions of the thin filament analysis listed in section 2.3.1 is that of constant material properties, including spinline viscosity, over the cross-section at a given axial position. However, this assumption may not apply if the difference in viscosity of the material in the boundary layer is very high relative to the bulk solution: the controlling viscosity may instead correspond to the viscosity of the concentrated boundary layer. Hence, the high rates of attenuation in the experimental spinline diameter profiles could potentially be produced by increases in the effective spinline viscosity due to diluent evaporation.

To account for this change in viscosity in the modified TFA for hollow fiber spinning, the PE–dodecanol spinning system viscosity η_o was correlated with temperature $\overline{T}$ and polymer concentration C_p (g/cm^3) as given by equation (5.1), a general relationship from the literature [1].

Using this equation, the pre-factor η_{0c} and the activation energy E_{0c} are recalculated with a linear regression to the experimental 30 wt-% PE-dodecanol viscosity measurements for different temperatures as shown in section 4.1.3; the pre-factor is calculated to be 4.04 x 10^{-14} Pa s, and the activation energy is 6151 cal/mol. Use of equation (5.1) presumes that the solution is above the *critical concentration* corresponding to the transition from a dilute polymer solution of separate, non-overlapping polymer chains to an entangled solution; this is reasonable for the 30 wt-% PE solution considered here [1].

$$\eta = \eta_{0c} \exp\left(\frac{E_{0c}}{R_g \overline{T}} \right) \left(C_p \right)^5 \qquad (5.1)$$

In order to calculate the effective spinline viscosity, a simulation of the modified TFA for fiber spinning was first performed with the temperature-dependent viscosity correlation used in Chapters 2 and 3 (viscosity pre-factor and activation energy given in Table 2.4). As described in section 3.2.2, calculated spinline temperature, radius, and axial velocity profiles were then used to calculate radial concentration gradients as functions of axial position. The resulting concentration gradients were then supplied to an additional program loop to calculate an area-average viscosity for the spinline cross-section at each axial position; this approach was taken in previous modeling efforts to apply the TFA to co-extrusion of two viscous fluids [2].

To do this calculation, the spinline cross-section at a given axial position was divided into 100 equally-spaced rings, and the calculated polymer concentration for each ring, resulting from the boundary layer analysis calculations, was used with equation (5.1) to calculate the viscosity of each ring. The resulting viscosities were multiplied by the corresponding ring area and the products summed before dividing the result by the total spinline cross-sectional area for a given axial position. The draw zone was divided into 1000 axial increments for the numerical calculations of the simulations represented here, and the area-average viscosity was calculated at each axial increment.

The calculated array of effective viscosity values, along with the calculated surface concentration values for each axial node, were then input to the TFA fiber spinning program and the entire calculation process repeated, iterating until consecutive predictions of the spinline variable profiles, the surface concentration profile, and the effective viscosity profile agreed to within 1%.

The results of this calculation for the 413 K spinning temperature case are presented in Figure 5.3 with the corresponding experimental diameter profile. The model-predicted diameter profile resulting from incorporating the generalized concentration-dependence of spinline viscosity shows better agreement with the experimental values. However, the attenuation rate of the experimental diameter data still exceeds that of the model-predicted diameter profile shown in Figure 5.3, and additional factors affecting spinline viscosity were considered.

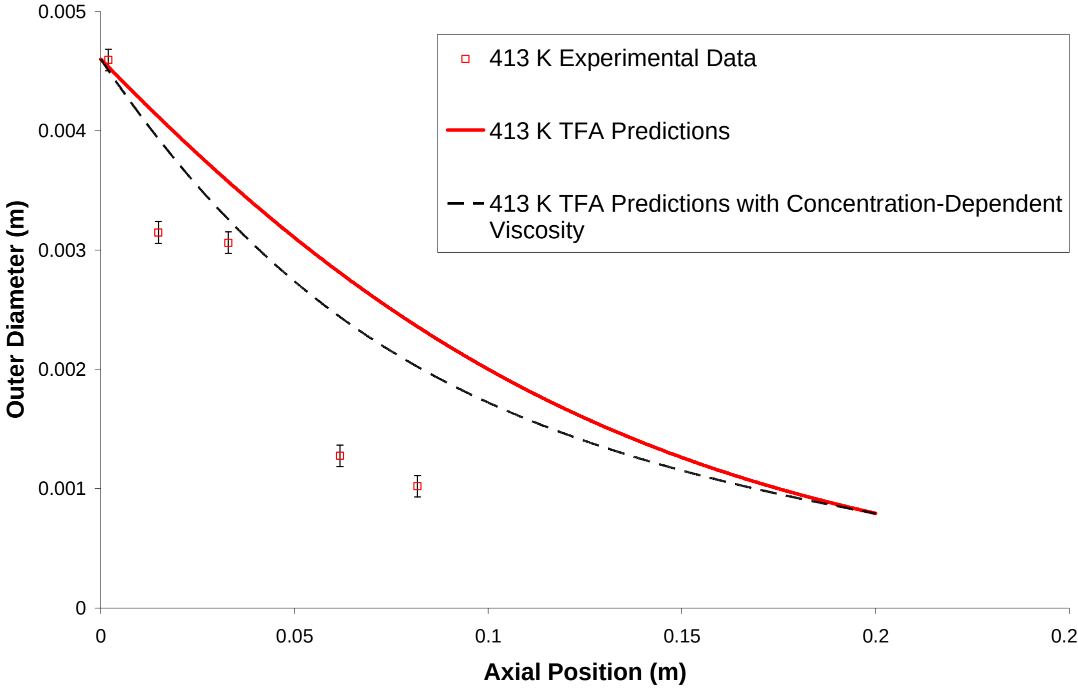

Figure 5.3 Including Concentration Dependence of Viscosity: Comparison of model-predicted and experimental spinline diameter profiles for trial 4 from Table 5.1

Specifically, the modified TFA for fiber spinning applies in the draw zone up to the point of phase separation, at which point the effective viscosity undergoes an exponential increase [3, 4]. This is analogous to conversion of a pure polymer melt to an undeformable solid at an appropriate transition temperature. At this point, elongation of the spinline stops [2], and the final value of spinline diameter is reached, essentially restricting the draw zone, or region of spinline elongation, to the portion of the air gap prior to this point. Thus, an exponential increase in the viscosity is a physical factor that halts elongation of the spinline, and the occurrence of phase separation is one possible cause of this effect.

As illustrated by the experimental data sets in Figure 5.2, the observed trend in the measured diameter profile for each temperature is an exponential drop to reach an asymptotic value comparable to the final diameter predicted by the modified TFA, arguably long before the end of the 0.200 ± 0.005 m air gap. Furthermore, during these spinning experiments, the spinline was visually observed to become cloudy at roughly $z = 15\ cm$, 5 cm prior to entering the water bath. Both the observed cloudiness and the apparent halt in elongation suggest that the spinline was phase separating in the air gap prior to water bath entry, possibly due to phase inversion spurred by interaction of the spinline with water vapor present in the air gap near the water bath [5].

To gauge the possible effect of phase separation occurring prior to the end of the air gap in addition to the increase in effective spinline viscosity due to diluent evaporation at the clad–air quench interface, simulations of the modified TFA for fiber spinning were performed using a draw zone length of 0.150 m along with the concentration-dependent viscosity calculation. The end of the draw zone sets the take-up velocity location; thus, these simulations forced the spinline to attenuate more rapidly with axial position. The predicted spinline diameter profile for this case with a 413 K spinning temperature appears in Figure 5.4 with the experimental data and the concentration-dependent viscosity result discussed previously.

Results shown in Figure 5.4 show that for cases with significant diluent evaporation at the spinline clad–air quench interface, including the concentration dependence of the spinline viscosity provides a more accurate means for predicting spinline diameter profiles for hollow fiber membrane spinning. Moreover, by incorporating the experimental evidence supporting the possible occurrence of phase separation prior to the end of the air gap, the predicted outer diameter profile shown in Figure 5.4 for the shorter draw zone length provides even better agreement with the experimental spinline diameter profile. Incorporating the concentration dependence in the generalized form presented by equation (5.1) and utilizing the iterative simulation routine discussed above provides an efficient and adequate method for including this variation. However, the occurrence of phase separation potentially complicates the variation of spinline viscosity within the air gap, and the modeling efforts considered here cannot fully capture these effects with the available viscosity data. More experimental data is necessary to quantify rigorously the dependence of the viscosity on concentration and temperature for PE–dodecanol, especially for a phase-separated system.

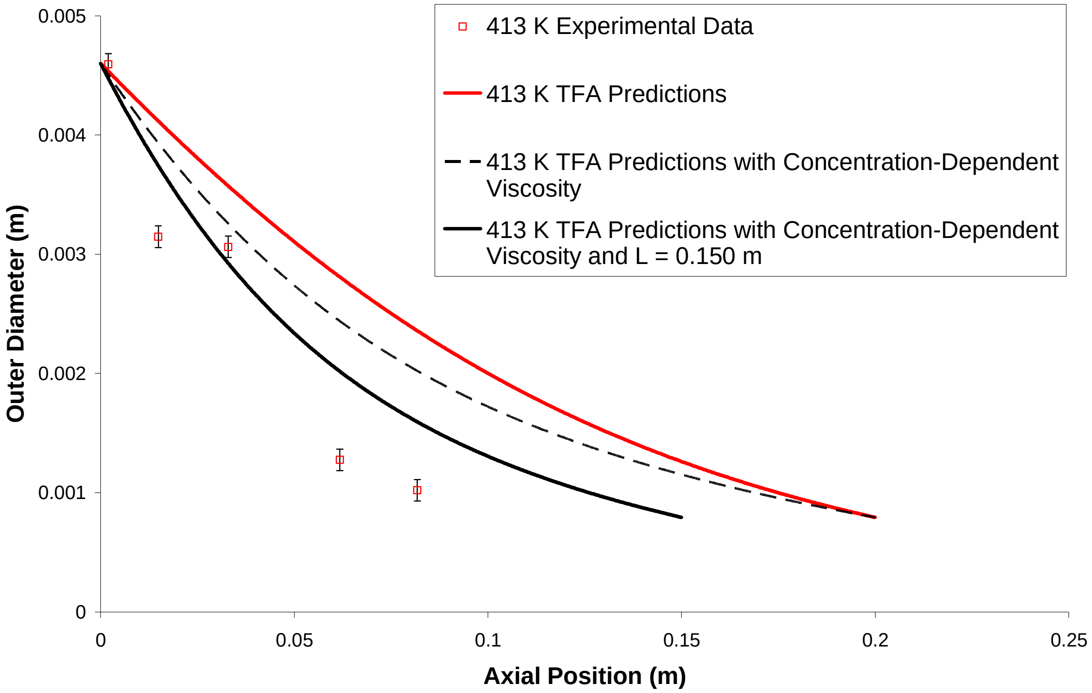

Figure 5.4 Ending the Draw Zone Prior to the End of the Air Gap: Comparison of model-predicted and experimental spinline diameter profiles for trial 4 from Table 5.1

Furthermore, additional simulations were conducted in order to gauge the relative effects of the concentration dependence of the spinline viscosity and the occurrence of phase separation prior to the end of the air gap by varying these parameters one at a time and simultaneously. Figure 5.5 shows the results for the 413 K case of trial 4 for six different data sets as explained on the figure legend. The data sets include the experimental diameter measurements (first legend entry); the TFA predictions for a draw zone length of 0.200 m and viscosity with only a temperature dependence (second legend entry); TFA predictions for *L = 0.200 m* and viscosity as a function of concentration (third legend entry); TFA predictions for *L = 0.150 m* and viscosity as a function of concentration (fourth legend entry); TFA predictions for *L = 0.150 m* and viscosity with only a temperature dependence (fifth legend entry); and TFA predictions for *L = 0.100 m* and viscosity with only a temperature dependence (fifth legend entry). Results show that both the concentration dependence of viscosity and the occurrence of phase separation prior to the end of the air gap significantly change the comparison of the experimental and predicted diameter profiles. The data presented here suggest that both factors may be important in terms of affecting spinline viscosity and thus the spinline elongation rate throughout the draw zone. More experimentation is warranted to come to more definitive conclusions pertaining to these factors.

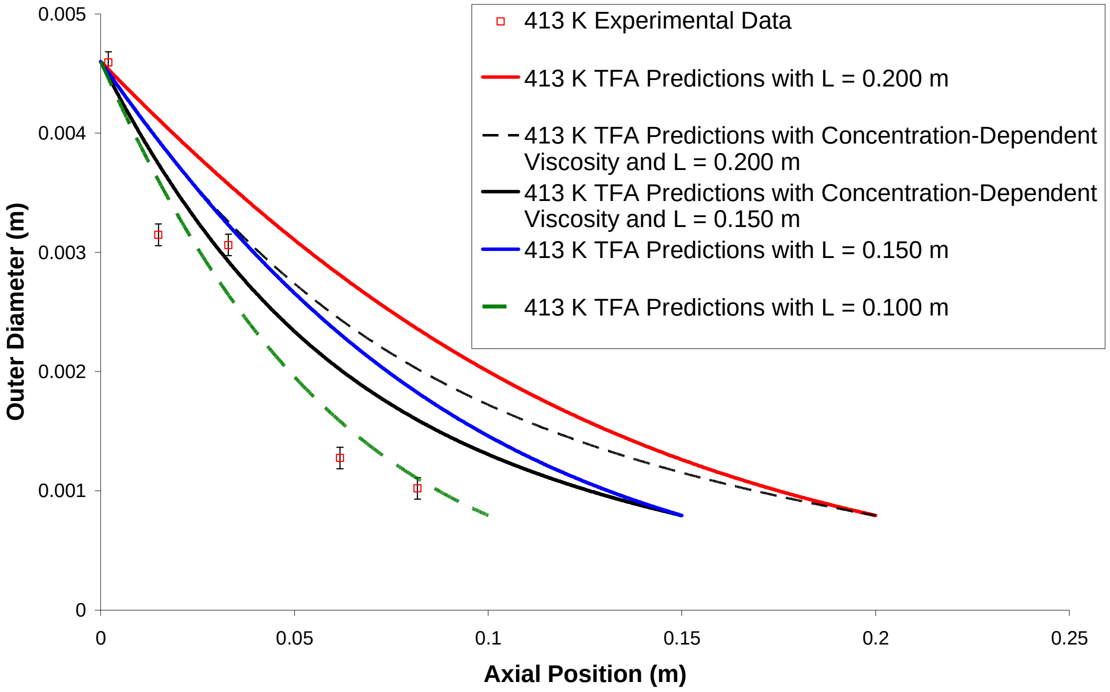

Figure 5.5 Accounting for Concentration-Dependent Viscosity and Phase Separation Prior to End of Air Gap: Comparison of Model-Predicted and Experimental Spinline Diameter Profiles for Trial 4 from Table 5.1

5.3.2 Draw Ratio Sensitivity Studies

Experimental and modified TFA model results for spinline outer diameter profiles for the draw ratio sensitivity study are presented in Figure 5.6. For this study, the draw ratio was varied by changing the take-up velocity, holding the extrusion velocity constant. To produce the tested draw ratios of 24, 29, and 34 (corresponding to trials 1–3 in Table 5.1), the velocities of both the motor-driven roller in the water quench bath and the take-up winder were varied as 25.0, 30.0, and 35.0 m/min. The extrusion velocity and all other spinning conditions for all three cases of draw ratio are listed in Tables 2.3 and 2.4.

Experimental outer diameter trends for each draw ratio show an exponential drop similar to that observed in the temperature sensitivity studies of section 5.3.1. Like the data reported in the spinning temperature sensitivity study, the modified TFA model-predicted outer diameter profiles decrease much more gradually than the experimental data trends. Furthermore, with the data obtained and the instrumental error of the videoscope, it is not possible to make well-defined quantitative comparisons between the data sets for different draw ratios. As with the temperature sensitivity study data in section 5.3.1, the differences between the modified TFA diameter predictions for the different draw ratios used here, chiefly more draw-down early in the spinline for higher draw ratios, fall within the instrumental error of the videoscope.

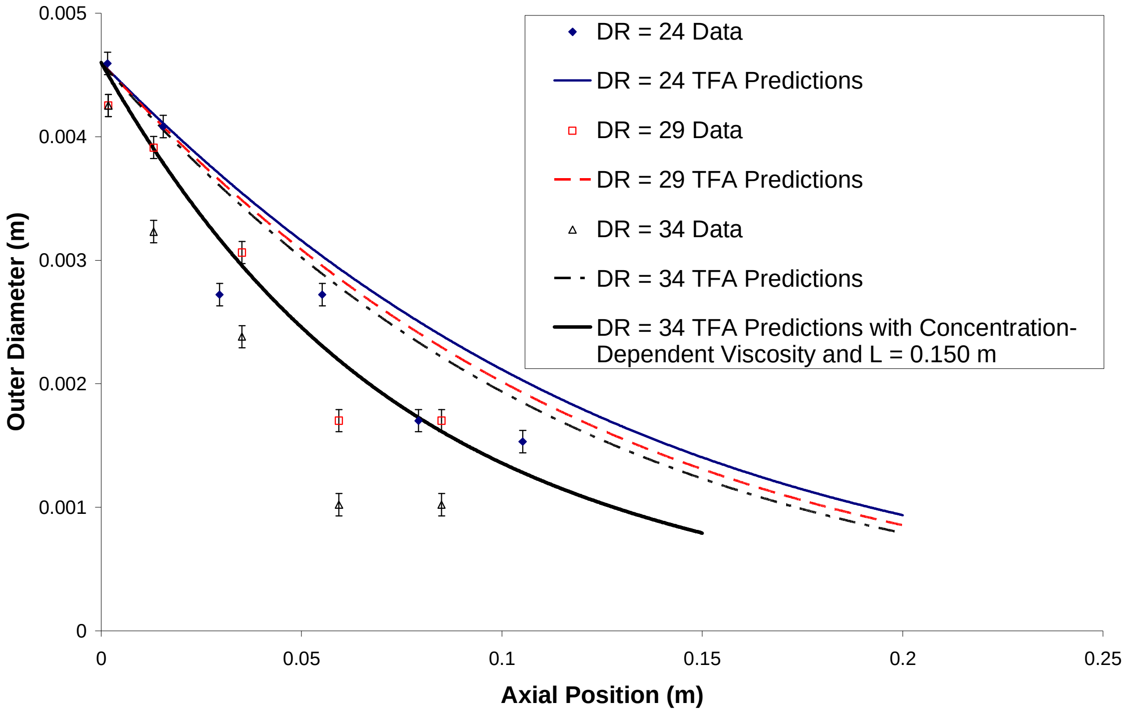

Figure 5.6 Draw Ratio Sensitivity of Spinline Diameter Profile for Trials 1, 2, and 3 from Table 5.1

Justification for the discrepancy in the experimental and model-predicted diameter profiles in Figure 5.6 is analogous to that for the temperature sensitivity studies in section 5.3.1. Included in Figure 5.6 is the predicted diameter profile for a simulation of the 34 draw ratio case (trial 3 in Table 5.1) in which the concentration dependence of spinline viscosity is included and the end of the draw zone is set as 0.150 m. As for the 413 K spinning case in section 5.3.1, the predicted diameter profile for this case compares more reasonably to the corresponding experimental diameter profile.

5.3.3 Core Gas Flow Rate Sensitivity Studies

Experimental and modified TFA model results for spinline outer diameter profiles for the core gas flow rate sensitivity study are presented in Figure 5.7 (corresponding to trials 4–6 in

Table 5.1). For this study, the core gas flow rate was varied using the mass flow controller as discussed in section 4.2.1, with the volumetric flow rates of 1.00, 3.00, and 5.00 SCCM used here representative of the respective constant core gas mass flow rates resulting from the calculation with the ideal gas law and conditions of standard temperature and pressure as given in Appendix A. All other spinning conditions for the core gas flow sensitivity study in this section are listed in Tables 2.3 and 2.4.

Experimental outer diameter trends for each core gas flow rate drop exponentially analogous to the data given in sections 5.3.1 and 5.3.2. As in sections 5.3.1 and 5.3.2, the modified TFA model-predicted outer diameter profiles decrease much more gradually than the experimental data. Furthermore, with the data obtained and the instrumental error of the videoscope, it is not possible to detect the difference between the data sets for the different core gas flow rates used here.

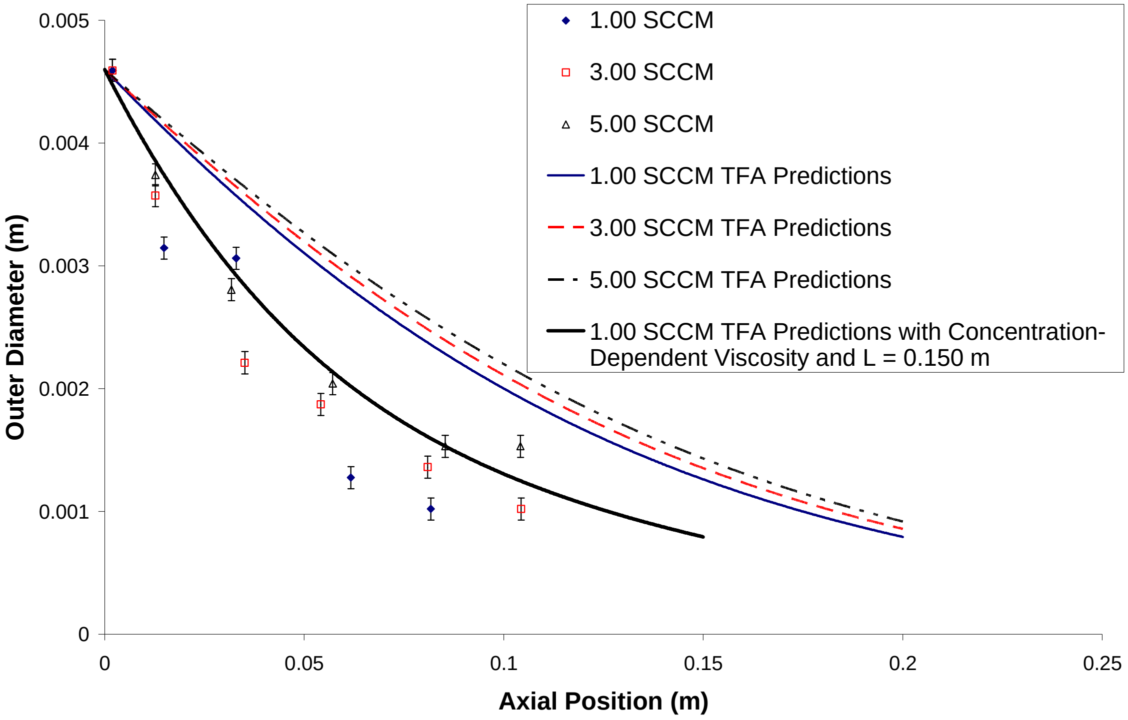

Figure 5.7 Core Gas Flow Rate Sensitivity of Spinline Diameter Profile for Trials 4, 5, and 6 from Table 5.1

Moreover, the predicted diameter profile for a simulation of the 1.00 SCCM case including the concentration dependence of viscosity and a shortened draw zone length is included in Figure 5.7. As for the temperature and draw ratio sensitivity studies in sections 5.3.1 and 5.3.2, the result for this predicted diameter profile compares reasonably to the observed experimental diameter profile for this case, which actually has spinning conditions identical to those for the 413 K spinning case shown in Figure 5.4.

5.3.4 Air Gap Length Sensitivity Studies

Experimental and modified TFA model results for spinline outer diameter profiles for the air gap length sensitivity study are presented in Figure 5.8. For this study, 0.100 and 0.200 ± 0.005 m air gap lengths were used (corresponding to trials 7 and 4 in Table 5.1). All other spinning conditions for the air gap length sensitivity study in this section are listed in Tables 2.3 and 2.4.

Experimental outer diameter trends show the exponential drop and the increased extent of draw-down early in the spinline as compared to the modified TFA model-predicted diameters as discussed in the preceding sections. Like the previous data sets, with the data obtained and the instrumental error of the videoscope, it is difficult to make well-defined quantitative comparisons between the data sets for the two air gap lengths; however, as shown by comparison of the modified TFA model predictions for the two air gap lengths in Figure 5.8, the shorter air gap requires the spinline to reach the take-up velocity in half the distance. Therefore, with all other spinning conditions the same for the two cases as given by the conditions in Tables 2.3 and 2.4, the final value of the outer radius must be reached earlier for the shorter air gap length, and there is a stronger predicted extent of attenuation for a given axial position. The experimental data qualitatively agree with this trend.

To address the modified TFA's under-prediction of the rate of fiber attenuation, simulations incorporating the concentration dependence of spinline viscosity and a draw zone length of 0.150 m were performed. The result is equivalent to that presented above for the core gas flow rate sensitivity study of Figure 5.7 and the temperature sensitivity study of Figure 5.4. In accordance with results presented for the temperature, draw ratio, and core gas flow rate sensitivity studies in the preceding sections, reasonable comparison between experimental and model results for the spinline diameter profile and an experimental air gap length of 0.200 ± 0.005 m are obtained by incorporating the concentration dependence of the spinline viscosity and the shortened draw zone length.

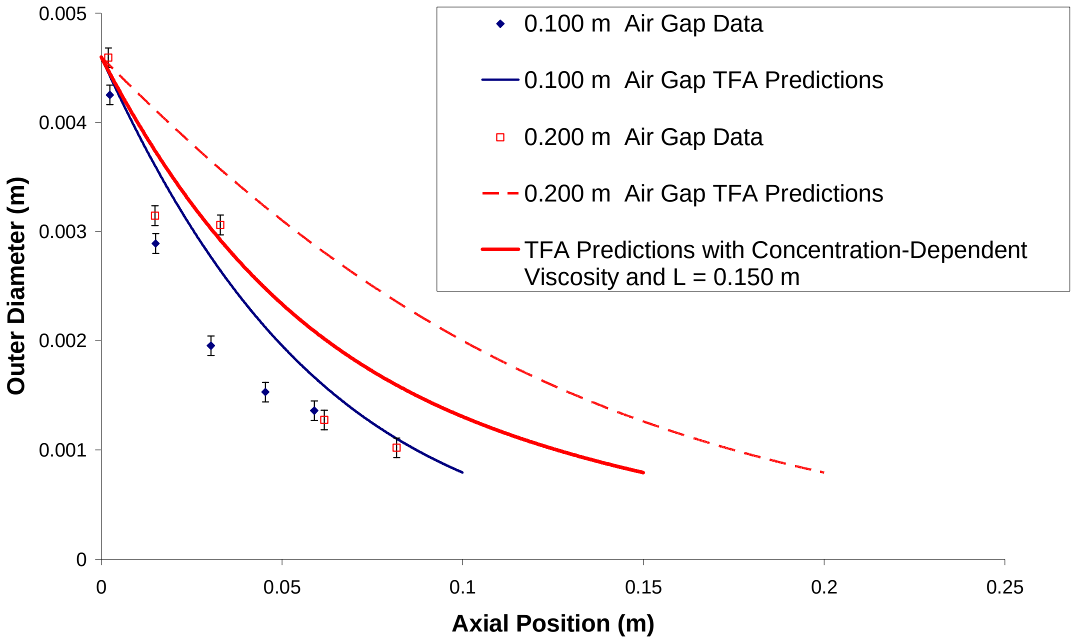

Figure 5.8 Air Gap Length Sensitivity of Spinline Diameter Profile for Trials 7 and 4 from Table 5.1

5.4 Spinline Axial Velocity Profiles

Spinline axial velocity measurements were performed for model validation using the same sensitivity studies as the outer diameter measurements discussed in section 5.3: effect of spinning temperature; effect of draw ratio; effect of core gas flow rate; and effect of air gap length. Because the discussion of the velocity profiles and the comparison of experimental and model predicted values follows the same rationale as the spinline diameter sensitivity studies, results for all the sensitivity studies for the axial velocity are presented here together in one section with minimal discussion. More details are given in the spinline diameter discussions of section 5.3 and in the summary presented in section 5.5.

Figure 5.9 shows representative spinline images used for obtaining the spinline axial velocity, with the polymer powder appearing as white streaks on the observed spinline image. As explained in section 4.2.2, the spinline velocity was calculated by observing the movement of polymer powder bits thrown at the spinline during video data collection. The velocity corresponding to the topmost spinline portion for a given set of video images is calculated by observing the distance that a bit of polymer powder moves between consecutive frames, which are 0.03 seconds apart.

Experimental error confuses the confidence level possessed by the velocity measurements using the videoscope—difficulty in focusing on the fast-moving polymer powder bits thrown at the spinline during video footage collection was a major stumbling block complicated by the difficulty in adjusting the supplemental lighting for proper image brightness. Selecting and tracking polymer powder markers between consecutive frames proved to be a chore. The margin of error for the measured velocities was propagated conservatively with an estimated 700 μm error on the measured distance moved by the powder marker between consecutive frames; this corresponds to four tick marks in the video images obtained. Representative error propagation is shown in Appendix A.

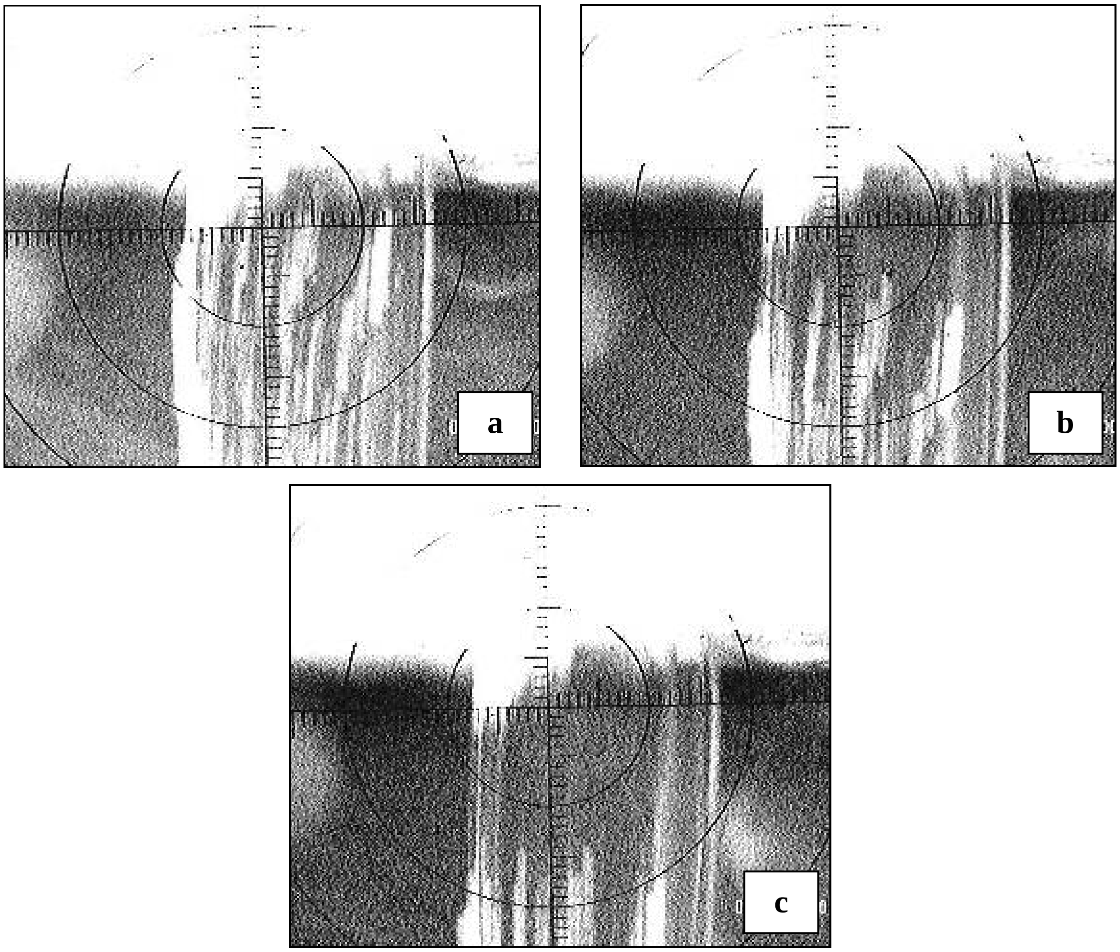

Figure 5.9 Spinline Videoscope Images for Determining Axial Velocity: (a)–(c) are each 0.03 seconds apart

Predicted spinline axial velocity profiles and measurements for the spinning temperature sensitivity study experiments appear in the semi-log plot shown in Figure 5.10. Experimental data shows that the velocity increases much more quickly than the modified TFA predictions indicate for any of the spinning temperatures, even with the conservative estimate of the error on the measured velocity values.

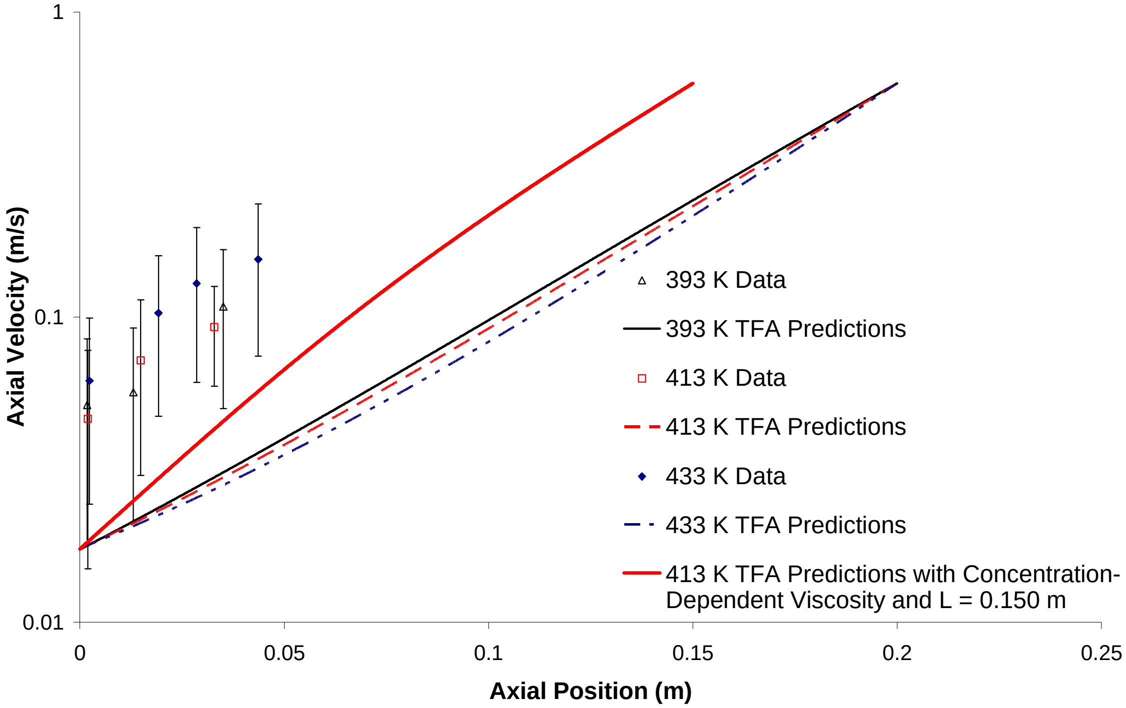

Figure 5.10 Temperature Sensitivity of Spinline Axial Velocity Profile for Trials 3, 4, and 8 from Table 5.1

Furthermore, as for the outer diameter measurements in section 5.3.1, differences in measured velocities for the three cases of spinning temperature are undetectable given the propagated error values for the velocity measurements. Due to the variation in spinline temperature profiles shown in Figure 3.3, the three spinning temperature cases produce slightly different predicted spinline viscosity profiles, with higher spinning temperatures resulting in a slightly slower predicted rate of change in viscosity, and thus mildly slower acceleration to the final spinline velocity value at the end of the draw zone.

Included in Figure 5.10 is the modified TFA model-predicted velocity profile for the 413 K spinning case with a concentration-dependent spinline viscosity and a draw zone length of 0.150 m. Results for this case are closer to the measured values for this temperature, but even with the presumed conservative estimate of the experimental error, values do not agree. More experimental data is necessary to make a meaningful comparison to the model-predicted axial velocities presented here.

Axial velocity profile results for the draw ratio, core gas flow rate, and air gap length sensitivity checks appear in semi-log form in Figures 5.11 through 5.13. Results and comparison of the experimental data and model-predicted values are analogous to that for the temperature sensitivity results shown in Figure 5.10. In addition, as stated above, the spinline diameter sensitivity studies of section 5.3 contain more in-depth discussion of the reasoning behind the incorporation of the concentration dependence of the spinline viscosity and a shortened draw zone length for the additional modified TFA simulations.

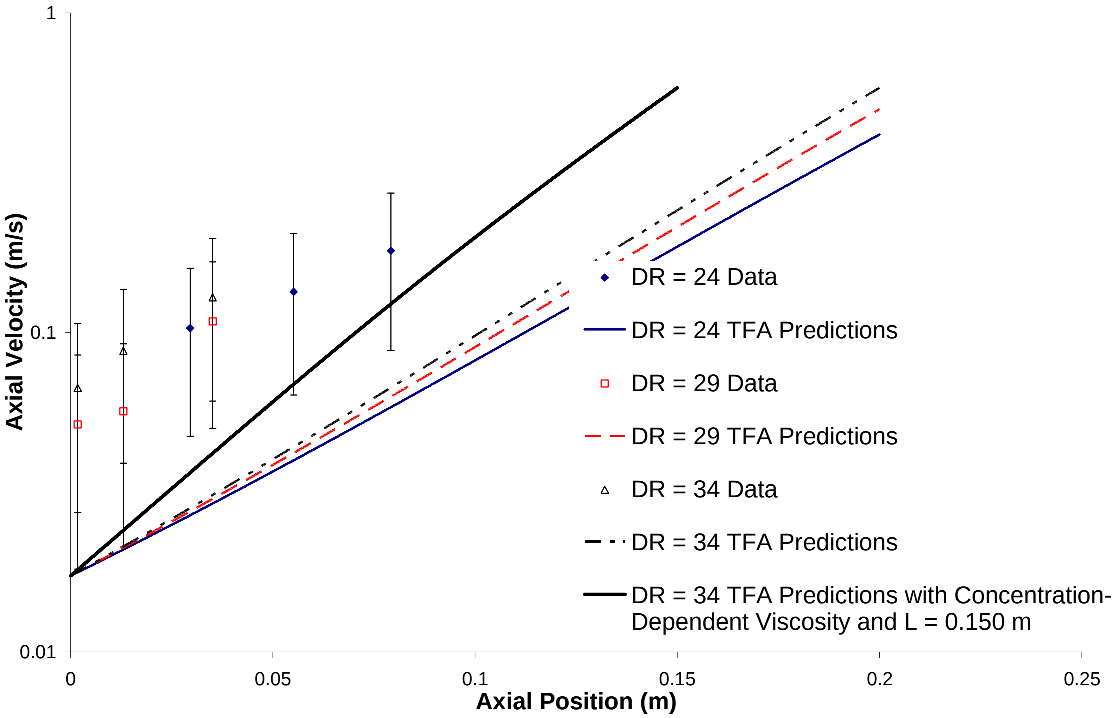

Figure 5.11 Draw Ratio Sensitivity of Spinline Axial Velocity Profile for Trials 1, 2, and 3 from Table 5.1

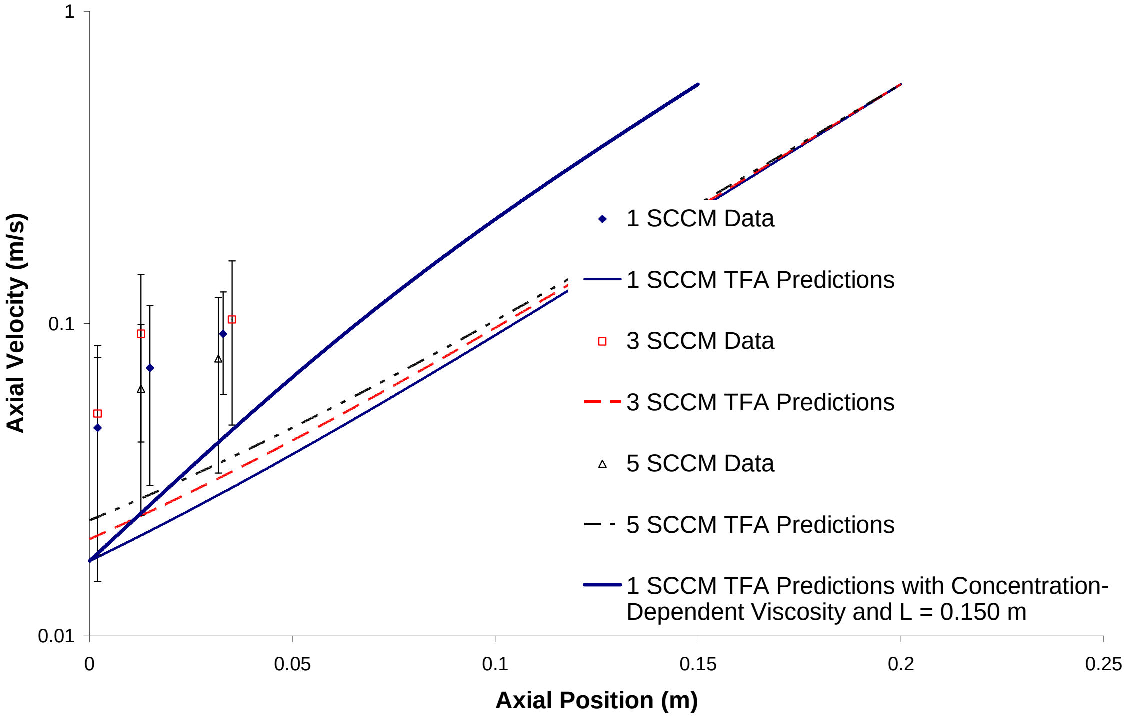

Figure 5.12 Core Flow Rate Sensitivity of Spinline Axial Velocity Profile for Trials 4, 5, and 6 from Table 5.1

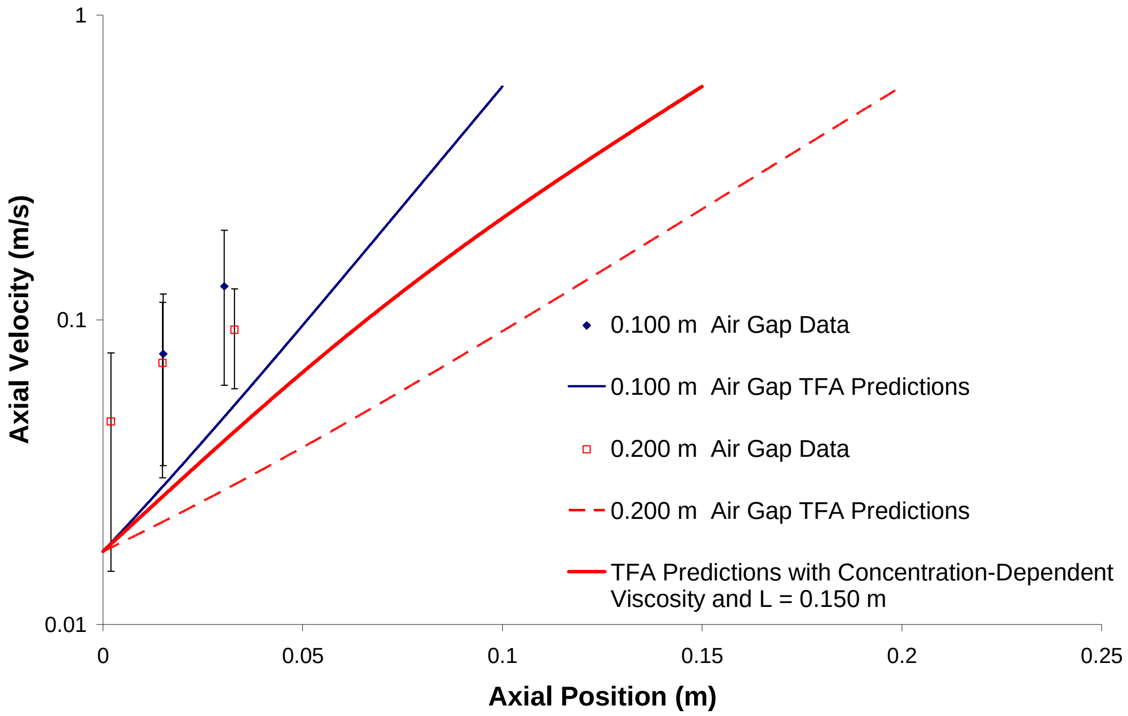

Figure 5.13 Air Gap Length Sensitivity of Spinline Axial Velocity Profile for Trials 7 and 4 from Table 5.1

5.5 Summary and Interpretation of the Spinline Diameter and Velocity Sensitivity Studies

Interpretation of the discrepancy between experimental and model-predicted results presented in the above sensitivity studies for spinning temperature, draw ratio, core gas flow rate, and air gap length was based on questioning the correlation for spinline viscosity as a function of axial position. The rates of elongation observed experimentally are much higher than those predicted by the modified TFA for fiber spinning derived in Chapters 2 and 3: there are much more drastic rates of change in the measured spinline outer diameter and axial velocity profiles along the draw zone.

The evolution of the axial velocity profile, established through the momentum balance in equation (2.30), is directly dependent on the system viscosity. The outer diameter is dictated by continuity and the evolution of both the spinline axial velocity and core gas density profiles, both of which depend on system viscosity. Thus, to produce the drastic rates of change observed experimentally for the diameter and velocity profiles, the rate of change in system viscosity must also be more drastic than that modeled using only a temperature dependence. Incorporating the change in viscosity with concentration is relevant to the work presented here, as the diluent evaporation can produce polymer-concentrated regions in the spinline cross-section which may increase overall spinline viscosity significantly.

In addition, the experimental results for the temperature sensitivity studies in particular suggest that the spinline undergoes phase separation prior to the end of the air gap. Combining this result with the concentration dependence of viscosity for the modified TFA simulations provides a more reasonable prediction of the spinline diameter and velocity profiles. However, methodical characterization of the PE–dodecanol system viscosity as a function of both concentration and temperature is necessary to model these variables rigorously. The results presented here indicate that a relatively simple analysis with a generalized viscosity concentration dependence and limited experimental viscosity data can be used to estimate these effects quickly.

Results for the experimental axial velocity profiles indicate a large disagreement with model-predicted values, even with a presumably conservative estimate of the experimental error and changing the spinline viscosity profile through shortening the draw zone length in the simulations and/or including the concentration dependence of viscosity. One source of error in the measurements may be in the calculation of the velocity for a given axial position: computed using the distance a polymer powder clump moves in a given time, this is really an average velocity value over a given spinline distance and not the velocity at a given axial position. If velocity gradients are large enough, this may factor in to the velocity calculation and make measured values reported for a given axial position incorrectly high.

In addition, another source of error in the experimental technique may be due to the method for distributing the polymer powder onto the spinline: a spatula full of the powder was thrown at the spinline generally with an arcing motion. If the powder fell onto the spinline and traveled via slip after completing a trajectory that gave it a positive axial velocity component in the positive axial direction (in the positive z-direction), its measured velocity could be greater than that of the spinline. These are factors that warrant additional experiments. Furthermore, as discussed in Appendix A, calculation of the Froude number Fr relative to the Reynolds number

Re indicates that gravity effects could be substantial for these hollow fiber membrane spins; this could create higher elongation rates throughout the draw zone than those predicted by the modified TFA that neglects gravity as reported here. This warrants more simulation work to examine the effects of gravity.

5.6 Membrane Extent of Anisotropy and Final OD/ID Ratio Results

The membrane extent of anisotropy was determined for PE–dodecanol hollow fibers spun for all of the sensitivity studies discussed above for the spinline diameter and axial velocity measurements. Fibers were prepared for examination of the microstructure via scanning electron microscopy (SEM) using the procedure detailed in section 4.2.1.

Two fiber cross-section samples for each of the experiments listed in Table 5.1 were examined via SEM. For each sample, several images of different locations in the cross-section at different magnifications were obtained and saved digitally in *.jpeg* file format. A summary of the routine for each sample is given in Table 5.2; the reported magnifications correspond to the original images viewed on-screen with the SEM setup.

Table 5.2 SEM Images Collected for PE–Dodecanol Samples

Number of Images Per Sample	Description	Magnification
1	Entire cross-section	70x or 100x
1	Fiber wall (inner to outer radius)	300x or 350x
3–5	Cross-section near inner radius	4000x, 5000x, and 25000x; sometimes 3000x and 3500x
3–5	Cross-section near outer radius	4000x, 5000x, and 25000x; sometimes 3000x and 3500x
1	Boundary of the anisotropic region near the outer radius	15000x
1	Region less than 20 μm from the boundary toward the outer radius	25000x
1	Region less than 20 μm from the boundary toward the inner radius	25000x

Examination of the cross-section near the outer radius shows a definite change in structure. The PE–dodecanol samples examined here were characterized in terms of the thickness of the region containing a pore size gradient. This is assumed to correspond to the thickness of the concentration boundary layer as a percentage of the wall thickness, or extent of anisotropy predicted by the model developed in Chapter 3. The SEM digital image files were examined using Image-Pro Plus (version 4.5.1.22, 1998–2002), which allows the user to specify a spatial calibration based on the scale bar for a given SEM. Measurements are then obtained using the mouse to click and drag a line to cover the region to be quantified. Values of the outer diameter, inner diameter, wall thickness, and thickness of the anisotropic region near the outer radius were obtained for all samples. Reported measurements for all of these quantities are the average of five measurements for a given sample; except where noted, the extent of anisotropy measurements are the average of results from two samples, with two images analyzed for each sample.

Representative SEMs for trial 5 in Table 5.1 appear in Figures 5.14 through 5.19; SEMs from samples for all other Table 5.1 experiments are given in Appendix A. Figure 5.14 of the entire fiber cross-section was used for the measurements of fiber outer and inner diameters and wall thickness. Figure 5.15 shows the entire fiber wall cross-section for the portion of the cross-section examined for anisotropy. Figure 5.16 focuses on the cross-section near the fiber outer radius and is an example of an image used to measure the width of the anisotropic region, which exhibits a pore size gradient in the radial direction. In Figure 5.16, the boundary of the anisotropic region is outlined with a box; this defines the region represented in the SEM of Figure 5.17. Figures 5.18 and 5.19 represent areas inside and outside the anisotropic region, respectively: Figure 5.19 is located toward the fiber inner wall within 10 μm of the anisotropic boundary depicted in Figure 5.17, and the larger average pore size in this region as compared to Figure 5.18 exemplifies the definition of the anisotropic region in these samples. Pores are on average much smaller in the anisotropic region near the outer radius, resulting from diluent evaporation in this region in the air gap during spinning. This creates the concentration gradients modeled using the boundary layer analysis discussed in Chapter 3, and the concentration gradients present at the time of phase separation create pore size gradients as expected from the results of kinetics studies of membrane structure development [6-9].

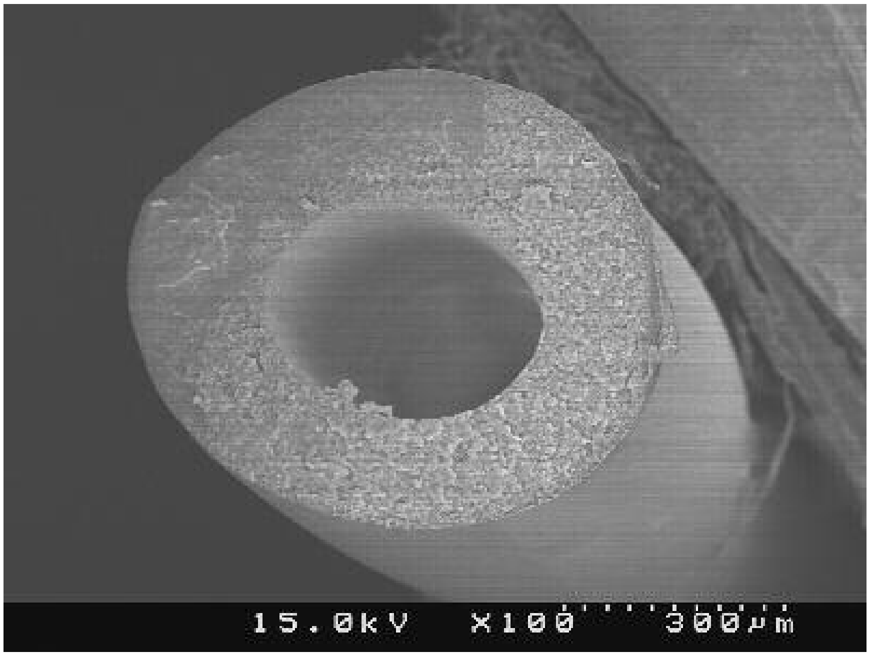

Figure 5.14 SEM of Fiber Cross-Section from Trial 5 in Table 5.1

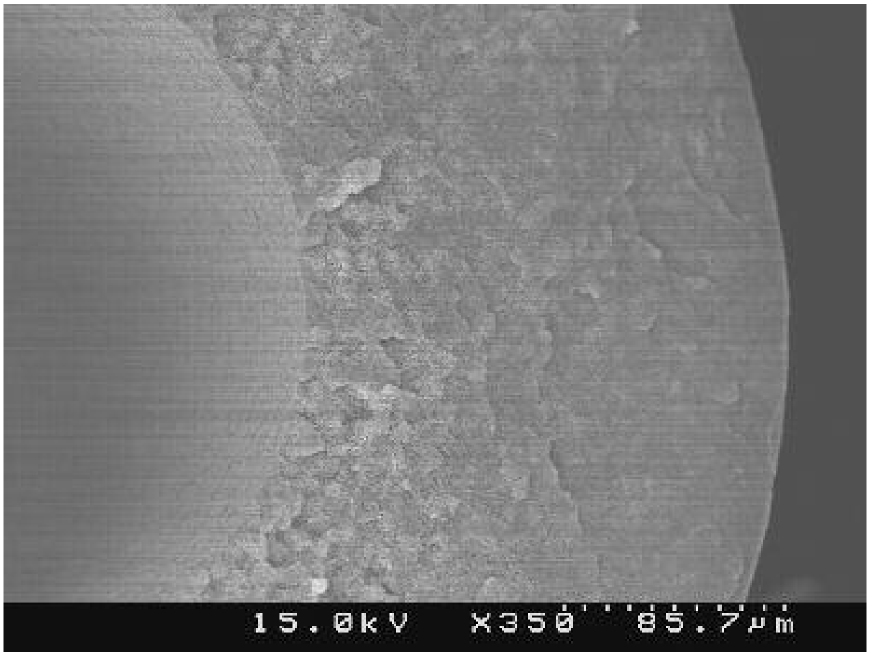

Figure 5.15 SEM of Cross-Section of Fiber Wall from Trial 5 in Table 5.1

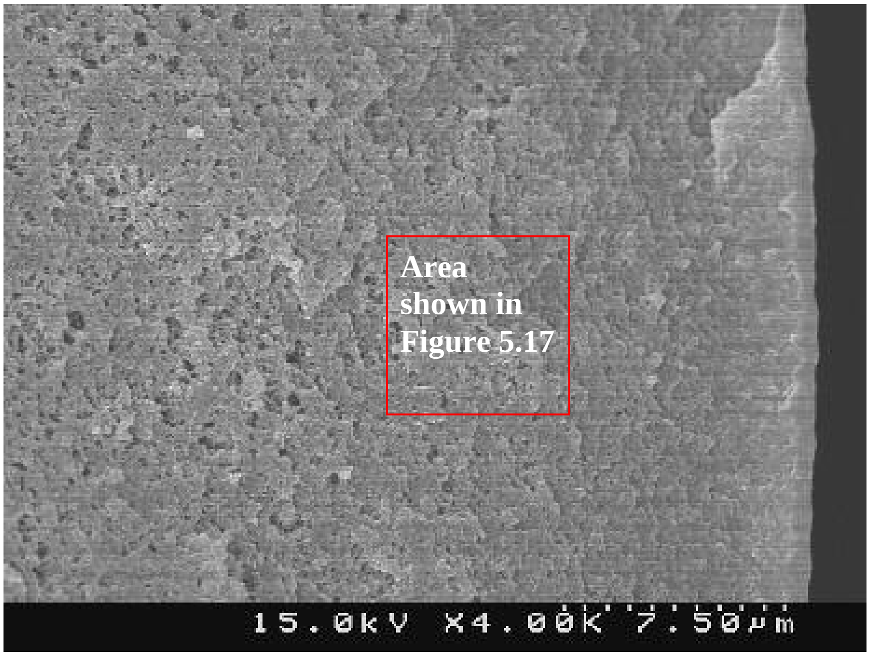

Figure 5.16 SEM of Cross-Section of Fiber Wall Showing Anisotropy Adjacent to Fiber Outer Radius at Right of Image: Boxed area is shown in Figure 5.17

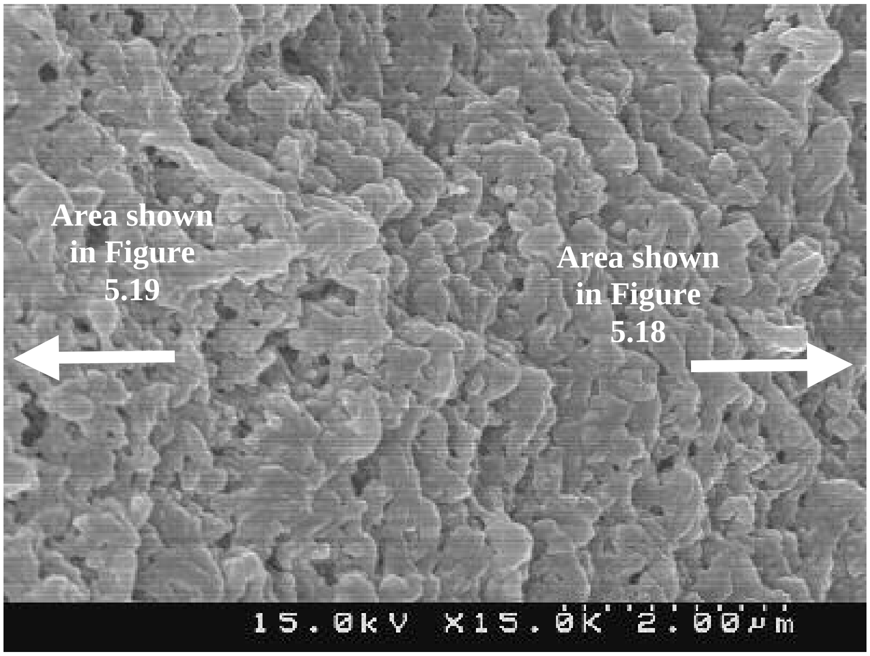

Figure 5.17 SEM of Cross-Section of Fiber Showing the Boundary of the Anisotropic Region near the Outer Radius

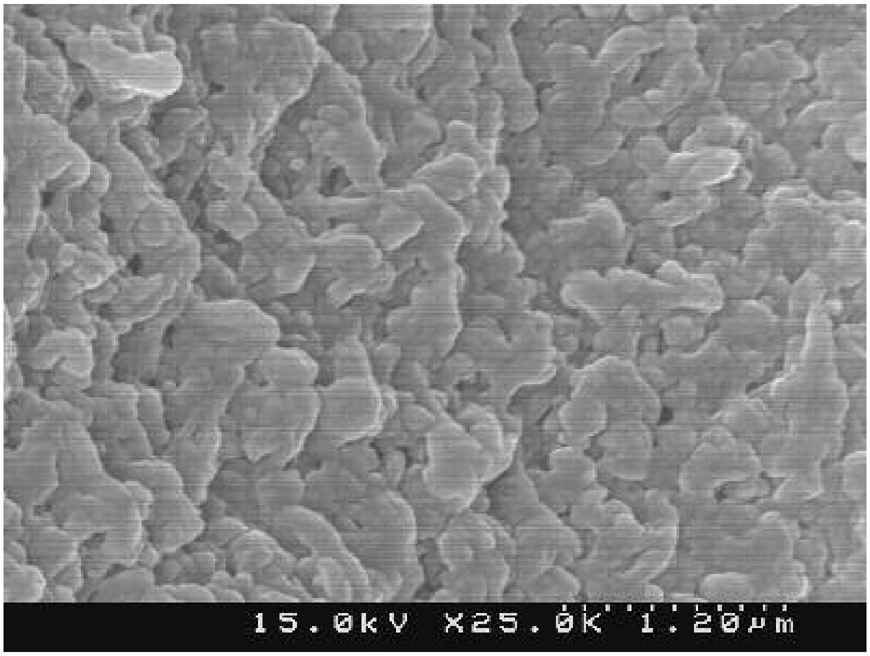

Figure 5.18 SEM of Cross-Section of Fiber Showing the Microstructure in the Anisotropic Region near the Outer Radius

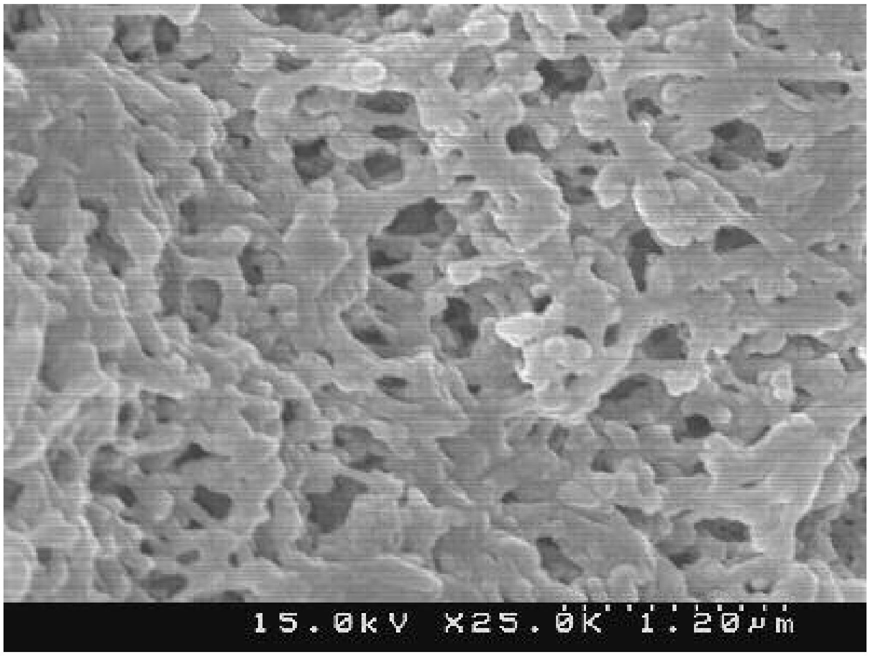

Figure 5.19 SEM of Cross-Section Outside of the Anisotropic Region (within 10 μm of the Anisotropic Boundary Defined by Figures 5.16 and 5.17)

From the images shown in Figures 5.13 to 5.19 and the additional images of the region near the outer radius obtained at additional SEM magnifications and for a second sample from trial 5, the average measured extent of anisotropy is 7.4 ± 0.6 %. Results for all other trials in Table 5.1 were obtained in a similar fashion; data for all trials are listed in Tables 5.3 (diameters and wall thicknesses) and 5.4 (membrane extents of anisotropy), categorized by sensitivity study. Errors in each quantity were calculated as the error in the average using the formula in equation (5.2), where SD is the standard deviation of the values, and N is the number of samples.

$$Error = \frac{SD}{\sqrt{N}} \qquad (5.2)$$

Results in Table 5.3 for the measured diameters are used to calculate the fiber's ratio of outer to inner diameter, OD/ID, propagating the error in this quantity using the errors in the measured outer and inner diameters (sample calculations are given in Appendix A). Also listed in Table 5.3 are the modified TFA model-predicted values of OD/ID at the end of the draw zone. For the case of the spinning temperature sensitivity study, the final OD/ID is predicted to decrease with increasing temperature; the measured values show the expected decrease between 413 K and 433 K, but from 393 K to 413 K the fiber's measured OD/ID value is constant within the propagated error.

For the draw ratio sensitivity study, OD/ID values are predicted to be practically the same for all draw ratios; measured OD/ID values for draw ratios of 29 and 34 are the same within the propagated error. The value for a draw ratio of 24 is only 2% lower than the other cases within the margin of error; thus, these results compare well with the model-predicted values. Similarly, core gas flow rate results for OD/ID ratios show a decreasing trend with increasing core gas flow rate. This matches the model-predicted trend; moreover, the measurements are at most 4% different from the predicted values.

Finally, for the air gap length sensitivity study, the model predictions for OD/ID ratio at the end of the draw zone show only a slight (less than 1%) increase in this parameter with a longer air gap. The measurements indicate a more significant increase in OD/ID for the longer air gap; however, for both air gap lengths, the model-predicted and experimentally measured final OD/ID values are at most 13% different.

Table 5.3 SEM Measurement Results for PE-Dodecanol Fiber Cross-Sections: Diameters and Wall Thickness Values for Spinning Trials of Table 5.1

Sensitivity Study	Trial	Measured Final Outer Diameter (μm)	Predicted Final Outer Diameter (μm)	Measured Final Inner Diameter (μm)	Predicted Final Inner Diameter (μm)	Measured Final Wall Thickness (μm)	Measured Final OD/ID	Predicted Final OD/ID
Spinning Temperature	3	645 ± 8	791	206 ± 4	225	217 ± 5	3.13 ± 0.07	3.51
	4	642 ± 5	793	197 ± 8	230	217 ± 2	3.3 ± 0.1	3.44
	8	609 ± 7	794	199 ± 1	236	204 ± 3	3.06 ± 0.04	3.37
Draw Ratio	1	727 ± 10	937	244 ± 3	268	249 ± 5	2.98 ± 0.05	3.50
	2	696 ± 7	855	218 ± 6	244	237 ± 5	3.19 ± 0.09	3.51
	3	645 ± 8	791	206 ± 4	225	217 ± 5	3.13 ± 0.07	3.51
Core Gas Flow Rate	4	642 ± 5	793	197 ± 8	231	217 ± 2	3.3 ± 0.1	3.44
	5	672 ± 7	858	331 ± 4	401	175 ± 5	2.03 ± 0.03	2.14
	6	723 ± 5	918	425 ± 20	516	150 ± 3	1.70 ± 0.08	1.78
Air Gap Length	7	646 ± 10	793	224 ± 5	233	214 ± 3	2.88 ± 0.08	3.41
	4	642 ± 5	793	197 ± 8	231	217 ± 2	3.3 ± 0.1	3.44

Table 5.4 Membrane Extent of Anisotropy Results

Sensitivity Study	Spinning Parameter Value	Measured Membrane Extent of Anisotropy (%)	Predicted Membrane Extent of Anisotropy (%)	Measured vs. Predicted?
Spinning Temperature T_0	393 ± 1 K	5.7 ± 0.4	2	Both increase with increasing T_0
	413 ± 1 K	5.3 ± 0.6	2	
	433 ± 1 K	11.3 ± 0.2	3	
Draw Ratio DR	24	4.4 ± 0.5	2	Both are nearly constant within the propagated error
	29	5.6 ± 0.6	2	
	34	5.7 ± 0.4	2	
Core Gas Flow Rate w_i	1.00 SCCM	5.3 ± 0.6	2	Both increase with increasing w_i
	3.00 SCCM	7.4 ± 0.6	3	
	5.00 SCCM	11.7 ± 0.5	3	
Air Gap Length	0.100 ± 0.005 m	5.8 ± 0.2	2	Both are constant within the propagated error
	0.200 ± 0.005 m	5.3 ± 0.6	2	

The results for membrane extent of anisotropy presented in Table 5.4 show obvious quantitative discrepancy: all of the measured values are larger than the model predictions for this parameter. The closest numerical agreement appears for the case of a draw ratio of 24, and the predicted and measured extents of anisotropy are still more than 50% different. However, not accounted for when comparing the experimental and model-predicted values for the membrane extent of anisotropy is the membrane shrinkage that could result from the diluent extraction process [10-12].

Nevertheless, it is important to note that the predicted trends for all of the sensitivity studies agree with the measured trends reported in Table 5.4. For example, the spinning temperature sensitivity results show measured extents of anisotropy that are the same within error for the cases of 393 and 413 ± 1 K, and the measured extent of anisotropy for the 433 ± 1 K spinning case is higher. These measured trends agree with the model-predicted trends.

Comparable results are obtained for the draw ratio sensitivity study: measured extent of anisotropy values for the different draw ratios agree within 8%. Although the predicted values are all the same and equal to 2%, their comparison to the measured results are reasonable given the simplicity of the concentration profile analysis detailed in Chapter 3: it requires very little computational time and is straightforward to apply.

Furthermore, the core gas flow rate sensitivity studies compare favorably also. The model predicts a higher extent of anisotropy as the core flow rate increases from 1.00 to 3.00 SCCM, with the same value predicted for 5.00 SCCM as for 3.00; the measured values all increase with increasing core flow rate. Thus, the model predictions apparently are not sensitive enough to the core flow rate, but the observed increase in extent of anisotropy is predicted for part of the examined range in the study.

Lastly, for the air gap length sensitivity studies, the model predicts that membrane extent of anisotropy is constant for the two air gaps considered. The experimental values agree with this prediction: the measured extents of anisotropy for the 0.100 and 0.200 ± 0.005 m cases are the same within propagated error.

5.7 References

1. J.R. Fried, Polymer Science and Technology, Prentice Hall, Englewood Cliffs, NJ, 1995.
2. G.G. Lipscomb, The melt hollow fiber spinning process: Steady-state behavior, sensitivity and stability, Polymers for Advanced Technologies, 5 (1994) 745-758.
3. T. Hasegawa, D.S. Martula, D.R. Lloyd, and R.T. Bonnecaze, Coalescence-induced coalescence: calculation of the velocity field, Phys. Fluids, in preparation (2000).
4. D.S. Martula, R.T. Bonnecaze, and D.R. Lloyd, The effects of viscosity on coalescence-induced coalescence, Int. J. Multiphase Flow, 29 (2003) 1265-1282.
5. G.G. Lipscomb, Personal Communication, 2004.
6. A. Laxminarayan, The kinetics of membrane formation via thermally induced liquid-liquid phase separation, Dissertation, The University of Texas at Austin, 1994.
7. G.B.A. Lim, S.S. Kim, Q. Ye, Y.F. Wang, and D.R. Lloyd, Microporous membrane formation via thermally-induced phase separation. IV. Effect of isotactic polypropylene crystallization kinetics on membrane structure, J. Membr. Sci., 64 (1991) 31-40.
8. K.S. McGuire, A. Laxminarayan, D.S. Martula, and D.R. Lloyd, Kinetics of droplet growth in liquid-liquid phase separation of polymer-diluent systems: model development, J. Colloid Int. Sci., 182 (1996) 46-58.
9. D.S. Martula, Coalescence-induced coalescence, Dissertation, The University of Texas at Austin, 2000.
10. S.S. Kim, Personal communication, 2000.
11. S.A. Altinkaya and B. Ozbas, Modeling of asymmetric membrane formation by dry-casting method, J. Membr. Sci., 230 (2004) 71-89.

12. R. Mahendran, R. Malaisamy, and D. Mohan, Preparation, characterization and effect of annealing on performance of cellulose acetate/sulfonated polysulfone and cellulose acetate/epoxy resin blend ultrafiltration membranes, European Polym. J., 40 (2004) 623-633.

Chapter 6. Conclusions and Recommendations

6.1 Conclusions

The goal of this research, developing the fundamental knowledge necessary to tailor the production of hollow fiber membranes, was accomplished by establishing a model describing the simultaneous heat, mass, and momentum transfer that occur during the spinning process. Model predictions of spinline variables were evaluated for sensitivity to surface tension, evaporative cooling effects, and system physical properties. Process variables and radial concentration gradients modeled as functions of axial position were linked to prediction of membrane extent of anisotropy. Conclusions from the work presented here are as follows:

1. For high-speed PET industrial melt spinning, surface tension sensitivity studies show that viscous effects due to spinline cooling dominate surface tension effects.
2. Surface tension sensitivity studies for low-speed laboratory spinning of PE–dodecanol membranes show measurable differences in the evolution of the predicted inner and outer radii, axial velocity, and core gas pressure profiles, which relates to future spinning instability studies.
3. Evaporative cooling effects were shown to affect noticeably the predicted temperature profile for PE–dodecanol membrane spinning.
4. The predicted hollow fiber membrane spinline temperature profile is sensitive to the initial spinning temperature, the air gap velocity, and the air gap length. The temperature gradient, a measure of the heat transfer rate for the spinline, is affected by the air gap air velocity and to a lesser extent by the air gap length.
5. The OD/ID ratio profile is strongly affected by changes in core gas flow rate and affected to a lesser degree by initial spinning temperature and air gap velocity.
6. The spinline axial viscous stress profile is sensitive to air gap length and also affected moderately by changes in spinning temperature, draw ratio, and air gap air velocity.
7. Membrane extent of anisotropy predictions, although 6% or less for all spinning conditions considered here, are most sensitive to initial spinning temperature, core gas

mass flow rate, air gap length, and diffusion coefficient, showing an increase in extent of anisotropy for some level of increase in these parameters.

8. Experimental results for spinline diameter and axial velocity profiles show that it is necessary to account for both the concentration and temperature dependence of spinline viscosity to obtain reasonable model predictions of diameter and velocity profiles for solution spinning. Furthermore, should phase separation occur in the air gap during spinning, its effect on spinline viscosity must also be taken into consideration.
9. Predicted and measured trends in membrane extent of anisotropy agree for all of the sensitivity studies validated experimentally: extent of anisotropy increases with increasing spinning temperature and core gas flow rate and stays approximately constant over a typical range of draw ratios and air gap lengths used for hollow fiber membrane spinning.

6.2 Recommendations for Future Work

As is the case for many applied engineering projects, the research described herein is very broad in scope: numerical simulations based on theory were developed to describe the transport phenomena of the spinning process, spinning system physical property data was collected for use with the simulations, simulations representing a range of spinning conditions were conducted, and the model predictions were compared to both in-line experimental results (fiber outer diameter and axial velocity profiles) and final hollow fiber membrane structure (extent of anisotropy and inner and outer diameters) to evaluate model applicability. The general conclusions listed in section 6.1 are significant contributions to the hollow fiber spinning community, but there are a number of pathways by which this research can be continued and expanded.

The first suggestion involves the diffusion coefficient used wth the boundary layer analysis for predicting spinline concentration gradients. As discussed in section 4.1.4, the diffusion coefficient is not constant as specified in the analysis here. This parameter actually varies in a complicated fashion with both concentration and temperature. Including the variance of the diffusion coefficient is a logical step for extending the modeling work presented here.

Moreover, some experimental efforts were undertaken in this research to obtain actual measurements of the diffusion coefficient. Mentioned in section 4.1.4 and discussed at length in Appendix A, these experiments made use of FTIR–ATR spectroscopy to monitor diluent diffusion through a thin PE–dodecanol film over time. These measurements were subject to a high level of experimental error due to difficulty with preparing the films for testing, in particular ensuring uniform film thickness and controlling the temperature during the spectroscopy procedure. Results for diffusion coefficients obtained in this work are significantly higher than diffusion coefficients predicted using the Zielinski–Duda method based on free-volume theory; this warrants more experimentation to determine the reliability of the FTIR–ATR results. Dynamic light scattering was also considered as a possible method for obtaining the diffusion coefficient as a function of concentration and temperature [1-4]; however, this was not an option due to high cost and limited equipment availability.

Per the comparison of the experimental spinline diameter and axial velocity profiles to those predicted by the modified TFA model presented here, accounting for the concentration dependence of spinline viscosity is useful for more accurately modeling solution spinning. The generalized concentration dependence of viscosity used in Chapter 5 provides an estimate of this parameter and brings model-predicted diameter and velocity profiles closer to those observed experimentally. However, additional system viscosity data is necessary to characterize fully the spinline variation with concentration. In addition, experimental data is necessary to characterize viscosity behavior expected at the occurrence of phase separation, and a more accurate means of detecting phase separation in an extruding spinline should be implemented.

Furthermore, as detailed in Appendix A, the effects of gravity may be significant for typical hollow fiber membrane spins. Not included with the simulations presented herein, the effects of gravity should be included with future modeling work to evaluate the importance of these effects in certain spinning processes.

A methodical experimental design should be used for complete validation of spinning model predictions. The sensitivity study approach used in this research provides broad estimates of expected spinning results in an efficient manner, and this approach is the easiest to apply due to the large number of spinning process variables and limitations imposed by condition sets that are non-spinnable. However, a statistically-designed experimental matrix, re-designed to exclude non-spinnable condition sets encountered during testing, is a logical approach to determining the applicability of the modified TFA spinning model. Statistical software packages, such as JMP-IN, are a starting point for the design of such a matrix of experiments.

Experimental parameters that were not methodically examined in these research efforts, but should be as part of future work, include starting solution composition (expected to affect system viscosity behavior and also membrane microstructure) and air flow conditions (velocity and temperature) in the air gap during spinning [5, 6]. Experiments have shown cross-flow cooling air to be inadequate for hollow fiber membrane spinning: resulting membranes are non-uniform in terms of membrane anisotropy [7]. Thus, additional model sensitivity studies and spinning experiments involving co- and counter-current cooling air flow in the air gap are warranted to make the efforts detailed here more complete in terms of membrane spinning, and such efforts should include a rigorous evaluation of the heat and mass transfer coefficient correlations. Relation of the predicted membrane extent of anisotropy to membrane permeability and rejection capabilities is a necessary supplement to the work presented here in terms of membrane research and development. Furthermore, application to additional spinning systems is a necessary step for complete modified TFA model validation and evaluation of model applicability.

The reported experimental measurements of membrane extent of anisotropy in Chapter 5 are consistently higher than model predictions, while the observed trends in this quantity with spinning parameter variation follow the model predictions. The effects of the sample preparation process for scanning electron microscopy (SEM), namely diluent removal by extraction and elimination of the extractant via evaporation, were not considered in the efforts detailed here. However, membrane shrinkage during extraction could affect the observed hollow fiber membrane macro- and microstructure, and this warrants further study of the effects of the extraction process on membrane structure [8].

As detailed in Appendix A, the infrared (IR) camera evaluated in this research cannot be used to measure accurately the PE–dodecanol hollow fiber spinline temperature due to the IR transparency properties of PE, which are exaggerated by typically low spinline diameter. An alternate system of isotactic polypropylene (iPP) in diphenyl ether (DPE) was considered for fiber spinning, but iPP presents IR transparency issues similar to those of PE. One possible solution is fitting the IR camera with a narrow bandpass filter at a 3.43 μm wavelength corresponding to polyethylene's strong absorption band due to C–H stretch. This action would significantly reduce the transmissive effects that hindered the spinline temperature measurement in this research. However, the spinning temperatures used for typical hollow fiber membrane fabrication may be too low to be detected when using such a filter, and careful evaluation is required before purchasing such an IR camera modification [9, 10].

An additional possibility for application of the modeling efforts presented here is extension to spinning instability studies, especially as related to the incorporation of surface tension in Chapter 2. Previous work has linked the occurrence of spinning instabilities such as draw resonance with the strength of surface tension forces relative to viscous forces for particular spinning operations. The results presented in Chapter 2 show that surface tension affects the evolution of spinline variable profiles, such as the outer diameter profile, during spinning. Depending on the susceptibility of a spinning system to disturbances that can disrupt flow during spinning, the differences in the rates of change in spinline variables brought on by different surface tension values may be important factors in characterizing spinning stability [11, 12].

A long-term goal of the modeling efforts described in this research is extension of the prediction of concentration gradients and temperature profiles during spinning to predict hollow fiber membrane microstructure in detail. Application of a model to forecast membrane average pore size and pore size distribution as functions of spinning parameters, and thus eliminating the largely trial-and-error approach that makes membrane development efforts so costly and time-consuming, is the goal. To begin the development of such a model, the modified TFA from this research should be expanded to include phase separation effects on the evolution of spinline concentration and temperature profiles. Phase separation was considered briefly in Chapter 5 in terms of its relevance to the momentum transfer: when the spinline was visually observed to become cloudy in the air gap, the modeled draw zone was shortened in the simulations to halt elongation before water bath entry due to the exponential viscosity increase expected to accompany phase separation. This produced more accurate predictions of the spinline diameter and axial velocity profiles for the spins considered here.

In-depth inclusion of phase separation effects on heat and mass transfer, and thus consideration of the concentration and temperature profiles that evolve after phase separation occurs, requires examining the effects of phase separation on system material properties. For example, if thermal conductivities of pure polymer and diluent are not significantly different at the temperatures typically present after phase separation occurs, energy conduction through the phase-separated mixture can be modeled in essentially the same way as for the homogeneous spinning solution. In terms of mass transfer, for a phase-separated mixture, a true diffusion coefficient no longer exists in the accepted sense of this term; however, a representative transport parameter could be established as an “apparent” diffusion coefficient to relate movement of one species relative to the other phase(s) as affected by interactions among the species that occur as a result of such movement [13]. Measurement of the apparent diffusion coefficient for a phase-separated polymer–diluent system can be done using static light scattering [14]; representative measurements for the PE–dodecanol system are presented in Appendix A. Detailed study of the transport through phase-separated systems is related to droplet kinetics studies conducted for phase-separated membrane formation systems and the interaction of the different phases in a phase-separated mixture [15-22].

In summary, the modified TFA for fiber spinning, including the prediction of spinline concentration gradients via a boundary layer analysis, was developed herein to include the effects of evaporative cooling and surface tension and an estimate of the concentration dependence of spinline viscosity. The model requires little computational time and can be applied in a straightforward fashion to any spinning system for which process conditions and physical properties are known. Encouraging comparison of model predictions with experimental diameter profiles and membrane extents of anisotropy for high-temperature, non-isothermal solution spinning of hollow fibers were obtained in these efforts. This indicates that the model developed in this research is a significant contribution to the fiber spinning community. As such, these efforts are an important precursor to development of a widely applicable model for predicting hollow fiber membrane microstructure, an important step toward accelerating the rate of membrane optimization and development.

6.3 References

1. G.D.J. Phillies, Probe diffusion in polymer solutions, SPIE Photon Correlation Spectroscopy: Multicomponent Systems, 1430 (1991) 118-131.

2. N.C. Ford, F.E. Karasz, and J.E.M. Owen, Rayleigh scattering from polystyrene solutions, Discussions of the Faraday Society, 49 (1970) 228-237.
3. B.J. Berne and R. Pecora, Dynamic Light Scattering with Applications to Chemistry, Biology, and Physics, John Wiley & Sons, New York, 1976. pages 376.
4. B. Chu, Laser Light Scattering, Academic Press, New York, 1974. pages 317.
5. S.J. Shilton, G. Bell, and J. Ferguson, The Rheology of Fiber Spinning and the Properties of Hollow-Fibre Membranes for Gas Separation, Polymer, 35 (1994) 5327-5335.
6. V. Simon, Analysis of fiber formation during air-gap wet spinning, AIChE J., 41 (1995) 1281-1294.
7. M.T. Batarseh, Formation of anisotropic hollow fiber membranes via TIPS, Dissertation, The University of Texas at Austin, 1999.
8. H. Matsuyama, M.-M. Kim, and D.R. Lloyd, Effect of extraction and drying on the structure of microporous polyethylene membranes prepared via TIPS, J. Membr. Sci., 204 (2002) 413-418.
9. K. Irani, telephone and e-mail, April 2004.
10. D. Bob, Infrared Community Forum, vol. 2004: Infrared Training Center (2004).
11. R.J. Fisher and M.M. Denn, Draw resonance in melt spinning, Applied Polymer Symposium, 27 (1975) 103-109.
12. P. Gospodinov and V. Roussinov, Nonlinear instability during the isothermal draw of optical fibers, Int. J. Multiphase Flow, 19 (1993) 1153-1158.
13. L.J. Hayes, 9-5-97 1997.
14. H. Matsuyama, S. Kudari, H. Kiyofuji, and Y. Kitamura, Kinetic studies of thermally induced phase separation in polymer–diluent system, J. Appl. Polym. Sci., 76 (2000) 1028-1036.
15. A. Laxminarayan, The kinetics of membrane formation via thermally induced liquid–liquid phase separation, Dissertation, The University of Texas at Austin, 1994.
16. G.B.A. Lim, S.S. Kim, Q. Ye, Y.F. Wang, and D.R. Lloyd, Microporous membrane formation via thermally-induced phase separation. IV. Effect of isotactic polypropylene crystallization kinetics on membrane structure, J. Membr. Sci., 64 (1991) 31-40.
17. K.S. McGuire, A. Laxminarayan, D.S. Martula, and D.R. Lloyd, Kinetics of droplet growth in liquid–liquid phase separation of polymer–diluent systems: model development, J. Colloid Int. Sci., 182 (1996) 46-58.
18. H. Matsuyama, M. Teramoto, T. Uesaka, M. Goto, and F. Nakashio, Kinetics of droplet growth in metastable region in cellulose acetate/aceton/nonsolvent system, J. Membr. Sci., 152 (1999) 227-234.
19. T. Hasegawa, D.S. Martula, D.R. Lloyd, and R.T. Bonnecaze, Coalescence-induced coalescence: calculation of the velocity field, Phys. Fluids, in preparation (2000).
20. D.S. Martula, Coalescence-induced coalescence, Dissertation, The University of Texas at Austin, 2000.
21. D.S. Martula, T. Hasegawa, D.R. Lloyd, and R.T. Bonnecaze, Coalescence-induced coalescence of inviscid droplets in a viscous fluid, J. Colloid Int. Sci., 232 (2000) 241-253.
22. D.S. Martula, R.T. Bonnecaze, and D.R. Lloyd, The effects of viscosity on coalescence-induced coalescence, Int. J. Multiphase Flow, 29 (2003) 1265-1282.

Appendix A. Miscellaneous Supplementary Material

A.1 MATLAB programs for solving the modified TFA for fiber spinning and calculating concentration gradients

A.1.1 TFA Fiber Spinning: Main Program

```
%%%%%%%%%%%%%%%%%%%%%%%%%%%%%%%%%%%%%%%%%%%
% Fiber spinning program
% PE_L_hfsolver_gam.m
% August 17, 2004
% Nonisothermal hollow fiber spinning
%
% This version includes surface tension effects and
%   requires that the draw zone length L be specified
%%%%%%%%%%%%%%%%%%%%%%%%%%%%%%%%%%%%%%%%%%%%%%%

% Specify input filenames for concentration-dependent viscosity and
%   concentration at outer radius as global variables for passing
%   easily to the equations file, PE_hf_gam_eqns_T.m
global progconcVisccalc progphidsurf

%%%%%%%%%%%%%%%%%%%%%%%%%%%%%%%%%%%%%%%%%%%%%%%
% SPECIFY OPERATING CONDITIONS AND PROCESS PARAMETERS
%%%%%%%%%%%%%%%%%%%%%%%%%%%%%%%%%%%%%%%%%%%%%%%

% T0 = initial temperature (K)
T0=413;
% v0 = initial velocity (m/s)
v0='calculated using continuity (Ro0 is specified)';
% vL = final velocity (m/s)
vL=35.0/60;
% L = draw zone length (m)
L=0.20;
% Pambient=pressure of external surrounding medium in draw zone (Pa)
Pambient=1.01325E5;
% pcore0=initial core gas gauge pressure (Pa)
pcore0=58;

%%%%%%%%%%%%%%%%%%%%%%%%%%%%%%%%%%%%%%%%%%%%%%%
% QUENCH FLUID PROPERTIES
% VALUES GIVEN HERE ARE FOR AN AIR QUENCH (AIR GAP SPINNING)
%%%%%%%%%%%%%%%%%%%%%%%%%%%%%%%%%%%%%%%%%%%%%%%
```

```
% Tq = quench fluid temperature (K)
Tq=298;
% Tq_F = quench fluid temperature (degrees F); needed for quench
%   fluid property calculations
Tq_F=1.8*(Tq-273.15)+32;
% etaq = quench fluid viscosity (Pa-s)
etaq=1.49e-4*(1.7e-3*Tq_F-1e-12*(Tq_F)^4+1.11)/10;
% kq = quench fluid thermal conductivity (W/m/K)
kq=4.134e-3*(3.79e-5*exp(0.9*log(Tq_F))+0.013)*4.1868*100;
% rhoq = quench fluid density (kg/m^3)
rhoq=(1.1383e-3)*560/(460+Tq_F)*1000;
% vq = quench fluid velocity (m/s)
vq=0.;
% Cpq = quench fluid heat capacity (J/kg/K)
Cpq=(2.8958E4+9390*(3012./Tq/sinh(3012./Tq))^2+7580*(1484/Tq/...
   cosh(1484/Tq))^2)/29;

%%%%%%%%%%%%%%%%%%%%%%%%%%%%%%%%%%%%%%%%%%%%%%%%
% SPECIFY PHYSICAL PROPERTIES AND FLOW RATES OF CORE AND CLAD
%%%%%%%%%%%%%%%%%%%%%%%%%%%%%%%%%%%%%%%%%%%%%%%%

% Md = diluent molecular weight
% rhop0 = density of polymer at T0 (kg/m^3)
% rhod0 = density of diluent at T0 (kg/m^3)
% polvolfrac0 = initial polymer volume fraction in spinning solution
% dilvolfrac0 = initial diluent volume fraction in spinning solution
% rhoo0 = clad density at z=0 (kg/m^3)
Md=186.338;
rhop0=(0.8674-6.313E-4*(T0-273.15)+0.367E-6*(T0-273.15)^2-...
   0.055E-8*(T0-273.15)^3)*1000;
rhod0=0.35818/(0.25626^(1+(1-T0/719.40)^0.29963))*Md;
polvolfrac0=0.30;
dilvolfrac0=1-polvolfrac0;
rhoo0=dilvolfrac0*rhod0+polvolfrac0*rhop0;
% rhoo = clad density = constant and equal to value at z=0 (kg/m^3)
rhoo=rhoo0;
% MWi = molecular weight of core gas (kg/kmol)
MWi=28;
% Rgas = ideal gas constant (J/kmol-K)
Rgas=8314;
% rhoi0 = initial core gas density (kg/m^3)
rhoi0=(Pambient+pcore0)*MWi/Rgas/T0;
% D = solution mutual diffusion coefficient (m^2/s), constant
% 140C:
D=7.21e-12;
```

```
% pumpRPM = pump speed (rpm)
pumpRPM=53.26;
% wo = clad mass flow rate (kg/s)
% For twin-screw extruder, melt pump gives 0.297 cc/rev
wo=pumpRPM*0.297/1E6/60*rhoo0;
% gasVFR = core gas volumetric flow rate (SCCM)
gasVFR=1.0;
% wi = core gas mass flow rate (kg/s)
wi=gasVFR*101325/60/1E6/Rgas/273.15*MWi;
% Define w_ratio for simplification of equation programming
w_ratio=(wo+wi)/wo;
%Ro0 = initial spinline outer radius (m)
Ro0=0.46e-2/2;
%If Ro0 is specified, calculate v0 using continuity
v0=1/pi/(Ro0^2)*(wo/rhoo0+wi/rhoi0);
% Ri0 = initial spinline inner radius (m), calculate from continuity
Ri0=(pi*v0*rhoi0/wi)^(-0.5);
% If v0 is specified as a boundary condition and not Ro0, calculate
%   Ro0 from continuity
%Ro0=((1+rhoi0/rhoo0*wo/wi)/pi/v0/rhoi0*wi)^0.5;
% etao0 = initial clad viscosity (Pa-s)
% Set viscosityconc = 1 to read concentration-dependent viscosity
%   values from file, progconcVisccalc.txt
viscosityconc=1;
%viscosityconc=0;
   if viscosityconc==1
      load 'c:\Group\Holly\MatLab\Excel data\progconcVisccalc.txt'
      etao0=progconcVisccalc(1);
% If viscosity has no concentration dependence (viscosityconc=0), or
%   if the dependence is unknown, use temperature dependence only
   else
      etao0=6.07e-3*exp(3.06e7/Rgas/T0);
   end
% nuo0 = initial clad kinematic viscosity (m^2/s)
nuo0=etao0/rhoo0;
% Mpn = polymer number-average molecular weight
% Cpo, Cpi = Specific heat capacities of clad and core (J/kg/K)
Mpn=43043;
Cpo=(4.325E-2*T0+17.919)/Mpn*1000*polvolfrac0+((5.1422E6-...
   5.497E4*T0+2.2872E2*T0^2)-4.0331E-1*T0^3.+2.5844E-4...
   *T0^4.)/Md*dilvolfrac0;
Cpi=(2.9105E4+8.6149E3*(1.7016E3/T0/sinh(1.7016E3/T0))^2+...
   1.0347E2*(9.0979E2/T0/cosh(9.0979E2/T0))^2)/MWi;
% gam = clad surface tension (N/m)
gam=0.030;
```

```
% Read surface concentration values (diluent concentration fractions
%   at outer radius) from file, progphidsurf.txt
load 'c:\Group\Holly\MatLab\Excel data\progphidsurf.txt'

%%%%%%%%%%%%%%%%%%%%%%%%%%%%%%%%%%%%%%%%%%%%%%%
% Specify domain (particular axial position values) for which
%   velocity, temperature, etc. data is desired
% num = number of axial position calculation points desired
%%%%%%%%%%%%%%%%%%%%%%%%%%%%%%%%%%%%%%%%%%%%%%%

num=1000;
% zspan = axial position values for which spinline variables will
%   be calculated (m)
zspan=zeros(1,num+1);
for i=1:num
   zspan(1,i+1)=zspan(1,i)+L/num;
end

%%%%%%%%%%%%%%%%%%%%%%%%%%%%%%%%%%%%%%%%%%%%%%%
% Use a secant method to calculate dvdz0 = derivative of axial
%   velocity with respect to axial position z at z=0 (1/s)
%%%%%%%%%%%%%%%%%%%%%%%%%%%%%%%%%%%%%%%%%%%%%%%

% Set options for error tolerances in ode45 execution
options2=odeset('RelTol',1E-8,'AbsTol',1E-8);
tol=0.000005; % convergence criterion for calculating dvdz0
error_vL=.2; % error in calculated vL; this is an initialization
dvdz0_1=.3370; %first guess (endpoint 1) for dvdz0 calculation
dvdz0_2=.3372; %second guess (endpoint 2) for dvdz0 calculation
newdvdz0=0; %initialization of new guess of dvdz0 to simplify loop
% Continue loop execution until dvdz0 calculation convergence is met
while abs(error_vL)>tol
   % For first iteration, calculate velocity profiles using ode45
   %   with both initial guesses of dvdz0; for all iterations
   %   thereafter, profiles are already calculated (just have to
   %   compare values of error_vL to calculate new dvdz0 guess
   %   if necessary)
   if (newdvdz0~=dvdz0_1|newdvdz0~=dvdz0_2)
      [z1,y1]=ODE45('PE_hf_gam_eqns_T',[zspan],[v0 rhoi0 T0],...
         options2,wo,wi,w_ratio,rhoo0,rhoo,etao0,v0,dvdz0_1,...
         gam,Ri0,Ro0,Cpi,Cpo,Tq,Tq_F,etaq,kq,rhoq,vq,Rgas,...
         MWi,Pambient,T0,rhod0,dilvolfrac0,vL,L,D,num);
      [z2,y2]=ODE45('PE_hf_gam_eqns_T',[zspan],[v0 rhoi0 T0],...
         options2,wo,wi,w_ratio,rhoo0,rhoo,etao0,v0,dvdz0_2,...
         gam,Ri0,Ro0,Cpi,Cpo,Tq,Tq_F,etaq,kq,rhoq,vq,Rgas,...
```

```
        MWi,Pambient,T0,rhod0,dilvolfrac0,vL,L,D,num);
elseif newdvdz0==dvdz0_1
    z1=znew;
    y1=ynew;
elseif newdvdz0==dvdz0_2
    z2=znew;
    y2=ynew;
end
% vLcalc1 = final calculated velocity with left-hand endpoint
% vLcalc2 = final velocity calculated with right-hand endpoint
[rows1 cols1]=size(y1);
vLcalc1=y1(rows1,1);
[rows2 cols2]=size(y2);
vLcalc2=y2(rows2,1);
 % error 1 = left-hand endpoint fractional error in calc'ed vL
% error 2 = right-hand endpoint fractional error in calc'ed vL

error1=(vLcalc1-vL)/vL
error2=(vLcalc2-vL)/vL

% The errors in the calculated vL values for each endpoint must
%   have opposite sign
if (error1*error2)>0
    'ERROR:  BAD INITIAL GUESSES FOR dvdz0'
    pause
end

% newdvdz0 = new guess of dvdz0 calculated using the
%   Regula-Falsi method
newdvdz0=dvdz0_2-(dvdz0_2-dvdz0_1)/(error2-error1)*error2

% Calculate the velocity profile using newdvdz0

[znew,ynew]=ODE45('PE_hf_gam_eqns_T',[zspan],[v0 rhoi0 T0],...
options2,wo,wi,w_ratio,rhoo0,rhoo,etao0,v0,newdvdz0,gam,...
Ri0,Ro0,Cpi,Cpo,Tq,Tq_F,etaq,kq,rhoq,vq,Rgas,MWi,Pambient,T0,...
rhod0,dilvolfrac0,vL,L,D,num);

% vLcalcnew = final velocity calculated with newdvdz0

[rowsnew colsnew]=size(ynew);
vLcalcnew=ynew(rowsnew,1);

% errornew = newdvdz0 fractional calc'ed error in vL
errornew=(vLcalcnew-vL)/vL
```

```
    % LHS and RHS are used to see where the sign change
    %   in the calculated error occurs:
    %      If LHS<0, sign change occurs between dvdz0_1 and newdvdz0
    %      If RHS<0, sign change occurs between newdvdz0 and dvdz0_2
    %   Use this to make a newdvdz0 calculated guess if necessary

    LHS=error1*errornew;
    RHS=errornew*error2;

    if LHS<0
       dvdz0_2=newdvdz0;
    elseif RHS<0
       dvdz0_1=newdvdz0;
    end

    % Define the error_vL as the new error to determine whether
    %   the loop will continue executing
    error_vL=errornew;

% End the while loop used to check for dvdz0 convergence
end

% Use the value of dvdz0 determined by the Regula Falsi method
%   (newdvdz0) to calculate spinline variable profiles

dvdz0calc=newdvdz0;

[z,y]=ODE45('PE_hf_gam_eqns_T',[zspan],[v0 rhoi0 T0],options2,...
    wo,wi,w_ratio,rhoo0,rhoo,etao0,v0,dvdz0calc,gam,Ri0,Ro0,Cpi,...
    Cpo,Tq,Tq_F,etaq,kq,rhoq,vq,Rgas,MWi,Pambient,T0,rhod0,...
    dilvolfrac0,vL,L,D,num);

%%%%%%%%%%%%%%%%%%%%%%%%%%%%%%%%%%%%%%%%%%%%%%%%%
% Use the calculated values of v, rhoi, and T to calculate the
%   radius, OD/ID ratio, core pressure, and axial viscous stresses
%%%%%%%%%%%%%%%%%%%%%%%%%%%%%%%%%%%%%%%%%%%%%%%%%

[rows cols]=size(y);
v=y(:,1); % axial velocity (m/s)
rhoi=y(:,2); % core gas density (kg/m^3)
T=y(:,3); % temperature (K)
TL=y(rows,3); % temperature at z=L (K)
% Size all matrices initially to speed up program operation
Ricalc=zeros(rows,1); % inner radius (m)
```

```
Rocalc=zeros(rows,1); % outer radius (m)
ODIDcalc=zeros(rows,1); % outer to inner spinline diameter ratio
pcore=zeros(rows,1); % core gas gauge pressure (Pa)
tau_zz=zeros(rows,1); % axial viscous stress (Pa)
etao=zeros(rows,1); % spinline shear viscosity (Pa-s)
nuo=zeros(rows,1); % spinline kinematic viscosity (m^2/s)
   for j=1:rows
      % Calculate inner and outer radii using continuity
      Rocalc(j)=((1+rhoi(j)*wo/rhoo/wi)*wi/pi/v(j)/rhoi(j))^0.5;
      Ricalc(j)=Rocalc(j)/((1+rhoi(j)*wo/rhoo/wi)^0.5);
      ODIDcalc(j)=Rocalc(j)/Ricalc(j);
       % Calculate core gas gauge pressure (MPa) from ideal gas law
      pcore(j)=(rhoi(j)*Rgas*T(j)/MWi-Pambient)/1E6;
      % If shear viscosity was specified with the input file
      %   progconcVisccalc.txt, use the file to define the
      %   shear viscosity values (Pa-s)
         if viscosityconc==1
            etao(j)=progconcVisccalc(j);
      % Otherwise, calculate clad shear viscosity using a
      %   temperature dependence only
         else
            etao(j)=6.07e-3*exp(3.06e7/Rgas/T(j));
         end
      % Calculate kinematic viscosity (m^2/s)
      nuo(j)=etao(j)/rhoo;
      % Calculate axial viscous stress (MPa)
      tau_zz(j)=2*etao(j)*(w_ratio/nuo(j)/3*v(j)*v(j)-w_ratio/...
         nuo(j)/3*v(j)*v0+nuo0*dvdz0calc/v0/nuo(j)*v(j)-pi/...
         nuo(j)/3/wo*gam*(Rocalc(j)+Ricalc(j)-Ro0-Ri0)*v(j))/1E6;
   end

%%%%%%%%%%%%%%%%%%%%%%%%%%%%%%%%%%%%%%%%%%%%%%
% Calculate the outer radius concentration profile by equating
%   diluent diffusive and convective fluxes at the outer radius
%%%%%%%%%%%%%%%%%%%%%%%%%%%%%%%%%%%%%%%%%%%%%%

% If Csurfcalc=0, skip surface concentration calculations (for
%   repeat runs or sensitivity studies not including concentration)
%Csurfcalc=0;
Csurfcalc=1;
if Csurfcalc==1
   % Daird = diluent diffusion coefficient in air (m^2/s), from
   %   Fuller equation, NOTE:  Pambient must be in atm
   Daird=1E-9*Tq^1.75/(Pambient/101325)/0.821*(1/29+1/Md)^0.5;
   % Eliminate the first row of the input variable arrays (have
```

```
%   known initial spinning solution concentration at z=0);
%   arrays for use with concentration calculaations are the
%   variable names with NEW appended
   for i=1:rows-1
      zNEW(i)=z(i+1);
      TNEW(i)=T(i+1);
      RoNEW(i)=Rocalc(i+1);
      vNEW(i)=v(i+1);
   end
% Calculate physical properties necessary to evaluate the
%   diffusive-convective flux equation as functions of z
   for i=1:rows-1
      % satP = vapor pressure of diluent (Pa)
      satP(i)=exp(386.78-24382./TNEW(i)-56.17*...
         log(TNEW(i))+0.043253*TNEW(i));
      % chi = polymer-diluent interaction parameter
      chi(i)=1392.8/TNEW(i)-2.9981;
      % h = heat transfer coefficient for cross-flow
      %   cooling (W/m^2/K)
      h(i)=0.42*kq/2/RoNEW(i)*(2*rhoq*vNEW(i)*RoNEW(i)...
         /etaq)^(1/3)*(1+(8*vq/vNEW(i))^2)^(1/6);
      % kc = mass transfer coefficient at outer radius (m/s)
      kc(i)=Rgas*Tq/Pambient*(rhoq*Daird/kq/Cpq)^0.5*h(i)/29;
   end
% Solve the diffusive-convective flux equation using fsolve
   % phidsurf = volume fraction of diluent at the outer radius
   % answer = used for storing phidsurf data as it's calculated
   % dphidr = derivative of diluent volume fraction with
   %   respect to radius (1/m)
   % rhodgas = diluent concentration in air adjacent to
   %   spinline outer radius (kg/m^3)
   % DiffFlux = diffusive radial flux of diluent through
   %   boundary layer (kg/m^2/s)
   % ConvFlux = convective flux of diluent at outer
   %   radius (kg/m^2/s)
options=optimset('MaxIter',4000,'MaxFunEvals',20000,'TolFun',...
   1E-10,'TolX',1E-10);
   for j=1:rows-1
      phidsurf=fsolve('FluxBCequ',[0.65],options,zNEW(j),...
         TNEW(j),RoNEW(j),vNEW(j),dilvolfrac0,D,satP(j),...
         Md,Rgas,chi(j),rhod0,rhop0,rhoo,kc(j));
      answer(j)=phidsurf;
      dphidr(j)=(answer(j)-dilvolfrac0)*(vNEW(j)/pi/D/...
         zNEW(j))^0.5;
      rhodgas(j)=satP(j)*Md/Rgas/TNEW(j)*answer(j)*...
```

```
            exp(1-answer(j)+chi(j)*(1-answer(j))^2);
         DiffFlux(j)=-1*D*rhod0/(1-answer(j)/rhoo*...
            (rhod0-rhop0))*(dphidr(j));
         ConvFlux(j)=kc(j)*rhodgas(j);
      end
   % Write calculated phidsurf output to file
   output=zeros(rows-1,6);
      for j=1:rows-1
      output(j,:)=[zNEW(j) answer(j) dphidr(j) rhodgas(j) ...
            DiffFlux(j) ConvFlux(j)];
      end
save 'c:\Group\Csurfoutput.txt' output -ascii -double -tabs
   % Write calculated physical property data to file
   propsoutput=zeros(rows-1,5);
      for j=1:rows-1
      propsoutput(j,:)=[zNEW(j) satP(j) chi(j) h(j) kc(j)];
      end
   save 'c:\Group\Propsoutput.txt' propsoutput -ascii -double -tabs
   % Save calculated phidsurf output to file including z=0 value
   phidsurfdata=zeros(rows,1);
      for j=1:rows
         if j==1
            phidsurfdata(j)=dilvolfrac0;
         else
            phidsurfdata(j)=answer(j-1);
         end
      end
   save 'c:\Group\phidsurf.txt' phidsurfdata -ascii -double -tabs
end

%%%%%%%%%%%%%%%%%%%%%%%%%%%%%%%%%%%%%%%%%%%%%%%%
% Calculate concentration gradients via the boundary layer analysis
%%%%%%%%%%%%%%%%%%%%%%%%%%%%%%%%%%%%%%%%%%%%%%%%

% If BLA=0, skip concentration gradient calculations (for repeat
%runs or sensitivity studies not including concentration)
%BLA=0;
BLA=1;
% fracs = number of radial points for calculating radial
%   concentration gradient
fracs=101;
% Size the output matrices for speeding up program
rcalc=zeros(fracs,1); % radial position
ycalc=zeros(fracs,1); % Rocalc-rcalc
gcalc=zeros(fracs,1); % Similarity variable g
```

```
etaconc=zeros(fracs,1); % Similarity variable eta
theta=zeros(fracs,1); % Dimensionless concentration
dilconcvfrac=zeros(fracs,1); % Calculated volume fraction of diluent
Cdoutput=zeros(rows-1,fracs+1); % Used for storing calc'ed
if BLA==1
   for i=1:rows-1
      Cdoutput(i,1)=z(i+1);
      for j=1:fracs
         rcalc(j)=Ricalc(i+1)+(j-1)*(Rocalc(i+1)-Ricalc(i+1))...
            /100;
         ycalc(j)=Rocalc(i+1)-rcalc(j);
         gcalc(j)=(v(i+1)/4/D/z(i+1))^0.5;
         etaconc(j)=ycalc(j)*gcalc(j);
         theta(j)=erf(etaconc(j));
         dilconcvfrac(j)=theta(j)*(dilvolfrac0-answer(i))+...
            answer(i);
         Cdoutput(i,j+1)=dilconcvfrac(j);
      end
   end
   %Write calculated concentration data to output file, Cdcalc.txt
   save 'c:\Group\Cdcalc.txt' Cdoutput -ascii -double -tabs
end

%%%%%%%%%%%%%%%%%%%%%%%%%%%%%%%%%%%%%%%%%%%%%%%%%
% Calculate concentration-dependent viscosity, area-averaged for
%   each axial position
%%%%%%%%%%%%%%%%%%%%%%%%%%%%%%%%%%%%%%%%%%%%%%%%%

% concVisc = concentration dependent viscosity at z (Pa-s)
concVisc=zeros(rows,1);
rcalc=zeros(fracs,1);
% Calculate viscosity at each axial position z
   for i=1:rows
   % Viscosity is only a function of temperature at z=0
      if i==1
         concVisc(i)=exp(-30.84)*exp(3095.6/T(i))*...
            (polvolfrac0*rhop0)^5;
   % Viscosity is a function of both concentration and...
   %   temperature at all other z
      else
         concViscsum=0;
         for j=1:fracs
            rcalc(j)=Ricalc(i)+(j-1)*(Rocalc(i)-Ricalc(i))/100;
         end
                  for j=1:fracs-1
```

```
                concViscArea(j)=((rcalc(j+1))^2-(rcalc(j))^2)*...
                    ((1-Cdoutput(i-1,j+2))*...
                rhop0)^5;
            concViscsum=concViscsum+concViscArea(j);
            end
            concVisc(i)=concViscsum/((Rocalc(i))^2-...
                (Ricalc(i))^2)*exp(-30.84)*exp(3095.6/T(i));
        end
    end
%Write calculated viscosity concentration data to output file,
%   concVisccalc.txt
    save 'c:\Group\concVisccalc.txt' concVisc -ascii -double -tabs

%%%%%%%%%%%%%%%%%%%%%%%%%%%%%%%%%%%%%%%%%%%%%%%%
% Plot final velocity, rhoi, temperature, radius, OD/ID,
%   core pressure, and stress profiles
%%%%%%%%%%%%%%%%%%%%%%%%%%%%%%%%%%%%%%%%%%%%%%%%

figure(1)
hold on
semilogy(z,v,'LineWidth',2);
title('Axial Velocity Profile');
xlabel('Distance (m)');
ylabel('Axial Velocity (m/s)');
figure(2)
hold on
plot(z,pcore,'LineWidth',2);
title('Core Gas Gauge Pressure Profile');
xlabel('Distance (m)');
ylabel('Core Gas Gauge Pressure (MPa)');
figure(3)
hold on
plot(z,rhoi,'LineWidth',2);
title('Core Gas Density Profile');
xlabel('Distance (m)');
ylabel('Core Gas Density (kg/m^3)');
figure(4)
hold on
plot(z,tau_zz,'LineWidth',2);
title('Axial Viscous Stress Profile');
xlabel('Distance (m)');
ylabel('Axial Stress (MPa)');
figure(5)
hold on
plot(z,T,'LineWidth',2);
```

```
title('Temperature Profile');
xlabel('Distance (m)');
ylabel('Temperature (K)');
figure(6)
hold on
plot(z,Ricalc,'LineWidth',2);
title('Spinline Inner Radius Profile');
xlabel('Distance (m)');
ylabel('Inner Radius (m)');
figure(7)
hold on
plot(z,Rocalc,'LineWidth',2);
title('Spinline Outer Radius Profile');
xlabel('Distance (m)');
ylabel('Outer Radius (m)');
figure(8)
hold on
plot(z,ODIDcalc,'LineWidth',2);
title('Spinline OD/ID Ratio Profile');
xlabel('Distance (m)');
ylabel('Outer to Inner Diameter Ratio, OD/ID');

%%%%%%%%%%%%%%%%%%%%%%%%%%%%%%%%%%%%%%%%%%%%%%%%%%%
% Save TFA spinline variable output data to file,
%   PELnonisoTFAHOLLOWoutput.txt
%%%%%%%%%%%%%%%%%%%%%%%%%%%%%%%%%%%%%%%%%%%%%%%%%%%

output=zeros(rows,9);
for j=1:rows
   output(j,:)=[z(j) v(j) pcore(j) rhoi(j) tau_zz(j) T(j)...
           Ricalc(j)Rocalc(j) ODIDcalc(j)];
end
save 'c:\PELnonisoTFAHOLLOWoutput.txt' output -ascii -double -tabs
```

A.1.2 TFA Fiber Spinning: Equations Program

```
%%%%%%%%%%%%%%%%%%%%%%%%%%%%%%%%%%%%%%%%%%%%%%%%%%
% PE_hf_gam_eqns_T.m
% August 17, 2004
%
% Nonisothermal hollow fiber spinning
% Equations required by ODE45
% These equations include surface tension (gam)
%%%%%%%%%%%%%%%%%%%%%%%%%%%%%%%%%%%%%%%%%%%%%%%%%%
```

```
function dydz=PE_hf_gam_eqns_T(z,y,options2,wo,wi,w_ratio,rhoo0,...
    rhoo,etao0,v0,dvdz0,gam,Ri0,Ro0,Cpi,Cpo,Tq,Tq_F,etaq,kq,rhoq,...
    vq,Rgas,MWi,Pambient,T0,rhod0,dilvolfrac0,vL,L,D,num);

% Specify input file values for concentration-dependent viscosity
%   and diluent concentration at the outer radius to be global
global progconcVisccalc progphidsurf

% Define velocity (m/s), core gas density (kg/m^3), temperature (K)
v=y(1);
rhoi=y(2);
T=y(3);

% Create integer counter for axial position step
zstep=z/L*num+1;
zcount=round(zstep);

% Set viscosityconc = 1 to use concentration-dependent viscosity
%   values read from input file, progconcVisccalc.txt
%viscconc=0;
viscconc=1;
    if viscconc==1
        etao=progconcVisccalc(zcount);
    % Otherwise, calculate etao as a function of temperature (Pa-s)
    else
        etao=6.07e-3*exp(3.06e7/Rgas/T);
    end
% nuo = Clad kinematic viscosity (m^2/s)
% nuo0 = Initial clad kinematic viscosity (m^2/s)
nuo=etao/rhoo;
nuo0=etao0/rhoo0;

% Calculate outer radius (m) using continuity
Ro=((1+rhoi*wo/rhoo/wi)*wi/pi/v/rhoi)^0.5;

% Calculate inner radius (m) using continuity
Ri=Ro/((1+rhoi*wo/rhoo/wi)^0.5);

% h = heat transfer coefficient for cross-flow cooling (W/m^2/K)
h=0.42*kq/2/Ro*(2*rhoq*v*Ro/etaq)^(1/3)*(1+(8*vq/v)^2)^(1/6);

% Specify dT/dz using the energy balance
    % To disregard evaporative cooling, set evapcool=0
    %evapcool=0;
    evapcool=1;
```

```
if evapcool==0
   dydz(3,1)=(1/(wo*Cpo+wi*Cpi))*(Tq-T)*(2*pi*Ro*h);
% Otherwise, account for evaporative cooling except at z=0
else
   if z==0
      dydz(3,1)=(1/(wo*Cpo+wi*Cpi))*(Tq-T)*(2*pi*Ro*h);
   else % Including evaporative cooling
      % Md = diluent molecular weight
      % dHvap = diluent heat of vaporization (J/kg)
      Md=186.33;
      dHvap=1.2925e8*(1.0-T0/719.4)^6.7609e-1/Md;
      % phidsurf = diluent volume fraction at outer radius
         % If file=1, take phidsurf from file
         file=1;
         %file=0;
         if file==1
            phidsurf=progphidsurf(zcount);
         % Otherwise, set phidsurf equal to some constant
         else
            phidsurf=0.40;
         end
   % Energy balance including evaporative cooling effects
   dydz(3,1)=1/(wi*Cpi+wo*Cpo)*2*pi*Ro0*(h*(Tq-T)+dHvap*...
      D*(rhod0*(phidsurf-dilvolfrac0)*(v/pi/D/z)^0.5));
   end
end
```

```
% Specify dv/dz using the momentum balance
dydz(1,1)=w_ratio/nuo/3*v*v-w_ratio/nuo/3*v*v0+nuo0*dvdz0/v0/nuo*...
   v-pi/nuo/3/wo*gam*(Ro+Ri-Ro0-Ri0)*v;

% Specify drhoi/dz using the stress balance and the ideal gas law
dydz(2,1)=(rhoi/etao)*(gam*(1/Ri+1/Ro)-(T*Rgas*rhoi/MWi-Pambient))...
   *(1+rhoo*wi/rhoi/wo)/v;
```

A.1.3 Boundary Layer Analysis: Program Determining the Concentration at the Outer Radius by Equating Diffusive and Convective Flux at the Clad–Air Quench Interface

```
%%%%%%%%%%%%%%%%%%%%%%%%%%%%%%%%%%%%%%%%%%%%
% FluxBCequ.m
% August 17, 2004
%
% Diffusive-Convective flux boundary condition used to calculate
%   diluent concentration at the outer radius
%%%%%%%%%%%%%%%%%%%%%%%%%%%%%%%%%%%%%%%%%%%%
```

```
function calcdata = fluxBCequ(params,z,T,Ro,v,phid0,D,satP,Md,...
    Rgas,chi,rhod,rhop,rhoo,kc)

% Define diluent volume fraction at outer radius
phidsurf=params(1);

% dphidr = derivative of diluent volume fraction with respect to
%   radius (1/m)
dphidr=(phidsurf-phid0)*(v/pi/D/z)^0.5;

% Combine diluent diffusive and convective flux terms to solve
%   for phidsurf
calcdata=-1*D*rhod/(1-phidsurf/rhoo*(rhod-rhop))*(dphidr)-kc*...
    satP*Md/Rgas/T*phidsurf*exp(1-phidsurf+chi*(1-phidsurf)^2);
```

A.2 Sample Calculations

Presented in this section are order-of-magnitude estimates used to justify neglecting certain terms in the TFA fiber spinning model developed in this research; the calculation used to convert the core flow rate from a volumetric value at standard temperature and pressure (STP) to a mass flow rate; and example error propagation for experimental results presented in Chapter 5.

A.2.1 Justification for Terms Neglected in Modeling Efforts

As described in Chapters 2 and 3, the TFA for fiber spinning as it is derived here neglects the effects of the following: air drag, gravity, radial convection, axial conduction, viscous dissipation, radiation, axial diffusion, and heat and mass transfer into the fiber lumen during spinning.

Air drag effects can be quantified by calculating the expected magnitude of the drag coefficient, C_D. The drag coefficient expresses the magnitude of the drag force relative to the inertial forces. Thus, deciding whether drag effects are significant involves calculating the product of the drag coefficient and the Reynolds number, *Re*; if this product is small, then viscous forces dominate drag, and drag can be neglected. The drag coefficient for fiber spinning can be calculated with the general correlation given by equation (A.1). In this relationship, ρ_q and η_q are the air density and viscosity, respectively; $\bar{v}$ is the fiber axial velocity; and R_o is the spinline outer radius [1].

$$C_D = 0.37\left(\frac{2\rho_q \bar{v} R_o}{\eta_q}\right)^{-0.61} \qquad \text{(A.1)}$$

The spinline *Re* is calculated with the clad density ρ_o and viscosity η_o as given in equation (A.2).

$$\mathrm{Re} = \frac{2R_o \bar{v} \rho_o}{\eta_o} \qquad \text{(A.2)}$$

Calculating the product of C_D and Re using the typical spinning parameters given in Table A.1 (as taken from the literature [2, 3] and Chapter 2 parameters for hollow fiber membrane spinning) results in a value of 7.3 x 10^{-4}, which indicates that viscous effects indeed dominate drag effects, and drag effects can be neglected.

Similarly, the effects of gravity relative to viscous effects can be estimated with the ratio of *Re* and the Froude number, Fr The dimensionless parameter Fr, defined in equation (A.3), specifies the magnitude of inertia forces relative to gravitational force effects. In this equation, *g* is the acceleration due to gravity, 9.80 m/s^2. Thus, if *Re/Fr* is small, then gravity can be neglected relative to the dominant viscous forces. In this calculation, the density term in the calculation of *Re* should be an area-average value due to the form of the TFA momentum balance including gravity, and instead of the characteristic length being the diameter, it should be the draw zone length to be consistent with the definition of *Fr* [4].

$$Fr = \frac{\bar{v}^2}{2gL} \qquad \text{(A.3)}$$

Calculating *Re/Fr* for the typical values of spinning parameters given in Table A.1 results in a value of 10, which shows that gravity effects may be important to membrane spinning processes. This should be explored in future work, especially in terms of including the effects of gravity in the modified TFA simulations: this could help reduce the discrepancy between the experimentally measured diameter and velocity profiles and the modified TFA predictions presented in Chapter 5.

Table A.1 Conditions for Estimating Effects of Various Parameters on Spinning Operations

Parameter	Value
ρ_o	758 kg/m^3
ρ_i	0.854 kg/m^3
$\bar{v}$	35 m/min
ρ_q	1.1877 kg/m^3
R_i	6.8 x 10^{-4} m
R_o	2.3 x 10^{-3} m
L	0.200 m
η_q	1.85 x 10^{-5} Pas
η_o	44.8 Pas
C_{po}	2134 J/kg-K
k_o	1.5 x 10^{-1} W/m-K

Radial convection and axial conduction are neglected in fiber spinning modeling efforts per calculations of the Peclet number, *Pe*, for heat transfer as defined by equation (A.4). In this equation, *V'* represents the characteristic velocity, different for the radial and axial cases; likewise, *L'* represents the characteristic dimension over which heat transfer is considered for the two cases. In addition, C_{po} is the clad specific heat capacity, and k_o is the clad thermal conductivity. Typical values of these parameters for spinning are given in Table A.1 [2, 3].

$$Pe = \frac{\rho_o V' C_{po} L'}{k_o} \qquad \text{(A.4)}$$

To evaluate the radial heat transfer case, the characteristic velocity is the radial velocity, v_r. This quantity is estimated as 2.9 x 10^{-4} using continuity, equation (2.1), with typical values for hollow fiber membrane spinning as given in Chapter 2. Furthermore, the characteristic dimension for this case is the spinline wall thickness, estimated using typical initial values for inner and outer spinline radii as given in Table A.1. The resulting radial *Pe* is on the order of 5, suggesting that radial convection and conduction effects are actually comparable. This should be considered in future evaluations of temperature predictions.

However, evaluation of the axial *Pe* with the fiber axial velocity and draw zone length (typical values given in Table A.1) results in a value on the order of 1×10^4. This is consistent with the assumption that heat transfer in the axial direction is dominated by convection.

Viscous dissipation of heat is also neglected in the modeling efforts presented here. These effects are proportional to various velocity gradients as given in this term from the standard form of the energy balance, shown in equation (A.5) for the axisymmetric case modeled here [5]. Calculating this value for the representative conditions used in this research gives a result that is insignificant with respect to heat transfer via convection at the outer radius, and this term is neglected.

$$\textit{heat transfer via viscous dissipation} = 2\eta_o \left[\left(\frac{\partial v_r}{\partial r} \right)^2 + \left(\frac{v_r}{r} \right)^2 + \left(\frac{d\bar{v}}{dz} \right)^2 \right] + \eta_o \left(\frac{\partial v_r}{\partial z} \right)^2 \qquad \text{(A.5)}$$

To evaluate the effects of radiant heat transfer, it is necessary to calculate the Boltzmann number, *Bo*, describing the ratio of convection to radiation. This parameter is calculated using equation (A.6) in which ε is the spinline emissivity, estimated as 0.95 as is typical of organic materials [6], σ is the Stefan–Boltzmann constant of 5.67×10^{-8} W/m^2-K^4, and T is the spinline temperature.

$$Bo = \frac{\rho_o C_{po} \bar{v}}{\varepsilon \sigma T^3} \qquad \text{(A.6)}$$

Calculating this value using the typical values for spinning given in Table A.1 for the hollow fiber membrane spins discussed in Chapter 2 gives a value of 2.4×10^5 for *Bo*. This indicates that convection dominates radiation strongly, and radiation can be neglected.

Continuing, neglecting axial diffusion in the mass transfer modeling efforts for the boundary layer analysis reported in this research involves examining the Peclet number for axial mass transfer, Pe_m. This term is calculated using equation (A.7), where D is the diffusion coefficient and the characteristic length is the draw zone length *L*. Table A.1 gives the typical values for spinning used to calculate Pe_m.

$$Pe_m = \frac{\bar{v}L}{D} \qquad \text{(A.7)}$$

The calculated Pe_m for typical hollow fiber membrane spinning is on the order of 10^{10}. This indicates that axial diffusion can be neglected.

Finally, hollow fiber scanning electron micrographs (SEM's) presented in Chapter 3 show that there is no pore size gradient in the cross-section adjacent to the inner wall: this region is isotropic. Supporting this observation, existing modeling efforts examining the radial concentration gradients that evolve in the hollow fiber spinline indicate that the heat and mass transfer to the lumen are negligible. That is, calculations show that the core gas becomes quickly saturated with diluent vapor in the first 1 cm of the draw zone, which limits mass transfer, and the heat transfer considerations relate only to diluent evaporative cooling effects at the lumen interface, which are insignificant also [7, 8].

A.2.2 Converting Core Volumetric Flow Rate to Mass Flow Rate

The core gas flow rate indicated by the Millipore flow controller used here has the units of SCCM. Standard temperature and pressure conditions (STP) of 273 K and 1 atm are used with the ideal gas law of equation (2.2) to convert the volumetric flow rate to a mass flow rate w_i in kg/s as shown in equation (A.8).

$$w_i = \frac{(VFR\ in\ SCCM)(101325\ Pa)}{\left(60\ \frac{s}{\min}\right)\left(1\times10^6\ \frac{cm^3}{m^3}\right)\left(8314\ \frac{J}{kmol-K}\right)(273.15\ K)\left(28\ \frac{kg}{kmol}\right)} \qquad \text{(A.8)}$$

A.2.3 Error Propagation for Chapter 5

Errors in calculated axial velocity and outer to inner diameter ratio (OD/ID) values obtained experimentally and reported in Chapter 5 were propagated using standard error propagation formulas [9]. The calculation for the axial velocity error $\sigma_{\bar{v}}$, based on the calculated velocity $\bar{v}$, the distance d traveled by the polymer powder on-screen in the measurement, the time t between consecutive video frames, and the instrumental errors on these quantities σ_d and σ_t is shown in equation (A.9). The propagation of the error in the calculated OD/ID ratio has an identical form, with the errors in the OD and ID values calculated as the error on the average value calculated using the Image-Pro Plus software measurements as described in section 5.6.

$$\sigma_{\bar{v}} = \bar{v}\sqrt{\left(\frac{\sigma_d}{d}\right)^2 + \left(\frac{\sigma_t}{t}\right)^2} \qquad \text{(A.9)}$$

A.3 Determining Molecular Weight of Dow Affinity PL-1840 Polyethylene

The Dow Affinity PL-1840 polyethylene used in this research, with properties listed in Chapter 4, was characterized by researchers at Universidad de Chile using gel permeation chromatography (GPC) to determine the number-, weight-, z-, and viscosity-average molecular weights. Three lots were examined. Results are summarized in Figure A.1.

A.4 Spinning Equipment and Procedure Details

This section presents the standard operating procedure (SOP) used with the Leistritz twin-screw extruder detailed in Chapter 4; calibration curves for take-up devices and feeders; and a list of equipment model numbers.

Sample Name:		Date Acquired:	08/22/03
Sample Type:	Broad Unknown	Date Processed:	09/01/03
Injection Volume:	315.50 µL	Processing Method:	Calibración Universal
Run Time:	45.0 Minutes	Proc. Chnl. Descr.:	Refractive Index

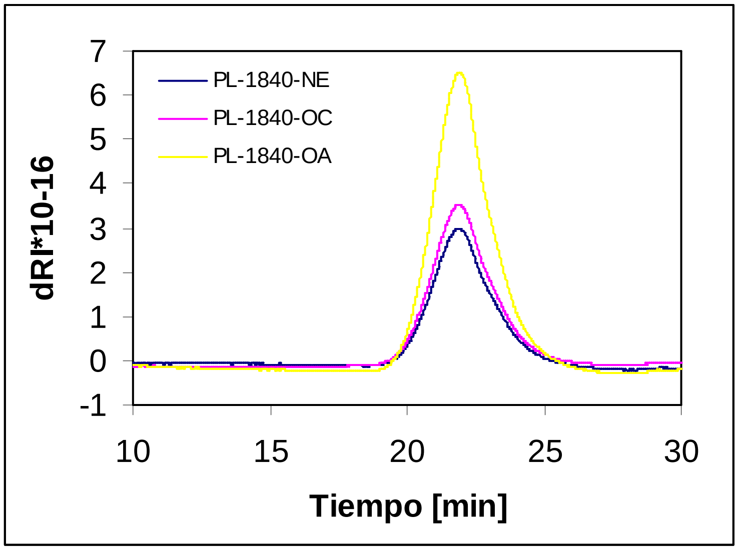

Sample	MN	MW	MP	MZ	Mz+1	Mv	Mw/Mn
PL-1840-OA	41913	80939	67733	133684	197864	75023	1.931
PL-1840-OC	42754	82395	69688	136644	201352	76304	1.927
PL-1840-NE	44461	83940	68979	142358	218884	77629	1.888

Figure A.1 GPC Results for Dow Affinity PL-1840 Samples

A.4.1 SOP for Leistritz Twin-Screw Extrusion Setup

Standard Operating Procedure: Leistritz Twin-Screw Extruder

Location: CPE 3.416
Written by Holly Balasubramanian, July 31, 2001

IN CASE OF EMERGENCY:

- Hit the EMERGENCY STOP switch on the extruder panel
- Hit the EMERGENCY STOP switch on the melt pump controller

- Hit the EMERGENCY STOP switch on the diluent delivery device
- Hit STOP and unplug the polymer feeder
- Turn OFF and unplug the spinneret heater and the take-up device
- Turn OFF the disconnect box switch for the chiller
- Turn OFF and unplug the vacuum pump
- Turn OFF the core flow

Safety and Equipment Hazards

- High temperatures—equipment may be very hot
- Diluent vapor present—check MSDS for hazards; ensure sufficient venting
- Do not run the melt pump or the extruder screws when cold

Possible Experimental Problems

- If pressure spikes to 300+ psig on the top red LED on the extruder panel, there is probably a plug, either due to low temperature or insufficient mixing.
- Clean the square connector for the end of the diluent delivery outlet hose with isopropanol or other suitable solvent after each use. Debris in the connector can clog the line and prevent extrusion. Install a pressure gauge in the line to detect clogs.
- Discontinuous polymer solution flow from the spinneret during extrusion indicates a problem, possibly due to presence of debris or incomplete mixing.
- Install a cooling water jacket for the polymer feed hopper—melting of polymer in the hopper can block the feed stream.

Procedure

1. Prepare diluent delivery system for operation
    a. Load diluent in pot.
    b. Turn power ON.
    c. Turn Zones 1-4 ON. Set all temperatures to appropriate values for ensuring diluent is liquid. Heating is indicated on each Zone's display by the appearance of the "OP1" light. *Special note for Zone 1:* Set point temperature for Zone 1 should not be too high due to slow thermocouple response; turn Zone 1 off after about 10 minutes to avoid overheating, and use a lower set point temperature (30° C for dodecanol, with Zones 2-4 set at 45° C). Zone locations are the following:
        i. Zone 1 = Diluent pot
        ii. Zone 2 = Inlet hose to diluent pump
        iii. Zone 3 = Diluent pump
        iv. Zone 4 = Diluent outlet hose to extruder

    d. To set the diluent input flow rate, input a set point value in g/min., then hit enter. Attach the connection block to the diluent outlet hose for joining it to the extruder. Before connecting the outlet to the extruder, check the diluent flow rate to ensure that it corresponds with the set point: EXERCISING CAUTION around the open pot of diluent, hold the diluent outlet hose over the open pot and use the heat gun on the unheated parts of the line, specifically the connection block at the outlet and the pump inlet and outlet fittings. To run the diluent pump, push the RESET button until lit; then press RUN/STOP to start or stop the pump. Measure the diluent flow rate by collecting diluent in a tared container over a set time. If the measured flow rate in g/min. does not match the set point value, either readjust the set point value and check the flow rate again, recalibrating the entire flow range if necessary, or re-program the diluent pump controller to display the desired range of values according to the manual instructions.
    e. Stop the diluent pump.

2. Start chiller operation and cooling water flow
    a. Make sure cooling water tubing is connected properly both for delivery of cooling water to chiller (cools extruder Zones 1-7) and circulation of fluid through extruder and back. Turn cooling water on at both taps.
    b. Turn chiller main power ON with the disconnect box switch.
    c. Turn power ON.
    d. Adjust set point temperature to a reasonably low temperature (≤ 45° C).
3. Prepare twin-screw extruder, melt pump, and spinneret for use
    a. Configure the barrel screws as desired and attach melt pump and spinneret assemblies. Install in-line filter prior to spinneret entry (heat zone 11) if desired.
    b. Turn extruder main power ON with the disconnect box switch.
    c. Turn extruder power ON with the transformer box switch.
    d. Turn ON all heat zones to be used (1-11 if in-line filter used; 1-10 if melt pump and spinneret attached; 1-8 if extruding directly into die from the extruder). Set all temperatures to appropriate values. Heating is indicated on each Zone's display by the appearance of the "OP1" light; Zones 1-7 also have cooling relays with an "OP2" operational indicator. Once polymer solution is mixed, any temperature greater than the cloud point may be used. Zone locations are the following:
        i. Zones 1-7 = Extruder barrel
        ii. Zone 8 = Extruder exit for direct die attachment (2 rod heaters attached)
        iii. Zone 9 = Transition from extruder barrel to melt pump
        iv. Zone 10 = Transition from melt pump to spinneret
        v. Zone 11 = Filter block (optional)
    e. Plug in and turn spinneret and core flow line temperature controller ON (use separate temperature controller with heating jackets or tape attached to spinneret and flow lines to the spinneret); adjust set point to desired spinning temperature.
    f. Plug in melt pump controller; adjust temperature set point to desired spinning temperature. DO NOT RUN THE MELT PUMP WHEN COLD.

   g. If flow rates to external melt pump assembly are higher than those desired for extrusion through the spinneret, turn on temperature control (using separate controller and heating tape) for the purge valve at the extruder exit. Valve should remain partially open during extrusion and temperature should be high enough to allow solution to flow through and exit prior to melt pump entry.
   h. Wait for the system to heat completely (about one hour for typical PE–dodecanol spinning temperatures of 140°C).

4. Connect the diluent delivery hose to the extruder
   a. WEARING HEAT-PROTECTIVE GLOVES, attach the diluent outlet hose to the extruder injector port (port 1, closest to polymer feed hopper) by first removing the port's cap. If after removing the two attachment screws the cap is still stuck to the extruder, screws can be put into the other two holes on the cap and used to pop the cap off.
   b. Hook up the diluent outlet hose to injector port 1 by placing the two attachment screws through the metal connection block.
5. Start the extrusion process
   a. When system is thoroughly heated, zero the pressure reading on the top red LED on the extruder panel.
   b. Start the flow of diluent by pressing RUN/STOP on the diluent delivery unit panel, making sure the flow rate is set for the desired value.
   c. Set the melt pump solution delivery speed by inputting the desired speed in rpm and pressing enter. Turn the melt pump ON by pressing RUN/STOP.
   d. Turn ON the core flow feed pressure and set desired flow rate in SCCM.
   e. Load polymer into the polymer feeder.
   f. Connect the polymer feed unit over the extruder hopper. DO NOT HEAT THE HOPPER: Molten polymer can clog the inlet and freeze operation.
   g. Turn on the extruder screws with the green button on the extruder control panel. Rotate the dial to the desired setting in rpm. For 30-wt% PE in dodecanol, 200 rpm is the typical value.
   h. When diluent begins to drip through the spinneret, plug in polymer feed unit and set delivery speed to desired value in rpm. See calibration data for corresponding speed in g/min. Start the polymer feed by pressing RUN.
   i. It should take <30 minutes to fill the barrel and begin to see polymer solution extruding; before data and sample collection, wait for a specified time to ensure proper mixing and arrival at steady state (for 30 wt-% PE in dodecanol, usually about 30 minutes).
   j. When steady flow out of spinneret begins, turn on the vacuum pump (if desired—keep in mind this will change the composition of the extrudate while possibly improving extrusion performance) and pump down to 0.2–0.6 bar.
   k. Manually start take-up, first passing through water bath and around driven roller if desired.
   l. Take measurements using the X–Z videoscope and IR camera if desired. Collect samples at desired intervals, changing spinning conditions and restarting take-up after a specified operational stabilization time as necessary.

Shutting Down

1. Turn off polymer feeder by pressing STOP and unplugging the unit.
2. Allow remaining polymer solution in the extruder to flow through. Clean system by continuing to pump pure diluent through at high temperature.
3. Stop the diluent pump. Decrease set point temperatures on diluent delivery unit Zones 1–4 to zero; turn off Zones 1–4 and shut off the power to the device.
4. Turn off the extruder screws (red button on the extruder control panel) and decrease their set point speed to zero.
5. Decrease temperatures on extruder Zones 1–11 to zero. Shut off Zones 8–11 only.
6. Stop the melt pump. Decrease melt pump set point temperature to zero; unplug melt pump.
7. Decrease set point of spinneret and core flow line temperature controller to zero; turn off the unit.
8. Turn off the core flow supply pressure and unplug the controller.
9. Turn off the vacuum pump.
10. WEARING HEAT-PROTECTIVE GLOVES, disconnect the diluent delivery system outlet hose from the extruder. Replace the square cover on injector port 1.
11. Remove the square connector from the end of the diluent delivery outlet hose. Clean with isopropanol or other suitable solvent. DEBRIS IN THE CONNECTOR CAN CLOG THE LINE AND PREVENT EXTRUSION.
12. When extruder Zones 1–7 read <45°C, shut them off and shut off the extruder power at the transformer box switch and the main switch on the disconnect box.
13. Turn off the chiller.
14. Allow entire system to cool thoroughly, and then clean as necessary. TO CLEAN: heat entire system to temperature suitable to melt the residual extruder contents; shut everything off; disconnect the external melt pump assembly and separate flow ports to clean; remove breaker plate from extruder (four screws); remove screws from barrel using screw removal tool; brush off hot polymer leftovers using wire brush; clean inside barrels with long-handled wire brush; replace screws; heat screw barrels; check for proper screw seating and operation.

A.4.2 Equipment Calibration Curves

Shown in Figures A.4.2 through A.4.5 are calibration plots for the Leistritz diluent feeder, K-Tron polymer feeder, motor-driven roller in the water bath, and the Randcastle fiber winder.

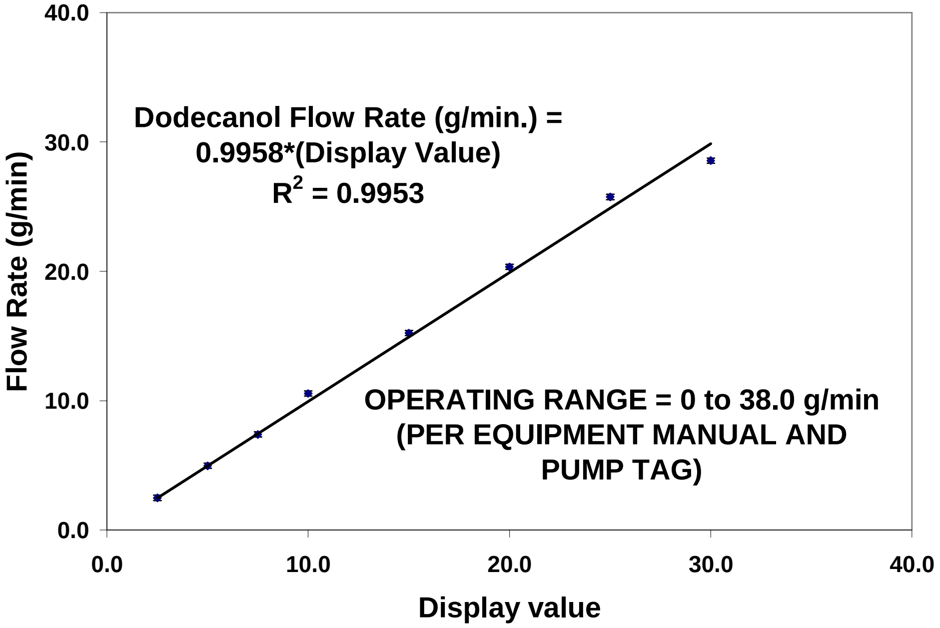

Figure A.2 Leistritz Diluent Feeder Calibration Plot

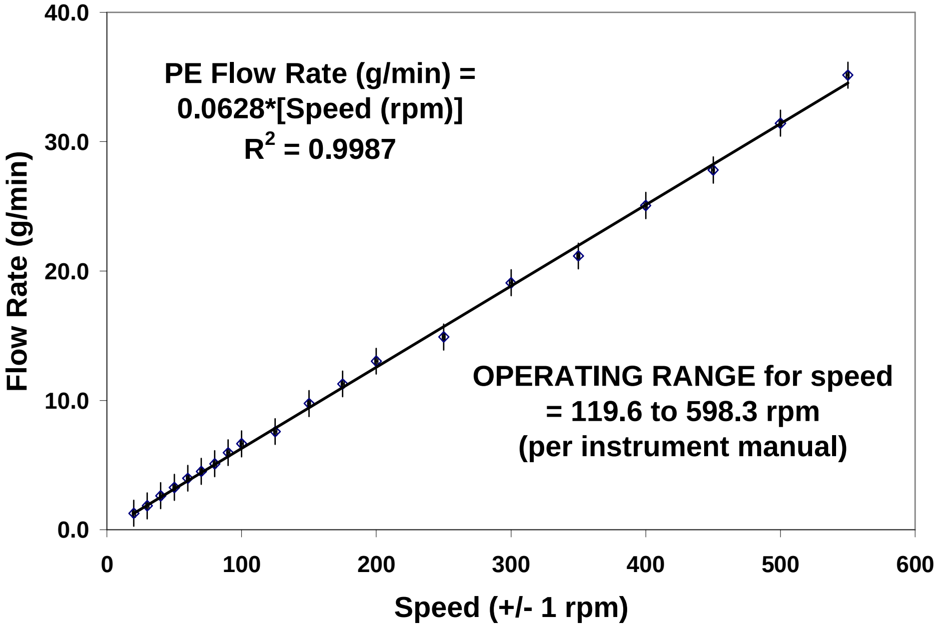

Figure A.3 K-Tron Polymer Feeder Calibration Plot

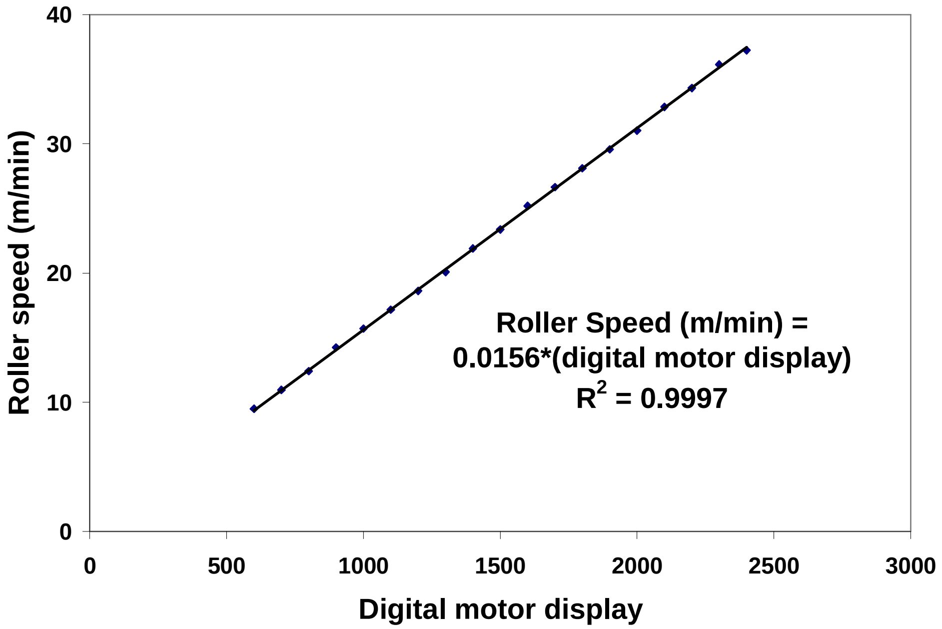

Figure A.4 Driven In-Bath Roller Calibration Plot

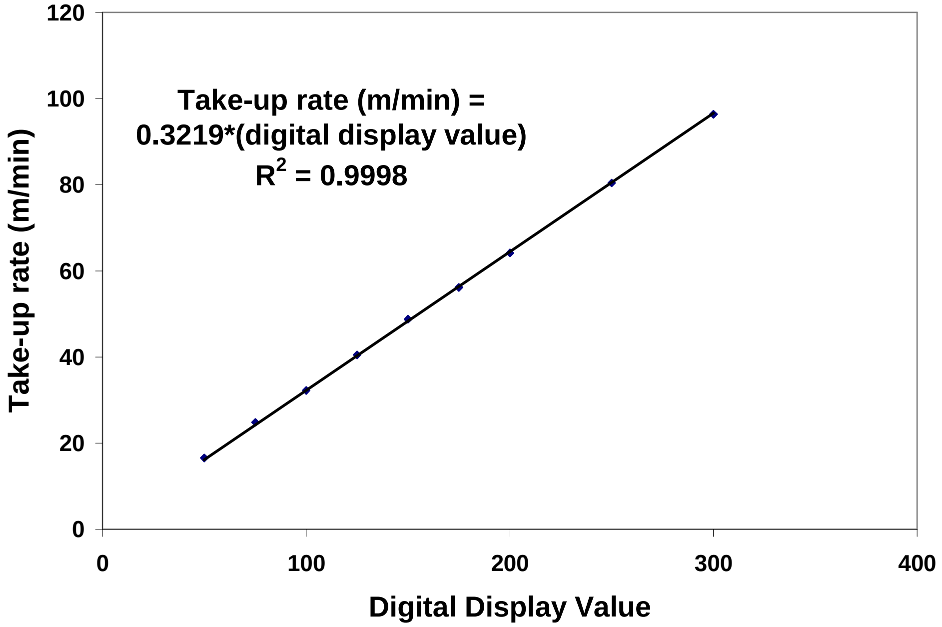

Figure A.5 Randcastle Fiber Winder Calibration Plot

A.4.3 Equipment Specifications

Listed in Table A.2 are the model numbers for the equipment used in this research. More equipment details, including pictures, are given in Chapter 4.

Table A.2 Leistritz Twin-Screw Extrusion Setup Equipment Specifications

Description	Company	Model	Serial Number
Extruder	Leistritz	MIC 18 GL/40D	2855
Polymer Feeder	K-Tron Soder	K2MVT20	S16623-0
Diluent Feeder	Leistritz	PO 3309	6206443JK-006
External Extruder Melt Pump	Leistritz	PO 3309	6206443JK-002
Chiller	Application Engineering and AEC, Inc.	TDC 1NX-Q	30F5668
Core Flow Controller	Millipore	LR-250-1-1-2-24	786
Core Flow Control Valve	Tylan	FC-260V-45	AA99033182
Core Flow Cable Assembly	Mykrolis	LC-260-0251	N/A
Spinneret and Tubing Heater	Love Controls	25013-986/J	GS 290-2429-1
Driven In-Bath Roller DC Gearmotor	Dayton	4Z726A	E47479
Driven In-Bath Roller Gearmotor Controller	DART Controls, Inc.	MD10P	G99-04367
Take-up Winder	Randcastle	Fiber Winder	J2543
Infrared Camera	Mikron	TH-5104	0070705
X–Z Axis Videoscope	Titan Tool Supply, Inc.	A-II	N/A
X–Z Video Adapter	Titan Tool Supply, Inc.	TSTVA-12	N/A

Table A.2 (continued)

Description	Company	Model	Serial Number
X–Z Video Illuminator	Titan Tool Supply, Inc.	FOI-1 Split Bifurcated Fiber Optic Bundle.	N/A
Camera and controller for use with X–Z Videoscope and Nikon Microscope	MTI	CCD-72X	01911
Microscope	Nikon	Optiphot2-Pol	N/A
Hot Stage	Linkam	HFS-91	N/A
Hot Stage Controller	Linkam	TMS-91	N/A
Differential Scanning Calorimeter (DSC)	Perkin-Elmer	DSC-7	N/A
Thermal Analysis Controller	Perkin-Elmer	TAC7/DX	N/A
Field Emission Scanning Electron Microscope (FESEM)	Hitachi	S-4500	unknown
Sputter Coater	Electron Microscopy Sciences	K575	unknown
FTIR Spectrometer	Nicolet Instrument Corporation	Magna-IR Spectrometer 550	unknown
Variable-Angle Horizontal ATR Accessory	Pike Technologies	ATRMax II	unknown
ATR Angle Adjustor	Pike Technologies	AutoPRO controller	unknown

A.5 Determination of PE–Dodecanol Diffusion Coefficient Using FTIR–ATR Spectroscopy

In addition to the predictive formulation for the mutual diffusion coefficient following the method of Zielinski and Duda, FTIR−ATR experiments were performed on the PE–dodecanol system [10-12] to obtain an experimental value of the diffusion coefficient. These experiments are based on calculating the diffusion coefficient by allowing evaporation of diluent from the surface of a thin film at constant temperature, monitoring the decline of the area of a diluent characteristic peak over time. For the PE–dodecanol system, the characteristic peak corresponds to the C–O stretch appearing in the 800–1200 cm^{-1} wavenumber range, present in the infrared spectrum of pure dodecanol, but not in that of PE. The equipment setup for the FTIR–ATR experiments appears in Figure A.6.

Figure A.6 FTIR–ATR Experimental Setup

For these experiments, thin films (500 ± 100 μm) of 30 wt-% PE–dodecanol solutions were cast onto a ZnSe crystal for use with FTIR–ATR spectroscopy (Nicolet Instrument Corporation Magna-IR Spectrometer 550; Pike Technologies ATRMax II variable angle horizontal ATR accessory with combined trough and plate system; and ATRMax II AutoPRO controller). The 30 wt-% solutions were prepared using the pot-in-oven setup shown in Figure 4.5 as discussed in section 4.1.3. Casting was performed inside the oven at 423 K, 20 K above the selected FTIR–ATR testing temperature of 403 ± 5 K, surrounded by a dodecanol-saturated atmosphere; directly after casting the films using a heated spatula and an aluminum tape spacer, the film–crystal assembly was covered with a glass slide. All of these steps were precautions against dodecanol evaporation (and thus altering of the sample composition) during casting.

Prior to the FTIR–ATR diffusion experiments, the spectrometer assembly was purged with low-flow (less than 5 psig) nitrogen gas for at least two hours to avoid interference due to humidity inside the cell. Furthermore, a background scan using a blank ZnSe crystal was performed before evaluating each sample. All measurements were taken with the ATR angle set to 45°; this is greater than the critical angle of 39° calculated by Snell's law for ZnSe refractive index of 2.4 and PE refractive index of 1.51 (or the dodecanol refractive index of 1.44, which gives a critical angle of 37°), as required to produce total internal reflection [13-16]. Temperature control was accomplished using a heated air gun (Master, model HG-301A) placed to blow air horizontally across the top surface of the film during testing. Placement of the heated air gun and adjustment of the gun's temperature vent were determined prior to testing with PE–dodecanol samples by measuring the average temperature of three areas on the blank ZnSe crystal after flowing heated air from the air gun at a particular position and setting over the crystal surface for at least 10 minutes.

FTIR–ATR peak absorbance measurements were recorded and analyzed using Omnic software (Nicolet version 4.1a, 1998) and a series scan over 30 minutes, with one spectrum collected every two minutes for the 800–1200 cm^{-1} region using a mirror velocity of 0.6329 cm/s, 16 scans per spectrum, and a resolution of 4 cm^{-1}. Upon starting the test, the glass slide covering the film sample on the ZnSe crystal was removed to allow dodecanol evaporation and diffusion to begin. The first scan of the series, occurring within the first 10 seconds of the test, was assumed to correspond to the initial 30 wt-% PE–dodecanol solution.

To analyze the resulting IR absorbance data and extract the diffusion coefficient for PE–dodecanol, the areas of the characteristic dodecanol peak were obtained using the Omnic software, consistently setting the baseline and integration regions as 927–1122 and 939–1103 cm^{-1}, respectively. In addition, all of the peak area measurements were normalized using the area from the initial spectrum, thus putting the absorbance data in the form of C/C_o, concentration relative to the initial concentration of 30 wt-% PE.

Normalized peak area measurements were plotted as a function of time, and a best fit to the data was obtained using TableCurve 2D software. In order to extract the system diffusion coefficient from the results, the theoretical solution to the equation for diffusion through a film of thickness l with diluent loss restricted to one side of the film into a medium of zero diluent concentration was used to calculate the expected normalized concentration profile according to equation (A.10) [17].

$$\frac{C}{C_o} = \frac{2}{C_o}\sum_{n=1}^{\infty}\left[\exp\left(-D\alpha_n^2 t\right)\right]\left[\frac{\left(h^2+\alpha_n^2\right)\cos\left(\alpha_n x\right)}{\left(\alpha_n^2+h^2\right)l+h}\right]\int_0^l \left.\frac{C}{C_o}\right|_{t=0}\cos\left(\alpha_n x\right)dx \qquad \text{(A.10)}$$

In equation (A.10), h is the ratio of the mass transfer coefficient for the diluent into the air outside the film to the diffusion coefficient, k_c/D; x represents the position in the film thickness, with $x = 0$ at the film surface in contact with the crystal, and $x = l$ the top, exposed surface of the film. The α_n terms comprise the positive roots of equation (A.11).

$$\alpha\tan(\alpha l) - h = 0 \qquad \text{(A.11)}$$

Furthermore, the mass transfer coefficient k_c is defined in equation (A.12) [18]. In this correlation, applying to forced air convection over a flat surface, D_{d-air} represents the diffusion coefficient of diluent into stagnant air, defined in equation (3.13); L_c is the characteristic length, here equal to the length of the film over which the heated air flows; ρ_{air} and μ_{air} are the air density and viscosity at the air temperature, defined by the relationships given in equations (2.38) and (2.39); and v_{air} is the velocity of the imposed air stream from the air gun, measured to be 4.0 L/min using an air flow meter.

$$k_c = 0.664\frac{D_{d-air}}{L_c}\left(\frac{\rho_{air}v_{air}L_c}{\mu_{air}}\right)^{1/2}\left(\frac{\mu_{air}}{\rho_{air}D_{d-air}}\right)^{1/3} \qquad \text{(A.12)}$$

The diffusion coefficient was determined by guessing its value, using this to calculate the theoretical C/C_o profile with time for the film, and comparing the result to the experimental data's trend, repeating the procedure (varying the guessed D) until the experimental results compared well to the theoretical values. The result for 403 ± 5 K and 30 wt-% PE in dodecanol is a diffusion coefficient of 1.5 x 10^{-10} m^2/s. Figure A.7 shows the experimental and theoretical concentration profiles.

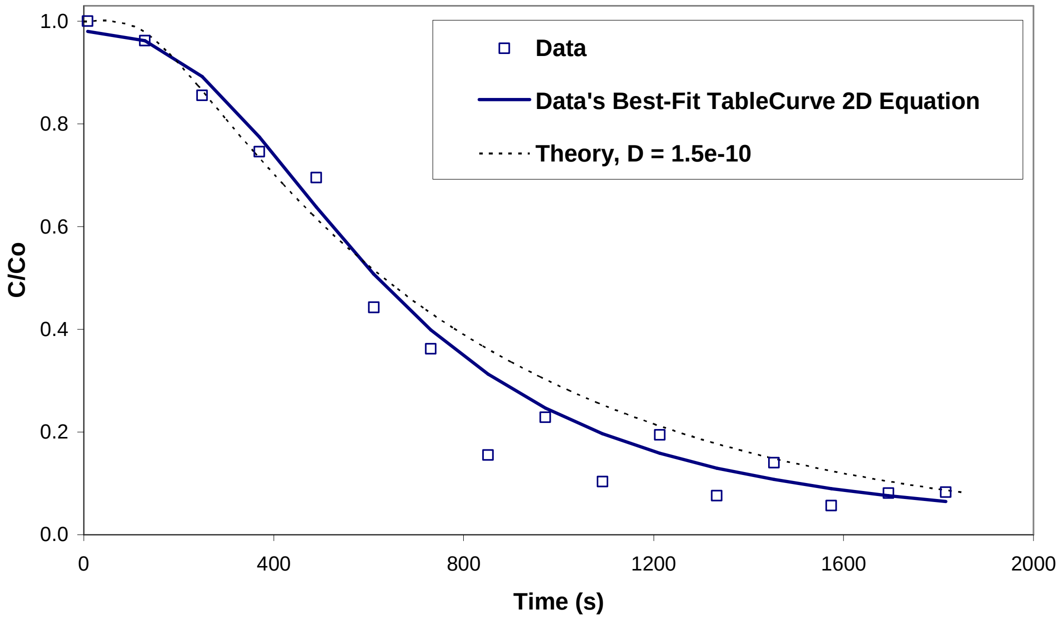

Figure A.7 PE–Dodecanol FTIR–ATR Diffusion Coefficient Calculation Results

The value of the diffusion coefficient determined experimentally using the FTIR–ATR method for 403 ± 5 K, 1.5 x 10^{-10} m^2/s, is two orders of magnitude higher than the value of *D* predicted by the Zielinski–Duda predictive correlation for 403 K, approximately 3.00 x 10^{-12} m^2/s. The level of uncertainty in the FTIR–ATR measurements is compounded by the many sources of experimental error, including the error on the sample temperature, which was difficult to determine during testing to ensure it was not affected by ambient air currents or other room disturbances. In addition, although precautions were taken to minimize diluent evaporation before the start of the infrared scans, it is possible that some diluent was lost and the sample composition altered. In addition, the analysis of the infrared peak area, a function of the instrument resolution and the strength of the signal, which was too weak to obtain meaningful data for some experiments whose measurements were disregarded, adds an additional source of uncertainty. Finally, the method of extracting the diffusion coefficient from this data through comparison with theory brings with it the error introduced due to the need for comparing the entire experimental data set as expressed by a “best fit” trendline. Thus, although the FTIR–ATR experiments performed here for measurement of the diffusion coefficient can supplement future investigation of this parameter for PE–dodecanol, which is recommended, this research relies on the Zielinski–Duda diffusion coefficient values predicted as a function of concentration and temperature.

A.6 Determining the Apparent Diffusion Coefficient for Phase-Separated PE–Dodecanol Mixtures

During a project exchange with Japan, static light scattering measurements were done under the guidance of Hideto Matsuyama at Kyoto Institute of Technology in order to obtain the apparent diffusion coefficient for 20 wt-% PE in dodecanol samples at temperatures near the phase separation temperature. These results could be included with model extensions to describe the transport through phase-separated polymer–diluent spinlines.

The procedure and calculation method were taken from the literature [19-22]. Results for the apparent diffusion coefficients, summarized in Table A.3, are the same order of magnitude as published results for other polymer–diluent systems; however, as temperature was decreased in these experiments, the value of the apparent diffusion coefficient also decreased, and literature results for other systems show the opposite trend [21].

If effects due to the molecular weight difference between polymer and diluent can be neglected, an equation involving the apparent diffusion coefficient and the chi interaction parameters at the actual temperature and the spinodal temperature can be used to convert the apparent diffusion coefficient to a translational diffusion coefficient, a parameter more closely related to diluent transport through the phase-separated mixture. Due to this stated dependence of the translational diffusion coefficient, the decreasing trend in the apparent coefficient observed with decreasing temperature may be due to the stronger change of the translational coefficient with temperature: if this quantity decreases with decreasing temperature, its effect on the apparent diffusion coefficient may be stronger than the effect of the chi parameters, which causes the apparent coefficient to increase with decreasing temperature [23]. More experimentation is warranted to evaluate the diffusion coefficients for phase-separated mixtures and apply the spinning transport modeling efforts to phase-separation spinlines.

Table A.3 Diffusion Coefficient Results from Static Light Scattering Measurements

Quench Temperature (°C)	Apparent Diffusion Coefficient (μm^2/s)	Standard Error (two times the standard deviation for each sample set)
103 (run 1)	0.35	0.04
103 (run 2)	0.61	0.08
101 (run 1)	0.08	0.01
101 (run 2)	0.15	0.02
99	0.07	0.01

A.7 Infrared (IR) Camera Evaluation

Experiments were performed to evaluate the use of an infrared camera (Mikron model TH-5104) for determining spinline surface temperature profiles. The camera has the capability to detect radiation in the 3.0–5.3 μm wavenumber range. A stainless steel ruler was used to focus the camera before all measurements. Accompanying software provides a method to gauge pixel-to-pixel temperature variation, and the camera can be interfaced with a computer for real-time measurements. Calibration procedures, relatively simple and automatic, were done regularly as recommended in the instrument manual.

Initial testing with the standard camera lens and a PE–dodecanol spinline in the air gap during spinning produced infrared images depicting an overall axial temperature drop much higher than that indicated by the TFA model or crudely measured with wire probe thermocouples along the spinline. Figure A.8 shows one of the IR camera spinline images taken with the standard lens.

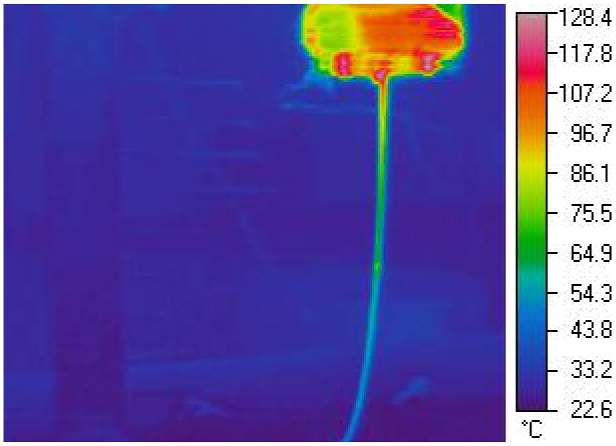

Figure A.8 IR Image of PE–Dodecanol Spinline Using Standard IR Camera Lens

However, during follow-up experiments, a 250 μm close-up lens, requiring manual focus with a working distance of 2.00 +/- 0.25 inches, was used to take additional PE–dodecanol spinline pictures. Results show a much less drastic temperature drop over the entire spinline, with a representative image of the spinline adjacent to the spinneret given in Figure A.9. These results indicate that the instantaneous field of view (IFOV) of the standard lens, which specifies the spatial resolution of the camera, is inadequate for measuring relatively small diameter spinline, and thus temperatures represented by the image in Figure A.8 are unreliable. However, the IR results using the close-up lens also indicated an axial temperature drop that did not agree with model predictions or crude thermocouple measurements: the IR profiles were consistently more drastic temperature drops.

Several sets of experiments were then performed using the IR camera; these involved examination of heated pure dodecanol flowing vertically out of ¼” tubing (detected temperature results matched probe-type thermocouple readings to within 1°C); the same measurements repeated for pure glycerol (with the same good comparison to thermocouple readings); extruding PE–mineral oil fibers (with an overly drastic—compared to the model predictions—measured temperature profile as with the PE–dodecanol spinline measurements); and additional PE–dodecanol measurements, using large “blobs” of heated PE–dodecanol solution (results show agreement of the IR-detected temperatures and probe-type thermocouple readings to within 1°C).

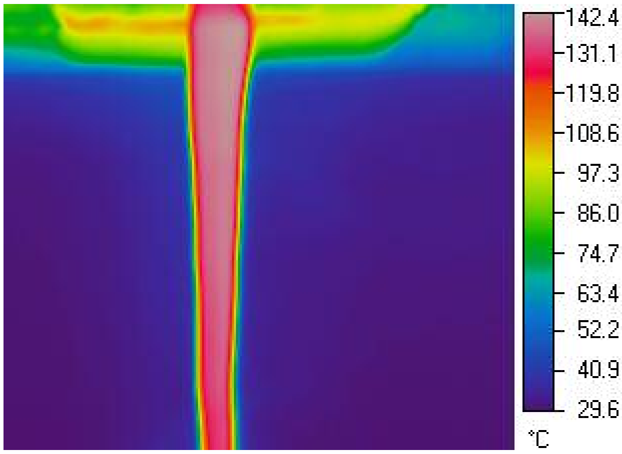

Figure A.9 IR Image of PE–Dodecanol Spinline Using Close-up Camera Lens

With the encouraging results for the large "blobs" of PE–dodecanol solution, experts and literature were consulted for advice [6, 24-26]. Unfortunately, the conclusion drawn was that properties of the PE–dodecanol spinning system make this IR camera inadequate for temperature measurements of the spinline. Specifically, PE transmits IR radiation for all of the wavelengths detected by the camera, and the spinline is too thin to overcome this effect [6].

Thus, spinline temperatures reported by the IR camera are subject to the temperature of background objects: their IR radiation is transmitted through the PE spinline and detected as the temperature of the PE. This occurs despite the fact that dodecanol, as an organic liquid, works well with the IR camera alone; this eliminates the possibility of simply using an IR-friendly substance as a "tracer" for detection of the spinline temperature via IR. Furthermore, placing different types of objects behind the spinline during IR measurement (including Teflon-coated aluminum sheets, black matte-painted plywood boards, and steel plates; at room temperature, heated, and iced) did not provide insight into the measurement results for PE–dodecanol. As a final attempt to try to remove the transmittance problem posed by the properties of PE, solid fibers were extruded through ¼" tubing, with the idea of increasing the spinline thickness enough to overcome transmission. The PE emits infrared radiation of its own, proportional to its temperature as with other substances. If a PE sample is thick enough, then its tendency to transmit the IR emitted from its background does not affect the measurement of its true temperature: the background IR radiation that is transmitted and detected belongs to the same PE sample with the same temperature. However, the ¼” diameter solid fiber experiments proved fruitless: the spinline thickness was still not significant enough to overcome the transmissive effects of PE. The measurement situation for the spinline may be complicated due to spinline motion during take-up; it is unclear how this affects IR-detected temperatures.

To quantify the transmittance of the PE–dodecanol system, transmittance measurements were taken as a function of fiber thickness using spun PE–dodecanol fibers at 298 K by UT Mechanical Engineering Department researchers. Results, shown in Figure A.10, can be used to quantify transmittance as a function of fiber thickness; these results can potentially be used to correct the IR-detected temperatures for spinline thicknesses where transmittance is significant. However, these results indicate relatively low transmittance values, even for very thin fibers; thus, it is recommended that these measurements be repeated for a range of temperatures to explore these measurements and their meaning in detail. Chapter 6 details further recommendations for future use of the IR camera to characterize the spinline temperature, including discussion of the possibility for narrow bandpass filter use to detect polyethylene spinline temperatures directly.

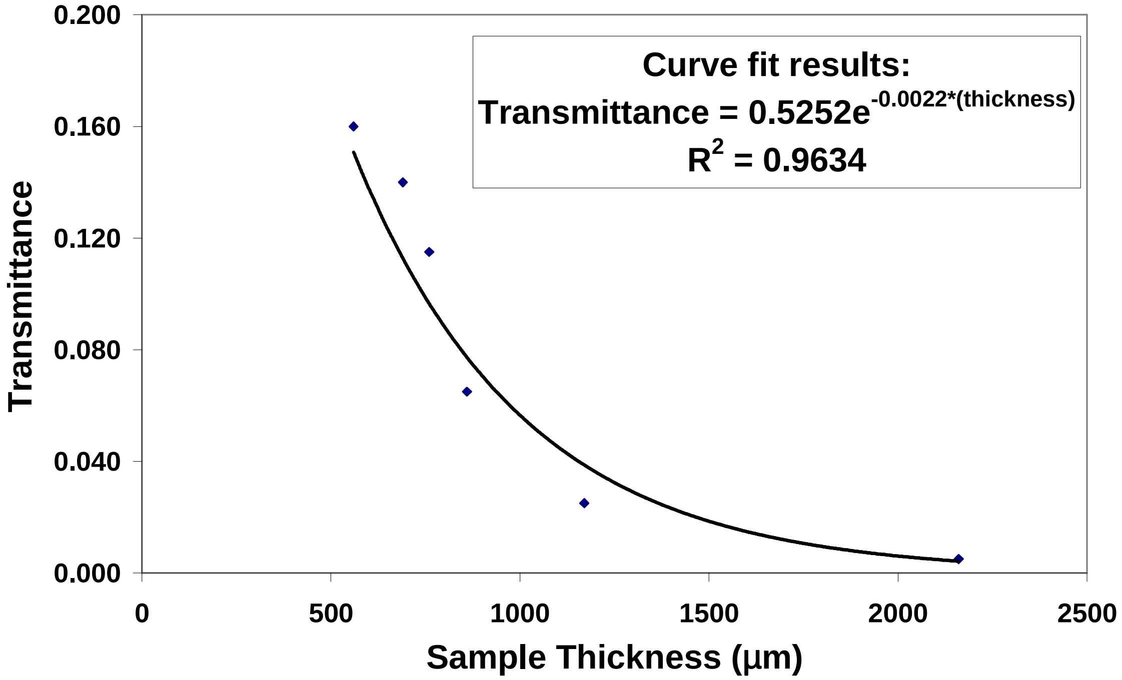

Figure A.10 PE–Dodecanol Fiber Transmittance Values at 298 K

A.8 Scanning Electron Micrographs (SEM's) of Hollow Fiber Membranes

This section presents the SEM's of hollow fiber membranes spun in this research under the conditions detailed in Table 5.1 for various membrane sensitivity studies. Not included in this section are the SEM's for trial 5, which are presented in section 5.6. These figures follow the same format as Figures 5.13 through 5.18: cross-section of the entire fiber, isolation of entire fiber wall thickness, focus on section adjacent to outer wall, close-up of anisotropic boundary, close-up of anisotropic region between boundary and the outer wall, and a close-up of the isotropic section outside the boundary layer. Figures here are specified by trial number from Table 5.1. Due to lack of space, only one sample for each trial is shown here; multiple samples were analyzed, however, as described in Chapter 5.

A.8.1 Trial 1 SEM's

Figure A.11Trial 1 Entire Cross-Section

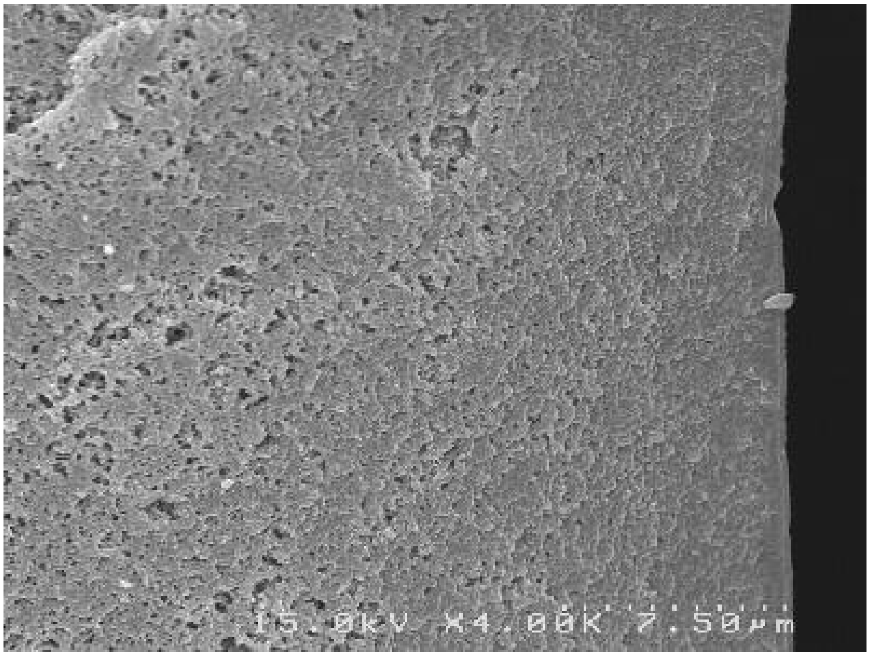

Figure A.12 Trial 1 Cross-Section Near Outer Wall

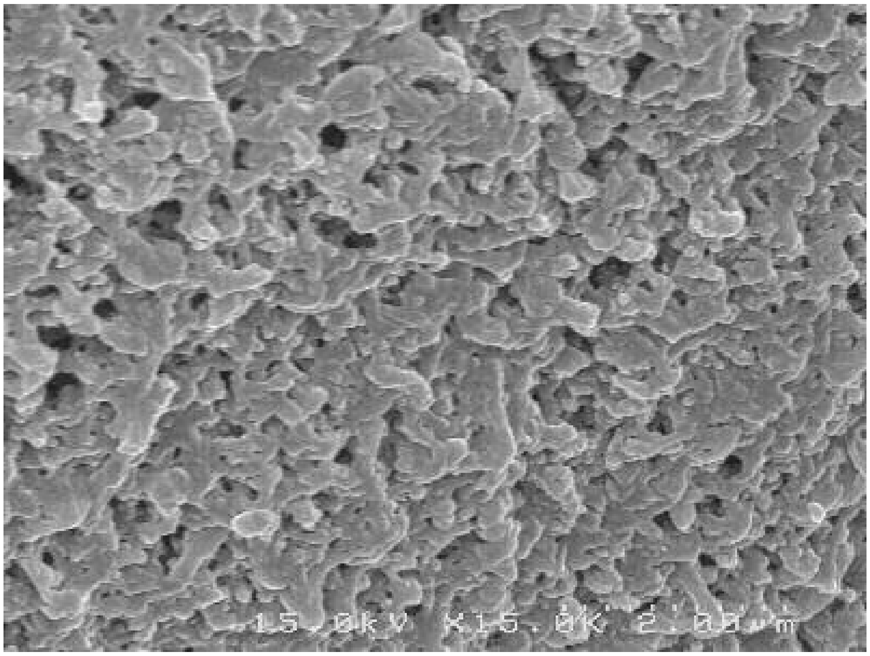

Figure A.13 Trial 1 Close-up of Anisotropic Boundary

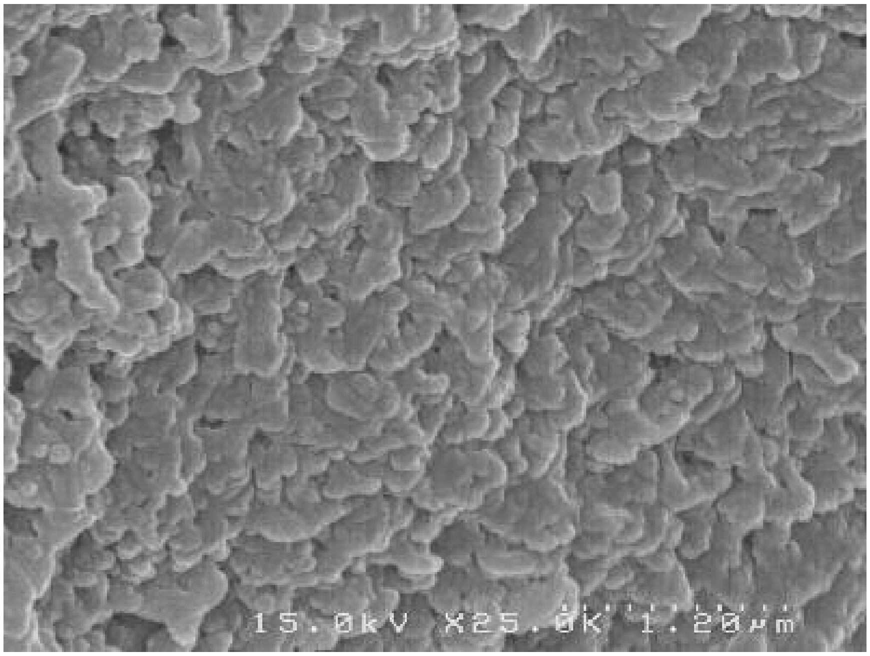

Figure A.14 Trial 1 Focus on Anisotropic Region

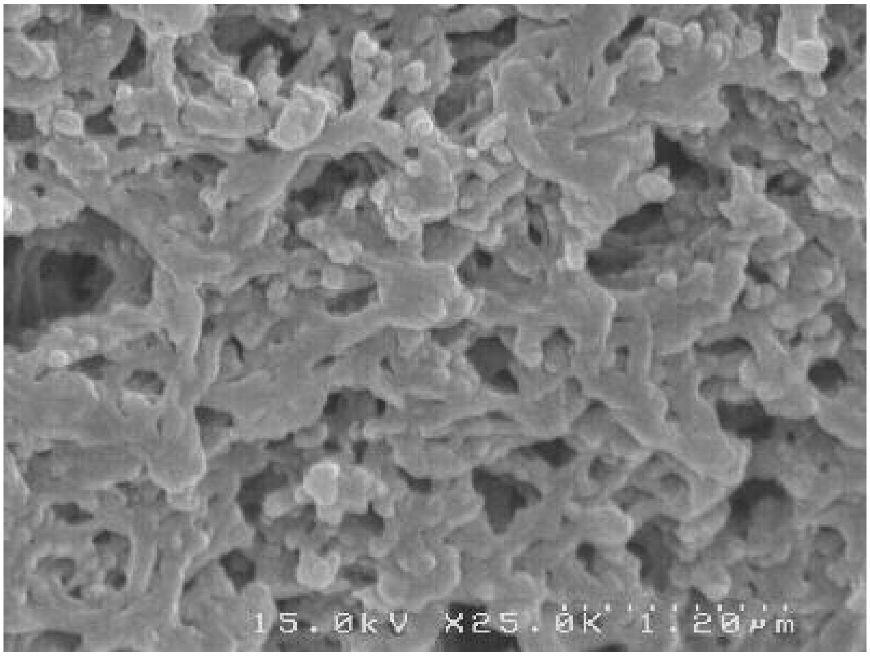

Figure A.15 Trial 1 Focus on Isotropic Region

A.8.2 Trial 2 SEM's

Figure A.16 Trial 2 Entire Cross-Section

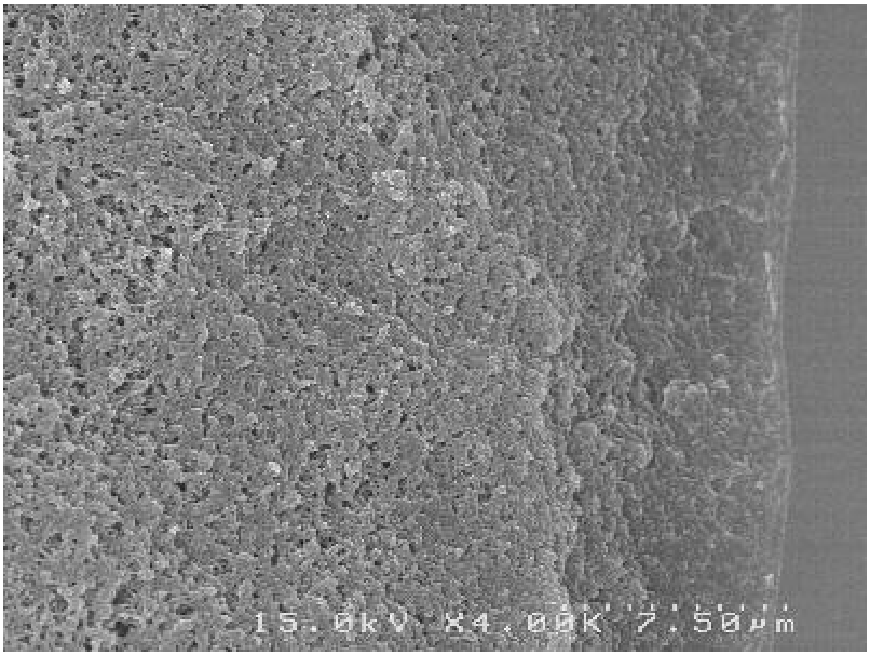

Figure A.17 Trial 2 Cross-Section Near Outer Wall

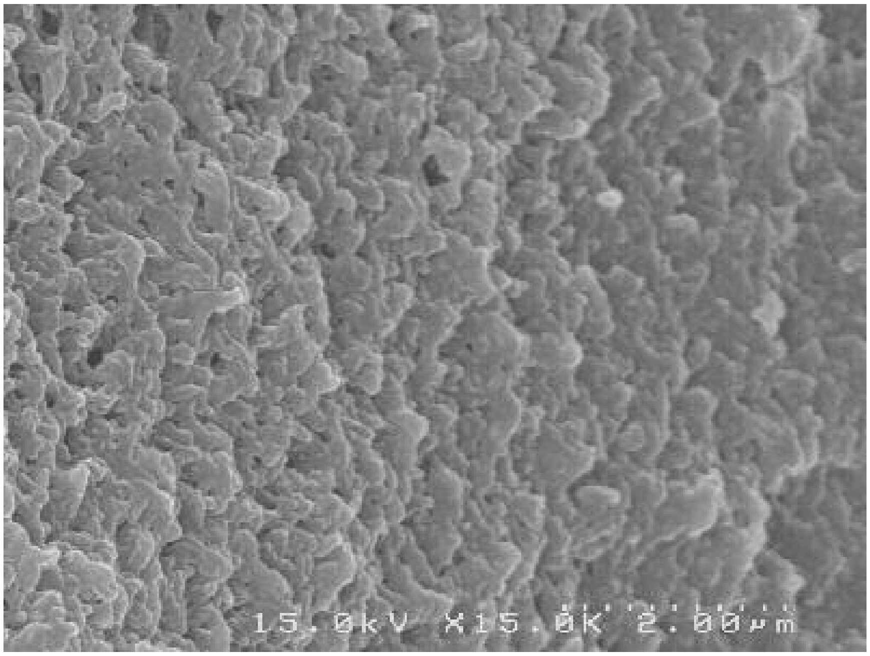

Figure A.18 Trial 2 Close-up of Anisotropic Boundary

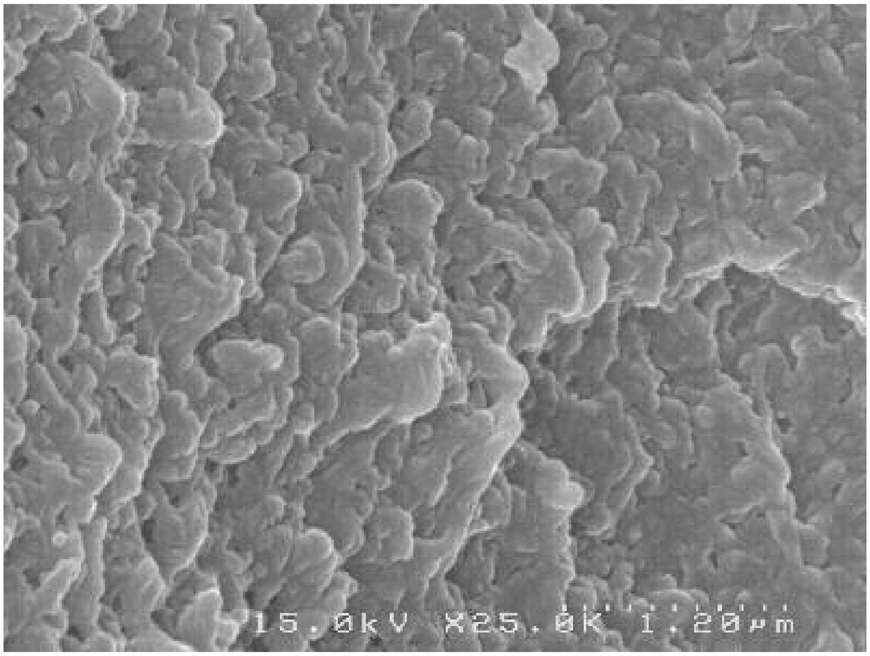

Figure A.19 Trial 2 Focus on Anisotropic Region

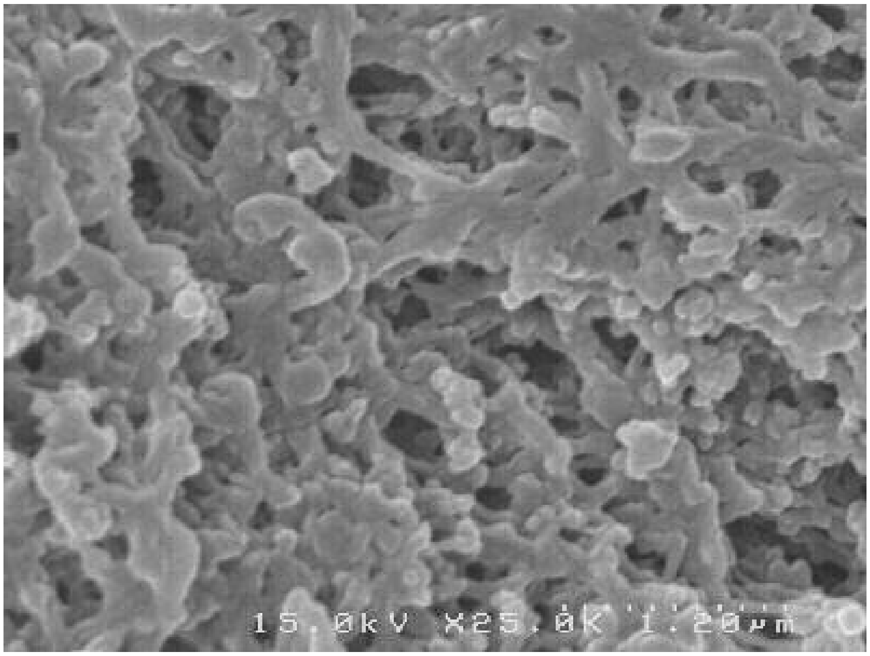

Figure A.20 Trial 2 Focus on Isotropic Region

A.8.3 Trial 3 SEM's

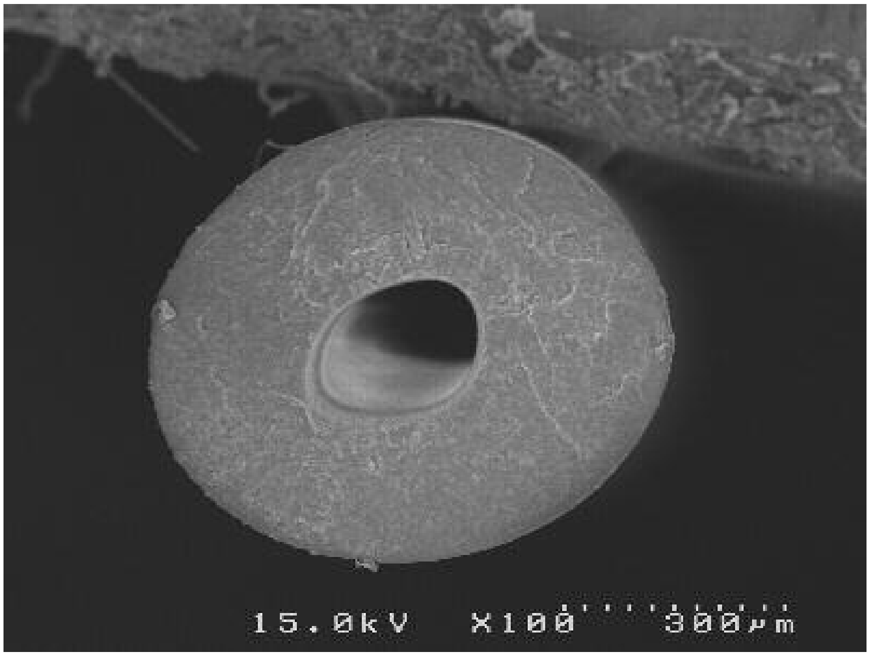

Figure A.21 Trial 3 Entire Cross-Section

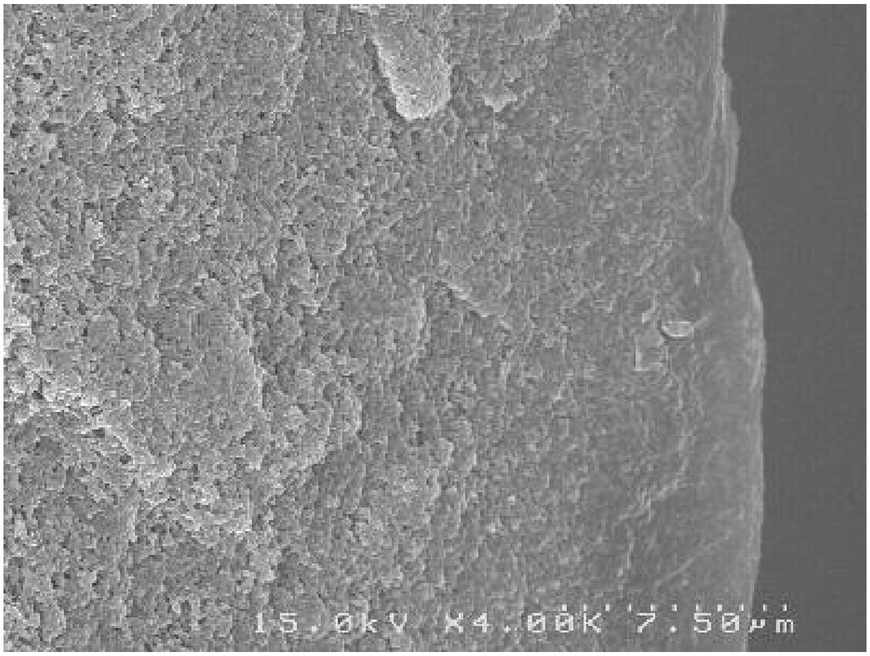

Figure A.22 Trial 3 Cross-Section Near Outer Wall

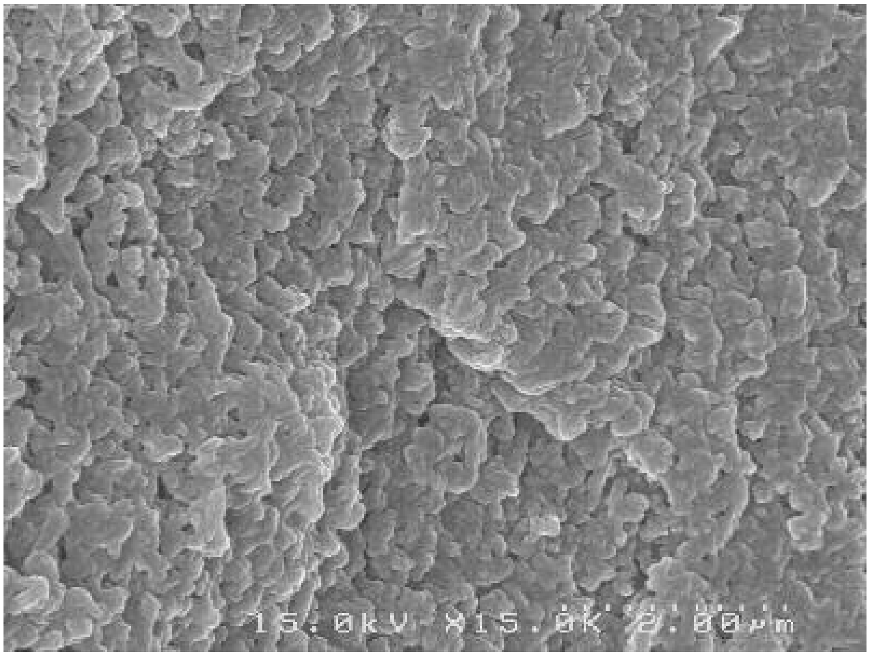

Figure A.23 Trial 3 Close-up of Anisotropic Boundary

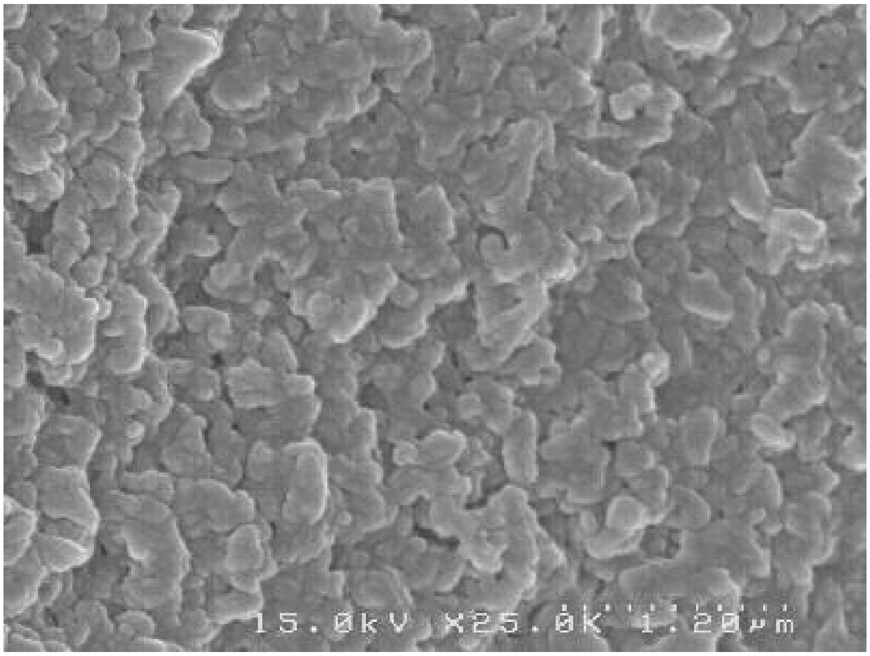

Figure A.24 Trial 3 Focus on Anisotropic Boundary

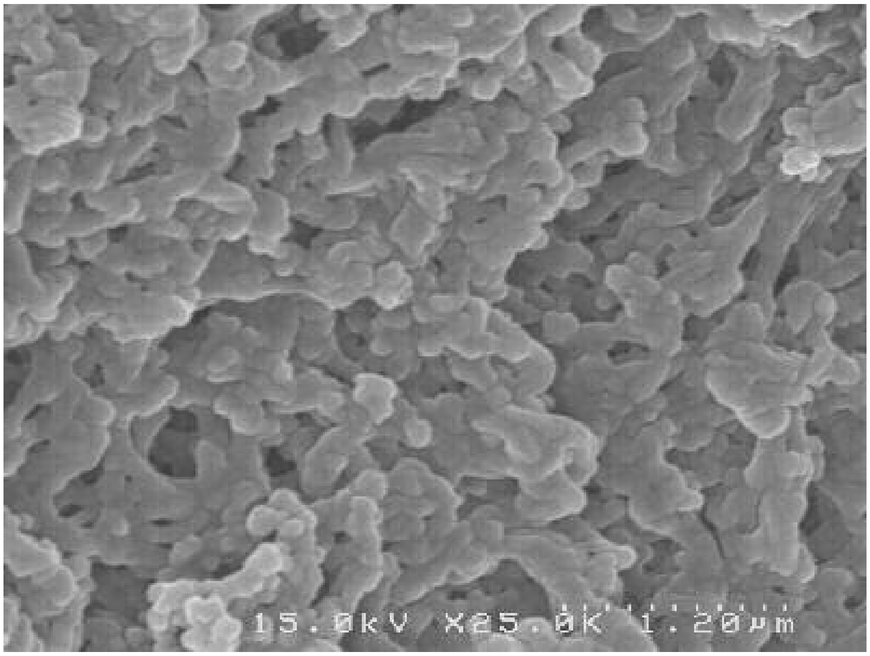

Figure A.25 Trial 3 Focus on Isotropic Boundary

A.8.4 Trial 4 SEM's

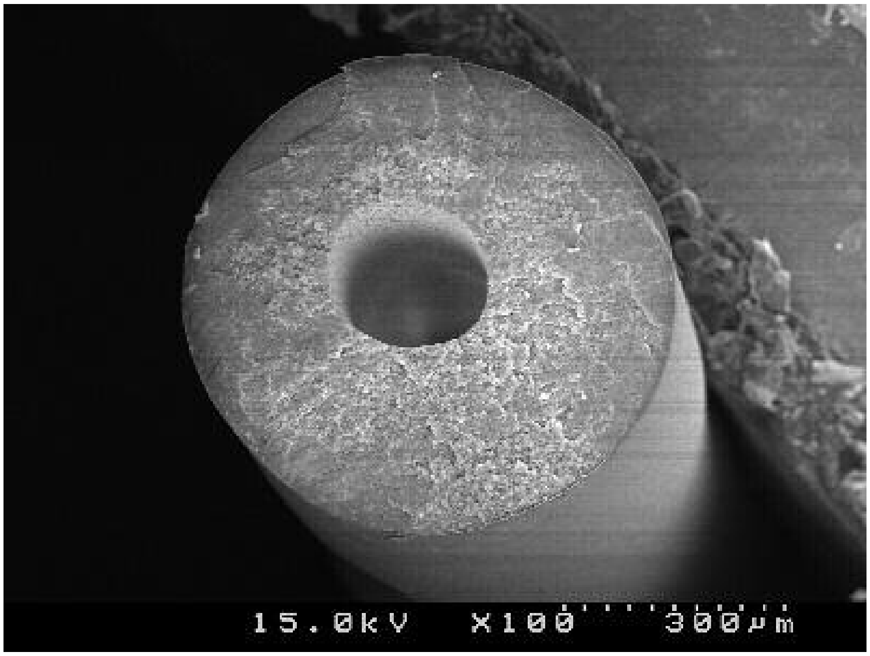

Figure A.26 Trial 4 Entire Cross-Section

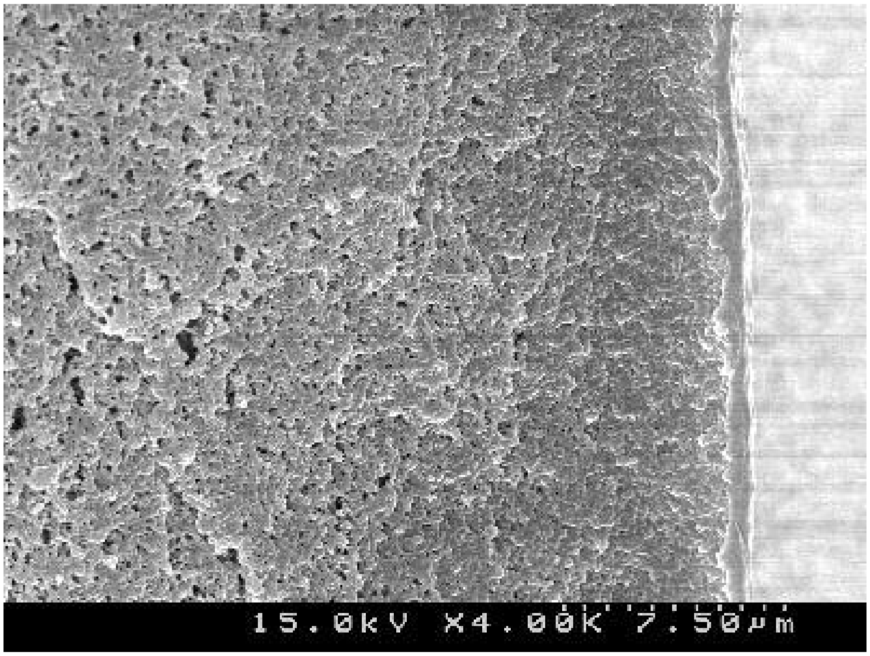

Figure A.27 Trial 4 Cross-Section Near Outer Wall

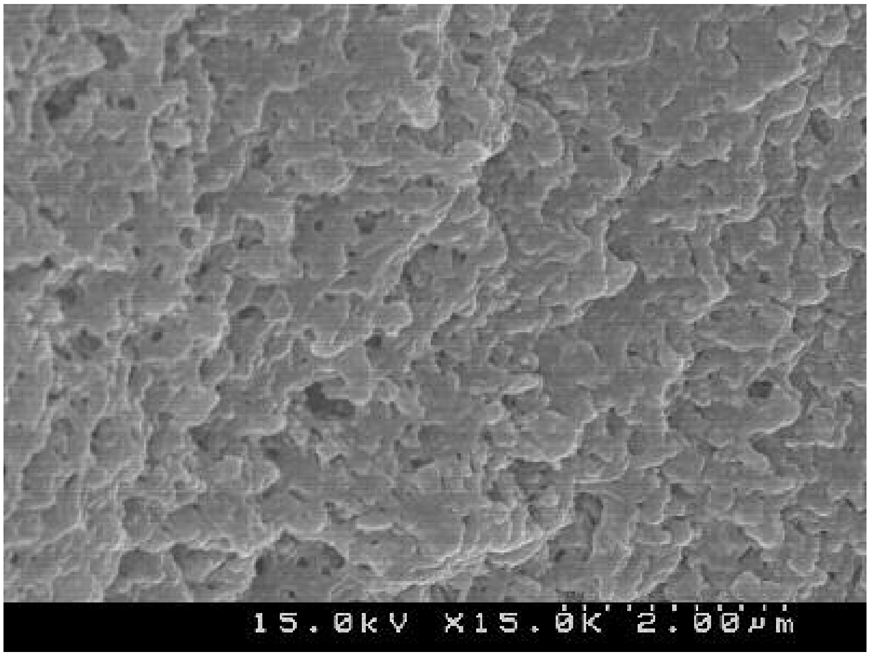

Figure A.28 Trial 4 Close-up of Anisotropic Boundary

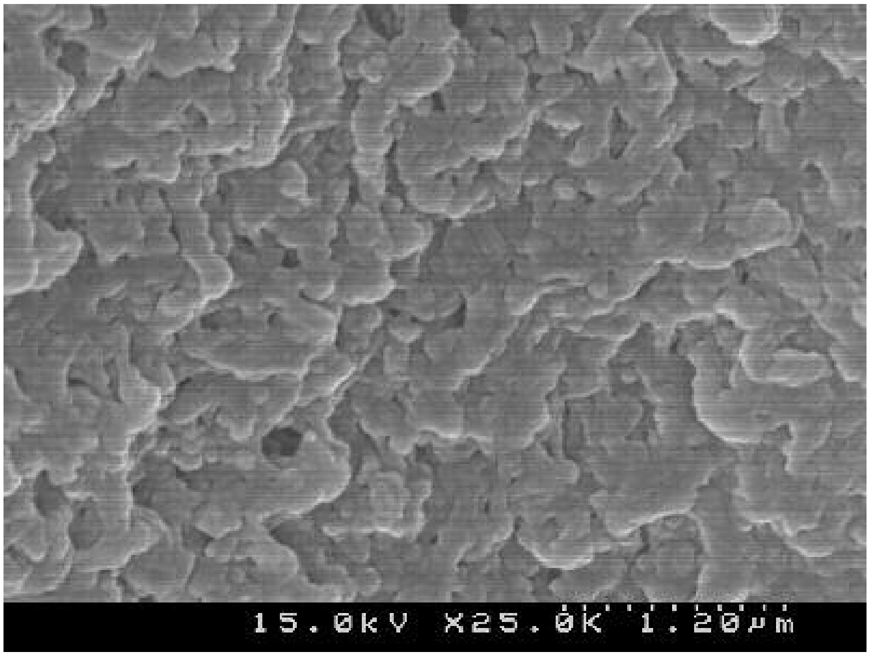

Figure A.29 Trial 4 Focus on Anisotropic Boundary

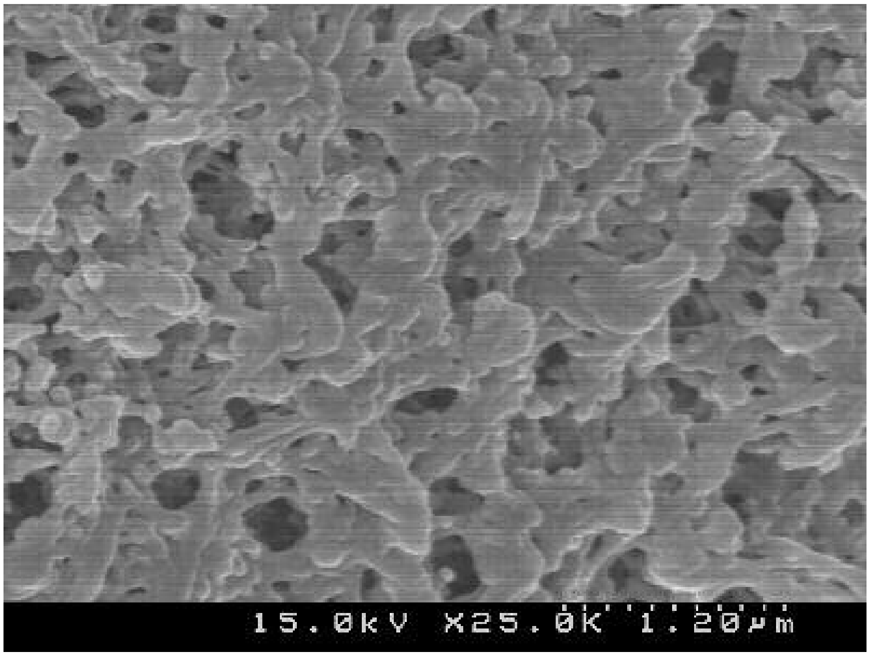

Figure A.30 Trial 4 Focus on Isotropic Boundary

A.8.5 Trial 6 SEM's

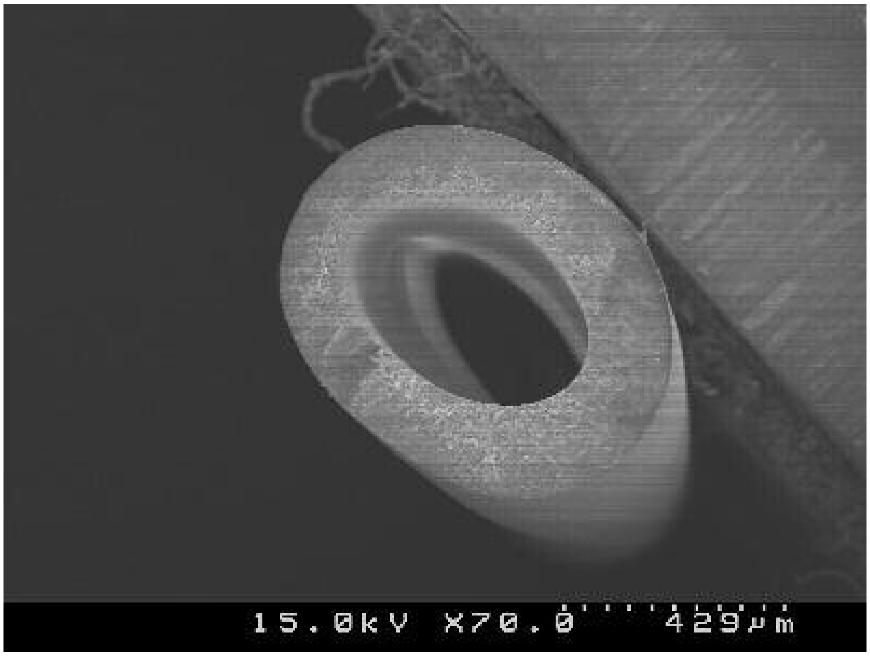

Figure A.31 Trial 6 Entire Cross-Section

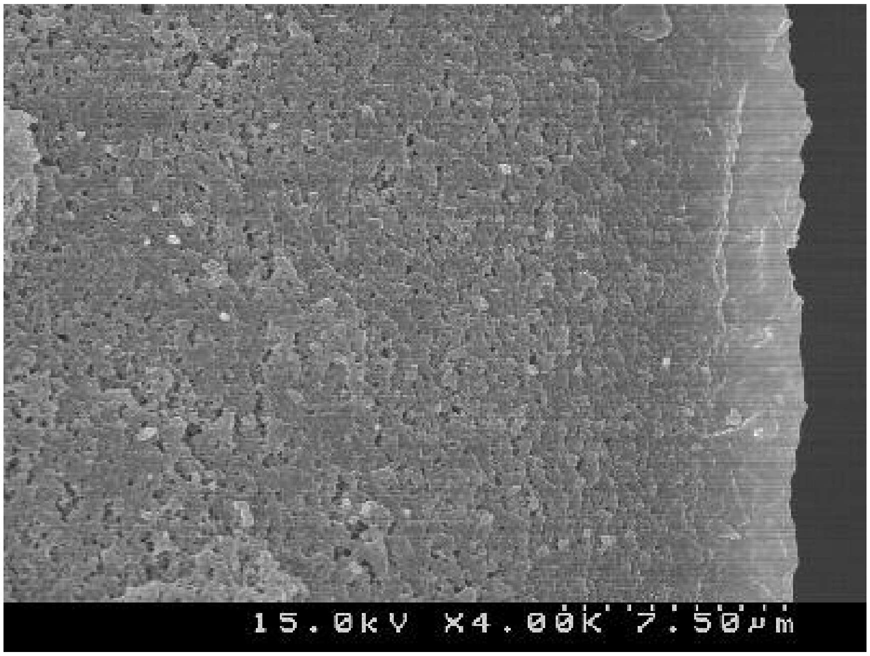

Figure A.32 Trial 6 Cross-Section Near Outer Wall

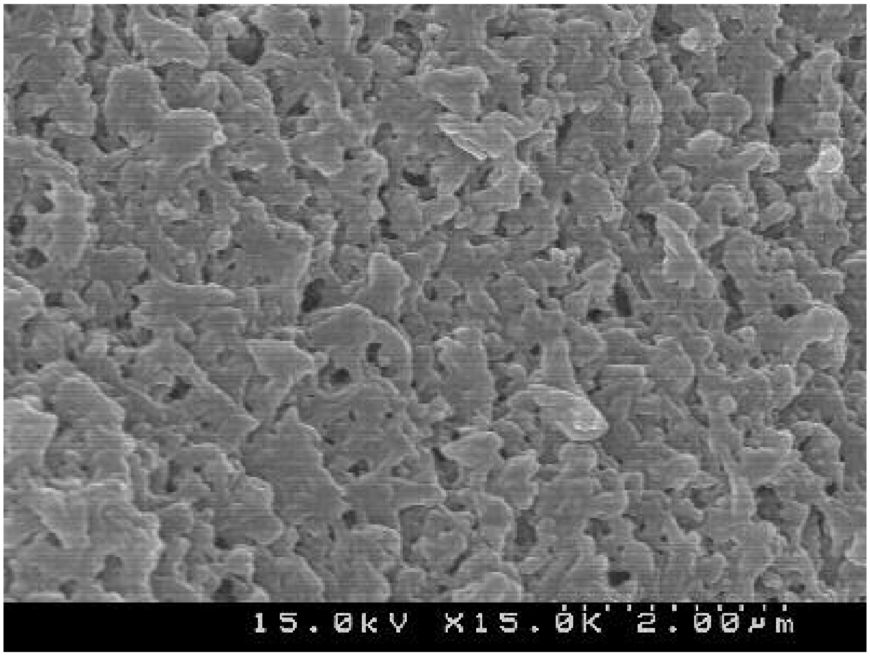

Figure A.33 Trial 6 Close-up of Anisotropic Boundary

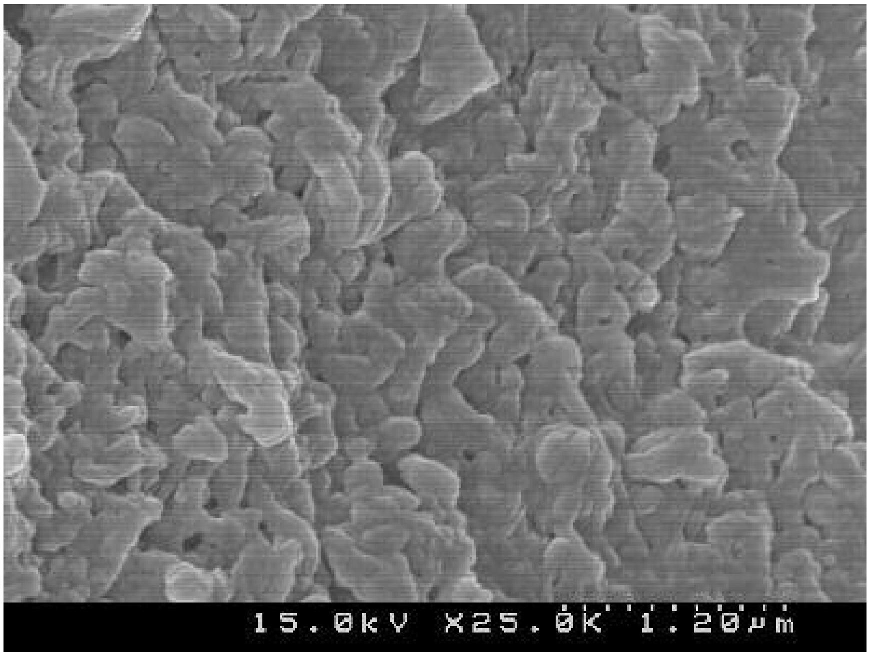

Figure A.34 Trial 6 Focus on Anisotropic Boundary

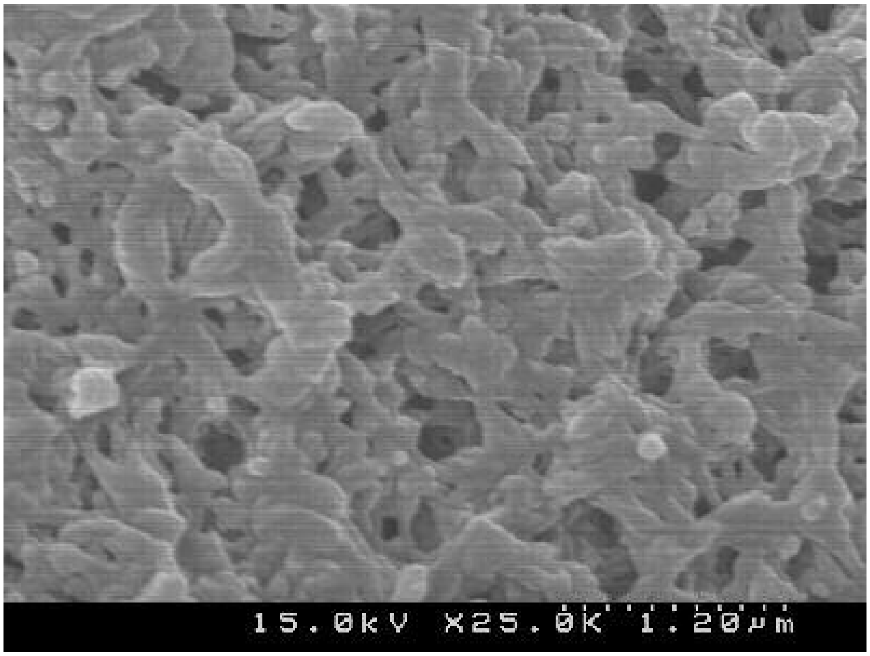

Figure A.35 Trial 6 Focus on Isotropic Boundary

A.8.6 Trial 7 SEM’s

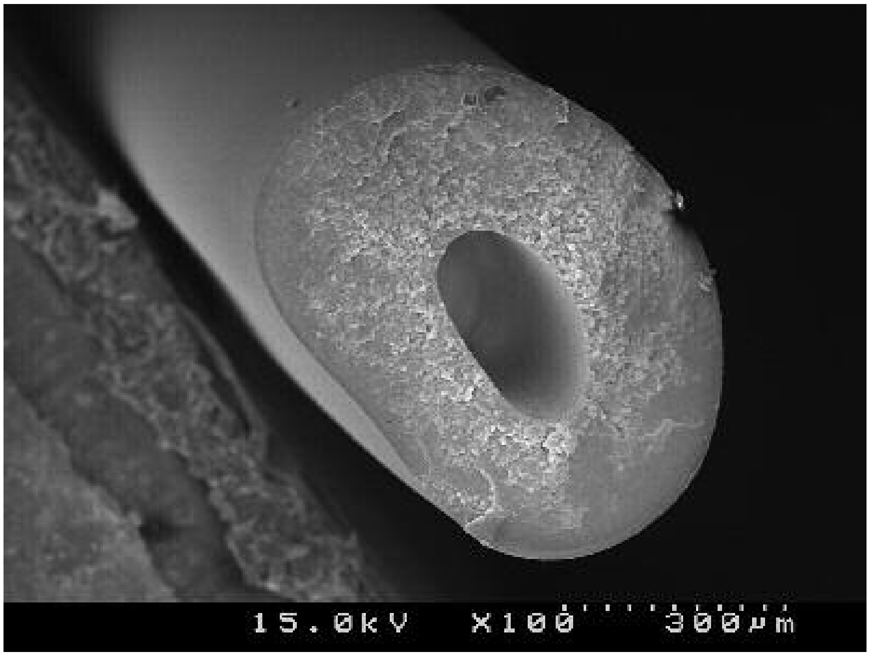

Figure A.36 Trial 7 Entire Cross-Section

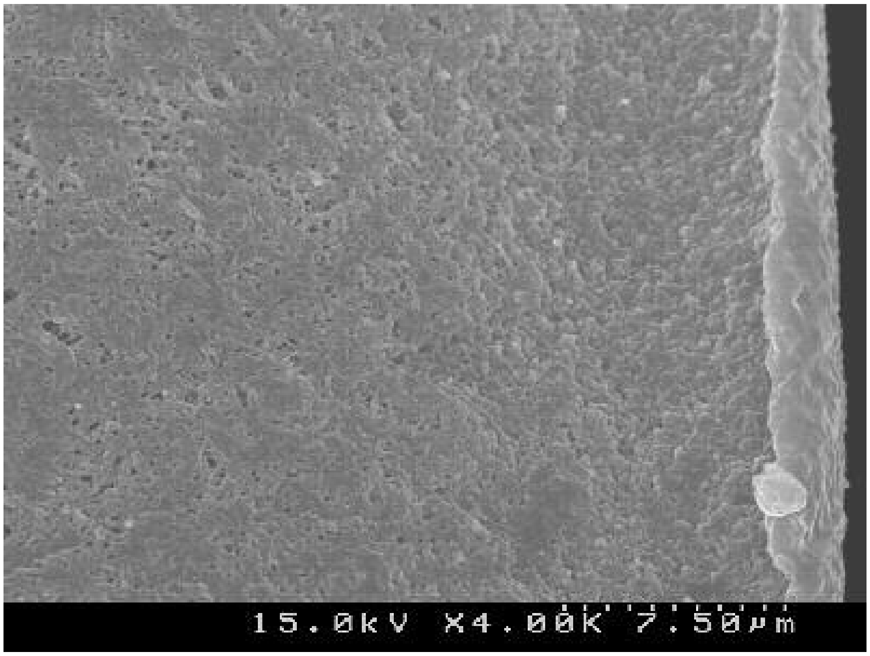

Figure A.37 Trial 7 Cross-Section Near Outer Wall

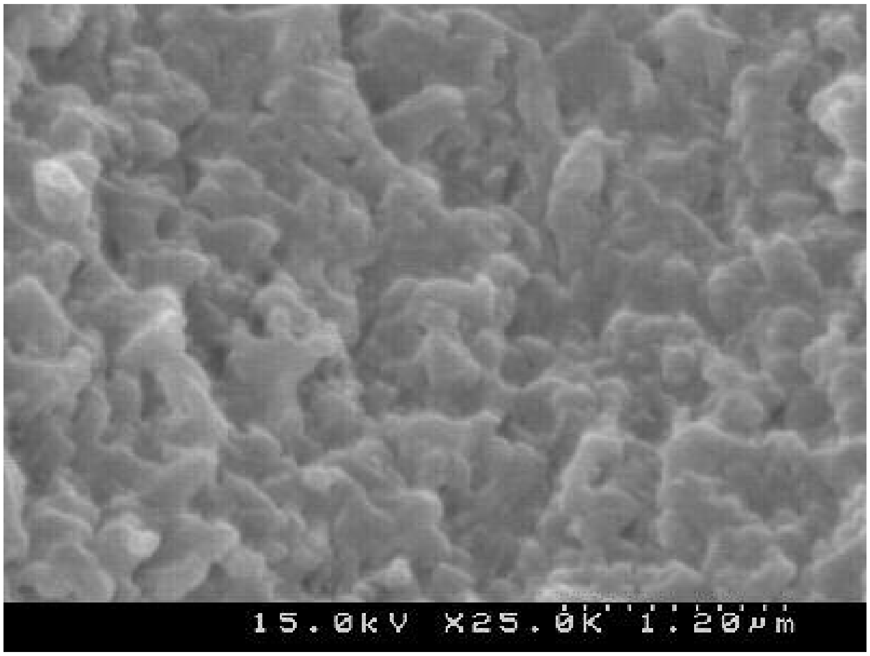

Figure A.38 Trial 7 Close-up of Anisotropic Boundary

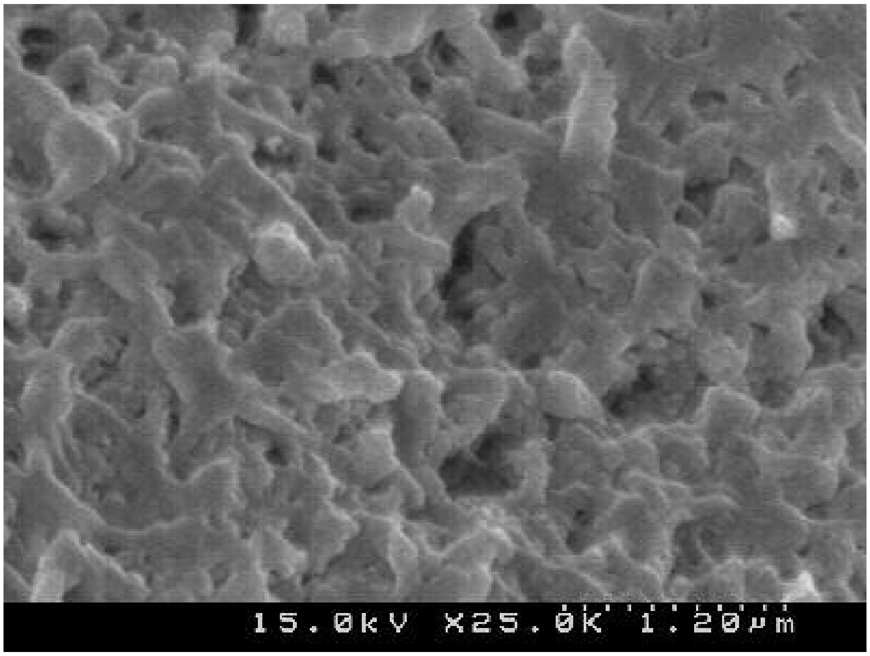

Figure A.39 Trial 7 Focus on Anisotropic Boundary

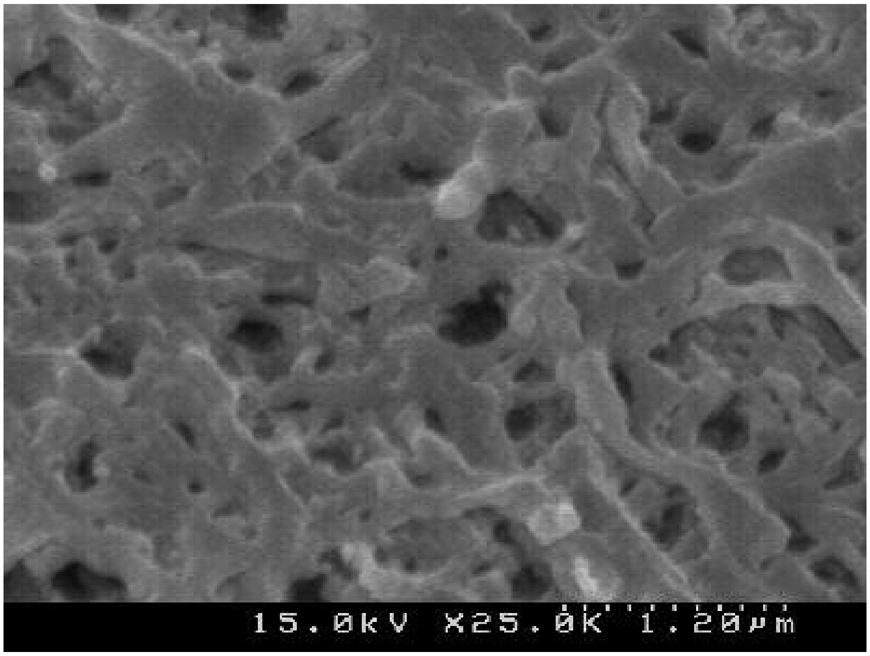

Figure A.40 Trial 7 Focus on Isotropic Boundary

A.8.7 Trial 8 SEM's

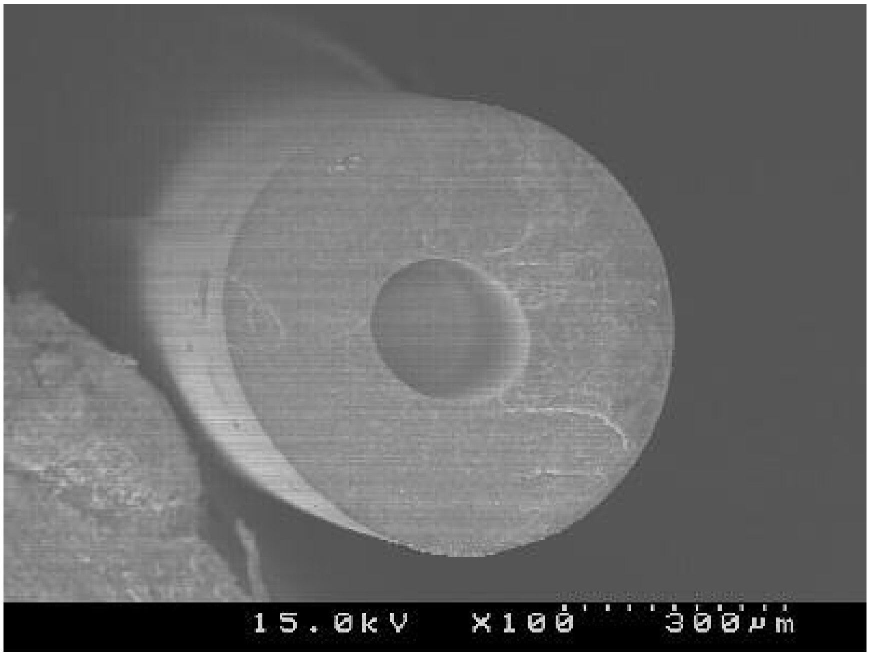

Figure A.41 Trial 8 Entire Cross-Section

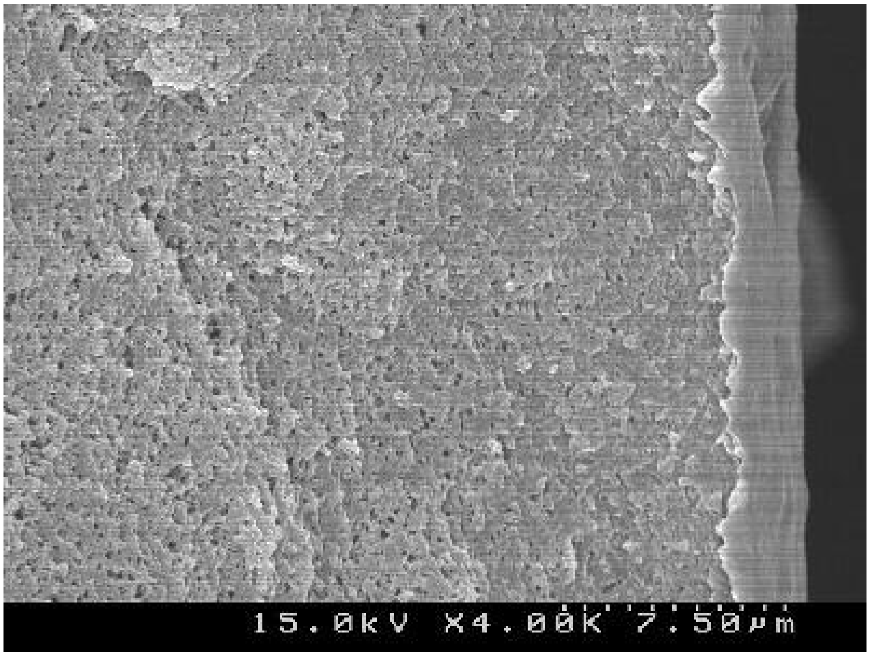

Figure A.42 Trial 8 Cross-Section Near Outer Wall

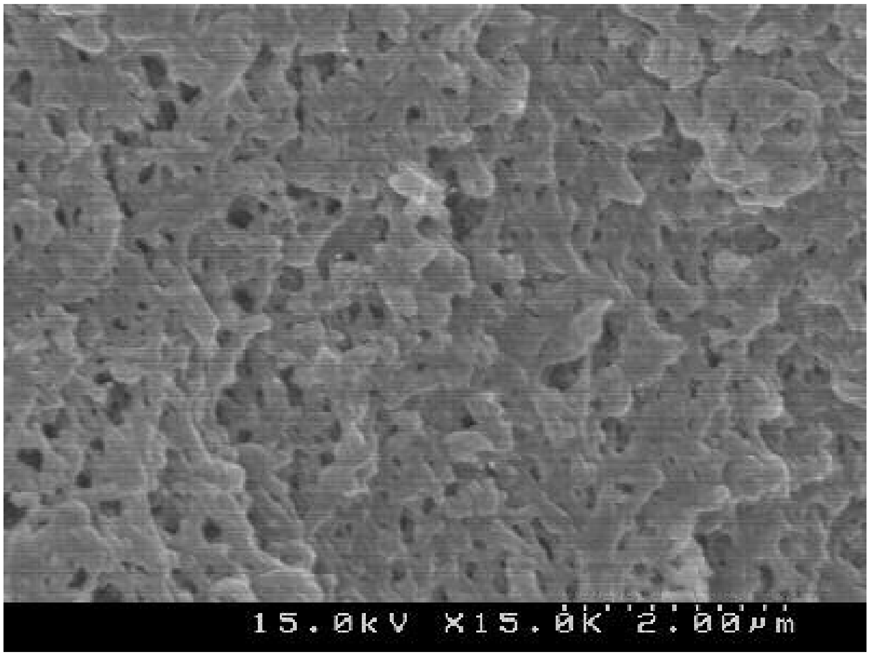

Figure A.43 Trial 8 Close-up of Anisotropic Boundary

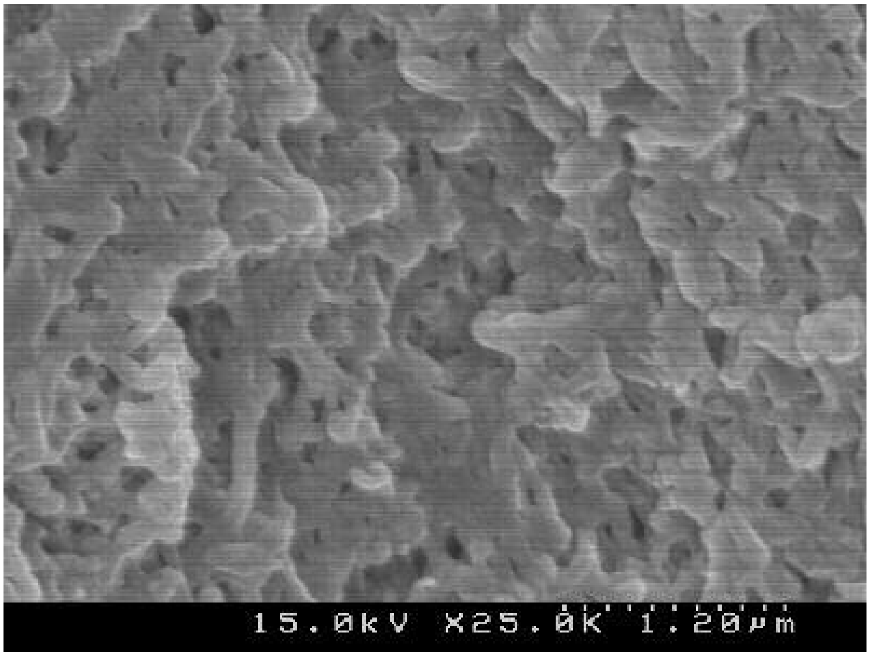

Figure A.44 Trial 8 Focus on Anisotropic Boundary

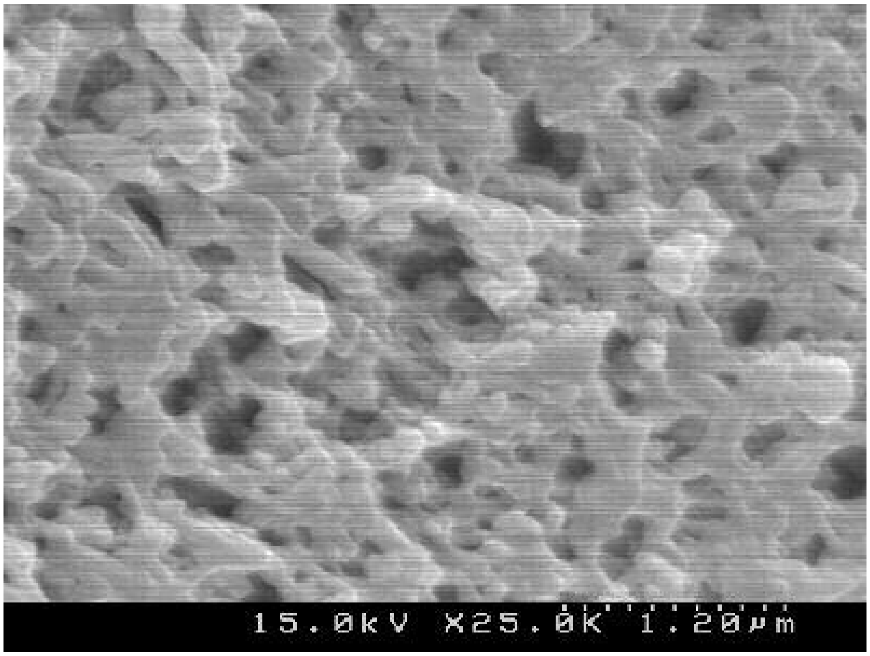

Figure A.45 Trial 8 Focus on Isotropic Boundary

A.9 Evaluating the Newtonian Fluid Assumption

The possible effects of non-Newtonian clad behavior were considered here. Figure 4.6 shows the experimentally measured shear viscosity as a function of shear rate for a temperature of 393 K. Data show that the 30 wt-% PE–dodecanol solution viscosity decreases as shear rate increases, indicating some shear-thinning behavior. However, a general rheology rule of thumb requires the viscosity to drop by a factor of 2 over the range of shears used in order to be classified as a shear-thinning fluid. The viscosity drop from approximately 70 Pa-s to approximately 40 Pa-s over the range of shears exhibited in Figure 4.6 is not significant enough to make this classification; in addition, the highest extension rates used here for membrane spinning, which can be compared to the range of shear rates for which shear thinning may be an issue, are on the order of 1 s^{-1}. Thus, the solution spun here should not exhibit significant shear-thinning effects for the range of operating conditions considered here. Furthermore, although not shown here, predicted diameter profiles for shear-thinning fluids have lower extension rates throughout the draw zone than Newtonian fluids [4]. From the measured diameter profiles reported for membrane spinning in Chapter 5, the model in its current form is not capturing an adequate rate of increase in spinline viscosity; that is, the extension rates are under-predicted using the modified TFA model with the Newtonian fluid constitutive equation. This supports the conclusion that the PE–dodecanol spinning system does not exhibit shear-thinning behavior for the range of conditions considered here.

Furthermore, viscoelastic effects were considered in terms of published results for solid fiber spinning [27]. The published results, presumably extending to hollow fiber spinning, indicate that in order for viscoelastic effects to be significant, the clad relaxation time must be on the order of 0.1 second for a typical hollow fiber membrane draw zone length of 0.200 m and a typical spinline maximum velocity of 0.02 m/s. This relaxation time is calculated based on the required value of the Weissenberg number, requiring a value of 0.01 for this parameter before viscoelasticity becomes important to spinline behavior. The viscosity-shear rate data, η_o and ω pairs, from Figure 4.6 was plotted following the general equation for a Maxwell fluid given in (A.13) to extract the value of the relaxation time λ [28]. In (A.13), C is a constant that could be used to express the temperature dependence of the spinline viscosity.

$$\frac{1}{\eta_o} = \frac{1}{C} + \frac{\lambda^2 \omega^2}{C} \qquad \text{(A.13)}$$

The result for the data of Figure 4.6 is a relaxation time on the order of 0.01 second, an order of magnitude faster than the value of 0.1 second necessary to produce significant spinline viscoelasticity. Thus, although the results published for solid fiber spinning indicate that viscoelasticity increase the elongation rate along the draw zone and would thus be expected to bring predicted and measured spinline diameter profiles into better agreement for the studies reported here, the calculated relaxation time indicates that these effects are not significant and the high observed rates of elongation are due to another source.

Finally, a general spinning sensivity study was performed using a factor of 10 to relate elongational viscosity to shear viscosity: for Newtonian fluids, *Trouton's ratio* of 3 applies, where the elongational viscosity is three times the shear viscosity value for a given temperature. Results indicate that consistently increasing all viscosities throughout the modeled draw zone in this fashion does not significantly change the predicted elongation rates, judging from the model-predicted diameter profiles. This indicates that it is the *rate of change* in viscosity throughout the draw zone that is important and not the viscosity magnitude for typical spinning operations.

A.10 References

1. M.M. Denn, Fibre Spinning, in: J.R.A. Pearson and S.M. Richardson (Eds.), Computational Analysis of Polymer Processing, Applied Science Publishers, London, 1983, pp. 179-216.
2. J. Brandrup, E.H. Immergut, and E.A. Grulke, (Eds.), Polymer Handbook, 4th ed., John Wiley & Sons, New York, 1999.
3. R.L. Rowley, W.V. Wilding, J.L. Oscarson, Y. Yang, R.J. Rowley, T.E. Daubert, and R.P. Danner, DIPPR® Data Compilation of Pure Compound Properties: Design Institute for Physical Property Data, AIChE®, New York, NY (2001).
4. G.G. Lipscomb, Personal Communication, 2004.
5. R.B. Bird, W.E. Stewart, and E.N. Lightfoot, Transport Phenomena, John Wiley & Sons, New York, 1960.
6. K. Irani, telephone and e-mail, April 2004 2004.
7. J.D. Stiehl, Undergraduate research report, The University of Texas at Austin May 1999.
8. M.T. Batarseh, Formation of anisotropic hollow fiber membranes via TIPS, Dissertation, The University of Texas at Austin, 1999.

9. J.C.d. Paula, Experimental Errors and Data Analysis, vol. 2004: Haverford College (2004).
10. G.T. Fieldson and T.A. Barbari, The Use of Ftir-Atr Spectroscopy to Characterize Penetrant Diffusion in Polymers, Polymer, 34 (1993) 1146-1153.
11. S.U. Hong, T.A. Barbari, and J.M. Sloan, Diffusion of methyl ethyl ketone in polyisobutylene: Comparison of spectroscopic and gravimetric techniques, Journal of Polymer Science Part B-Polymer Physics, 35 (1997) 1261-1267.
12. S.U. Hong and T.A. Barbari, Transport of toluene/methyl ethyl ketone mixtures polyisobutylene, Journal of Polymer Science Part B-Polymer Physics, 39 (2001) 908-914.
13. http://buphy.bu.edu/py106/notes/Refraction.html, Boston University, PY106--Elementary Physics II. United States (2000).
14. http://www.goodfellow.com/csp/active/static/A/ET31.HTML, Goodfellow Corporation, (2004).
15. F.J.P. Schuurmans, M. Megens, D. Vanmaekelbergh, and A. Lagendijk, Light scattering near the localization transition in macroporous GaP networks, Phys. Rev. Lett., 83 (1999) 2183-2186.
16. A. Harvey, http://www.madsci.org/posts/archives/nov2000/974149753.Ch.r.html, MadSci Network, (2000).
17. H.S. Carslaw and J.C. Jaeger, Conduction of Heat in Solids, Oxford University Press, Oxford, UK, 1959.
18. N.P. Cheremisinoff, (Ed.), Handbook of Heat and Mass Transfer, Gulf Publishing Co., Houston, 1986.
19. J. Lal and R. Bansil, Light-scattering study of kinetics of spinodal decomposition in a polymer solution, Macromolecules, 24 (1991) 290-297.
20. T. Hashimoto, J. Kumaki, and H. Kawai, Time-resolved light scattering studies on kinetics of phase separation and phase dissolution of polymer blends. 1. Kinetics of phase separation of a binary mixture of polystyrene and poly(vinyl methyl ether), Macromolecules, 16 (1983) 641-648.
21. K. Binder, Collective diffusion, nucleation, and spinodal decomposition in polymer mixtures, J. Chem. Phys., 79 (1983) 6387-6409.
22. H. Matsuyama, S. Kudari, H. Kiyofuji, and Y. Kitamura, Kinetic studies of thermally induced phase separation in polymer-diluent system, J. Appl. Polym. Sci., 76 (2000) 1028-1036.
23. H. Matsuyama, Personal Communication, 2003.
24. J.R. Howell, Personal Communication, 2003.
25. R. Siegel and J.R. Howell, Thermal Radiation Heat Transfer, 4th ed, Taylor & Francis, New York, 2002.
26. J.R. Howell, A Catalog of Radiation Configuration Factors, McGraw-Hill, New York, 1982. pages 243.
27. M.M. Denn, C.J.S. Petrie, and P. Avenas, Mechanics of Steady Spinning of a Viscoelastic Liquid, AIChE J., 21 (1975) 791-799.
28. M.M. Denn, Process Fluid Mechanics, 1st ed, Prentice-Hall, Inc., Englewood Cliffs, New Jersey, 1980. pages 383.

Appendix B. Detailed Derivation of the Thin Filament Analysis (TFA) for Fiber Spinning, Including Boundary Layer Analysis Specifics

NOTE: All symbols used in Appendix B are defined in the Glossary.

B.1 Continuity equation

B.1.1 Continuity equation for the clad

Standard form for cylindrical coordinates gives [1]:

$$\frac{\partial \rho_o}{\partial t} + \frac{1}{r}\frac{\partial}{\partial r}\left(\rho_o r v_{or}\right) + \frac{1}{r}\frac{\partial}{\partial \theta}\left(\rho_o v_\theta\right) + \frac{\partial}{\partial z}\left(\rho_o v_z\right) = 0 \qquad \text{(B.1)}$$

For an axisymmetric (about the z-axis) system at steady state and uniaxial extension in the z-direction, (B.1) can be reduced to (B.2).

$$\frac{1}{r}\frac{\partial}{\partial r}\left(\rho_o r v_{or}\right) + \frac{\partial}{\partial z}\left(\rho_o \bar{v}\right) = 0 \qquad \text{(B.2)}$$

Average each term over the clad cross-sectional area as shown in (B.3) through (B.5), invoking the assumption of constant clad density:

First term on the left-hand side:

$$\begin{aligned} 2\pi c\int_{Ri}^{Ro} r\left[\frac{1}{r}\frac{\partial}{\partial r}\left(\rho_o r v_{or}\right)\right]dr &= 2\pi\rho_o c\left(r v_{or}\right)\Big|_{Ri}^{Ro} \\ &= 2\pi\rho_o c\left(R_o v_{or}\big|_{Ro} - R_i v_{or}\big|_{Ri}\right) \qquad \text{(B.3)} \end{aligned}$$

where

$$c = \frac{1}{\pi\left(R_o^2 - R_i^2\right)} \qquad \text{(B.4)}$$

Second term on the left-hand side:

$$2\pi c\int_{Ri}^{Ro} r\frac{\partial}{\partial z}\left(\rho_o \bar{v}\right)dr = \pi c\rho_o \frac{d}{dz}\left[\left(R_o^2 - R_i^2\right)\bar{v}\right] - 2\pi c\rho_o r\frac{\partial r}{\partial z}\bar{v}\Bigg|_{Ri}^{Ro} \qquad \text{(B.5)}$$

Use the kinematic boundary condition, which states that no fluid crosses the interface between the fiber and the surrounding air or the lumen, to determine v_{or} at R_i and R_o. Steps leading to the equations given by (B.7) and (B.9) are given boxed as equations (B.6) and (B.8), respectively.

$$\boxed{\begin{aligned}
&v_o\big|_{Ro} = 0\\
&\left(v_o \bullet n_o^{\perp}\right)\Big|_{Ro} = 0\\
&\left(v_{or} \cdot n_{or}^{\perp} + \bar{v} \cdot n_{oz}^{\perp}\right)\Big|_{Ro} = 0\\
&\textit{where}\\
&n_{or}^{\perp} = 1 \; and \; n_{oz}^{\perp} = -\frac{dR_o}{dz}\\
&\textit{So}\\
&\left[\left(v_{or} \cdot 1\right) + \bar{v} \cdot \left(-\frac{dR_o}{dz}\right)\right]\Bigg|_{Ro} = 0
\end{aligned}} \tag{B.6}$$

$$v_{or}\big|_{Ro} = \left(\frac{dR_o}{dz}\bar{v}\right)\Bigg|_{Ro} \tag{B.7}$$

$$\boxed{\begin{aligned}
&v_o\big|_{Ri} = 0\\
&\left(v_o \bullet n_i^{\perp}\right)\Big|_{Ri} = 0\\
&\left(v_{or} \cdot n_{ior}^{\perp} + \bar{v} \cdot n_{iz}^{\perp}\right)\Big|_{Ri} = 0\\
&\textit{where}\\
&n_{ir}^{\perp} = -1 \; and \; n_{iz}^{\perp} = \frac{dR_i}{dz}\\
&\textit{So}\\
&\left[v_{or} \cdot \left(-1\right) + \bar{v} \cdot \left(\frac{dR_i}{dz}\right)\right]\Bigg|_{Ri} = 0
\end{aligned}} \tag{B.8}$$

$$v_{or}\big|_{Ri} = \left(\frac{dR_i}{dz}\bar{v}\right)\Bigg|_{Ri} \tag{B.9}$$

Combine the results shown in (B.2) through (B.10) to result in the clad continuity equation given by (B.10).

$$\pi\rho_o\left(R_o^2 - R_i^2\right)\bar{v} = w_o \qquad \text{(B.10)}$$

B.1.2 Continuity equation for the core

Average each term in (B.2) over the core cross-sectional area, assuming the core gas is well-mixed (no radial variation of the core gas density) and the spinline is undergoing uniaxial extension in the z-direction to give equations (B.11) and (B.12).

First term:

$$\frac{2\pi}{\pi R_i^2}\int_0^{Ri} r\frac{1}{r}\frac{\partial}{\partial r}\left(\rho_i r v_{ir}\right)dr = \frac{2}{R_i^2}\left(\rho_i r v_{ir}\right)\Big|_0^{Ri} = \frac{2}{R_i^2}\left[\rho_i R_i v_{ir}\big|_{Ri}\right] \qquad \text{(B.11)}$$

Second term:

$$\frac{2\pi}{\pi R_i^2}\int_0^{Ri} r\frac{\partial}{\partial z}\left(\rho_i\bar{v}\right)dr = \frac{2}{R_i^2}\frac{d}{dz}\left[\left(R_i^2\right)\rho_i\bar{v}\right] - \frac{2}{R_i^2}R_i\frac{\partial R_i}{\partial z}\rho_i\bar{v}\Big|_{Ri} \qquad \text{(B.12)}$$

Combine the results in (B.11) and (B.12) and apply the result in (B.9) to give the core continuity equation shown in (B.13).

$$\pi\left(R_i^2\right)\rho_i\bar{v} = w_i \qquad \text{(B.13)}$$

B.1.3 Combine continuity equations for clad and core

Solve core continuity (B.13) for R_i^2 to give (B.14).

$$R_i^2 = \frac{w_i}{\pi\rho_i\bar{v}} \qquad \text{(B.14)}$$

Solve clad continuity (B.10) for R_o^2 to give (B.15).

$$R_o^2 = \frac{w_o}{\pi\rho_o\bar{v}} + R_i^2 \qquad \text{(B.15)}$$

Combine (B.14) and (B.15) to get the complete fiber spinline continuity equation given in (B.16). This can be compared to equation (22) reported in the existing TFA cited here [2].

$$\boxed{\left(\frac{R_o}{R_i}\right)^2 = \frac{w_o}{R_i^2\pi\rho_o\bar{v}} + 1 = 1 + \frac{\rho_i w_o}{\rho_o w_i} = R_o^2\left(\frac{\pi\bar{v}\rho_i}{w_i}\right)} \qquad \text{(B.16)}$$

B.1.4 Radial velocity for incompressible fluids

Equation (B.17) results from continuity.

$$\frac{1}{r}\frac{\partial}{\partial r}\left(\rho r v_r\right)+\frac{\partial}{\partial z}\left(\rho v_z\right)=\rho\left[\frac{1}{r}\frac{\partial}{\partial r}\left(r v_r\right)+\frac{\partial}{\partial z}\left(v_z\right)\right]=0 \quad \text{(B.17)}$$

The density has been removed from the derivatives because it is assumed constant. Setting the term from (B.17) in square brackets to zero, multiplying by *r*, and integrating gives (B.18).

$$\int\frac{\partial}{\partial r}\left(r v_r dr\right)=-\int\frac{\partial}{\partial z}\left(v_z\right)r dr \quad \text{(B.18)}$$

Assuming v_z is a function of *z* only (uniaxial extension case), equation (B.19) results.

$$v_r=-\frac{r}{2}\frac{d\bar{v}}{dz}+\frac{C_j}{r} \qquad \text{(B.19)}$$

The C_j in (B.19) is a constant of integration, with $j = i$ for the core and $j = o$ for the clad. For the core, $v_{ir} = 0$ at $r = 0$, so $C_i = 0$. For the clad, $v_{ir} = v_{or}$ at $r = R_i$, so $C_o = 0$ and equation (B.20) results. This is equation (12) reported for the existing TFA cited here [2].

$$v_{ir}=v_{or}=-\frac{r}{2}\frac{d\bar{v}}{dz} \qquad \text{(B.20)}$$

B.1.5 Radial velocity for compressible fluids

Equation (B.21) expresses continuity for the clad.

$$\frac{1}{r}\frac{\partial}{\partial r}\left(\rho_o r v_{or}\right)+\frac{\partial}{\partial z}\left(\rho_o v_{oz}\right)=-\frac{\partial}{\partial t}\left(\rho_o\right) \qquad \text{(B.21)}$$

Multiplying (B.21) by *r* and integrating gives (B.22).

$$\int\frac{r}{r}\frac{\partial}{\partial r}\left(\rho_o r v_{or}\right)dr+\int\frac{\partial}{\partial z}\left(\rho_o v_{oz}\right)r dr=-\int\frac{\partial}{\partial t}\left(\rho_o\right)r dr \quad \text{(B.22)}$$

If v_z and ρ_o are functions of *z* and *t* only, (B.22) can be rewritten as (B.23).

$$\begin{aligned}
&\int\frac{r}{r}\frac{\partial}{\partial r}\left(\rho_o r v_{or}\right)dr=\int d\left(\rho_o r v_{or}\right)=\rho_o r v_{or}\\
&\int\frac{\partial}{\partial z}\left(\rho_o v_{oz}\right)r dr=\frac{r^2}{2}f_o(z,t) \qquad \text{(B.23)}\\
&\int\frac{\partial}{\partial t}\left(\rho_o\right)r dr=\frac{r^2}{2}g_o(z,t)
\end{aligned}$$

Therefore, continuity from (B.21) becomes (B.24).

$$\rho_o r v_{or}=-\frac{r^2}{2}f_o-\frac{r^2}{2}g_o+h_o=-\frac{r^2}{2}\frac{\partial}{\partial z}\left(\rho_o v_{oz}\right)-\frac{r^2}{2}\frac{\partial}{\partial t}\left(\rho_o\right)+h_o \quad \text{(B.24)}$$

In (B.24), h_o may be a function of *z* and *t*. Dividing (B.24) by *r* gives (B.25).

$$\rho_o v_{or}=-\frac{r}{2}f_o-\frac{r}{2}g_o+\frac{h_o}{r}=-\frac{r}{2}\frac{\partial}{\partial z}\left(\rho_o v_{oz}\right)-\frac{r}{2}\frac{\partial}{\partial t}\left(\rho_o\right)+\frac{h_o}{r} \qquad \text{(B.25)}$$

The same procedure leads to equation (B.26) for the core.

$$\rho_i v_{ir} = -\frac{r}{2} f_i - \frac{r}{2} g_i + \frac{h_i}{r} = -\frac{r}{2}\frac{\partial}{\partial z}\left(\rho_i v_{iz}\right) - \frac{r}{2}\frac{\partial}{\partial t}\left(\rho_i\right) + \frac{h_i}{r} \qquad \text{(B.26)}$$

For the core, $h_i = 0$ since the velocity is finite at $r = 0$ and (B.26) becomes (B.27) with the uniaxial extension assumption.

$$\begin{aligned} \rho_i v_{ir} &= -\frac{r}{2}\frac{\partial}{\partial z}\left(\rho_i v_{iz}\right) - \frac{r}{2}\frac{\partial}{\partial t}\left(\rho_i\right) = -\frac{r}{2}\left(\rho_i \frac{\partial}{\partial z}\left(v_{iz}\right) + v_{iz}\frac{\partial}{\partial z}\left(\rho_i\right) + \frac{\partial}{\partial t}\left(\rho_i\right)\right) \\ &= -\frac{r}{2}\left(\rho_i \frac{d}{dz}\left(\bar{v}\right) + \frac{D}{Dt}\left(\rho_i\right)\right) \end{aligned} \qquad \text{(B.27)}$$

The substantial derivative of the core gas density is defined in (B.28) since the core density is dependent only on time and axial position.

$$\frac{D\rho_i}{Dt} = \frac{\partial \rho_i}{\partial t} + v \bullet \nabla \rho_i = \frac{\partial \rho_i}{\partial t} + v_{ir}\frac{\partial \rho_i}{\partial r} + \frac{v_{i\theta}}{r}\frac{\partial \rho_i}{\partial \theta} + v_{iz}\frac{\partial \rho_i}{\partial z} = \frac{\partial \rho_i}{\partial t} + v_{iz}\frac{\partial \rho_i}{\partial z} \qquad \text{(B.28)}$$

Dividing (B.28) by the core density and noting that $v_{iz} = \bar{v}_z$ gives (B.29), which is equation (11b) in the existing TFA for fiber spinning [2].

$$v_{ir} = -\frac{r}{2}\left(\frac{d}{dz}\left(\bar{v}\right) + \frac{1}{\rho_i}\frac{D}{Dt}\left(\rho_i\right)\right) = -\frac{r}{2}\left(\frac{d}{dz}\left(\bar{v}\right) + \frac{D}{Dt}\left(\ln \rho_i\right)\right) \qquad \text{(B.29)}$$

Equation (B.30) applies to the clad.

$$\rho_o v_{or} = -\frac{r}{2}\frac{\partial}{\partial z}\left(\rho_o v_{oz}\right) - \frac{r}{2}\frac{\partial}{\partial t}\left(\rho_o\right) + \frac{h_o}{r} \qquad \text{(B.30)}$$

Equating $v_{ir} = v_{or}$ at R_i, the clad–core interface, gives (B.31).

$$\begin{aligned} v_{ir}\big|_{R_i} = -\frac{R_i}{2}\left(\frac{d}{dz}\left(\bar{v}\right) + \frac{D}{Dt}\left(\ln \rho_i\right)\right) = v_{or}\big|_{Ri} &= -\frac{R_i}{2}\left(\frac{\partial}{\partial z}\left(v_{oz}\right) + \frac{v_{oz}}{\rho_o}\frac{\partial}{\partial z}\left(\rho_o\right) + \frac{1}{\rho_o}\frac{\partial}{\partial t}\left(\rho_o\right)\right) \\ &+ \frac{h_o}{\rho_o R_i} \end{aligned} \qquad \text{(B.31)}$$

Equation (B.31) can be rewritten as (B.32).

$$\frac{d\bar{v}}{dz} + \frac{D\ln \rho_i}{Dt} = \frac{\partial v_{oz}}{\partial z} + \frac{v_{oz}}{\rho_o}\frac{\partial \rho_o}{\partial z} + \frac{1}{\rho_o}\frac{\partial \rho_o}{\partial t} - \frac{2h_o}{\rho_o R_i^2} = \frac{d\bar{v}}{dz} + \frac{D\ln \rho_o}{Dt} - \frac{2h_o}{\rho_o R_i^2} \qquad \text{(B.32)}$$

Therefore, equation (B.33) results.

$$\frac{2h_o}{\rho_o R_i^2} = \frac{d\bar{v}}{dz} + \frac{D\ln \rho_o}{Dt} - \frac{d\bar{v}}{dz} - \frac{D\ln \rho_i}{Dt} = \frac{D\left[\ln\left(\rho_o/\rho_i\right)\right]}{Dt} \qquad \text{(B.33)}$$

Equation (B.33) gives the result shown in (B.34).

$$h_o = \frac{\rho_o R_i^2}{2}\frac{D\left[\ln\left(\rho_o/\rho_i\right)\right]}{Dt} \qquad \text{(B.34)}$$

Substituting from (B.34) into the expression for the clad radial velocity given in (B.30) gives (B.35). This is equation (11a) in the previously published TFA cited here [2].

$$v_{or} = -\frac{r}{2}\left(\frac{\partial \overline{v}}{\partial z} + \frac{D\ln\rho_o}{Dt}\right) + \frac{R_i^2}{2r}\frac{D\left[\ln\left(\rho_o/\rho_i\right)\right]}{Dt} \qquad \text{(B.35)}$$

B.2 Momentum equations

B.2.1 Clad axial momentum balance

Standard form of an axial momentum balance in cylindrical coordinates [3]:

$$\begin{gathered}\rho_o\left(\frac{\partial v_{oz}}{\partial t} + v_{or}\frac{\partial v_{oz}}{\partial r} + \frac{v_{o\theta}}{r}\frac{\partial v_{oz}}{\partial \theta} + v_{oz}\frac{\partial v_{oz}}{\partial z}\right) = \\ -\frac{\partial p}{\partial z} + \left[\frac{1}{r}\frac{\partial}{\partial r}\left(r\tau_{orz}\right) + \frac{1}{r}\frac{\partial \tau_{o\theta z}}{\partial \theta} + \frac{\partial \tau_{ozz}}{\partial z}\right] + \rho g\end{gathered} \qquad \text{(B.36)}$$

For steady state, negligible gravity effects (gravity can be included by interpreting the pressure term as the equivalent pressure $p - \rho_o g$), and an axisymmetric (about the z-axis) case with uniaxial extension in the z-direction, equation (B.37) applies.

$$\rho_o\left(\underbrace{v_{or}\frac{\partial \overline{v}}{\partial r}}_{\text{Term 1}} + \underbrace{\overline{v}\frac{\partial \overline{v}}{\partial z}}_{\text{Term 2}}\right) = -\underbrace{\frac{\partial p}{\partial z}}_{\text{Term 3}} + \left[\underbrace{\frac{1}{r}\frac{\partial}{\partial r}\left(r\tau_{orz}\right)}_{\text{Term 4}} + \underbrace{\frac{\partial \tau_{ozz}}{\partial z}}_{\text{Term 5}}\right] \qquad \text{(B.37)}$$

Average term 1 (including the ρ_o factor) over the clad cross-sectional area using integration by parts to yield (B.38) for a constant density clad.

$$\rho_o 2\pi c\int_{Ri}^{Ro} r v_{or}\frac{d\overline{v}}{dr}dr = 2\pi c\rho_o r v_{or}\overline{v}\Big|_{Ri}^{Ro} - 2\pi c\rho_o\int_{Ri}^{Ro}\overline{v}\frac{\partial}{\partial r}\left(r v_{or}\right)dr \qquad \text{(B.38)}$$

where c is defined by equation (B.4). Continuity, shown in (B.2), gives

$$\rho_o\frac{\partial}{\partial r}\left(r v_{or}\right) = -\rho_o r\frac{\partial}{\partial z}\left(\overline{v}\right) \qquad \text{(B.39)}$$

Substitute the result from (B.39) into (B.38) to give (B.40).

$$\rho_o 2\pi c\int_{Ri}^{Ro} r v_{or}\frac{d\overline{v}}{dr}dr = \rho_o 2\pi c r v_{or}\overline{v}\Big|_{r=Ri}^{r=Ro} + \int_{Ri}^{Ro} 2\pi c\overline{v} r\frac{\partial}{\partial z}\left(\rho_o\overline{v}\right)dr \qquad \text{(B.40)}$$

Average term 2 from (B.37), including the ρ_o factor, over the clad cross-sectional area and add the result to (B.40) to get (B.41).

$$\int_{Ri}^{Ro}\left(\rho_o v_{or}\frac{\partial \overline{v}}{\partial r} + \rho_o\overline{v}\frac{\partial \overline{v}}{\partial z}\right)\left(2\pi c r\right)dr = 2\pi c r\rho_o v_{or}\overline{v}\Big|_{r=Ri}^{r=Ro} + \int_{Ri}^{Ro} 2\pi c\rho_o r\left[\frac{\partial\left(\overline{v^2}\right)}{\partial z}\right]dr \qquad \text{(B.41)}$$

The Leibniz rule, given in (B.42), is used next.

$$\begin{aligned}2\pi\int_{Ri}^{Ro}\frac{\partial\psi}{\partial z}rdr &= \pi\left(R_o^2-R_i^2\right)\frac{d\overline{\psi}}{dz}-2\pi\left[r\frac{dr}{dz}\left(\psi-\overline{\psi}\right)\right]\Bigg|_{r=Ri}^{r=Ro} \\ &= \frac{d}{dz}\left[\pi\left(R_o^2-R_i^2\right)\overline{\psi}\right]-2\pi r\frac{dr}{dz}\psi\Bigg|_{r=Ri}^{r=Ro}\end{aligned} \tag{B.42}$$

Use (B.42) with (B.41) to get equation (B.43).

$$\begin{aligned}\int_{Ri}^{Ro}\left(\rho_o v_{or}\frac{\partial\overline{v}}{\partial r}+\rho_o\overline{v}\frac{\partial\overline{v}}{\partial z}\right)(2\pi cr)dr &= 2\pi cr\rho_o v_{or}\overline{v}\Big|_{r=Ri}^{r=Ro}+\pi c\rho_o\frac{d}{dz}\left[\left(R_o^2-R_i^2\right)\left(\overline{v^2}\right)\right] \\ &\quad -2\pi c\rho_o r\frac{dr}{dz}\left(\overline{v^2}\right)\Bigg|_{r=Ri}^{r=Ro}\end{aligned} \tag{B.43}$$

Apply the kinematic BC's, (B.7) and (B.9), to (B.43) to get equation (B.44) for the clad cross-sectional area average of terms 1 and 2 in (B.37).

$$\int_{Ri}^{Ro}\left(\rho_o v_{or}\frac{\partial\overline{v}}{\partial r}+\rho_o\overline{v}\frac{\partial\overline{v}}{\partial z}\right)(2\pi cr)dr=\rho_o\pi c\frac{d}{dz}\left[\left(R_o^2-R_i^2\right)\left(\overline{v^2}\right)\right] \tag{B.44}$$

Average term 3 in (B.37) over the clad cross-sectional area and use (B.42) to get (B.45).

$$-\int_{Ri}^{Ro}2\pi c\frac{\partial p}{\partial z}rdr=-\pi c\frac{d}{dz}\left[\left(R_o^2-R_i^2\right)\overline{p}\right]+2\pi cr\frac{dr}{dz}p\Bigg|_{r=Ri}^{r=Ro} \tag{B.45}$$

Average term 4 in (B.37) over the clad cross-sectional area to get (B.46).

$$2\pi c\int_{Ri}^{Ro}\frac{\partial}{\partial r}\left(r\tau_{orz}\right)dr=2\pi cr\tau_{orz}\Big|_{r=Ri}^{r=Ro} \tag{B.46}$$

Average term 5 in (B.37) over the clad cross-sectional area and use (B.42) to get (B.47).

$$2\pi c\int_{Ri}^{Ro}r\frac{\partial\tau_{ozz}}{\partial z}dr=\pi c\frac{d}{dz}\left[\left(R_o^2-R_i^2\right)\overline{\tau_{ozz}}\right]-2\pi cr\frac{dr}{dz}\tau_{ozz}\Bigg|_{r=Ri}^{r=Ro} \tag{B.47}$$

Combine the results for terms 1-5 from (B.37) by adding (B.44)–(B.47) to get (B.48).

$$\frac{d}{dz}\left[\pi\left(R_o^2 - R_i^2\right)\left(\rho_o \overline{v^2}\right)\right] = \pi\frac{d}{dz}\left[\left(R_o^2 - R_i^2\right)\left(\overline{\tau_{ozz}} - \overline{p}\right)\right] + 2\pi r\left(\tau_{orz} - \frac{dr}{dz}\tau_{ozz} + \frac{dr}{dz}p\right)\Bigg|_{r=Ri}^{r=Ro} \qquad \text{(B.48)}$$

Combine the deviatoric stress terms (τ_{jk}'s) with the pressure terms to write as Newtonian total stress tensors; substitute for the clad area $A_o = \pi\left(R_o^2 - R_i^2\right)$; and expand the last term on the right hand side of (B.48) to get equation (B.49).

$$\frac{d}{dz}\left[\left(\rho_o \overline{v^2} A_o\right)\right] = \frac{d}{dz}\left[A_o \overline{\sigma_{ozz}}\right] + 2\pi R_o\left[\sigma_{orz}\big|_{Ro} - \frac{dR_o}{dz}\left(\sigma_{ozz}\big|_{Ro}\right)\right] + 2\pi R_i\left[-\sigma_{orz}\big|_{Ri} - \frac{dR_i}{dz}\left(\sigma_{ozz}\big|_{Ri}\right)\right] \qquad \text{(B.49)}$$

B.2.2 Core axial momentum balance

The derivation for the core momentum balance is analogous to that for the clad. Starting from the standard form given in (B.36) and radial averaging over the core cross-sectional area produces equation (B.50). As with the clad, gravity can be included by interpreting the pressure term as the equivalent pressure p_i–$\rho_i g$.

$$\frac{d}{dz}\left[\left(\rho_i \overline{v^2} A_i\right)\right] = \frac{d}{dz}\left[A_i \overline{\sigma_{izz}}\right] + 2\pi R_i\left[\sigma_{irz}\big|_{Ri} - \frac{dR_i}{dz}\left(\sigma_{izz}\big|_{Ri}\right)\right] \qquad \text{(B.50)}$$

Force balances at the interface are required to express the stress tensor terms applying at R_o and R_i in (B.49) and (B.50). A radial momentum balance is necessary to express the average clad pressure, implicit in the $\overline{\sigma_{ozz}}$ Newtonian fluid stress tensor term in (B.49), as a function of other spinline variables.

B.2.3 Interfacial stress balances

These stress balances are the key to including surface tension effects in the TFA for fiber spinning. The derivation is shown here including surface tension, with the final results reduced to the existing TFA conditions [2] by setting surface tension equal to zero.

B.2.3.1 Stress balances at the core–clad interface at R_i

The normal stress balance including surface tension that applies at the core–clad interface at R_i appears in (B.51).

$$\left[\sigma_o \bullet \left(-n_i^{\perp}\right) \bullet n_i^{\perp} + \sigma_i \bullet n_i^{\perp} \bullet n_i^{\perp} = \gamma\left(\nabla \bullet n_i^{\perp}\right)\right]\Big|_{Ri} \qquad \text{(B.51)}$$

The components of the unit normal vector $n_i^{\perp}$ appear in (B.8). For cylindrical coordinates, the divergence of the normal vector results in (B.52).

$$\nabla \bullet n_i^{\perp}\Big|_{Ri} = \frac{1}{R_i}\left[-1 + R_i \frac{\partial^2 R_i}{\partial z^2}\right] \qquad \text{(B.52)}$$

In (B.52), the second term on the right hand side can be neglected due to the thin filament assumption. With this result, the normal stress balance at *R*R_i shown in (B.51) becomes (B.53).

$$\left[\sigma_o \bullet n_i^{\perp} \bullet n_i^{\perp} = \sigma_i \bullet n_i^{\perp} \bullet n_i^{\perp} + \frac{\gamma}{R_i}\right]\Bigg|_{Ri} \qquad \text{(B.53)}$$

Computing the dot products in (B.53), assuming symmetric Newtonian fluid stress tensors and a core gas with negligible viscosity and invoking the thin filament assumption, produces (B.54).

$$\left(\sigma_{orr} - 2\frac{dR_i}{dz}\sigma_{orz} = -\overline{p}_i + \frac{\gamma}{R_i}\right)\Bigg|_{Ri} \qquad \text{(B.54)}$$

The tangential stress balance at the clad–core interface at R_i is not affected by surface tension and appears in (B.55). The components of the unit tangent vector n_i^{ll} appear in (B.8).

$$\left[\sigma_o \bullet n_i^{\perp} \bullet n_i^{ll} = \sigma_i \bullet n_i^{\perp} \bullet n_i^{ll}\right]\Big|_{Ri} \qquad \text{(B.55)}$$

Computing the dot products in (B.55), assuming symmetric Newtonian fluid stress tensors and a core gas with negligible viscosity and invoking the thin filament assumption, produces (B.56). This is the expression for tangential stress equilibrium at the core–clad interface at R_i.

$$\boxed{\left[\sigma_{orz} = \frac{dR_i}{dz}\left(\sigma_{ozz} - \sigma_{orr}\right)\right]\Bigg|_{Ri}} \qquad \text{(B.56)}$$

Substituting from (B.56) into (B.54) and invoking the thin filament assumption results in (B.57), the expression for normal stress equilibrium at the core–clad interface at R_i.

$$\boxed{\left(\sigma_{orr} = \frac{\gamma}{R_i} - \overline{p}_i\right)\Bigg|_{Ri}} \qquad \text{(B.57)}$$

As stated in section B.2.3, setting surface tension equal to zero recovers the normal stress equilibrium expression from the existing TFA for fiber spinning as given by (B.58).

$$\boxed{\left(\sigma_{orr} = -\overline{p}_i\right)\Big|_{Ri}} \qquad \text{(B.58)}$$

B.2.3.2 Stress balances at the clad–air quench interface at R_o

The correlations in this section are developed analogous to those in section B.2.2.1 for the core–clad interface at R_i. The normal stress balance including surface tension that applies at the clad–air quench interface at R_o appears in (B.59).

$$\left\lfloor \sigma_o \bullet \left(-n_o^{\perp}\right) \bullet n_o^{\perp} = \gamma\left(\nabla \bullet n_o^{\perp}\right)\right\rfloor\Big|_{Ro} \qquad \text{(B.59)}$$

The components of the unit normal vector $n_o^{\perp}$ appear in (B.6). For cylindrical coordinates, the divergence of the normal vector results in (B.60).

$$\nabla \bullet n_o^{\perp}\Big|_{Ro} = \frac{1}{R_o}\left[1 - R_o\frac{\partial^2 R_o}{\partial z^2}\right] \qquad \text{(B.60)}$$

In (B.60), the second term on the right hand side can be neglected due to the thin filament assumption. With this result, the normal stress balance at R_o shown in (B.59) becomes (B.61).

$$\left[\sigma_o \bullet n_o^{\perp} \bullet n_o^{\perp} = -\frac{\gamma}{R_o}\right]\Bigg|_{Ro} \qquad \text{(B61)}$$

Computing the dot products in (B.61), assuming symmetric Newtonian fluid stress tensors and invoking the thin filament assumption, produces (B.62).

$$\left(\sigma_{orr} - 2\frac{dR_o}{dz}\sigma_{orz} = -\frac{\gamma}{R_o}\right)\Bigg|_{Ro} \qquad \text{(B.62)}$$

The tangential stress balance at the clad–air quench interface at R_o is not affected by surface tension and appears in (B.63). The components of the unit tangent vector n_o^{ll} appear in (B.6).

$$\left\lfloor \sigma_o \bullet n_o^{\perp} \bullet n_o^{ll} = 0\right\rfloor\Big|_{Ro} \qquad \text{(B.63)}$$

Computing the dot products in (B.63), assuming symmetric Newtonian fluid stress tensors and invoking the thin filament assumption, produces (B.64). This is the expression for tangential stress equilibrium at the clad–air quench interface at R_o.

$$\boxed{\left[\sigma_{orz} = \frac{dR_o}{dz}\left(\sigma_{ozz} - \sigma_{orr}\right)\right]\Bigg|_{Ro}} \qquad \text{(B.64)}$$

Substituting from (B.64) into (B.62) and invoking the thin filament assumption results in (B.65), the expression for normal stress equilibrium at the clad–air quench interface at R_o.

$$\boxed{\left(\sigma_{orr} = -\frac{\gamma}{R_o}\right)\Bigg|_{Ro}} \qquad \text{(B.65)}$$

As for the stress balance at R_i, setting surface tension equal to zero recovers the normal stress equilibrium expression from the existing TFA for fiber spinning as given by (B.66).

$$\boxed{\left(\sigma_{orr} = 0\right)\Big|_{Ro}} \tag{B.66}$$

B.2.4 Clad radial momentum balance

Standard form of a radial momentum balance in cylindrical coordinates [3]:

$$\begin{aligned} &\rho_o\left(\frac{\partial v_{or}}{\partial t} + v_{or}\frac{\partial v_{or}}{\partial r} + \frac{v_{o\theta}}{r}\frac{\partial v_{or}}{\partial \theta} - \frac{v_{o\theta}^2}{r} + v_{oz}\frac{\partial v_{or}}{\partial z}\right) = \\ &\qquad -\frac{\partial p}{\partial r} + \left[\frac{1}{r}\frac{\partial}{\partial r}\left(r\tau_{orr}\right) + \frac{1}{r}\frac{\partial \tau_{or\theta}}{\partial \theta} - \frac{\tau_{o\theta\theta}}{r} + \frac{\partial \tau_{orz}}{\partial z}\right] \end{aligned} \tag{B.67}$$

For steady state; an axisymmetric (about the z-axis) case; uniaxial extension in the z-direction; and negligible radial inertia due to the high clad viscosity, equation (B.68) applies.

$$0 = -r\frac{\partial p}{\partial r} + \left[\frac{\partial}{\partial r}\left(r\tau_{orr}\right) - \tau_{o\theta\theta} + r\left(\frac{\partial \tau_{orz}}{\partial z}\right)\right] \tag{B.68}$$

Radial averaging over the clad cross-sectional area, analogous to the procedure for the axial component of momentum given in section B.2.1, followed by combining the deviatoric stress tensor terms $\overline{\tau_{ojk}}$ with the pressure terms that result gives equation (B.69). Radial averaging the first and second terms on the right hand side of (B.68) requires integration by parts; the procedure for the third term is straightforward integration; and the fourth term requires the use of the Leibniz rule given in (B.42).

$$\begin{aligned} &-A_o\left(\overline{\sigma_{orr}} + \overline{\sigma_{o\theta\theta}}\right) + 2\pi\left(R_o^2\,\sigma_{orr}\big|_{Ro} - R_i^2\,\sigma_{orr}\big|_{Ri}\right) - 2\pi R_o^2\left(\frac{dR_o}{dz}\right)\left(\sigma_{orz}\big|_{Ro}\right) \\ &\qquad + 2\pi R_i^2\left(\frac{dR_i}{dz}\right)\left(\sigma_{orz}\big|_{Ri}\right) + \frac{d}{dz}\int_{Ri}^{Ro} 2\pi r^2\,\sigma_{orz}\,dr = 0 \end{aligned} \tag{B.69}$$

The last term on the right hand side of (B.69) is assumed to be proportional to the drag force at the clad–air quench interface and is thus neglected in this analysis to be consistent with the assumption of negligible drag. Thus, the clad radial momentum balance is given by (B.70).

$$\begin{aligned} &-A_o\left(\overline{\sigma_{orr}} + \overline{\sigma_{o\theta\theta}}\right) + 2\pi\left(R_o^2\,\sigma_{orr}\big|_{Ro} - R_i^2\,\sigma_{orr}\big|_{Ri}\right) - 2\pi R_o^2\left(\frac{dR_o}{dz}\right)\left(\sigma_{orz}\big|_{Ro}\right) \\ &\qquad + 2\pi R_i^2\left(\frac{dR_i}{dz}\right)\left(\sigma_{orz}\big|_{Ri}\right) = 0 \end{aligned} \tag{B.70}$$

B.2.5 Core radial momentum balance

The procedure here is analogous to that for the clad in section B.2.4. For steady state; an axisymmetric (about the z-axis) case; uniaxial extension in the z-direction; and negligible radial inertia due to the low core gas density, equation (B.71) applies.

$$0 = -r\frac{\partial \overline{p_i}}{\partial r} + \left[\frac{\partial}{\partial r}\left(r\tau_{irr}\right) - \tau_{i\theta\theta} + r\left(\frac{\partial \tau_{irz}}{\partial z}\right)\right] \qquad \text{(B.71)}$$

Radial averaging over the core cross-sectional area, analogous to the procedure for the axial component of momentum given in section B.2.2, followed by combining average deviatoric stress tensor terms $\overline{\tau_{ijk}}$ with pressure terms and neglecting terms that scale with the low core gas viscosity gives equation (B.72).

$$-A_i\left(\overline{\sigma_{irr}} + \overline{\sigma_{i\theta\theta}}\right) + 2\pi R_i^2\left(\sigma_{irr}\big|_{Ri}\right) = 0 \qquad \text{(B.72)}$$

B.2.6 Combining radial momentum balances for clad and core

Combining the radial momentum balances for clad and core given in (B.70) and (B.72), assuming Newtonian clad and core, and neglecting terms that scale with the low core gas viscosity gives (B.73).

$$\begin{aligned}-A_o\left(\overline{\sigma_{orr}} + \overline{\sigma_{o\theta\theta}}\right) - A_i\left(\overline{\sigma_{irr}} + \overline{\sigma_{i\theta\theta}}\right) + 2\pi\left(R_o^2\sigma_{orr}\big|_{Ro} - R_i^2\sigma_{orr}\big|_{Ri}\right) - 2\pi R_i^2\overline{p_i}& \\ -2\pi R_o^2\left(\frac{dR_o}{dz}\right)\left(\sigma_{orz}\big|_{Ro}\right) + 2\pi R_i^2\left(\frac{dR_i}{dz}\right)\left(\sigma_{orz}\big|_{Ri}\right) = 0&\end{aligned} \qquad \text{(B.73)}$$

Applying to (B.73) the results from the interfacial stress balances including surface tension, given in equations (B.56), (B.57), (B.64), and (B.65) and invoking the thin filament assumption results in equation (B.74). The conditions ignoring surface tension can be used instead when neglecting these effects; however, the result for the case accounting for surface tension will be shown here with the intermediate momentum balance result, as the final momentum equation reduces to the existing TFA with surface tension set to zero.

$$A_o\left(\overline{\sigma_{orr}} + \overline{\sigma_{o\theta\theta}}\right) + A_i\left(\overline{\sigma_{irr}} + \overline{\sigma_{i\theta\theta}}\right) + 2\pi\gamma\left(R_o + R_i\right) = 0 \qquad \text{(B.74)}$$

For Newtonian clad and core and negligible core gas viscosity, (B.74) reduces to (B.75).

$$-A_o\left(\overline{\tau_{orr}} - 2\overline{p} + \overline{\tau_{o\theta\theta}}\right) + 2A_i\overline{p_i} - 2\pi\gamma\left(R_o + R_i\right) = 0 \qquad \text{(B.75)}$$

The average stress terms in (B.75) can be expressed by the definitions of these for a Newtonian clad, integrating the relationships over the clad cross-sectional area A_o. The results for these calculations are given in (B.76) and (B.77), where the (D/Dt) terms represent substantial derivatives with respect to time.

$$\overline{\tau_{orr}} = \eta_o\left[\frac{2A_i}{A_o}\left(\frac{D\ln\rho_i}{Dt}\right)\ln\left(\frac{R_o}{R_i}\right) - \frac{d\bar{v}}{dz}\right] \qquad \text{(B.76)}$$

$$\overline{\tau_{o\theta\theta}} = -\eta_o \left[\frac{2A_i}{A_o}\ln\left(\frac{R_o}{R_i}\right)\frac{D\ln\rho_i}{Dt} + \frac{d\bar{v}}{dz}\right] \qquad \text{(B.77)}$$

Substituting the results given in (B.76) and (B.77) into (B.75) gives (B.78), which expresses the average clad pressure $\bar{p}$ in terms of other spinline variables.

$$\boxed{-A_o\bar{p} = \eta_o A_o \frac{d\bar{v}}{dz} + A_i\overline{p_i} - \pi\gamma\left(R_o + R_i\right)} \qquad \text{(B.78)}$$

B.2.7 Hoop stress balance

The purpose of the hoop force balance shown here is to define the $\overline{\sigma_{o\theta\theta}}$ term. However, this can be done instead using the interfacial stress balances and calculating the cross-sectional average stress terms. The development here is given to explain the derivation of equation (8c) in the existing TFA for fiber spinning [2]. The hoop stress balance is done over half the clad cross-section: a semicircular section with inner radius R_i, outer radius R_o, and an arbitrary thickness l in the axial direction. The hoop stress correlation given here balances two force contributions. The first is due to the $\overline{\sigma_{o\theta\theta}}$ stresses, which arise in processes with draw-down because $\sigma_{o\theta\theta}$ is a function of $\tau_{o\theta\theta}$, which is a function of the clad radial velocity. The second is the force due to the core gas pressure, which acts on the inner surface area of the hollow fiber spinline. The derivation is shown in (B.79).

$$\boxed{\begin{aligned} &F_{\sigma-stress} = F_{\overline{pi}-stress} \\ &2\overline{\sigma_{o\theta\theta}}\left(R_o - R_i\right)l = 2\overline{p_i}R_i l \\ &\overline{\sigma_{o\theta\theta}} = \left(\frac{R_i}{R_o - R_i}\right)\overline{p_i} \\ &-\bar{p} + \overline{\tau_{o\theta\theta}} = \left(\frac{R_i}{R_o - R_i}\right)\overline{p_i} \end{aligned}} \qquad \text{(B.79)}$$

Substituting for the average clad pressure from the radial momentum balance in (B.78) gives (B.80).

$$\left(\frac{R_i^2}{R_o^2 - R_i^2}\right)\overline{p_i} - \frac{1}{2}\left(\overline{\tau_{orr}} + \overline{\tau_{o\theta\theta}}\right) + \overline{\tau_{o\theta\theta}} = \left(\frac{R_i}{R_o - R_i}\right)\overline{p_i} \qquad \text{(B.80)}$$

Rearranging equation (B.80) by combining the stress terms and the pressure terms gives (B.81).

$$\left(\frac{R_o R_i}{R_o^2 - R_i^2}\right)\overline{p_i} = \frac{1}{2}\left(\overline{\tau_{o\theta\theta}} - \overline{\tau_{orr}}\right) \qquad \text{(B.81)}$$

Substituting for the radial-average stress terms gives (B.82).

$$\left(\frac{R_o R_i}{R_o^2 - R_i^2}\right)\overline{p_i} = \frac{1}{2}\left(-2\eta_o\left[\frac{1}{2}\frac{d\bar{v}}{dz} - \frac{\ln\left(R_o/R_i\right)}{R_o^2 - R_i^2}\frac{d}{dz}\left(R_i^2\bar{v}\right)\right]\right) - \frac{1}{2}\left(-2\eta_o\left[\frac{1}{2}\frac{d\bar{v}}{dz} + \frac{\ln\left(R_o/R_i\right)}{R_o^2 - R_i^2}\frac{d}{dz}\left(R_i^2\bar{v}\right)\right]\right) \tag{B.82}$$

Rearranging (B.82) gives (B.83).

$$\left(\frac{R_o R_i}{2\eta_o \ln\left(R_o/R_i\right)}\right)\overline{p_i} = \frac{d}{dz}\left(R_i^2\bar{v}\right) \tag{B.83}$$

Note that the hoop stress equation, the last equation given in (B.79), can be rewritten as (B.84).

$$\boxed{\int_{R_i}^{R_o}\sigma_{o\theta\theta}dr = R_i\,\overline{p_i} = R_i\left(-\tau_{irr}\big|_{R_i} + \overline{p_i}\right) = -\int_0^{R_i}\sigma_{irr}dr = -R_i\sigma_{irr}\big|_{R_i}} \tag{B.84}$$

In (B.84), the last three terms are valid because $\tau_{irr}\big|_{R_i}$ is approximately zero (the core gas viscosity is small) and the pressure does not vary with radial position. The last equality is the same as Equation (8c) from the existing published TFA [2].

B.2.8 Combining axial momentum balances for clad and core

Adding the axial momentum balances for the clad and core given by (B.49) and (B.50) gives (B.85).

$$\frac{d}{dz}\left[\left(\rho_o\overline{v^2}A_o + \rho_i\overline{v^2}A_i\right)\right] = \frac{d}{dz}\left[A_o\overline{\sigma_{ozz}} + A_i\overline{\sigma_{izz}}\right] + 2\pi R_o\left[\sigma_{orz}\big|_{Ro} - \frac{dR_o}{dz}\left(\sigma_{ozz}\big|_{Ro}\right)\right] + 2\pi R_i\left[-\sigma_{orz}\big|_{Ri} - \frac{dR_i}{dz}\left(\sigma_{ozz}\big|_{Ri}\right) + \sigma_{irz}\big|_{Ri} - \frac{dR_i}{dz}\left(\sigma_{izz}\big|_{Ri}\right)\right] \tag{B.85}$$

Since the constant mass flow rates of clad and core are defined as $w_o = \rho_o\bar{v}A_o$ and $w_i = \rho_i\bar{v}A_i$, respectively, (B.85) can be rewritten as (B.86).

$$\left(w_o + w_i\right)\frac{d\bar{v}}{dz} = \frac{d}{dz}\left[A_o\overline{\sigma_{ozz}} + A_i\overline{\sigma_{izz}}\right] + 2\pi R_o\left[\sigma_{orz}\big|_{Ro} - \frac{dR_o}{dz}\left(\sigma_{ozz}\big|_{Ro}\right)\right] + 2\pi R_i\left[-\sigma_{orz}\big|_{Ri} - \frac{dR_i}{dz}\left(\sigma_{ozz}\big|_{Ri}\right) + \sigma_{irz}\big|_{Ri} - \frac{dR_i}{dz}\left(\sigma_{izz}\big|_{Ri}\right)\right] \tag{B.86}$$

Applying the results from the interfacial stress balances given in (B.56), (B.57), (B.64), and (B.65) and neglecting terms that scale as the low core gas viscosity gives (B.87). Alternatively, the normal stress balances neglecting surface tension can be applied, using (B.58) and (B.66) in place of (B.57) and (B.65); the result is the same as equation (B.87) with surface tension set equal to zero.

$$\left(w_o + w_i\right)\frac{d\bar{v}}{dz} = \frac{d}{dz}\left[A_o\overline{\sigma_{ozz}} + A_i\overline{\sigma_{izz}}\right] + 2\pi\gamma\left(\frac{dR_o}{dz} + \frac{dR_i}{dz}\right) \qquad \text{(B.87)}$$

Rewrite (B.87) using the definition of the Newtonian fluid stress tensors, neglecting terms that scale with the low core gas viscosity to produce (B.88).

$$\left(w_o + w_i\right)\frac{d\bar{v}}{dz} = \frac{d}{dz}\left[A_o\overline{\tau_{ozz}} - A_o\bar{p} - A_i\overline{p_i}\right] + 2\pi\gamma\left(\frac{dR_o}{dz} + \frac{dR_i}{dz}\right) \qquad \text{(B.88)}$$

Substitute for the average clad pressure term from the radial momentum balance in (B.78) to produce (B.89).

$$\left(w_o + w_i\right)\frac{d\bar{v}}{dz} = \frac{d}{dz}\left[A_o\overline{\tau_{ozz}} + \eta_o A_o\frac{d\bar{v}}{dz} - \pi\gamma\left(R_o + R_i\right)\right] + 2\pi\gamma\left(\frac{dR_o}{dz} + \frac{dR_i}{dz}\right) \qquad \text{(B.89)}$$

The remaining average stress term in (B.89) is calculated as the clad cross-sectional average value from the definition for a Newtonian fluid as given in (B.90).

$$\overline{\tau_o} =_z 2\eta_{\alpha}\frac{d\bar{v}}{d} \qquad \text{(B.90)}$$

Subsotit (tBu.t8n9)g g
fiber spinning

$$\boxed{\left(w_o + w_i\right)\frac{d\bar{v}}{dz} = \frac{d}{dz}\left[3\eta_o A_o\frac{d\bar{v}}{dz}\right] + \pi\gamma\left(\frac{dR_o}{dz} + \frac{dR_i}{dz}\right)} \qquad \text{(B.91)}$$

The result for the existing TFA [2] is recovered if surface tension is set to zero as shown in (B.92).

$$\boxed{\left(w_o + w_i\right)\frac{d\bar{v}}{dz} = \frac{d}{dz}\left[3\eta_o A_o\frac{d\bar{v}}{dz}\right]} \qquad \text{(B.92)}$$

B.3 Existing TFA momentum equation [2] from axial and radial momentum balances

In the published TFA for fiber spinning cited here [2], the non-steady state axial and radial momentum balances for the spinline are given by (B.93) and (B.94). These equations are reported as equations (8a) and (8b) in the existing TFA.

$$\left(\rho_o A_o + \rho_i A_i\right)\left(\frac{\partial\bar{v}}{\partial t} + \bar{v}\frac{\partial\bar{v}}{\partial z}\right) = \frac{\partial}{\partial z}\left(A_o\overline{\sigma_{ozz}} + A_i\overline{\sigma_{izz}}\right) \qquad \text{(B.93)}$$

$$A_o\left(\overline{\sigma_{orr}} + \overline{\sigma_{o\theta\theta}}\right) + A_i\left(\overline{\sigma_{irr}} + \overline{\sigma_{i\theta\theta}}\right) = 0 \qquad \text{(B.94)}$$

Combining these balances for the clad and core separately results in (B.95) for the incompressible clad and (B.96) for the core (core gas density varies with axial position only since temperature and pressure vary with axial position only).

$$\frac{D\ln\rho_o}{Dt} = \frac{1}{\rho_o}\frac{D\rho_o}{Dt} = \frac{1}{\rho_o}\left[v_{or}\frac{\partial\rho_o}{\partial r} + \bar{v}\frac{\partial\rho_o}{\partial z}\right] = 0 \qquad \text{(B.95)}$$

$$\frac{D\ln\rho_i}{Dt} = \frac{1}{\rho_i}\frac{D\rho_i}{Dt} = \frac{1}{\rho_i}\left[v_{ir}\frac{\partial\rho_i}{\partial r} + \bar{v}\frac{\partial\rho_i}{\partial z}\right] = \frac{\bar{v}}{\rho_i}\frac{\partial\rho_i}{\partial z} \qquad \text{(B.96)}$$

B.4 Axial variation of core gas density

Defining σ_{orr} for an incompressible Newtonian clad gives equation (B.97).

$$\sigma_{orr} = \eta_o\left[\frac{R_i^2}{r^2}\left(\bar{v}\frac{d\ln\rho_i}{dz}\right) - \frac{d\bar{v}}{dz}\right] \qquad \text{(B.97)}$$

Inserting the above result into the interfacial normal stress balances including surface tension, given in (B.57) and (B.65), results in (B.98) and (B.99).

$$\left.\left\{\eta_o\left[\left(\bar{v}\frac{d\ln\rho_i}{dz}\right) - \frac{d\bar{v}}{dz}\right] = -\overline{p_i} + \frac{\gamma}{R_i}\right\}\right|_{Ri} \qquad \text{(B.98)}$$

$$\left.\left\{\eta_o\left[\frac{R_i^2}{R_o^2}\left(\bar{v}\frac{d\ln\rho_i}{dz}\right) - \frac{d\bar{v}}{dz}\right] = -\frac{\gamma}{R_o}\right\}\right|_{Ro} \qquad \text{(B.99)}$$

Subtracting (B.99) from (B.98) gives (B.100).

$$-\frac{\overline{p_i}\rho_i}{\eta_o} = \bar{v}\left(\frac{R_o^2 - R_i^2}{R_o^2}\right)\frac{d\rho_i}{dz} - \frac{\gamma\rho_i}{\eta_o}\left(\frac{1}{R_i} + \frac{1}{R_o}\right) \qquad \text{(B.100)}$$

Rearranging and substituting for the radius terms using continuity, equation (B.16), gives (B.101).

$$\bar{v}\frac{d\rho_i}{dz} = \left(1 + \frac{\rho_o w_i}{\rho_i w_o}\right)\left[\gamma\left(\frac{1}{R_i} + \frac{1}{R_o}\right) - \left(\frac{\rho_i\overline{p_i}}{\eta_o}\right)\right] \qquad \text{(B.101)}$$

Setting surface tension equal to zero recovers equation (25) from the existing published TFA [2] as shown in (B.102). This result could be derived directly using the normal interfacial stress balances neglecting surface tension, equations (B.58) and (B.66).

$$\bar{v}\frac{d\rho_i}{dz} = -\left(\frac{\rho_i\overline{p_i}}{\eta_o}\right)\left(1 + \frac{\rho_o w_i}{\rho_i w_o}\right) \qquad \text{(B.102)}$$

Moreover, (B.102) can also be derived from the core continuity equation in (B.13), expressed as the axially constant product of core gas density, core cross-sectional area, and spinline axial velocity. This approach reflects the fact that the core gas mass flow rate is constant, and the core gas pressure must therefore vary with axial position due to changes in the axial velocity, the core cross-sectional area, and the spinline temperature (for non-isothermal spinning). The result is the final equation in (B.103), a slightly different form of the equation expressing the axial variation of core gas density, perhaps less useful than (B.102) derived above.

$$\boxed{\begin{aligned}
&\frac{\partial}{\partial z}\left(\rho_i A_i \bar{v}\right)=0\\
&\frac{\partial}{\partial z}\left(\rho_i A_i \bar{v}\right)=\rho_i\frac{\partial}{\partial z}\left(A_i \bar{v}\right)+A_i\bar{v}\frac{\partial}{\partial z}\left(\rho_i\right)\\
&\frac{\partial}{\partial z}\left(\rho_i A_i \bar{v}\right)=\rho_i\frac{\partial}{\partial z}\left(A_i \bar{v}\right)+A_i\bar{v}\frac{\partial \rho_i}{\partial \overline{p_i}}\frac{\partial \overline{p_i}}{\partial z}+A_i\bar{v}\frac{\partial \rho_i}{\partial \overline{T}}\frac{\partial \overline{T}}{\partial z}\\
&-A_i\bar{v}\frac{\partial \rho_i}{\partial \overline{p_i}}\frac{\partial \overline{p_i}}{\partial z}=\rho_i\frac{\partial}{\partial z}\left(A_i \bar{v}\right)+A_i\bar{v}\frac{\partial \rho_i}{\partial \overline{T}}\frac{\partial \overline{T}}{\partial z}
\end{aligned}} \qquad \text{(B.103)}$$

B.5 TFA energy balance

Assume the following:

1. Axi-symmetry
2. Axial conduction << Axial convection ($Pe_{axial} >> 1$)
3. Radial convection << Radial conduction ($Pe_{radial} << 1$)
4. Negligible viscous dissipation of energy ($\tau : \nabla v << 1$, for more information, see [1]).

The general form of the internal energy balance appears in (B.104) [1].

$$\rho\frac{D\hat{U}}{Dt}=-\left(\nabla \bullet q\right)-p\left(\nabla \bullet v\right)-\left(\tau : \nabla v\right) \qquad \text{(B.104)}$$

In (B.104), the substantial derivative is the rate of gain of internal energy per unit volume, the first term on the right of the equality is the rate of internal energy input by conduction per unit volume, the second term is the reversible rate of internal energy increase per unit volume by compression, and the third term is the irreversible rate of internal energy increase per unit volume by viscous dissipation.

For the clad, assuming constant density allows the second term on the right of the equality to be neglected. The third term is also neglected per assumption (4) above. Substituting for the internal energy and taking the clad density and thermal conductivity as constants gives (B.105).

$$\rho_o\hat{C}_{po}\frac{DT}{Dt}=k_o\nabla^2 T_o \qquad \text{(B.105)}$$

For a cylindrical coordinate system, (B.105) can be rewritten as (B.106).

$$\rho_o \hat{C}_{po} \bar{v} \frac{\partial T_o}{\partial z} = k_o \left(\frac{1}{r}\right) \frac{\partial}{\partial r}\left(r \frac{\partial T_o}{\partial r}\right) \qquad \text{(B.106)}$$

In (B.106), four terms are neglected with the listed justifications given in (B.107).

$$\boxed{\begin{array}{l} \frac{\partial T_o}{\partial t} = 0, \quad steady-state \\ \frac{\partial T_o}{\partial \theta} = \frac{\partial^2 T_o}{\partial \theta^2} = 0, \quad axisymmetric \\ \rho_o \hat{C}_{po} v_{or} \frac{\partial T_o}{\partial r} << k_o \left(\frac{1}{r}\right) \frac{\partial}{\partial r}\left(r \frac{\partial T_o}{\partial r}\right), \quad Pe_{radial} << 1 \\ k_o \frac{\partial^2 T_o}{\partial z^2} << \rho_o \hat{C}_{po} \bar{v} \frac{\partial T_o}{\partial z}, \quad Pe_{axial} << 1 \end{array}} \qquad \text{(B.107)}$$

For the core, neglecting the same terms as for the clad gives (B.108).

$$\rho_i \hat{C}_{pi} \bar{v} \frac{\partial T_i}{\partial z} = k_i \left(\frac{1}{r}\right) \frac{\partial}{\partial r}\left(r \frac{\partial T_i}{\partial r}\right) \qquad \text{(B.108)}$$

Additionally, (B.109) is assumed to hold.

$$T_i \left(\frac{\partial p}{\partial T_i}\right)_\rho (\nabla \bullet v) \sim 0 \qquad \text{(B.109)}$$

The term in (B.109) appears in the energy equation due to the dependence of the fluid's internal energy on specific volume. This term is neglected relative to the axial convection and radial conduction terms retained in the energy equation. For sufficiently small bore pressure and temperature changes this assumption is justified.

Multiplying the clad equation in (B.106) by $2\pi r$ and integrating across the clad cross-section gives (B.110).

$$\int_{R_i}^{R_o} (2\pi r) \rho_o \hat{C}_{po} \bar{v} \frac{\partial T_o}{\partial z} dr = \int_{R_i}^{R_o} 2\pi k_o \left(\frac{r}{r}\right) \frac{\partial}{\partial r}\left(r \frac{\partial T_o}{\partial r}\right) dr \qquad \text{(B.110)}$$

Assuming constant clad material properties leads to (B.111) from (B.110).

$$\rho_o \hat{C}_{po} \bar{v} \int_{R_i}^{R_o} \frac{\partial T_o}{\partial z} (2\pi r) dr = 2\pi k_o \int_{R_i}^{R_o} d\left(r \frac{\partial T_o}{\partial r}\right) \qquad \text{(B.111)}$$

Using Leibniz's rule, given in (B.42), on the left hand side of (B.111) gives (B.112).

$$\rho_o \hat{C}_{po}\bar{v}\left[\frac{d}{dz}\left(A_o\frac{\int_{R_i}^{R_o} T_o(2\pi r)dr}{A_o}\right) - 2\pi R_o T_o\big|_{R_o}\frac{dR_o}{dz} + 2\pi R_i T_o\big|_{R_i}\frac{dR_i}{dz}\right] =$$
$$\rho_o \hat{C}_{po}\bar{v}\left[\frac{d\left(A_o\bar{T}_o\right)}{dz} - 2\pi R_o T_o\big|_{R_o}\frac{dR_o}{dz} + 2\pi R_i T_o\big|_{R_i}\frac{dR_i}{dz}\right] = 2\pi k_o\left(r\frac{\partial T_o}{\partial r}\right)\Bigg|_{R_i}^{R_o} \qquad \text{(B.112)}$$

The bar over the clad temperature T_o indicates a radial-average quantity and A_o is the clad cross-sectional area. Expanding the derivative gives (B.113) from this term in (B.112).

$$\frac{d\left(A_o\bar{T}_o\right)}{dz} = A_o\frac{d\bar{T}_o}{dz} + \bar{T}_o\frac{dA_o}{dz} = A_o\frac{d\bar{T}_o}{dz} + 2\pi\bar{T}_o\left(R_o\frac{dR_o}{dz} - R_i\frac{dR_i}{dz}\right) \qquad \text{(B.113)}$$

Neglecting all terms involving dR_o/dz or dR_i/dz gives (B.114) from (B.113).

$$\rho_o\hat{C}_{po}\bar{v}A_o\frac{d\bar{T}_o}{dz} = w_o\hat{C}_{po}\frac{d\bar{T}_o}{dz} = 2\pi k_o\left(R_o\frac{\partial T_o}{\partial r}\bigg|_{R_o} - R_i\frac{\partial T_o}{\partial r}\bigg|_{R_i}\right) \qquad \text{(B.114)}$$

The boundary conditions for this equation are given in (B.115). In this equation, T_q is the quench fluid temperature.

$$@\, r = R_o, \quad -k_o\frac{\partial T_o}{\partial r}\bigg|_{R_o} = h\left(T_o\big|_{R_o} - T_q\right)$$
$$@\, r = R_i, \quad -k_o\frac{\partial T_o}{\partial r}\bigg|_{R_i} = -k_i\frac{\partial T_i}{\partial r}\bigg|_{R_i} \quad and \quad T_o\big|_{R_i} = T_i\big|_{R_i} \qquad \text{(B.115)}$$

Integrating the core equation gives the same result as above for the clad except the limits of integration are changed to R_i and 0; the result is shown in (B.116).

$$\rho_i\hat{C}_{pi}\bar{v}A_i\frac{d\bar{T}_i}{dz} = w_i\hat{C}_{pi}\frac{d\bar{T}_i}{dz} = 2\pi k_i\left(R_i\frac{\partial T_i}{\partial r}\bigg|_{R_i} - 0\right) \qquad \text{(B.116)}$$

An additional boundary condition, given in (B.117), is necessary for the core equation in (B.116).

$$@\, r = 0, \quad -k_i\frac{\partial T_i}{\partial r}\bigg|_{0} = 0 \qquad \text{(B.117)}$$

Adding the equations for the core and clad gives (B.118).

$$w_o\hat{C}_{po}\frac{d\bar{T}_o}{dz} + w_i\hat{C}_{pi}\frac{d\bar{T}_i}{dz} = 2\pi k_o\left(R_o\frac{\partial T_o}{\partial r}\bigg|_{R_o} - R_i\frac{\partial T_o}{\partial r}\bigg|_{R_i}\right) + 2\pi k_i\left(R_i\frac{\partial T_i}{\partial r}\bigg|_{R_i}\right) \qquad \text{(B.118)}$$

Assuming the average core and clad temperatures are equal and substituting the boundary conditions gives (B.119).

$$\left(w_i\hat{C}_{pi} + w_o\hat{C}_{po}\right)\frac{d\bar{T}}{dz} = -2\pi R_o h\left(\bar{T} - T_q\right) \qquad \text{(B.119)}$$

Note that the inclusion of evaporative cooling requires modifying the boundary condition applying at R_o given in (B.115) to that given in (B.120). In (B.120), $\Delta H_{d,mol}^{vap}$ is the latent heat of vaporization (J/mole) and j is the solvent flux at the outer radius (moles/area/time).

$$@\, r = R_o, \quad -k_o \left.\frac{\partial T_o}{\partial r}\right|_{R_o} = h\left(T_o\big|_{R_o} - T_q\right) + \Delta H_{d,mol}^{vap}\, j \qquad \text{(B.120)}$$

B.6 Boundary layer analysis for modeling radial concentration gradients

B.6.1 General form of the conservation of mass equation

For steady-state mass transfer in fluids with constant density and diffusivity the conservation of mass equation in a cylindrical coordinate system is given by (B.121) [1]. In (B.121), axial convection is neglected and axi-symmetry is assumed.

$$v_r \frac{\partial c}{\partial r} + v_z \frac{\partial c}{\partial z} = D \frac{1}{r} \frac{\partial}{\partial r}\left(r \frac{\partial c}{\partial r} \right) \qquad \text{(B.121)}$$

Changing the coordinate system in (B.121) from (r, z) to ($y = R_o - r$, z) requires use of the chain rule as expressed by the relationships in (B.122).

$$\boxed{\begin{aligned} \frac{\partial}{\partial r} &= \frac{\partial}{\partial y}\frac{\partial y}{\partial r} + \frac{\partial}{\partial z}\frac{\partial z}{\partial r} = -\frac{\partial}{\partial y} \\ \frac{\partial}{\partial z} &= \frac{\partial}{\partial y}\frac{\partial y}{\partial z} + \frac{\partial}{\partial z}\frac{\partial z}{\partial z} = \frac{dR_o}{dz}\frac{\partial}{\partial y} + \frac{\partial}{\partial z} \\ \frac{\partial}{\partial r}\left(\frac{\partial c}{\partial r}\right) &= \frac{\partial}{\partial r}\left(-\frac{\partial c}{\partial y}\right) = \frac{\partial^2 c}{\partial y^2} \end{aligned}} \qquad \text{(B.122)}$$

Substituting into (B.121) gives (B.123).

$$-v_r \frac{\partial c}{\partial y} + v_z\left(\frac{dR_o}{dz}\frac{\partial c}{\partial y} + \frac{\partial c}{\partial z}\right) = -\left(v_r - v_z \frac{dR_o}{dz}\right)\frac{\partial c}{\partial y} + v_z \frac{\partial c}{\partial z} = D\left[\frac{\partial^2 c}{\partial y^2} - \frac{1}{R_o - y}\left(\frac{\partial c}{\partial y}\right)\right] \qquad \text{(B.123)}$$

Combining the results for constant clad and core density from equation (B.20) and the kinematic boundary condition given in (B.7) gives the result in (B.124).

$$\left(v_r - v_z \frac{dR_o}{dz}\right) = \frac{R_o - r}{2}\frac{dv_z}{dz} = \frac{y}{2}\frac{dv_z}{dz} \qquad \text{(B.124)}$$

The conservation of mass equation, (B.123), becomes (B.125) neglecting the effects of curvature.

$$.-\frac{y}{2}\frac{dv_z}{dz}\frac{\partial c}{\partial y} + v_z \frac{\partial c}{\partial z} = D\frac{\partial^2 c}{\partial y^2} \qquad \text{(B.125)}$$

B.6.2 Solving the conservation of mass equation using a similarity transform

The similarity variable η is defined in (B.126).

$$\eta = y\sqrt{\frac{v_z}{4Dz}} \qquad \text{(B.126)}$$

Applying a similarity transform to (B.125) requires use of the chain rule as outlined by the relationships in (B.127).

$$\boxed{\begin{aligned} \frac{\partial c}{\partial y} &= \frac{dc}{d\eta}\frac{\partial \eta}{\partial y} = \frac{\eta}{y}\frac{dc}{d\eta} \\ \frac{\partial c}{\partial z} &= \frac{dc}{d\eta}\frac{\partial \eta}{\partial z} = \left(\frac{y^2}{8\eta D}\right)\left(\frac{1}{z}\frac{dv_z}{dz} - \frac{v_z}{z^2}\right)\frac{dc}{d\eta} \end{aligned}} \qquad \text{(B.127)}$$

As a result, the left hand side of the conservation of mass equation in (B.125) becomes (B.128).

$$\left(-\frac{y}{2}\frac{dv_z}{dz}\frac{\eta}{y} + v_z\left(\frac{y^2}{8\eta D}\right)\frac{1}{z}\frac{dv_z}{dz} - v_z\left(\frac{y^2}{8\eta D}\right)\frac{v_z}{z^2}\right)\frac{dc}{d\eta} = \left(-\frac{\eta}{2}\frac{dv_z}{dz} + \left(\frac{y^2 v_z}{\eta 4Dz}\right)\frac{1}{2}\frac{dv_z}{dz} - \left(\frac{y^2 v_z}{\eta 4Dz}\right)\frac{v_z}{2z}\right)\frac{dc}{d\eta} =$$

$$\left(-\frac{\eta}{2}\frac{dv_z}{dz} + \left(\frac{\eta^2}{\eta}\right)\frac{1}{2}\frac{dv_z}{dz} - \left(\frac{\eta^2}{\eta}\right)\frac{v_z}{2z}\right)\frac{dc}{d\eta} = -\frac{\eta v_z}{2z}\frac{dc}{d\eta}$$

(B.128)

Additionally, the chain rule and product rule for differentiation yields (B.129).

$$\frac{\partial}{\partial y}\left(\frac{\partial c}{\partial y}\right) = \frac{\partial}{\partial y}\left(\frac{\eta}{y}\frac{dc}{d\eta}\right) = \frac{\eta}{y}\frac{\partial}{\partial y}\left(\frac{dc}{d\eta}\right) = \frac{\eta}{y}\frac{d^2c}{d\eta^2}\frac{\partial \eta}{\partial y} = \left(\frac{\eta}{y}\right)^2\frac{d^2c}{d\eta^2} = \frac{v_z}{4Dz}\frac{d^2c}{d\eta^2} \qquad \text{(B.129)}$$

Therefore, the right hand side of the conservation of mass equation in (B.125) becomes (B.130).

$$D\left(\frac{v_z}{4Dz}\frac{d^2c}{d\eta^2}\right) = \frac{v_z}{4z}\frac{d^2c}{d\eta^2} \qquad \text{(B.130)}$$

Equating the left and right hand sides given in (B.128) and (B.130) results in (B.131).

$$-\frac{\eta v_z}{2z}\frac{dc}{d\eta} = \frac{v_z}{4z}\frac{d^2c}{d\eta^2} \qquad \text{(B.131)}$$

Simplifying (B.131) gives (B.132).

$$-2\eta\frac{dc}{d\eta} = \frac{d^2c}{d\eta^2} \qquad \text{(B.132)}$$

Equation (B.132) is integrated as shown in (B.133).

$$-\int 2\eta d\eta = \int \frac{d\left(\frac{dc}{d\eta}\right)}{\frac{dc}{d\eta}} \longrightarrow -\eta^2 + C = \ln\left(\frac{dc}{d\eta}\right) \qquad \text{(B.133)}$$

In (B.133), C is a constant of integration. Solving for the derivative term in (B.133) and integrating gives (B.134).

$$c = K_1 \int_o^{\eta} \exp\left(-x^2\right) dx + K_2 \qquad \text{(B.134)}$$

One can evaluate the integration constants by noting the boundary conditions: $c = c_0$ when $\eta = 0$ and $c = c_\infty$ when $\eta \to \infty$. The results are given in (B.135).

$$K_2 = c_0$$

$$K_1 = \left(c_\infty - c_0\right)\frac{2}{\sqrt{\pi}} \qquad \text{(B.135)}$$

Thus, the final boundary layer equation to describe concentration gradients is (B.136).

$$\Theta = \frac{c - c_0}{c_\infty - c_0} = \frac{2}{\sqrt{\pi}} \int_o^{\eta} \exp\left(-x^2\right) dx = \mathbf{erf}(\eta) \qquad \text{(B.136)}$$

B.7 References

1. R.B. Bird, W.E. Stewart, and E.N. Lightfoot, Transport Phenomena, John Wiley & Sons, New York, 1960.
2. G.G. Lipscomb, The melt hollow fiber spinning process: Steady-state behavior, sensitivity and stability, Polymers for Advanced Technologies, 5 (1994) 745-758.
3. W.M. Deen, Analysis of transport phenomena, Oxford University Press, New York, 1998.

Glossary

Quantity	**Definition**
A_i	core cross-sectional area
A_o	clad cross-sectional area
A_{oL}	clad cross-sectional area at end of draw zone
Bo	Boltzmann number
c	component concentration
Ca	Capillary number
C_d	diluent mass concentration
C_{d0}	diluent mass concentration at the spinline outer radius
$C_{d\infty}$	diluent mass concentration in the spinline outside of the boundary layer
C_D	drag coefficient
C_p	polymer mass concentration
C_{pi}	heat capacity of the bore gas
C_{po}	heat capacity of the clad
C_{pq}	heat capacity of the quench air
D	spinning solution diffusion coefficient
D_{do}	diffusion coefficient calculation pre-exponential factor
D_d^*	diluent self-diffusion coefficient
D_{d-air}	diluent diffusion coefficient in air
DR	draw ratio
E_o	activation energy for viscosity in terms of its temperature dependence
E_{oc}	activation energy for viscosity in terms of its temperature dependence when also including concentration dependence of viscosity
F^L	total force applied to core and clad at end of draw zone
Fr	Froude number
g	acceleration due to gravity
$g(z)$	expression used with similarity transform in boundary layer analysis
h	convective heat transfer coefficient
j	diluent molar flux at spinline outer radius
k_c	mass transfer coefficient of diluent into the air at the spinline outer radius

Quantity	**Definition**
k_o	clad thermal conductivity
k_q	quench air thermal conductivity
K_{1d}	diluent free volume parameter 1
K_{2d}	diluent free volume parameter 2
K_{1p}	polymer free volume parameter 1
K_{2p}	polymer free volume parameter 2
L	draw zone length
L'	characteristic dimension for heat transfer
M_d	diluent molecular weight
MW_i	core gas molecular weight
MW_q	quench air molecular weight
$n_i^{\perp}$	unit normal to the core–clad interface
$n_{ir}^{\perp}$	radial component of the unit normal to the core–clad interface
$n_{iz}^{\perp}$	axial component of the unit normal to the core–clad interface
n_i^{ll}	unit tangent to the core–clad interface
n_{ir}^{ll}	radial component of the unit tangent to the core–clad interface
n_{iz}^{ll}	axial component of the unit tangent to the core–clad interface
$n_o^{\perp}$	unit normal to the clad–air quench interface
$n_{or}^{\perp}$	radial component of the unit normal to the clad–air quench interface
$n_{oz}^{\perp}$	axial component of the unit normal to the clad–air quench interface
n_o^{ll}	unit tangent to the clad–air quench interface
n_{or}^{ll}	radial component of the unit tangent to the clad–air quench interface
n_{oz}^{ll}	axial component of the unit tangent to the clad–air quench interface
N	number of samples for propagating error in average quantity
p	pressure
$\overline{p}$	radial-average pressure in the clad
p_{atm}	atmospheric pressure (pressure of the air in the air gap)
P_d^o	diluent vapor pressure
Pe	Peclet number

Quantity	**Definition**
Pe_m	Peclet number for mass transfer
$\overline{p}_i$	core gas pressure
$\overline{p}_i^o$	core gas pressure at the beginning of the draw zone
r	radial direction or radial coordinate
Re	Reynolds number
R_g	universal gas constant
R_i	clad inner radius
R_i^0	initial clad inner radius
R_i^L	final clad inner radius
R_o	clad outer radius
R_o^0	initial clad outer radius
R_o^L	final clad outer radius
SD	standard deviation
t	time
T	temperature
$\overline{T}$	radial-average temperature of the spinline
$\overline{T}^o$	radial-average temperature at the beginning of the draw zone
$\overline{T}^L$	radial-average temperature at the end of the draw zone
T_i	core temperature
T_o	clad temperature
T_{gd}	diluent glass transition temperature
T_{gp}	polymer glass transition temperature
T_q	air quench temperature in the air gap
$\overline{v}$	axial velocity of the spinline
$\overline{v}^o$	axial velocity of the spinline at the beginning of the draw zone
$\overline{v}^L$	axial velocity of the spinline at the end of the draw zone
V'	characteristic velocity
v_{atom}	atomic volume
V_d^*	specific hole free volume of diluent required for a jump related to diffusion
V_p^*	specific hole free volume of polymer required for a jump related to diffusion
v_q	quench air velocity
v_r	radial velocity

Quantity	**Definition**
v_{ir}	core radial velocity
v_{iz}	core axial velocity
v_{or}	clad radial velocity
v_{oz}	clad axial velocity
v_z	axial velocity
v_θ	velocity in the theta direction in cylindrical coordinates
VFR	volumetric flow rate
We	Weber number
w_i	core gas mass flow rate
w_o	clad mass flow rate
x	ratio of polymer molar volume to diluent molar volume
y	radial direction coordinate for boundary layer analysis
z	axial position
χ	chi interaction parameter
$\Delta\hat{H}_{vap}^{d}$	diluent heat of vaporization per unit mass
$\Delta H_{d,mol}^{vap}$	diluent heat of vaporization per mole
ε	emissivity
ϕ_d	volume fraction of diluent
ϕ_d^0	volume fraction of diluent in initial spinning solution
ϕ_p	volume fraction of polymer
ϕ_2^α	volume fraction of polymer in phase α
ϕ_2^β	volume fraction of polymer in phase β
γ	spinline surface tension
η	similarity variable for boundary layer analysis
η_o	clad viscosity
η_{oc}	viscosity pre-factor in terms of its temperature dependence when also including concentration dependence of viscosity
η_o^0	viscosity pre-factor for viscosity temperature dependence
η_o^L	clad viscosity at end of draw zone
η_q	quench air viscosity
φ	free volume overlap factor

Quantity	**Definition**
λ	spinline solution relaxation time
π	pi
θ	theta direction in cylindrical coordinates
Θ	dimensionless concentration in the boundary layer analysis
ρ	spinline solution density
ρ_i	core gas density
ρ_o	clad density
ρ_q	quench air density
ρ_d^0	pure diluent density
ρ_p^0	pure polymer density
ρ_d^g	diluent concentration in the air adjacent to the spinline
σ	Stefan−Boltzmann constant
σ_i	total stress tensor associated with the core
σ_{ijk}	component *jk* of the core total stress tensor
σ^i_{jk}	component *jk* of the core total stress tensor
σ_o	total stress tensor associated with the clad
σ_{ojk}	component *jk* of the clad total stress tensor
σ^o_{jk}	component *jk* of the clad total stress tensor
τ_{ijk}	component *jk* of the core deviatoric stress tensor
τ^i_{jk}	component *jk* of the core deviatoric stress tensor
τ_{ojk}	component *jk* of the clad deviatoric stress tensor
τ^o_{jk}	component *jk* of the clad deviatoric stress tensor
ω	shear rate
ω_d	diluent mass fraction
ω_p	polymer mass fraction
ξ	ratio of critical molar volumes for diluent and polymer molar jumping units

Bibliography

1. Agrawal, A. K. and R. Bhalla (2003). "Advances in the production of poly(lactic acid) fibers. A review." Journal of Macromolecular Science-Polymer Reviews C43(4): 479-503.
2. Alkemper, J., V. A. Snyder, et al. (1999). "Dynamics of late-stage phase separation: a test of theory." Physical Review Letters 82(13): 2725-2728.
3. Altinkaya, S. A. and B. Ozbas (2004). "Modeling of asymmetric membrane formation by dry-casting method." Journal of Membrane Science 230(1-2): 71-89.
4. Alwattari, A. A. and D. R. Lloyd (1991). "Microporous membrane formation via thermally-induced phase separation. VI. Effect of diluent morphology and relative crystallization kinetics on polypropylene membrane structure." Journal of Membrane Science 64: 55-68.
5. Arthanareeswaran, G., K. Srinivasan, et al. (2004). "Studies on cellulose acetate and sulfonated poly(ether ether ketone) blend ultrafiltration membranes." European Polymer Journal 40(4): 751-762.
6. Ashman, B. (1998). Stability of Hollow Fiber Spinning. Department of Chemical Engineering. Toledo, University of Toledo.
7. Atkinson, P. M. (1999). Formation of anisotropic flat sheet membranes via evaporative TIPS. Chemical Engineering. Austin, The University of Texas at Austin.
8. Atkinson, P. M. and D. R. Lloyd (2000). "Anisotropic flat sheet membrane formation via TIPS: Forced convection and molecular weight effects." Journal of Membrane Science 175(2): 225-238.
9. Atkinson, P. M. and D. R. Lloyd (2000). "Anisotropic flat sheet membrane formation via TIPS: Thermal effects." Journal of Membrane Science 171: 1-18.
10. Batarseh, M. T. (1999). Formation of anisotropic hollow fiber membranes via TIPS. Department of Chemical Engineering. Austin, The University of Texas at Austin.
11. Batarseh, M. T., H. A. Balasubramanian, et al. (2004). "Anisotropic hollow fiber membrane formation. I. Prediction of concentration profiles." In preparation.
12. Batarseh, M. T., H. A. Balasubramanian, et al. (2004). "Anisotropic hollow fiber membrane formation. II. Prediction of cooling rate profiles." In preparation.
13. Berghmans, S., H. Berghmans, et al. (1996). "Spinning of hollow porous fibres via the TIPS mechanism." Journal of Membrane Science 116: 171-189.
14. Berne, B. J. and R. Pecora (1976). Dynamic Light Scattering with Applications to Chemistry, Biology, and Physics. New York, John Wiley & Sons.
15. Beysens, D. (1997). "Kinetics and morphology of phase separation in fluids: the role of droplet coalescence." Physica A 239(1-3): 329-339.
16. Binder, K. (1983). "Collective diffusion, nucleation, and spinodal decomposition in polymer mixtures." J. Chem. Phys. 79(12): 6387-6409.
17. Bird, R. B., W. E. Stewart, et al. (1960). Transport Phenomena. New York, John Wiley & Sons.
18. Bob, D. (2004). Infrared Community Forum, Infrared Training Center. 2004.
19. Brandrup, J., E. H. Immergut, et al., Eds. (1999). Polymer Handbook. New York, John Wiley & Sons.

20. Brazinsky, I., A. G. Williams, et al. (1975). "The dry spinning process: comparison of theory with experiment." Polymer Engineering and Science 15(12): 834-841.
21. Bulters, M. J. H. and H. E. H. Meijer (1990). "Analogy between the modelling of pullout in solution spinning and the prediction of the vortex size in contraction flows." Journal of Non-Newtonian Fluid Mechanics 38: 43-80.
22. Cabasso, I. (1987). Membranes. Encyclopedia of Polymer Science and Engineering. J. I. Kroschwitz. New York, John Wiley & Sons. 9.
23. Caneba, G. T. and D. S. Soong (1985). "Polymer membrane formation through the thermal-inversion process. 2. Mathematical modeling of membrane structure formation." Macromolecules 18: 2545-2555.
24. Carslaw, H. S. and J. C. Jaeger (1959). Conduction of Heat in Solids. Oxford, UK, Oxford University Press.
25. Castellari, C., R. Francesconi, et al. (1988). "Latent skin in asymmetric Loeb-type hollow fiber membrane." Polymer Engineering and Science 28(2): 113-119.
26. Castro, A. J. (1981). Methods for making microporous products. US, Akzona Inc.
27. Chandler, K. W., J. Peddieson, et al. (2002). "An improved 1D fiber dry spinning mass transfer model." Mechanics Research Communications 29(5): 351-357.
28. Chang, J. C., M. M. Denn, et al. (1981). "Effects of Inertia, Surface-Tension, and Gravity on the Stability of Isothermal Drawing of Newtonian Fluids." Industrial & Engineering Chemistry Fundamentals 20(2): 147-149.
29. Cheng, L.-P. (1993). Mechanism Of Microporous Membrane Formation By Precipitation Of Semicrystalline Polymers (Polyamides), Columbia University, New York.
30. Cheremisinoff, N. P., Ed. (1986). Handbook of Heat and Mass Transfer. Houston, Gulf Publishing Co.
31. Chu, B. (1974). Laser Light Scattering. New York, Academic Press.
32. Chung, B. T. F. and V. Iyer (1992). "Heat transfer from moving fibers in melt spinning process." Journal of Applied Polymer Science 44: 663-670.
33. Chung, T.-S., Z.-L. Xu, et al. (1999). "Fundamental understanding of the effect of air-gap distance on the fabrication of hollow fiber membranes." Journal of Applied Polymer Science 72: 379-395.
34. D'Andrea, R. G. and C. B. Weinberger (1976). "Effects of surface tension and gravity forces in determining the stability of isothermal fiber spinning." AIChE Journal 22(5): 923-925.
35. Deen, W. M. (1998). Analysis of transport phenomena. New York, Oxford University Press.
36. Denn, M. M., C. J. S. Petrie, et al. (1975). "Mechanics of Steady Spinning of a Viscoelastic Liquid." Aiche Journal 21(4): 791-799.
37. Denn, M. M. (1980). "Continuous drawing of liquids to form fibers." Annual Reviews of Fluid Mechanics 12: 365-387.
38. Denn, M. M. (1983). Computational analysis of polymer processing. Computational analysis of polymer processing. S. M. Richardson. London, Applied Science Publishers.
39. Denn, M. M. (1983). Fibre Spinning. Computational Analysis of Polymer Processing. J. R. A. Pearson and S. M. Richardson. London, Applied Science Publishers: 179-216.
40. Doi, S. and K. Hamanaka (1991). "Pore-Size Control Technique in the Spinning of Polysulfone Hollow Fiber Ultrafiltration Membranes." Desalination 80(2-3): 167-180.

41. Doufas, A. K. and A. J. McHugh (2001). "Two-dimensional simulation of melt spinning with a microstructural model for flow-induced crystallization." Journal of Rheology 45(4): 855-879.
42. Fieldson, G. T. and T. A. Barbari (1993). "The Use of Ftir-Atr Spectroscopy to Characterize Penetrant Diffusion in Polymers." Polymer 34(6): 1146-1153.
43. Fisher, R. J., and M. M. Denn (1977). "Mechanics of nonisothermal polymer melt spinning." AIChe Journal 23(1): 23-28.
44. Fisher, R. J. and M. M. Denn (1975). "Draw resonance in melt spinning." Applied Polymer Symposium 27: 103-109.
45. Flory, P. J. (1953). Principles of polymer chemistry, Cornell University Press.
46. Ford, N. C., F. E. Karasz, et al. (1970). "Rayleigh scattering from polystyrene solutions." Discussions of the Faraday Society 49: 228-237.
47. Freeman, B. D., M. M. Denn, et al. (1986). "Profile development in drawn hollow tubes." Journal of Polymer Engineering 6(1-4): 171-186.
48. Fried, J. R. (1995). Polymer Science and Technology. Englewood Cliffs, NJ, Prentice Hall.
49. Gabelman, A. and S. T. Hwang (1999). "Hollow fiber membrane contactors." Journal of Membrane Science 159(1-2): 61-106.
50. Gospodinov, P. and V. Roussinov (1993). "Nonlinear instability during the isothermal draw of optical fibers." International Journal of Multiphase Flow 19(6): 1153-1158.
51. Gou, Z. M. and A. J. McHugh (2003). "A comparison of Newtonian and viscoelastic constitutive models for dry spinning of polymer fibers." Journal of Applied Polymer Science 87(13): 2136-2145.
52. Hagen, T. (2002). "On the effects of spinline cooling and surface tension in fiber spinning." Zeitschrift Fur Angewandte Mathematik Und Mechanik 82(8): 545-558.
53. Hagen, T. C. (1998). Elongational flows in polymer processing. Mathematics. Blacksburg, VA, Virginia Polytechnic Institute and State University: 96.
54. Harvey, A. (2000). http://www.madsci.org/posts/archives/nov2000/974149753.Ch.r.html, MadSci Network.
55. Hasegawa, T., D. S. Martula, et al. (2000). "Coalescence-induced coalescence: calculation of the velocity field." Physics of Fluids in preparation.
56. Hashimoto, T., J. Kumaki, et al. (1983). "Time-resolved light scattering studies on kinetics of phase separation and phase dissolution of polymer blends. 1. Kinetics of phase separation of a binary mixture of polystyrene and poly(vinyl methyl ether)." Macromolecules 16: 641-648.
57. Hayes, L. J. (1997). Modeling hollow fiber spinning transport phenomena after phase separation. M. Batarseh. Austin, TX.
58. Hill, J. W. and J. A. Cuculo (1974). "An experimental study of threadline dynamics with emphasis on the effect of molecular weight on the elongational viscosity of melt-spun poly(ethylene terephthalate)." Journal of Applied Polymer Science 18: 2569-2588.
59. Hines, A. L. and R. N. Maddox (1985). Mass transfer: fundamentals and applications. Englewood Cliffs, PTR Prentice Hall.
60. Ho, W. S. W. (2003). "Recent developments and applications for hollow-fiber membranes." Journal of the Chinese Institute of Chemical Engineers 34(1): 75-89.

61. Ho, W. S. W. and K. K. Sirkar (1992). Membrane Handbook. New York, Van Nostrand Reinhold.
62. Hong, S. U. and T. A. Barbari (2001). "Transport of toluene/methyl ethyl ketone mixtures polyisobutylene." Journal of Polymer Science Part B-Polymer Physics 39(9): 908-914.
63. Hong, S. U., T. A. Barbari, et al. (1997). "Diffusion of methyl ethyl ketone in polyisobutylene: Comparison of spectroscopic and gravimetric techniques." Journal of Polymer Science Part B-Polymer Physics 35(8): 1261-1267.
64. Howell, J. R. (1982). A Catalog of Radiation Configuration Factors. New York, McGraw-Hill.
65. Howell, J. R. (2003). Infrared Measurement of Polyethylene Spinlines. H. Balasubramanian. Austin, TX.
66. http://buphy.bu.edu/py106/notes/Refraction.html (2000). Boston University, PY106--Elementary Physics II. United States.
67. http://www.goodfellow.com/csp/active/static/A/ET31.HTML (2004). Goodfellow Corporation.
68. Hyun, J. C. (1978). "Theory of draw resonance: Part II. Power law and maxwell fluids." AIChE Journal 24(3): 423-426.
69. Idris, A., A. F. Ismail, et al. (2002). "Optimization of cellulose acetate hollow fiber reverse osmosis membrane production using Taguchi method." Journal of Membrane Science 205(1-2): 223-237.
70. Irani, K. (2004). Use of infrared thermography for detecting polyethylene temperature. H. Balasubramanian. Austin, TX.
71. Kase, S. and T. Matsuo (1967). "Studies on melt spinning. II. Steady-state and transient solutions of fundamental equations compared with experimental results." Journal of Applied Polymer Science 11: 251-287.
72. Kesting, R. E. (1985). Phase inversion membranes. Materials Science of Synthetic Membranes. D. R. Lloyd. Washington, DC, ACS Press. 269: 131-163.
73. Kim, I. C. and K. H. Lee (2004). "Effect of poly(ethylene glycol) 200 on the formation of a polyetherimide asymmetric membrane and its performance in aqueous solvent mixture permeation." Journal of Membrane Science 230(1-2): 183-188.
74. Kim, S. S. (2000).
75. Kim, S. S., G. B. A. Lim, et al. (1991). "Microporous membrane formation via thermally-induced phase separation. V. Effect of diluent mobility and crystallization on the structure of isotactic polypropylene membranes." Journal of Membrane Science 64: 41-53.
76. Kim, S. S. and D. R. Lloyd (1991). "Microporous membrane formation via thermally-induced phase separation. III. Effect of thermodynamic interactions on the structure of isotactic polypropylene membranes." Journal of Membrane Science 64: 13-29.
77. Kim, S. Y., T. Kanamori, et al. (2004). "Preparation of porous poly(D,L-lactide) and poly(D,L-lactide-co-glycolide) membranes by a phase inversion process and investigation of their morphological changes as cell culture scaffolds." Journal of Applied Polymer Science 92(4): 2082-2092.
78. Kopp, C. V., R. J. W. Streeton, et al. (1995). Hollow fibre membrane extrusion. US, Memtec Limited.

79. Lal, J. and R. Bansil (1991). "Light-scattering study of kinetics of spinodal decomposition in a polymer solution." Macromolecules 24: 290-297.
80. Laxminarayan, A. (1994). The kinetics of membrane formation via thermally induced liquid-liquid phase separation, The University of Texas at Austin.
81. Li, S. G., G. H. Koops, et al. (1994). "Wet Spinning of Integrally Skinned Hollow-Fiber Membranes by a Modified Dual-Bath Coagulation Method Using a Triple Orifice Spinneret." Journal of Membrane Science 94: 329-340.
82. Lim, G. B. A. (1990). Effects of nucleating agent on thermally induced phase separation membrane formation, The University of Texas at Austin.
83. Lim, G. B. A., S. S. Kim, et al. (1991). "Microporous membrane formation via thermally-induced phase separation. IV. Effect of isotactic polypropylene crystallization kinetics on membrane structure." Journal of Membrane Science 64: 31-40.
84. Lipscomb, G. G. (1994). "The melt hollow fiber spinning process: Steady-state behavior, sensitivity and stability." Polymers for Advanced Technologies 5: 745-758.
85. Liu, Y., G. H. Koops, et al. (2003). "Characterization of morphology controlled polyethersulfone hollow fiber membranes by the addition of polyethylene glycol to the dope and bore liquid solution." Journal of Membrane Science 223(1-2): 187-199.
86. Lloyd, D. R. (1985). Materials Science of Synthetic Membranes. Washington, DC, ACS Press.
87. Lloyd, D. R., J. W. Barlow, et al. (1988). Microporous membrane formation via thermally-induced phase separation. New Membrane Materials and Processes for Separation, AIChE Symposium Series 261. K. K. Sirkar and D. R. Lloyd. New York.
88. Lloyd, D. R., S. S. Kim, et al. (1991). "Microporous membrane formation via thermally-induced phase separation. II. Liquid-liquid phase separation." Journal of Membrane Science 64: 1-11.
89. Lloyd, D. R., K. E. Kinzer, et al. (1990). "Microporous membrane formation via thermally-induced phase separation. I. Solid-liquid phase separation." Journal of Membrane Science 52: 239-261.
90. Mahendran, R., R. Malaisamy, et al. (2004). "Preparation, characterization and effect of annealing on performance of cellulose acetate/sulfonated polysulfone and cellulose acetate/epoxy resin blend ultrafiltration membranes." European Polymer Journal 40(3): 623-633.
91. Mark, J. E., Ed. (1996). Physical properties of polymers handbook. AIP series in polymers and complex materials. Woodbury, N.Y., AIP Press.
92. Martula, D. S. (2000). Coalescence-induced coalescence. Department of Chemical Engineering. Austin, The University of Texas at Austin.
93. Martula, D. S., R. T. Bonnecaze, et al. (2003). "The effects of viscosity on coalescence-induced coalescence." International Journal of Multiphase Flow 29: 1265-1282.
94. Martula, D. S., T. Hasegawa, et al. (2000). "Coalescence-induced coalescence of inviscid droplets in a viscous fluid." Journal of Colloid and Interface Science 232: 241-253.
95. Matovich, M. A. and J. R. A. Pearson (1969). "Spinning a Molten Threadline. Steady-State Isothermal Viscous Flows." Ind. Eng. Chem. Fundam. 8(3): 512-520.
96. Matsuyama, H. (2003). Apparent Diffusion Coefficient Results. H. Balasubramanian.

97. Matsuyama, H., S. Berghmans, et al. (1998). "Effects of thermal history on anisotropic and asymmetric membranes formed by thermally induced phase separation." Journal of Membrane Science 142: 27-42.
98. Matsuyama, H., S. Berghmans, et al. (1999). "Formation of anisotropic membranes via thermally induced phase separation." Polymer 40: 2289-2301.
99. Matsuyama, H., M.-M. Kim, et al. (2002). "Effect of extraction and drying on the structure of microporous polyethylene membranes prepared via TIPS." Journal of Membrane Science 204: 413-418.
100. Matsuyama, H., S. Kudari, et al. (2000). "Kinetic studies of thermally induced phase separation in polymer-diluent system." journal of Applied Polymer Science 76: 1028-1036.
101. 100.Matsuyama, H., M. Teramoto, et al. (1999). "Kinetics of droplet growth in metastable region in cellulose acetate/aceton/nonsolvent system." Journal of Membrane Science 152: 227-234.
102. 101.McGuire, K. S. (1995). Membrane formation via liquid-liquid thermally induced phase separation, The University of Texas at Austin.
103. 102.McGuire, K. S., A. Laxminarayan, et al. (1994). "A simple method of extrapolating the co-existence curve and predicting the melting point depression curve cloud point data for polymer-diluent systems." Polymer 35: 4404-4407.
104. 103.McGuire, K. S., A. Laxminarayan, et al. (1995). "Kinetics of droplet growth in liquid-liquid phase separation of polymer-diluent systems: experimental results." Polymer 36(26): 4951-4960.
105. 104.McGuire, K. S., A. Laxminarayan, et al. (1996). "Kinetics of droplet growth in liquid-liquid phase separation of polymer-diluent systems: model development." Journal of Colloid and Interface Science 182: 46-58.
106. 105.McGuire, K. S., D. R. Lloyd, et al. (1993). "Microporous membrane formation via thermally-induced phase separation. VII. Effect of dilution, cooling rate, and nucleating agent addition on morphology." Journal of Membrane Science 79: 27-34.
107. 106.McKelvey, S. A., D. T. Clausi, et al. (1997). "A guide to establishing hollow fiber macroscopic properties for membrane applications." Journal of Membrane Science 124: 223-232.
108. 107.Mulder, M. H. V. (1991). Basic principles of membrane technology. Dordrecht, Kluwer Academic Press.
109. 108.Nakajima, A., H. Fujiwara, et al. (1966). "Phase relationships and thermodynamic interactions in linear polyethylene-diluent systems." Journal of Polymer Science: Part A-2 4: 507-518.
110. 109.Oh, T. H., M. S. Lee, et al. (1998). "Studies on melt-spinning process of hollow fibers." Journal of Applied Polymer Science 68(8): 1209-1217.
111. 110.Ohzawa, Y. and Y. Nagano (1970). "Studies on dry spinning. II. Numerical solutions for some polymer-solvent systems based on the assumption that drying is controlled by boundary-layer mass transfer." Journal of Applied Polymer Science 14: 1879-1899.
112. 111.Ohzawa, Y., Y. Nagano, et al. (1969). "Studies on dry spinning. I. Fundamental equations." Journal of Applied Polymer Science 13: 257-283.
113. Paula, J. C. d. (2004). Experimental Errors and Data Analysis, Haverford College. 2004.

114. Pearson, J. R. A. and Y. T. Shah (1972). "On the stability of nonisothermal fiber spinning--general case." Ind. Eng. Chem. Fundam. 11(2): 150-153.
115. Petrie, C. J. S. and M. M. Denn (1976). "Instabilities in polymer processing." American Institute of Chemical Engineers Journal 22(2): 209-236.
116. Phillies, G. D. J. (1991). "Probe diffusion in polymer solutions." SPIE Photon Correlation Spectroscopy: Multicomponent Systems 1430: 118-131.
117. Porter, M. C. (1990). Handbook of Industrial Membrane Technology. Park Ridge, NJ, Noyes Publishing.
118. Rovère, A. D., B. P. Grady, et al. (2002). "The influence of processing parameters on the properties of melt-spun polypropylene hollow fibers." Journal of Applied Polymer Science 83(8): 1759-1772.
119. Rovère, A. D. and R. L. Shambaugh (2001). "Melt-Spun Hollow Fibers: Modeling and Experiments." Polymer Engineering and Science 41(7): 1206-1219.
120. Rowley, R. L., W. V. Wilding, et al. (2001). DIPPR® Data Compilation of Pure Compound Properties, Design Institute for Physical Property Data, AIChE®, New York, NY.
121. Sanchez, I. C. (1992). Encyclopedia of Physical Science and Technology, Academic Press, Inc.
122. Schlichting, H. (1960). Boundary Layer Theory. New York, McGraw-Hill.
123. Schuurmans, F. J. P., M. Megens, et al. (1999). "Light scattering near the localization transition in macroporous GaP networks." Physical Review Letters 83(11): 2183-2186.
124. Scott, K. (1995). Handbook of Industrial Membranes, Elsevier Science Publishers, Ltd.
125. Shilton, S. J., G. Bell, et al. (1994). "The Rheology of Fiber Spinning and the Properties of Hollow-Fibre Membranes for Gas Separation." Polymer 35(24): 5327-5335.
126. Shojaie, S. S., W. B. Krantz, et al. (1992). "Development and validation of a model for the formation of evaporatively cast polymeric films." Journal of Materials Processing and Manufacturing Science 1: 181-194.
127. Shojaie, S. S., W. B. Krantz, et al. (1994). "Dense polymer film and membrane formation via the dry-cast process, Part I. Model development." Journal of Membrane Science 94: 255-280.
128. Shojaie, S. S., W. B. Krantz, et al. (1994). "Dense polymer film and membrane formation via the dry-cast process, Part II. Model validation and morphological studies." Journal of Membrane Science 94: 281-298.
129. Siegel, R. and J. R. Howell (2002). Thermal Radiation Heat Transfer. New York, Taylor & Francis.
130. Simon, V. (1994). "The temperature of fibers during air-gap wet spinning: Cooling by convection and evaporation." International Journal of Heat and Mass Transfer 37: 1133-1142.
131. Simon, V. (1995). "Analysis of fiber formation during air-gap wet spinning." AIChE Journal 41: 1281-1294.
132. Stiehl, J. D. (1999). Undergraduate research report, The University of Texas at Austin.
133. Sun, H., K. B. Rhee, et al. (2000). "HDPE hollow fiber membrane via thermally induced phase separation II. Factors affecting the water permeability of the membrane." Journal of Applied Polymer Science 75: 1235-1242.

134. Tan, L., W. B. Krantz, et al. (1995). "Studies of convective transport in evaporative casting of dense polymer films." Journal of Membrane Science 108: 245-255.
135. Tompa, H. (1956). Polymer Solutions. London, Butterworths.
136. Tsai, C.-C., T.-J. Liu, et al. (1997). "Numerical simulation of an optical fiber-forming process." Chemical Engineering Science 52(2): 221-235.
137. Tsay, C. S. and A. J. McHugh (1990). "Mass transfer modeling of asymmetric membrane formation by phase inversion." Journal of Polymer Science: Part B: Polymer Physics 28: 1327-1365.
138. Tsay, C. S. and A. J. McHugh (1991). "The combined effects of evaporation and quench steps on asymmetric membrane formation by phase inversion." Journal of Polymer Science: Part B: Polymer Physics 29: 1261-1270.
139. Tsay, C. S. and A. J. McHugh (1991). "Mass transfer dynamics of the evaporation step in membrane formation by phase inversion." Journal of Membrane Science 64: 81-92.
140. Vrentas, J. S. and J. L. Duda (1977). "Diffusion in Polymer-Solvent Systems. I. Reexamination of the Free-Volume Theory." Journal of Polymer Science: Polymer Physics Edition 15: 403-416.
141. Wienk, I. M., F. H. A. Olde Scholtenhuis, et al. (1995). "Spinning of hollow fiber ultrafiltration membranes from a polymer blend." Journal of Membrane Science 106: 233-243.
142. Yarin, A. L., and P. Gospodinov (1994). "Stability loss and sensitivity in hollow fiber drawing." Physics of Fluids 6(4): 1454-1463.
143. Ziabicki, A. (1976). Fundamentals of fibre formation. New York, John Wiley.
144. Zielinski, J. M. and J. L. Duda (1992). "Predicting Polymer/Solvent Diffusion Coefficients Using Free-Volume Theory." AIChE Journal 38(3): 405-415.

VITA

Holly Ann Balasubramanian was born in Nashville, Tennessee on January 6, 1977, the daughter of Melba Ruth Dyer Balasubramanian and K. Balasubramanian. She graduated from Dickson County High School in June 1994 as co-valedictorian and gold medalist of her class, continuing her education at Tennessee Technological University in Cookeville, Tennessee. Completing her B.S. degree in chemical engineering with a double major in chemistry and a minor in mathematics, she graduated In Cursu Honorum, Summa Cum Laude in May 1999 and began chemical engineering graduate studies at The University of Texas at Austin in July 1999. Prior to finishing her doctoral studies, she obtained an M.S. in chemical engineering in May 2003. After graduation, Holly will join The Procter and Gamble Company as a research and development engineer in Cincinnati, Ohio.

Permanent address: 1529 Roy Brown Road, Burns, TN 37029

This dissertation was typed by the author.